HPFRC AND RC SLAB-BEAM-COLUMN CONNECTIONS UNDER EXTREME EARTHQUAKE LOADING AND FURTHER IMPROVEMENT OF NOVEL DOUBLE-BEAM-COUPLING BEAMS

by

YOUNGJAE CHOI

Presented to the Faculty of the Graduate School of

The University of Texas at Arlington in Partial Fulfillment

of the Requirements

for the Degree of

DOCTOR OF PHILOSOPHY

THE UNIVERSITY OF TEXAS AT ARLINGTON

December 2018

Acknowledgements

I would like to acknowledge and thank each of the members of my dissertation committee. I especially want to thank to my advisor Dr. Shih-Ho Chao for his great assistant and advises during my doctoral program. This doctoral program would have been impossible without support from my wife and family. I shall be always grateful for their love and support throughout the process.

November 20, 2018

Abstract

HPFRC AND RC SLAB-BEAM-COLUMN CONNECTIONS UNDER EXTREME EARTHQUAKE LOADING AND FURTHER IMPROVEMENT OF NOVEL DOUBLE-BEAM-COUPLING BEAMS

YOUNGJAE CHOI, PhD

The University of Texas at Arlington, 2018

Supervising Professor: SHIH-HO CHAO

The work presented in this dissertation is divided into two parts. Each part has drawn its own results.

Reinforced concrete (RC) buildings resist a strong earthquake through structural foundations, diaphragms, and vertical elements. Moment-resisting frames and shear walls are primary-used vertical elements in RC buildings. The moment-resisting frames consist of columns, beams that frame into the column and beam column joints where the columns and beams meet. A key point of designing the moment-resisting frames against a strong earthquake is to ensure beam-column connections to dissipate as much energy possible. The shear wall often becomes two separate slender cantilever walls due to the requirement for openings over its height. It is the coupling beams that connect these two walls to act as a single wall. This system is called coupled wall. A key point of designing the coupled wall is to assure the coupling beams to resist large rotations, maintaining their strength and stiffness.

For the past decades, there has been remarkable achievement on improving the seismic performance of those vertical elements. Although it seems their performance against a strong earthquake is in a safe zone, there have been issues that are related to their construction. Both elements are often found to be very difficult to construct due to either steel reinforcement congestions or difficult steel reinforcement details. The research presented in this dissertation is results of attempts to make their construction much practicable by using either different materials or different steel reinforcement details.

Table of Contents

List of Illustrations

List of Tables

Chapter 1

INTRODUCTION TO THE FIRST PHASE

1.1 Design Philosophy of Reinforced Concrete Special Moment-Resisting Frames

Reinforced concrete special moment-resisting frames (RC-SMFs, Figure 1.1) are commonly used as a seismic force-resisting system in high-seismic zones. RC-SMFs consist of columns, beams framing into the columns, and joints where the columns and beams meet. For RC-SMFs to develop stable seismic responses, ACI 318 (ACI, 2014) provisions recommend: 1) the strong-column/weak-beam (SCWB) principle to assure plastic hinges form in the beams, 2) a flexural yielding mechanism in the beams, and 3) a capacity design approach to prevent less ductile failure modes such as shear failure in beams.

The strong-column/weak-beam (SCWB) principle leads RC-SMFs to the beam mechanism in which columns are designed stronger and stiffer than beams. Consequently, damage is concentrated in the beams, allowing a uniform distribution of the lateral drift over the height of the building. This failure mechanism is desirable since it minimizes a localized damage in the building. A failure of achieving the strong-column/weak-beam principle can localize the damage in columns of a few stories and the resultant drift can exceed the drift capacity of those columns. This failure mechanism that is called story mechanism can jeopardize entire building since unlike the beams columns usually support entire weight of the building above them (Figure 1.2). For this purpose, ACI 318 -14 requires the nominal strength of columns to be 1.25 times greater than that of beams of RC-SMFs.

The beam mechanism requires beams to yield in flexure. Shear failure in any members, such as beams, columns and beam-column joints, need to be avoided since it is sudden and decreases the strength and stiffness of the members rapidly (Figure 1.3). A capacity design approach is used in design to prevent the shear failure. It is important in the capacity design to find the regions where flexure yielding

can develop. In RC-SMFs, the flexure yielding is likely to occur in beam-column connections. The beam-column connections are defined where the regions of beams and columns adjacent beam-column joints. Then, determine design shear based on probable moment strengths. The probable moment strengths are results of consideration of actual yield strength and strain hardening of steel reinforcement (multiply 1.25 to specified yield strength of steel reinforcement).

Once beams yield in flexure, ductile responses are required. The ductile response of RC-SMFs can be achieved by placing a good amount of steel transverse reinforcement, such as hoops and crossties. When the transverse reinforcement is placed in compression member such as columns, it detains compression failure of concrete by increasing the usable compressive strain of the concrete. In addition, providing confinement in beams' plastic hinge regions (near column faces where flexural yielding occurs) keeps concrete integrity during earthquakes, which allows concrete to resist shear force by forming a truss mechanism. Furthermore, properly detailed transverse reinforcement prevents the buckling of longitudinal reinforcement and provides adequate shear strength in the plastic hinge regions

.

As shown in Figure 1.4, failure in beam-column joints can affect the stability of an entire building. For a moderate earthquake, the joints need to behave in an elastic domain, while some inelastic behavior is allowed for a strong earthquake. The joints are subjected to relatively high shear force during earthquakes, which is approximately five times higher than that in columns. Figure 1.5 illustrates the resultant moment, shear, and axial force that act around the joints. Figure 1.6 and 1.7 show the internal stress resultants on a beam-column joint and shear calculation of the joint. ACI 318-14 considers only concrete contribution to joint shear strength. Therefore, the shear in a beam-column joint is resisted only by a concrete strut as seen in Figure 1.6. The joint shear strength is calculated by Equation 1-1. And, it generally depends on the size of joints, since b_j and h represent beam width and joint depth, respectively.

$$V_n = \gamma \sqrt{f_c'} b_j h \qquad 1.1$$

γ is 1 for normal concrete. However, the code still requires plenty of transverse reinforcement to confine the concrete in the joints for ductile behavior during a strong earthquake.

1.2 Previous works, Research Objectives, and Scope.

Modern RC buildings often have perimeter RC-SMFs to resist seismic force. These RC-SMFs are usually combined with an interior post-tensioned slab-column system to carry the gravity loads. Since only a few RC-SMFs are used to resist the lateral forces and provide lateral stiffness, the size of the spandrel beams and columns in the perimeter frames can be very large. Visnjic et al. (2016) tested two large size cantilever beams with 48 in. depth. The beams were connected to a big RC block which was anchored to the strong floor. Consequently, the joint behavior was not considered in their testing. Their test results showed that: 1) beams with a deeper depth were much more vulnerable to the buckling of longitudinal reinforcement than the beams with a normal depth, 2) beam failure was eventually triggered by rebar buckling in its plastic hinge region, and 3) bar buckling can be delayed by reducing the spacing of the transverse reinforcement in the plastic hinge region.

Due to the concerns about the adequacy of longitudinal bar buckling restraint and confinement, ACI 318 changed its provision in the 2011 edition by reducing the spacing of the transverse reinforcement for large beams. This code change introduces additional reinforcement in the already congested plastic hinging regions. This congestion together with the required transverse reinforcement for confinement in beam-column joints makes the construction of beam-column connection less practicable. The construction difficulties due to the congestion have been an issue in RC-SMFs for many years.

To resolve the issue, a balanced damage concept is introduced in this study. The balanced damage concept has been investigated in steel SMFs and utilizes both beam-column joint (panel zone) and beams as major energy-dissipating components to prevent concentrated damage in beams (Choi et al., 2003). This is achieved because the shear response of a steel panel zone shows highly ductile

behavior. Unlike steel SMFs, however, beam-column joints of RC SMFs are conventionally designed not to be the major energy-dissipating components. If this concept can be applied to RC-SMFs, bar yielding and buckling in the beam plastic regions can be delayed.

In addition, a ductile RC joint could be achieved by using the tensile ductility high-performance fiber-reinforced concrete (HPFRC), which also provides high shear resistance and confinement capability (Parra-Montesions et al. 2005), thereby reducing the need for congestive transverse reinforcement in the plastic hinge regions. This research presents an experimental study which evaluates the feasibility of utilizing both the HPFRC joints and beams as major sources of energy-dissipating components in modern high-rise perimeter RC-SMFs.

The potential advantages of the balanced damage concept are: 1) preventing concentrated damage in beam plastic hinge regions and delaying the yielding penetration of beams longitudinal reinforcement, thereby delaying or preventing the rebar buckling, even without transverse reinforcement, 2) minimizing the need for repair after moderate earthquakes, and 3) enhancing the energy-dissipating capability of RC beam-column joints even with limited confining reinforcement.

To ensure the balanced damage concept meets modern performance-based criteria, this study refers to ACI Committee 374 criteria (ACI, 2013) in which structural performance is described by four respective levels as a function of lateral story drift ratio (Figure 1.8). For primary components such as beams, columns, and joints, ACI 374 allows minor hair line cracks at the operational level, while accepting limited yielding at the immediate occupancy level with an SDR not exceeding 1%. It also permits extensive cracking and hinge formation in ductile elements for the collapse prevention level with an SDR not exceeding 4%.

This paper presents an experimental study on the seismic performance of reinforced concrete (RC) perimeter interior special moment frames (SMFs), which use high-performance fiber-reinforced concrete (HPFRC) in joint and beam plastic hinge regions. This research evaluates the feasibility of

utilizing both HPFRC joint and beams as major sources of energy dissipation in an effort to reduce overall damage and repair cost after earthquakes and to provide ease of construction for beam-column connections. A balanced damage concept was used so the energy dissipation was shared by the joint and beam plastic hinges, thereby preventing severe damage from occurring to the beams. This concept together with the mechanical properties provided by HPFRC, including high shear and bond strength, reduce the need of placing a large number of transverse reinforcement in the joint and beam plastic hinge regions. A full-scale HPFRC slab-beam-column (SBC) subassemblage designed with this concept was tested under large displacement reversals. This specimen used a small amount of transverse reinforcement in the joint and no transverse reinforcement in the beam plastic hinge regions thus significantly enhancing the constructability. Counterpart two conventional RC specimen compliant with ACI 318-14 were tested under two different types of loading protocols; the same loading used for the HPFRC specimen and the loading that represents a near collapse.

All specimens showed stable hysteretic responses up to 3.5% column drift ratio without significant strength degradation, which meets the collapse prevention structural performance according to the criteria given in ACI 374. Experimental results show that the damage in the HPFRC specimen was distributed in both joint and beam ends, whereas the conventional RC specimens had severe damage concentrated in the beam plastic hinging regions. This research proves the feasibility of utilizing ductile HPFRC joint to dissipate seismic energy, thereby balancing the damage between the joint and beams.

1.3 Research Significance

Current design practice on RC-SMFs results in unnecessary construction difficulties because it requires an excessive amount of transverse reinforcement in the joint and plastic hinge regions. This research presents a pilot test, which investigates a balanced damage concept utilizing HPFRC in the joint and beam plastic hinge regions that not only can enhance constructability but also minimize the overall repair work after earthquakes.

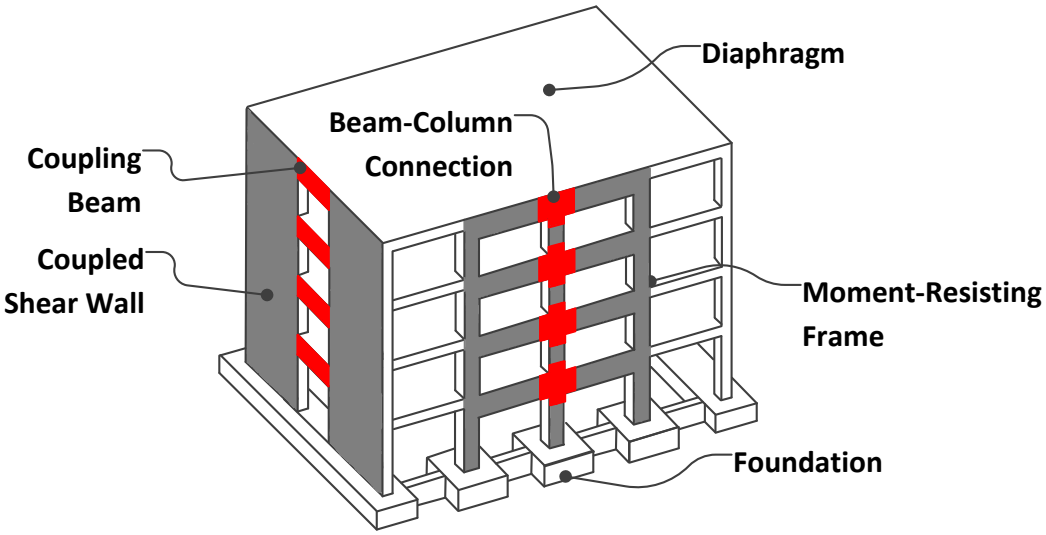

1.1 Reinforced concrete moment-resisting frame

1.2 Building collapse due to story mechanism (Chi-Chi, Taiwan, 1999)

1.3 Column shear failure (Moehle et al., 2008)

1.4 Joint shear failure

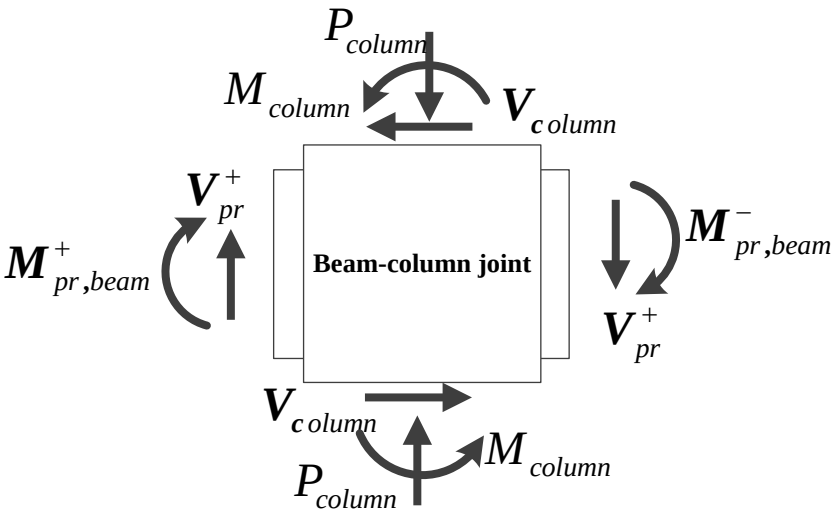

1.5 Moment, shear, and axial force around beam-column joint

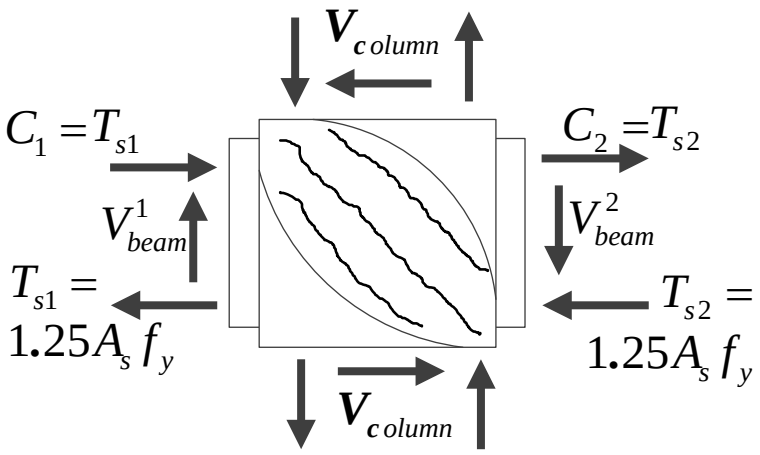

1.6 Internals stress resultants on beam-column joint

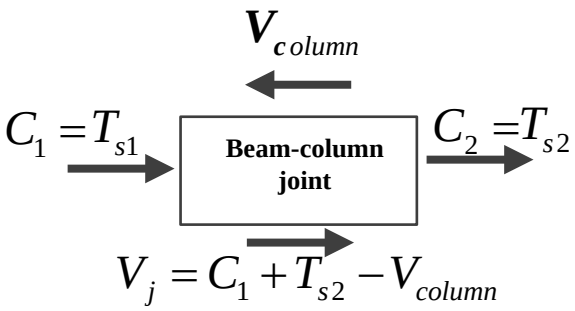

1.7 Shear calculation of beam-column joint

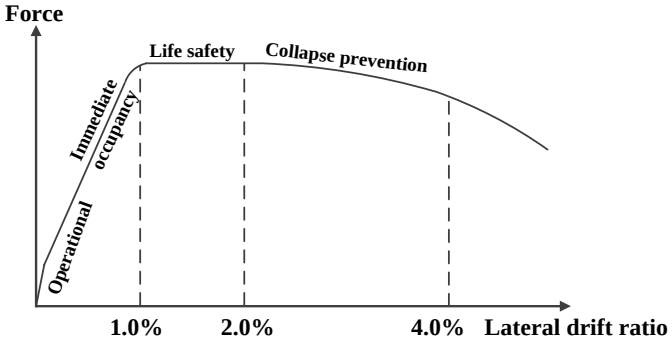

1.8 Structural performance levels (ACI, 2013)

Chapter 2

EXPERIMENTAL PROGRAM

2.1 Properties of Concrete Materials

Details of the mix design and properties of the steel fibers used in this study are shown in Table 2.1 and 2.2, respectively. Fibers used in the HPFRC were twisted steel fibers with a diameter of 0.02 in. and an ultimate tensile strength of 355 ksi. Both 2 in. long and 0.55 in. short fibers were used with volume fractions of 1.2% and 0.5% and aspect ratio of 100 and 28, respectively, and a total volume fraction of 1.7% (8.43 lb/ft^3). HPFRC was made by adding twisted high-strength steel fibers into a ready-mix concrete mix.

Table 2-1 Relative composition of concrete mixture by weight and compressive strength

Cement (Type Ш)	Fly Ash[1]	Sand[2]	Coarse Aggregate[3]	Super-plasticizer	Water	Steel Fiber	f_c' MPa
1	0.5	2.3	1	0.00077	0.55	0.316	6.7

Note: [1] Class C; [2] Fine aggregate; [3] Maximum size of 3/8 in.

Table 2-2 Properties of steel fibers

Fiber Type	Equivalent Diameter, in.	Length, in.	Aspect Ratio	Tensile Strength, ksi	Elastic Modulus, ksi
Long Twisted	0.02	2	100	355	29000
Short Twisted	0.02	0.55	28	355	29000

Prior research shows that this type of fibers exhibits high bond performance and a composite tensile strain-hardening behavior (Chao et al. 2009), which can improve the shear, bond, and ductility of plain concrete. In general, smaller or shorter fibers bridge and control the growth of microcracks, which can lead to a higher tensile strength of the composite, while the longer fibers can arrest the propagation of macrocracks and result in a substantial improvement in the toughness and residual strength of the

composite. Using long fibers with a high aspect ratio can obtain good bond performance between the fiber and concrete, but a higher dosage of long fibers can cause fiber balling and clumping, which decreases workability and material homogeneity. On the other hand, combining short and long fibers can increase workability and achieve consolidation (Blunt and Ostertag, 2009).

The HPFRC composition was made up of cement (Type III), fly ash (class C), fine aggregate (sand), coarse aggregate with a maximum size of 0.375 in., super-plasticizer, and water with a weight ratio of 1: 0.5: 2.3: 1: 0.00077: 0.55, respectively. A concrete-based composite was used so that the advantages coming from the aggregate, such as higher stiffness and aggregate interlock (which resists shear) could still be available. These attributes can be reduced in a cement-based composite. The maximum aggregate size was 0.375 in. This size was chosen to minimize the nonuniform distribution of fibers due to the presence of coarse aggregates.

Figure 2.1 and 2.2 shows the construction, test setup, and typical tensile stress versus strain response of one of the developed HPFRC material from a direct tensile test using dog-bone shaped specimens cast together with the full-scale HPFRC specimen. And Figure 2.3 illustrates the HPFRC dog-bone specimen after failure. The cross-section of the tensile specimen was 4 in. by 4 in. As can be seen in Figure 2.2, the first cracking tensile strain (ε_{cc}) and strength (σ_{cc}) are 0.01% and 240 psi, respectively. Strain-hardening of the composite started from this point up to the composite peak post-cracking tensile strain, ε_{pc}, of 0.6% with a tensile strength of 450 psi. The descending curve is very gradual, maintaining 80% of the peak tensile strength at 2% tensile strain.

2.2 Specimen Design and Steel Reinforcement Details

2.2.1 Prototype Building and Specimen Dimension

A 20-story reinforced concrete building located in Los Angeles, CA was used as a prototype building for this study. The building has six bays along each orthogonal direction with a center-to-center span length of 20 ft for each bay. The lateral force resisting system consists of three RC-SMFs at the perimeter of the building. The first story has a center-to-center height of 15 ft and all the other stories have a height of 13 ft. The perimeter SMFs resist lateral loads while interior columns and post-tensioned two-way slabs support gravity loads. Because only a few SMFs are resisting the lateral forces and providing the lateral stiffness, the beams and columns in the SMFs are very large.

Three full-scale slab-beam-column (SBC) subassemblages were designed. The configuration of all the three specimen are the same. The beam and column length were longer than that in the prototype frame. The specimens had an equivalent center-to-center column space of 27.6 ft and an equivalent column height (the distance between the bottom surface of the crosshead and the center of the clevis) of 18 ft to accommodate the available locations and heights for the testing equipment. Consequently, the clear span to effective depth ratios for the beams in the prototype frame and the test specimen are 5.1 and 7.4, respectively. The three SBC subassemblages, designated as RC-SP-NL, RC-SP-CL, and HPFRC-SP-CL, consisted of a column (depth: 42 in × width: 32 in.) and two beams (42 in. × 32 in.) framing into the column as well as a post-tensioned slab (8 in. × 52 in.) on only one side. RC and HPFRC represent concrete reinforced by steel bars and concrete reinforced by high performance fibers, respectively. SP stands for specimen and NL and CL denote types of loading, such as near collapse and cyclic loading. The compressive strengths of ready-mix plain concrete and HPFRC and strength of the steel reinforcement are listed in Table 2.3. Design details, configuration and dimensions of the specimens are given in Table 2.4 and Figure 2.4, respectively.

Table 2-3 Material properties

	Concrete compressive strength, f_c' [1]		Yielding strength of reinforcing bars from coupon tests, f_y			
Specimen	Beam plastic hinging region (including joint), ksi	Top column[2] (bottom column), ksi	No. 11 (beam), ksi	No. 11 (column), ksi	No. 5[3] (slab and skin§), ksi	No. 5 (hoop), ksi
RC-SP-NL	7.3	8.2	64	65	69	68
RC-SP-CL	7.2	8.4 (7.2)	71	65	69	68
HPFRC-SP-CL	6.7	8.3 (7.5)	68	65	69	68

Note: [1] Tested on the day of the testing; [2] Top and bottom column elements were constructed separately; [3] §skin reinforcement

Table 2-4 Design parameters

Specimen	RC-SP-NL	RC-SP-CL	HPFRC-SP-CL
$M^{+}_{pr,b}$ ($M^{-}_{pr,b}$), k-in.[1]	22,139 (25,659)	22,139 (25,659)	26,677 (29,350)
$\sum M_{n,c} / \sum M_{n,b}$ [2]	1.60	1.60	1.33
Joint shear stress, v_j, psi	770	770	1014
Normalized Joint shear stress, v_j, psi	$10.89\sqrt{f'_c}$	$10.89\sqrt{f'_c}$	$14.34\sqrt{f'_c}$
Joint transverse reinforcement ratio[3] (%)	1.15	1.15	0.18

Note:[1] $M_{pr,b}$ is probable moment of beams; [2] $M_{n,c}$ is nominal moment of columns and $M_{n,b}$ is nominal moment of beams; [3] area ratio; [4] Half plastic hinging region (42 in. from column faces).

2.2.2 Design of RC Specimens

Specimen RC-SP-NL and RC-SP-CL were designed in compliance with ACI 318 (ACI, 2014) and ACI 352 (ACI, 2002). The reinforcement details for the RC specimens are shown in Figure 2.5 through 2.7. Cheung et al. (1991) shows that when a joint has low shear stress, sufficient transverse reinforcement, and sufficient bond strength, the joint can be strong enough to limit the joint behavior within an elastic domain. The joint of RC-SP-NL and CL was designed as a “strong joint.” The design joint

shear stress of this specimen was $10.89\sqrt{f'_c}$ in psi, which was about 1.4 times less than the nominal joint strength calculated according to ACI 318-14. A set of the transverse reinforcement consisted of three hoops (one big hoop with two small hoops) and one crosstie was placed in the joint. The spacing of the transverse reinforcement was 4.5 in. with a reinforcement ratio of 1.15% (area ratio between the reinforcement and the concrete cross section). The joint depth (column depth) was 30 times the diameter of the largest beams' longitudinal reinforcement (No. 11). Note that ACI 318-14 requires the joint depth to be at least 20 times greater than the diameter of the largest beams' longitudinal reinforcement. Although ACI 318 allows a beam longitudinal (flexural) reinforcement ratio up to 2.5%, RC-SP1 only had a 0.64% longitudinal reinforcement ratio because a large cross-sectional area of the beam and column was used to control the frame stiffness and increase joint strength. Not that according to ACI 318 14, the following equation is used to calculation the joint strength of the beam-column connection confined by beams on two sides. Here λ is the constant related to the type of concrete and A_j is the area of a joint. Therefore, increasing the area leads to increased shear strength of a joint.

$$15\lambda\sqrt{f_c'}A_j \qquad 2.1$$

The spacing of the transverse reinforcement in the beam plastic hinge regions was controlled by buckling-prevention and confinement requirements (i.e. $s \leq d/4$; ACI 318-14 Section 18.6.4.4). Note that according to ACI318-14 Section 27.7.2.3, every alternate longitudinal bar needs to be supported by the comer of a tie. As seen in Figure 2.6, four No. 5 bars were placed at each corner of the big hoops. Therefore, the main No. 11 bars right next to the No. 5 bars were not engaged in any hoops or ties, forcing the alternate bars to be supported by ties. This increased the area of transverse bars in the beam plastic hinge regions. If the No. 4 bars, which were place for construction purpose, did not exist, only one tie with one big hoop will be needed in the region. The placement of construction bars (No. 4 bars) is up to designer's decision and common practice in U.S. It is not forced by provision. Note that the additional tie increased shear resistance of the beam plastic hinge region. The first hoops were located 2 in. away from column faces followed by 6 in. of spacing after the first hoop (ACI 318-14 Section 18.6.4.4).

The total area of column longitudinal reinforcement was 1.6%. The sum of nominal flexure moment strength of the column was about 1.6 times greater than that of the beams which meets the requirement for minimum flexural strength of columns (ACI 318-14 Section 18.7.3.2). For the top column, the axial force used for the calculation of its flexural strength is the axial force that comes from the crosshead (this will be explaining later on). The weight of the top column and beams were included to the axial force used for the calculation of the flexural strength for the bottom column. The transverse reinforcement design in the column was controlled by confinement in the region where flexure yielding is likely to occur, with 4.5 in. spacing and 6 in. spacing beyond the region.

As shown in Figure 2.6 and 2.7, the width of the beams and column was the same. To avoid the conflict with column longitudinal bars in the joint, the beam's longitudinal bars were moved about 2.75 in. toward the center of the beam section from each corner of beam transverse reinforcement. No. 5 bars (construction bars) were placed at the corners to support the beam transverse reinforcement, and six additional No. 5 bars (skin reinforcement) were evenly distributed along the beam depth to control crack width. These No. 5 bars were terminated immediately before the joint in order not to increase beam and joint shear demand. The above arrangement is a common practice used in the U.S. The complete design satisfies ACI 318-14 Sections 18.6 to 18.8 for RC special moment frames. The joint stress was estimated considering a tensile stress of flexural reinforcement equal to $1.25f_y$ (ACI 318 Section 18.8.2.1) and the contribution from slab reinforcement within the effective flange width (ACI 318 Section R18.7.3).

2.2.3 Design of HPFRC Specimen

Specimen HPFRC-SP was designed in the same manner as the RC-SPs except: 1) HPFRC was used in the joint and beam plastic hinge regions (Figure 2.8); 2) the joint was designed to experience large deformation as a "yielding joint." Kurose et al. (1998) showed that if a concrete compressive strength is approximately more than 5 ksi (34.5 MPa), beam-column connections with a joint stress of approximately $15\sqrt{f'_c}$ psi ($1.25\sqrt{f'_c}$ MPa) are likely to experience yielding in both joints and beam plastic

hinge regions. Parra-Montesions et al. (2005) also reported that HPFRC joints exhibits elastic behavior up to a shear stress of approximately $14.4\sqrt{f'_c}$ (psi) ($1.2\sqrt{f'_c}$ (MPa)) with a few transvers reinforcement, experiencing ductile inelastic behavior for larger joint shear stress (note that the tensile strength and ductility of HPFRCC used in their research are similar to what is used in this study). Reinforcement details for this specimen is given in Figure 2.9 and 2.10. The design shear stress of the joint of the HPFRC–SP-CL was $14.34\sqrt{f'_c}$ psi ($1.19\sqrt{f'_c}$ MPa). This was done by extending the construction and skin reinforcements through the joint (note that the sum of nominal flexure moment strength of the columns was 1.33 times that of the beams). For the calculation of the probable moment, M_{pr}, of HPFRC-SP-CL, a reasonable approximation has been adapted to determine the effective depth (Park and Paulay, 1974). As seen in Figure 2.11, the effective depth was chosen to be the distance between the center of the top and bottom reinforcement. In this method, the calculation can be much easier with close values. Most of the steel hoops and ties in the joint were eliminated. The volume of the conventional transverse steel reinforcement for the joint in the HPFRC-SP-CL was 22% of that used in the RC-SP-NL and CL. Although it has been demonstrated by Parra-Montesions et al. (2005) that HPFRC can provide sufficient confinement with the joint after yielding, a few more transverse reinforcements were placed in the joint of the HPFRC-SP-CL for additional confinement. This amount of transverse reinforcement is unlikely to increase the joint strength. This very low transverse reinforcement used in this study will provide a baseline performance of an HPFRC joint; 3) No transverse reinforcement in the beam plastic hinge regions were placed. Prior studies had given sufficient evidence on the ability of HPFRC in providing high shear strength and confinement (Parra-Montesions et al. 2005; Lequesne et al., 2010). Past research shows that HPFRC coupling beam can resist a shear strength of approximately $5\sqrt{f'_c}$ (psi) ($0.42\sqrt{f'_c}$ (MPa)) under large displacement reversals.

HPFRC beam-column connections tested by Parra-Montesions et al. (2005) also indicated that there was no shear damage in the plastic hinge regions of HPFRC beams under a stress of $2.4\sqrt{f'_c}$ (psi) ($0.2\sqrt{f'_c}$ (MPa)). When designing the HPFRC specimen, it was decided not to use any transverse reinforcement in the beam plastic hinging regions because: 1) the estimated beam shear stresses were below $2.4\sqrt{f'_c}$ (psi) ($0.2\sqrt{f'_c}$ (MPa)); and 2) the balanced damage concept used to design the HPFRC

specimen would decrease the damage in the plastic hinging regions as the damage is shared by the joint. To verify that transverse reinforcement was not needed in HPFRC specimen, four sets of transverse reinforcement were placed in the left-side beam (Figure 2.8). These transverse reinforcing bars are identical to those used in the RC specimen.

2.2.3 Slab Design

Reinforcement details and posttensioning plan for the slab are shown in Figure 2.12. It is common practice to reduce the posttensioning force near beams so as to reduce contribution of the posttensioning force to the negative moment strength. This consequently reduces shear demand in the joints. ACI 318-14 requires a minimum area of passive reinforcement to be placed over the support, where un-bonded tendons are used. The minimum reinforcement was lumped with the top reinforcement in the beams. The reinforcement for temperature and shrinkage is required where the average pre-compression is below 100 psi. Since the posttensioning force in the slab is higher than 100 psi, the reinforcement for temperature and shrinkage was omitted.

2.3 Specimen Construction

The specimens were constructed at two different places. The lower parts which includes lower columns, slab, and beams were constructed at the Civil Engineering Laboratory Building at the University of Texas, Arlington, and the upper part that contains upper columns and loading and base blocks were built and cast at the MAST lab at the University of Minnesota. This was done by splicing column longitudinal reinforcement by Type 2 mechanical splices (ACI 318-14 Section 18.2.7) at 22 in. above the top of the beams.

As seen in Figure 2.13, laid down on the strong floor, reinforcement cages for beams was built first. Then, transverse reinforcement for the beam-column joint was inserted into the joint region. The

longitudinal reinforcement for the lower column were slide into the beam reinforcement cage passing through the joint region and tied to the beam longitudinal reinforcement. Afterward, the transverse reinforcement for the lower column was placed. As seen in Figure 2.14, a plate with shear studs welded on it was located at the bottom of the lower column. This plat was to connect the lower column to a clevis (this will be explained later on). Then, formworks were placed all around the reinforcement cage. A piece of plywood in which several holes were drilled was used as a formwork to prevent concrete leaking from the top of the cage (Figure 2.15). Complete views of the reinforcement cage and formworks placed around the cage are shown in Figure 2.16 through 2.19. Note that as can be seen in Figure 2.17 and Figure 2.18, constructions for the reinforcement cages of HPFRC-SP-CL was much easier than that of RC-SP-NL or CL because a large amount of transverse reinforcement in HPFRC-SP was eliminated.

For RC-SP-NL and RC-SP-CL, the entire concrete casting for the lower part was done at once. On the other hand, HPFRC was cast into the joint and plastic hinge regions of HPFRC-SP-CL, then the remaining parts was cast with normal concrete. This was done by placing wooden formworks at the ends of the plastic hinge regions. After casting the beams, the side surface of the beams, where the slab was located, was roughened to enhance the cohesion and interlock. Then, the slab was cast. The lower part of each specimen was shipped overland to the MAST facility on a flatbed trailer along with all steel rienforment for the remaining construction at MAST. The reinforcement cage for the upper part and base blocks were built and cast at MAST. Figure 2.20 show a specimen after arrival at MAST. It was elected by placing supports under the column and beams. Then, the longitudinal reinforcement for column was spliced by using Type 2 mechanical splices (Figure 2.21). After placing transverse reinforcement for the upper column, formworks for the column and loading block were placed and concrete was cast. Entire specimen after the removal of the formworks Is shown in Figure 2.22.

2.4 Test Setup

2.4.1 Specimen Installation

For lifting purpose, loading blocks were post-tensioned to beams by using four 1 in. diameter threaded rods. Then, specimens was lifted by an overhead crane using lifting chains and straps which passed through 2 in. horizontal through-holes in each direction of the loading block. A crosshead and two of 6 – DOF vertical actuators at MAST were removed. The base block was moved onto the strong floor by using an overhead crane and a plate was located on the top of it. They were post-pensioned to the strong floor by post-tensioning by eight (8) 2 in diameter rods. Then, a clevis was placed on the top of the plat with 1-in.diameter A490 bolts.

The specimens with installation brackets were moved into the test area, the installation bracket was removed from the specimens and the specimens were placed on the top of the clevis, supported by two column supporters. The posttensioning rods and column supporters were removed after the specimens was placed on the clevis and ancillary actuators were attached to the beams by transverse beams. The crosshead was attached to the loading block by 16 – 1.5 in. diameter ASTM A354 GT BD bars and the 6 DOF actuators was moved back to their original place. Posttensioning prestress of 125 psi was applied perpendicularly to the beam axis, to simulate the typical prestress applied in two-way slabs and to further increase the friction between the slab and beam thus maintaining the integrity when the specimens were loaded. The same amount of post-tensioning prestress was also applied in the slab along the axis of the beams.

The test setup and a location of the specimens on the strong floor are shown in Figure 2.23 through 2.25. The specimens were rotated 45 degree about the principle axis of the strong floor. The loading block was connected to the six degrees of freedom crosshead, which imposed lateral and axial loads on the specimens allowing zero moment at the bottom of the crosshead. The crosshead can displace specimens up to ±20 in. and loads them up to ±1326 kips in the vertical direction. Displacements

of up to ±16 in. and loads up to ±877 kips can be achieved in each of the two horizontal directions. Four vertical ancillary actuators are attached to the specimen by load transfer beams. The ancillary actuators have a load capacity of ±219 kips with a displacement range of ±10 in. While these actuators allowed the beams to rotate about the *z* axis (direction perpendicular to the specimen), vertical displacements of the beams at the location of the actuator were restrained. The lower end of the column was attached to the clevis, which simulates an inflection point of the lower column. Lateral support was provided at the bottom of the column, while no lateral support was provided to the slab.

2.4.2 Components for Test Setup

Test setup components are shown in Figure 2.26, which includes transverse beams, a clevis, base and loading block. These components were designed based on the horizontal force at the crosshead, $V_{crosshead}$, and vertical force at the tip of each beam, V_{beam}, as shown in Figure 2.27. Equation 2.2 through 2.4 give the calculations for $V_{crosshead}$ and V_{beam}.

$$V_{col} = \left[\left(M_{pr}^{+} + M_{pr}^{-}\right) + \left(V_{pr}^{+} + V_{pr}^{-}\right)2 / h\right] / \ell_2 \qquad 2.2$$

$$V_{crosshead} = V_{col} + (P\Delta / \ell_2) \qquad 2.3$$

$$V_{beam} = \frac{V_{crosshead} \cdot \ell_2}{\ell_1} \qquad 2.4$$

Here, M_{pr} is the probable moment which is calculated by multiplying 1.25 to the specified yield strength of beam longitudinal reinforcement. V_{pr} is the shear force in the beams near column faces. And h is the depth of the column and ℓ_1 and ℓ_2 are the distance between the ancillary actuators and the distance between the bottom of the crosshead and the center of the clevis, respectively. P is the axial force from the crosshead. This force was constant during the test.

Figure 2.28 shows details of the transverse beams. The transverse beams are to connect the ancillary actuators to the specimens to simulate inflection points at tips of the beams. They are located between the ancillary actuators and tips of the beams of the specimens. The transverse beams has been conservatively designed to resist the vertical forces, V_{beam}, considering slip-critical condition. Six 1.5" ASTM A354 GR BD bars was used as fasteners to achieve enough capacity for the vertical force. Figure 2.29 shows how the transverse beams connect the ancillary actuators to specimens. The transverse beams are a built-up member consisting of two plats for flange, one plat for web, and one for end plate. The web is wleded to the flange by ½ double fillet welding, and the web and flange are connected to the end plat by the combination of double fillet and CJP welding.

Figure 2-30 shows dimensions of the loading and base block. The loading block has been designed to attach the specimens to the crosshead. Details of the connection part between the loading block and crosshead is shown in Figure 2-31. The connection was achieved with 16 - 1.5 in. diameter ASTM A354 GR BD bars. All bars was tensioned up to 125 kips. The role of the base block is to adjust the height of the specimens for the crosshead. 8 - 2 in. diameter rods was used to attach the base block to the strong floor (Figure 2.32). The clevis was to connect the base block to the lower columns. It is to simulate an inflection point at the bottom of the lower columns. Details of the clevis is shown in Figure 2.33. The clevis connects the specimen to base block by placing two plates which are located at the top and bottom of the clevis. Details of the plates are also shown in Figure 2-33. A plate, with shear studs welded on it to resist shear force, is embedded into the bottom of the lower columns. 20 shear studs are welded on the embedded plate. 16 – 1 3/8 in. A325 bolts was used to attach the top plate of the clevis to the embedded plate through threaded holes on the embedded plate. Figure 2-34 shows details of the connection part between the clevis and bottom of the column. A lateral support was installed to prevent specimen from the out plane force stemmed from the un-symmetric shape of the specimens.

2.5 Instrumentation

2.5.1 Strain Gauge

Figure 2.35 through 2.38 show locations of strain gauges. The strain gauges were mounted on longitudinal and transverse reinforcing bars in the plastic hinge regions of the beams and longitudinal reinforcing bars in the columns at column-joint interfaces. The strain gauges on the reinforcing bars in the beams are to investigate the bond between concrete and the reinforcing bars within plastic hinge regions including beam-column joints, to measure plastic hinge length in the beams, and to defect yielding points within the plastic hinge regions. The strain gauges in the columns are to verify the strong column-weak beam behavior by capturing the initiation of any yielding in the longitudinal reinforcing bars. To examine the participation of slabs, strain gauges were also placed on longitudinal reinforcing bars in the sabs near the beam-column interfaces (Figure 2.38). Note that CSS series represents concrete strain gauges.

2.5.2 LVDTs

Figure 3.39 and 3..340 show locations of required LVDTs. They were placed:

1. in the plastic hinge regions of the beams to measure beam rotations.
2. on upper and lower columns adjacent the beam column joint to measure column rotations.
3. on the bottom of the crosshead to measure the slip between the crosshead and loading block.
4. on the strong floor to measure the slip between the base block and strong floor.
5. on the base block to measure the slip between the base block and plate under the clevis.
6. on the plate (strong floor plate) under the clevis to measure the slip between the clevis and plate.
7. near the bottom part of the lower column to measure the slip between the clevis and specimens.

2.5.3 String Potentiometer

Figure 2.39 also shows locations of required string potentiometers. They were placed:

1. on the front side of joint region to measure the shear distortion of the joint.
2. on the front side of beam at both sides within the plastic hinge regions to measure the shear distortion.
3. at beam tips to measure the horizontal and vertical displacements of the specimens.

2.5.4 Load Cell

Forces from the ancillary actuators was measured by built-up load cells. A clevis load pin cell was placed to measure the vertical force to the specimens from the crosshead.

2.6 Loading Protocol

As shown in Figure 2.41, test units were rotated 45 degrees with respect to the principal directions of the footing and laboratory floor. Thus, the corresponding control coordinate system was rotated by 45 degrees about the Z axis to an x'-y'-z' system as shown in Figure 2.42. The general orientation of the MAST laboratory was kept for identification of the specimen surfaces. The loading and control along the six degrees of freedom of the MAST laboratory were defined in the schematics in Figure 2.43. It was of interest to use the 6-DOF control of MAST to control the position of the point of inflection (zero moment) at the bottom of the crosshead. The loading and control of the test was done with respect to the rotated (or primed) coordinate system as shown in Figure 2.43. The corresponding active and constrained degrees of freedom were as shown in Table 2.5.

The lateral load was applied based on the loading protocol shown in Fig. 2.44 and 2.45, while the axial load was maintained vertically and constant throughout the testing. This allowed the P-Δ effect to be considered in the test. The applied vertical load represented 10 percent of the product of the gross column cross-sectional area and the

Table 2-5 Control mode of the 6-DOFs

DOF	Control Mode	Note
Translation x'; $(\Delta_{x'})_{crosshead}$	Displacement	Specified history (Figure 4 and Table 2)
Translation y'	Displacement	$\Delta_{y'} = 0$
Translation z'	Force (kips)	Constant axial compression $P = 0.1 \times A_g \times f'_{c(28\text{-}day)} = 672$ kips (downward)
Rotation x'	Displacement	$\theta_{x'} = 0$
Rotation y'	Force (kips-in.)	$M_{y'} = 0$
Rotation z'	Displacement	$\theta_{z'} = 0$

Note: $f'_{c(28\text{-}day)}$ = nominal design strength = 5 ksi

nominal concrete comprehensive strength (0.1Agf'c), which was based on structural analysis of a 20-story prototype building. This axial force was due to the gravity load only because the earthquake induced axial force is relatively small for this interior column at the perimeter frame. While there is no strong evidence that the axial load could enhance the shear strength of the joint (e.g., Bonacci and Pantazopoulou, 1993), previous research indicated that high column axial force leads to increased confinement pressure which in turn enhance the bond resistance for the bars in the joint (Eligehausen et al. 1983; Li and Leong, 2015). Therefore, an axial force of 0.1Agf'c can be conservative for the joint design. Note that the loading protocol used in this research has a much higher accumulated displacement ductility demand than that of the previously tested 86 specimens (Bonacci and Pantazopoulou, 1993). The loading procedure was as follows:

Loading procedure for RC-SP-NL Test – Near-Collapse Loading:

1. Apply vertical (axial) load to the specimen equal to 10 percent of the gross concrete compression capacity (i.e., 0.10f 'cAg= 672 kips), and maintain this load constant during the entire test.

2. Record the height at the four ancillary actuators and maintain this height throughout the entire test by using displacement control of the four ancillary actuators.

3. Apply lateral displacements at a rate of approximately 1 in./min, according to the displacement history given in Table 2.6. The displacement is to be controlled according to the displacement measured at crosshead.

4. In addition to (2), still images will be taken by using the 8 MAST telepresence cameras at the beginning of the test. Also pause the loading at the corresponding drift levels for both the maximum positive and negative peaks. Additional images are to be taken as needed.

5. Continue loading and pausing, as described in steps 2) and 3), until the Group #11 is completed (Table 2.6).

6. Continue loading in a monotonic manner at a rate of 1 in./min. until the MAST crosshead reaches the maximum displacement allowed (+D1). Pause the loading after every 1 inch of displacement to take pictures using all 8 telepresence cameras.

7. Continue loading in the opposite direction at a rate of 1 in./min. until the MAST crosshead reaches the maximum displacement allowed (-D2), at this displacement, if the lateral resistance of the specimen degrades to 20% or less of the peak resistance exhibited during the test, then go to Step (8). Pause the loading after every 1 inch of displacement to take pictures using all 8 telepresence cameras.

8. Repeat the same loading and pausing, as described in steps 5) and 6). Maintain the same displacement values, +D1 and –D2, in the two directions.

9. Unload the specimen at a rate of 1 in./min without pausing for pictures until the crosshead returns to the initial (undeflected) configuration and stop.

Table 2-6 Near-collapse cyclic loading

Group	Column Drift Ratio (%)	Target Displacement at bottom of crosshead = Drift Ratio × 219"/100 (in.)	No. of Cycles
Baby Cycle*			
1	0.30	0.66	1
2	0.50	1.10	1
3	0.75	1.64	1
4	1.00	2.19	1
5	+5.00	+10.95	-
6	+2.50	+5.48	-
7	+6.00	+13.14	-
8	+3.50	+7.67	-
9	+7.00	+15.33	-
10	+4.50	+9.86	-
11	+8.00	+17.52	-
12	Monotonic loading in both directions Drift Ratio= *x*/219×100	*x*	-

*A small displacement cycle (0.05-in.) in both directions. This would give an approximate lateral force of 25 kips, and maximum flexural tensile stress in concrete about 250 psi in beams and 282 psi in the column (should not induce any cracking of concrete, considering a uniform compression of about 500-psi will be applied before the lateral load is applied).

Loading Protocol for both RC-SP-CL and HPFR-SP-CL Test – Far-Collapse Loading:

1) Apply vertical (axial) load to the specimen equal to 10 percent of the gross concrete compression capacity (i.e., 0.10f 'cAg= 672 kips), and maintain this load constant during the entire test.

2) Record the height at the four ancillary actuators and maintain this height throughout the entire test by using displacement control for the four ancillary actuators.

3) Apply lateral displacements (Figure 2.45) at a rate of approximately 1 in./min, according to the displacement history given in Table 2.7. The displacement is to be controlled according to the displacement measured at crosshead. The intermediate drift level between major drift levels (after 1% drift) is 0.33%.

5) Continue loading and pausing, as described in steps 3, until : (a) MAST crosshead reaches the maximum displacement allowed, or (b) the lateral resistance of the specimen degrades to 20% or less of the peak resistance exhibited during the test in both directions.

6) Unload the specimen at a rate of 1 in./min without pausing for pictures until the crosshead returns to the initial (undeflected) configuration and stop.

Table 2-7 Reversed cyclic loading

Group	Column Drift Ratio (%)	Target Displacement at bottom of crosshead = Drift Ratio × 217"/100 (in.)	No. of Cycles
		Baby Cycle*	
1	0.200	0.43	3
2	0.250	0.54	3
3	0.350	0.76	3
4	0.500	1.09	3
5	0.750	1.63	3
6	1.000	2.17	2
7	0.330	0.72	1
8	1.750	3.80	2
9	0.330	0.72	1
10	2.750	5.97	2
11	0.330	0.72	1
12	3.500	7.60	2
13	0.330	0.72	1
14	4.375	9.49	1
15	0.330	0.72	1
16	5.500	11.94	1
17	0.330	0.72	1
18	6.875	14.92	1
19	7.500	16.28	1

*A small displacement cycle (0.05-in.) in both directions. This would give an approximate lateral force of 25 kips, and maximum flexural tensile stress in concrete about 250 psi in beams and 282 psi in the column (should not induce any cracking of concrete, considering a uniform compression of about 500-psi will be applied before the lateral load is applied).

(a) (b)

Figure 2.1 HPFRC test (a) construction and (b) test setup

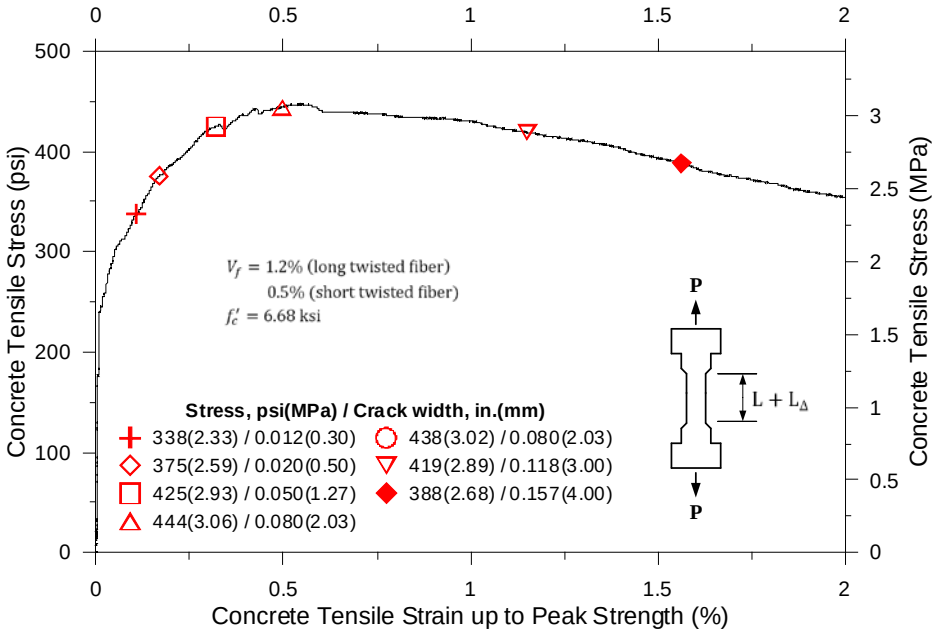

Figure 2.2 Tensile stress vs. tensile strain response of HPFRC

Figure 2.3 HPFRC dog-bone specimen after test

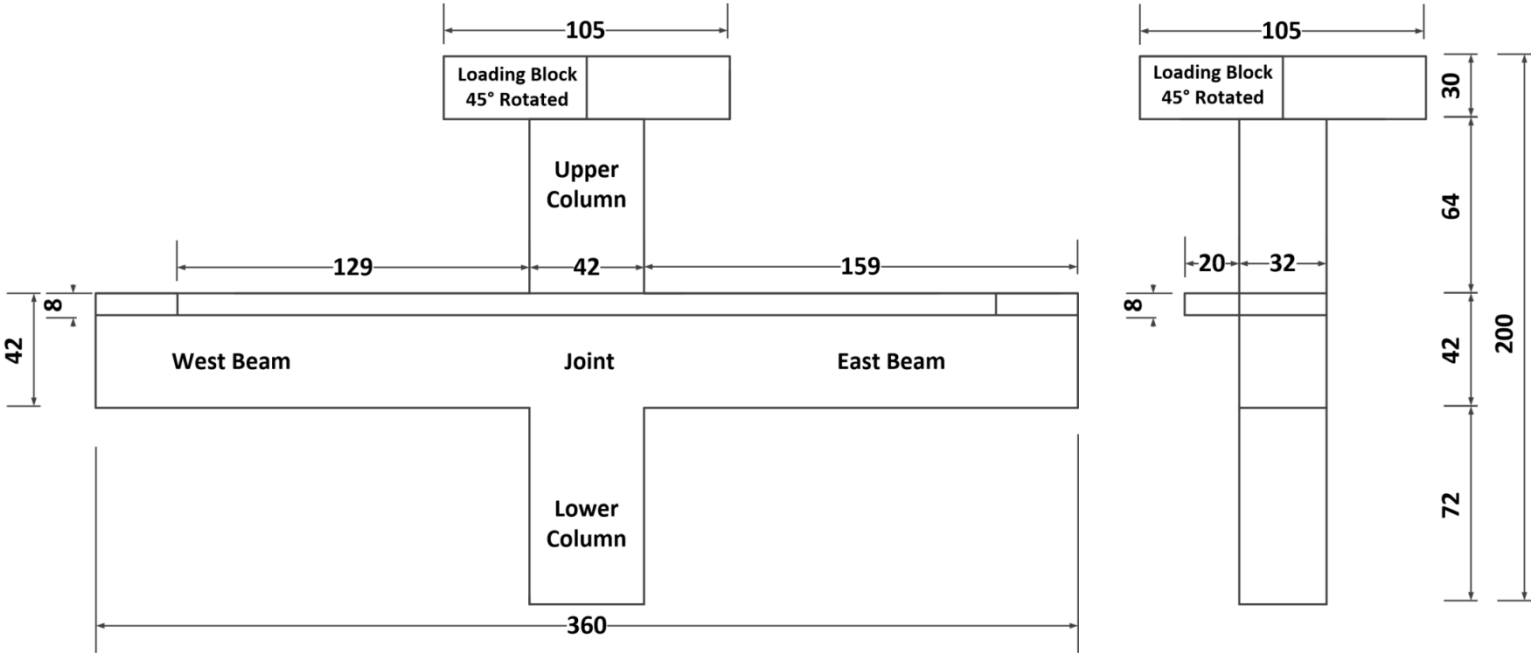

Figure 2.4 Configuration and dimensions of specimens

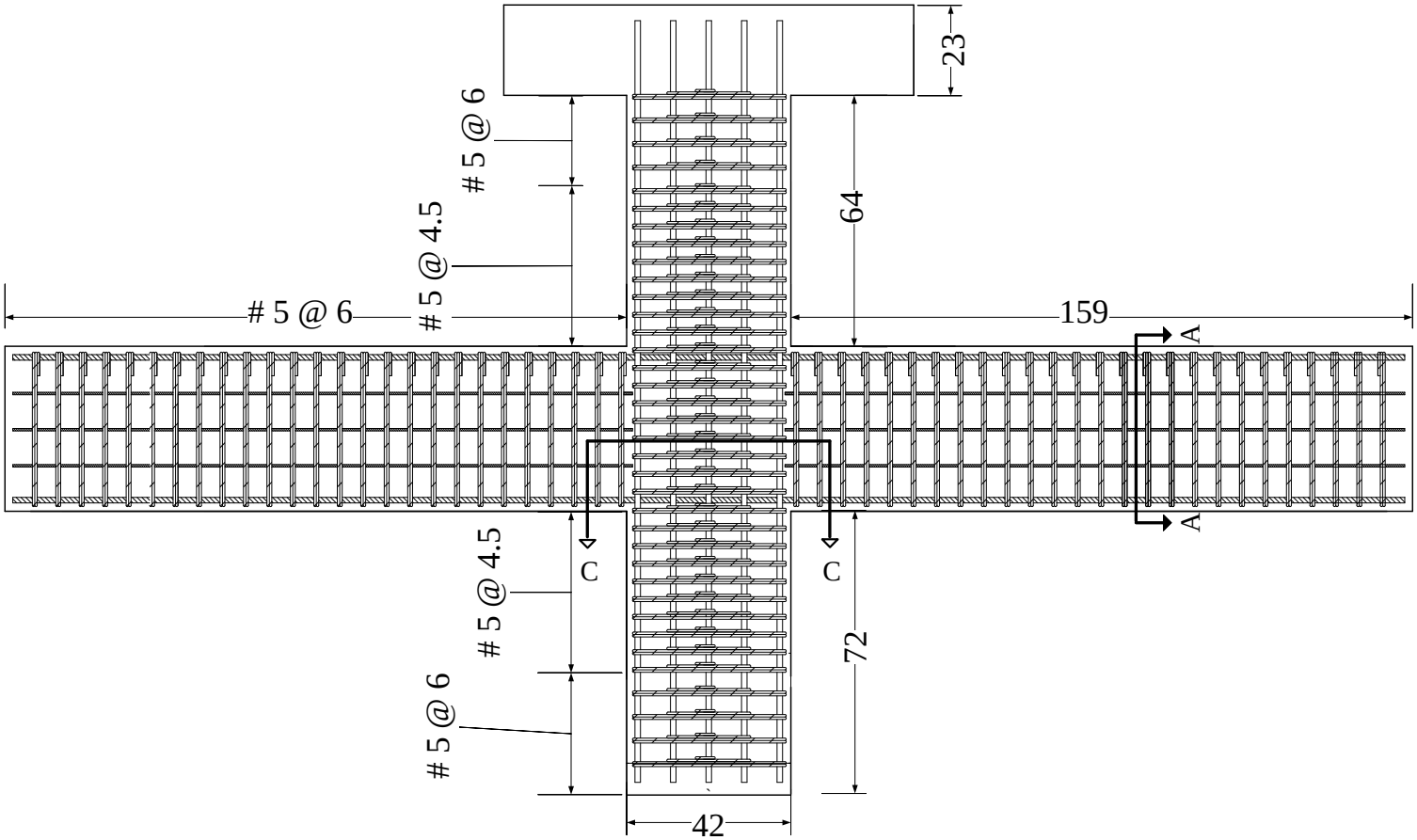

Figure 2.5 Reinforcement detail of RC specimen

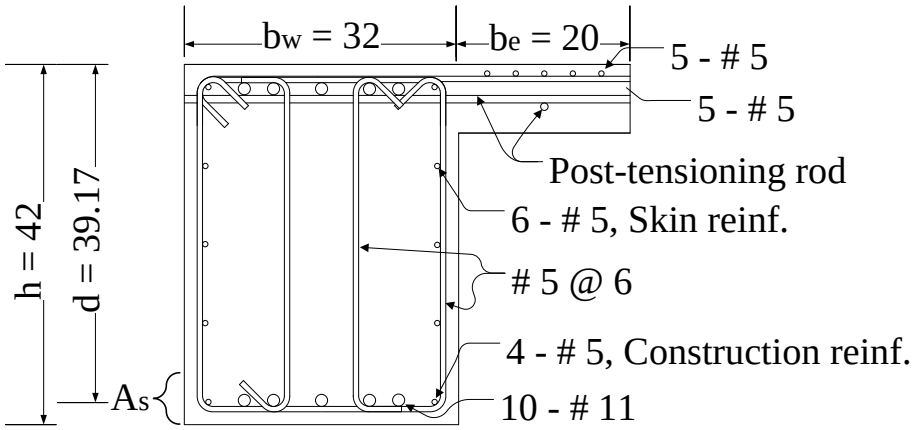

Figure 2.6 Beam cross section of RC specimen

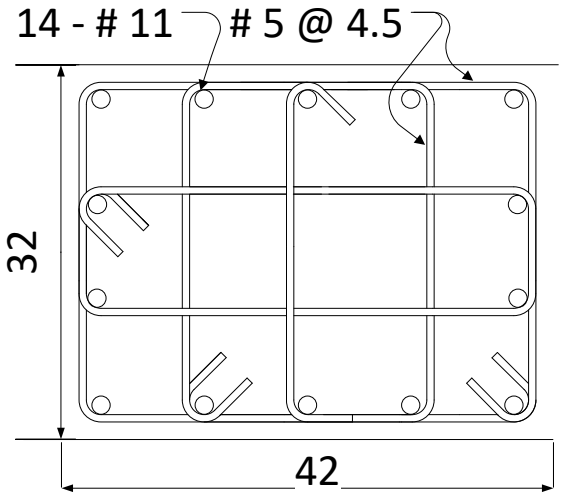

Figure 2.7 Column cross section of RC specimen

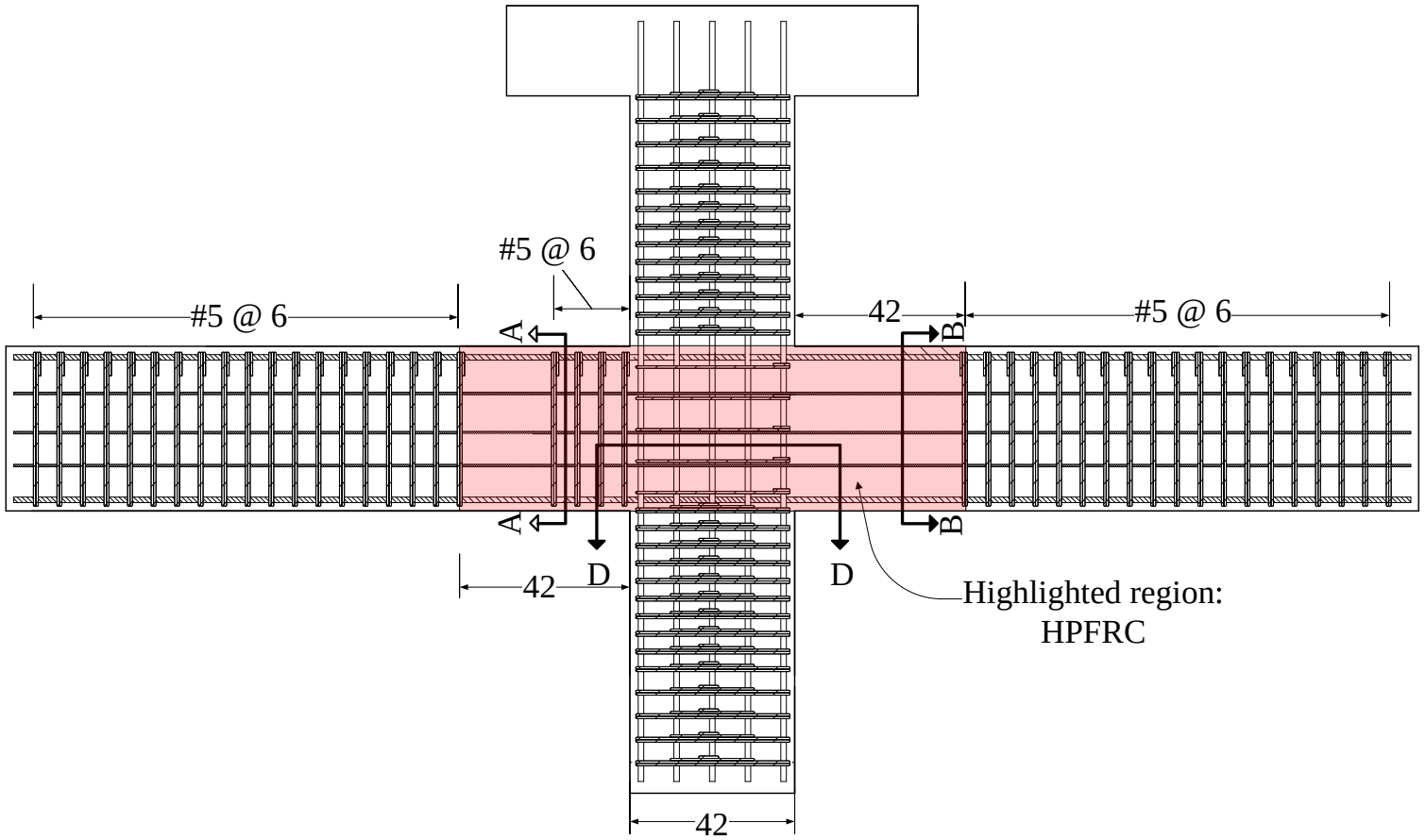

Figure 2.8 Reinforcement detail of HPFRC-SP-CL

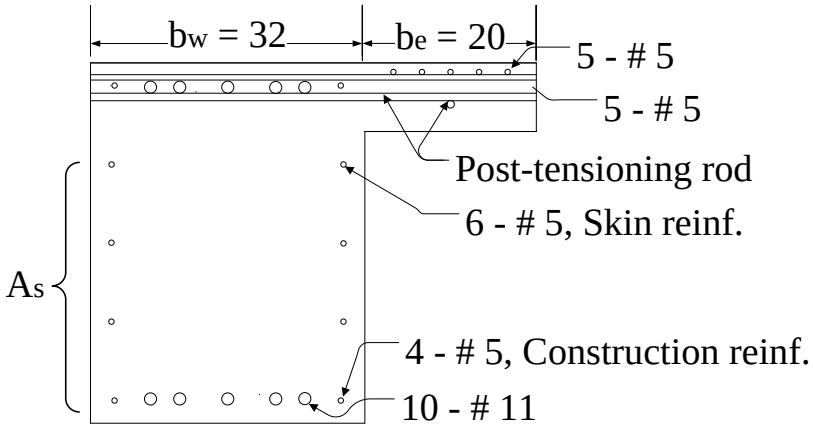

Figure 2.9 Beam cross section of HPFRC-SP-CL

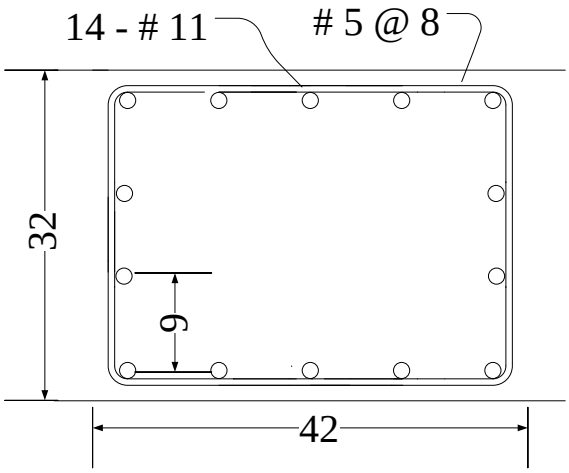

Figure 2.10 Column cross section of HPFRC-SP-CL

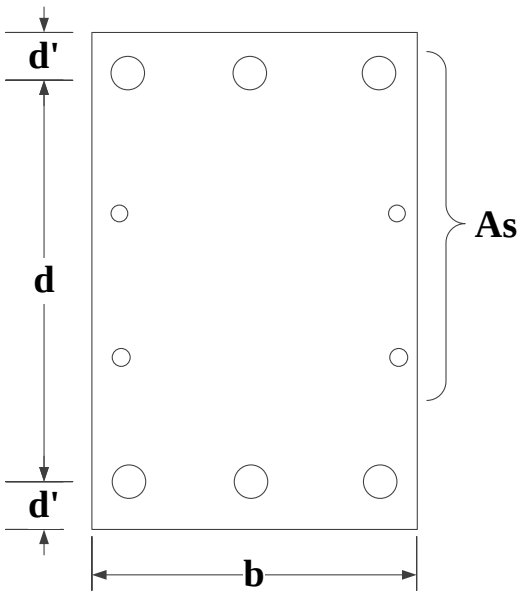

Figure 2.11 Approximation of effective depth

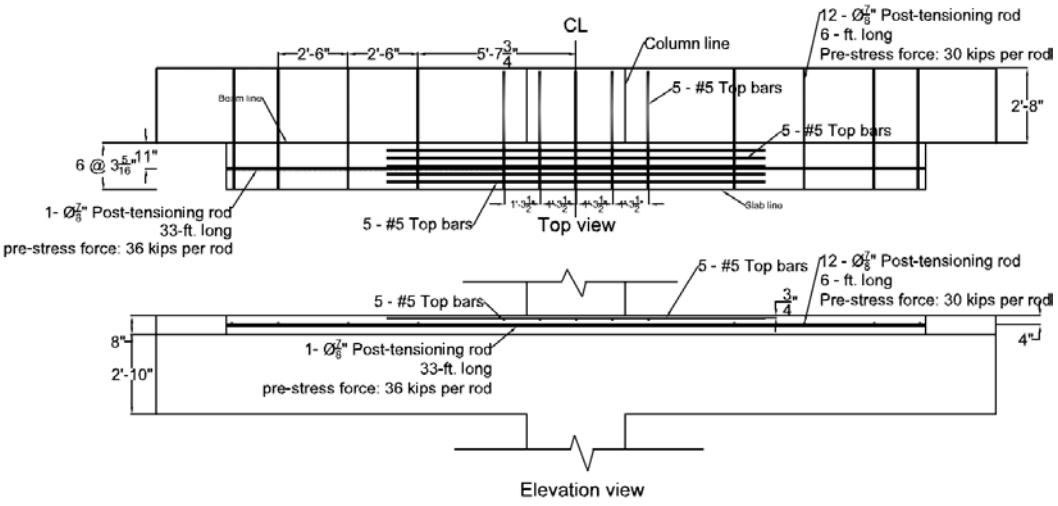

Figure 2.12 Details of steel reinforcement and posttensioning plan for slab

Figure 2.13 Reinforcement cage for beams

Figure 2.14 Plat with shear studs

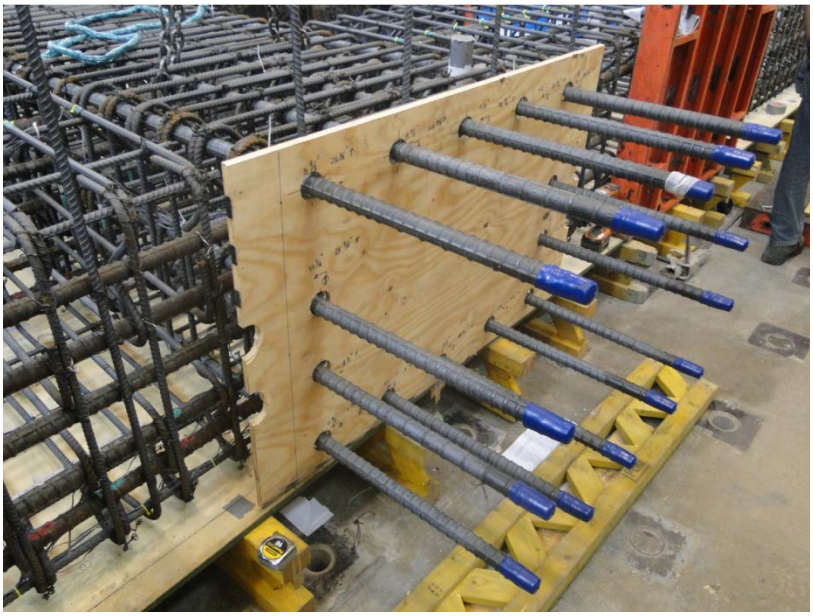

Figure 2.15 Plywood with drilled holes

2-16 Final reinforcement cage for beams and lower column

Figure 2.17 Reinforcement in the Joint of RC specimen

Figure 2.18 Reinforcement in the Joint of HPFRC specimen

2.19 Formworks for lower part of specimen

Figure 2.20 Lower part of specimen at MAST

Figure 2.21 Reinforcement cage for top column

Figure 2.22 Specimen after removal of formworks

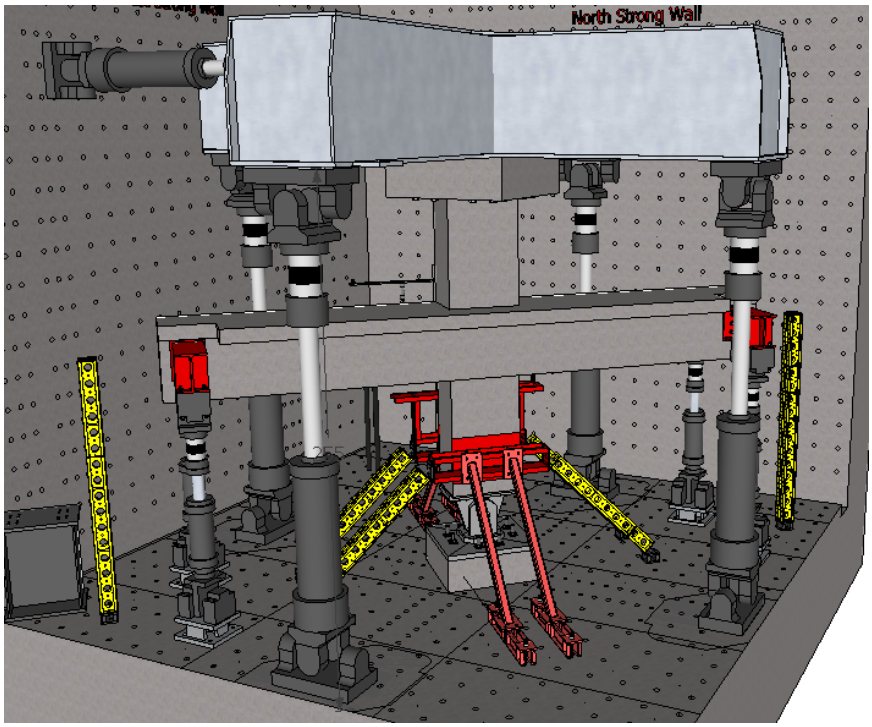

Figure 2.23 Test setup in 3D view

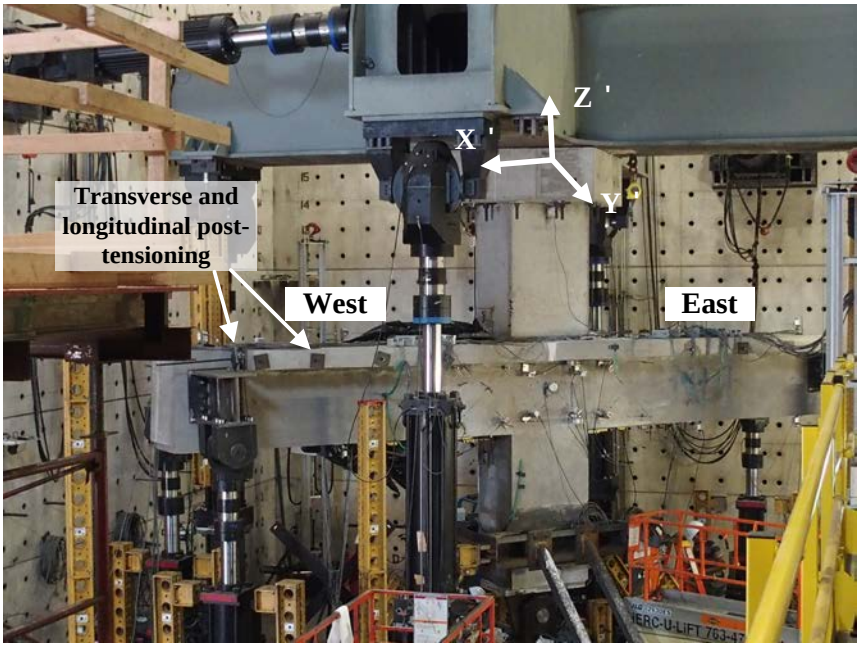

Figure 2.24 Photo of Test setup

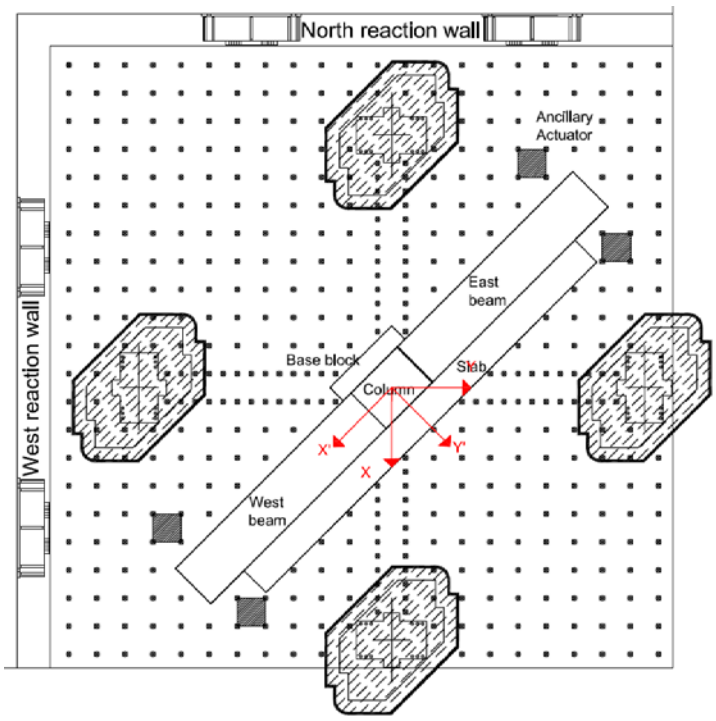

Figure 2.25 Location of specimens on strong floor

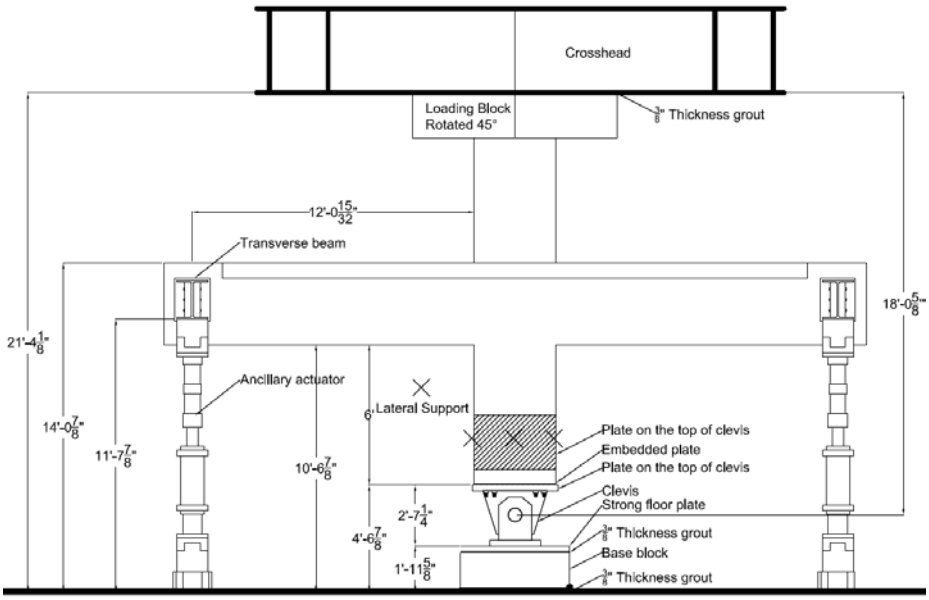

Figure 2.26 Components of test setup

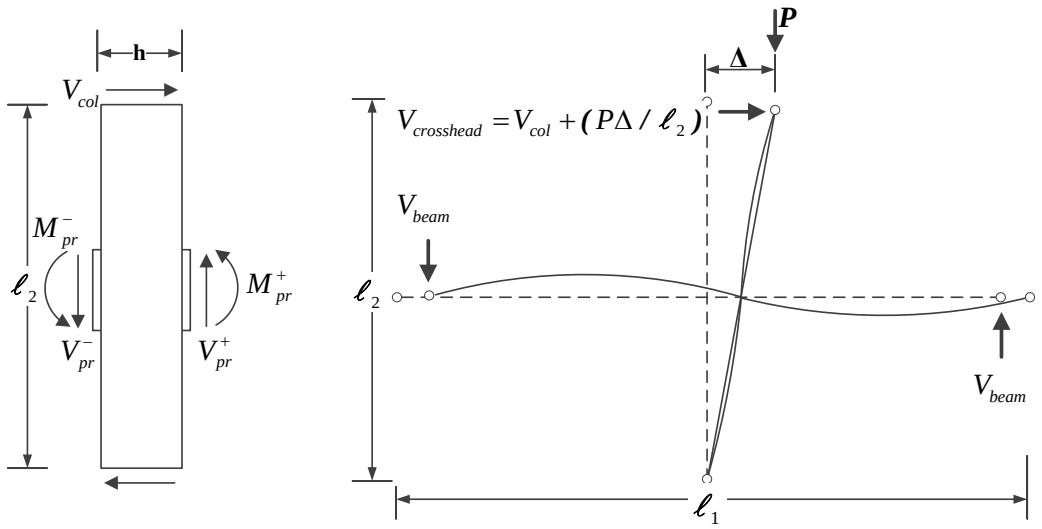

Figure 2.27 Determination of horizontal and vertical forces

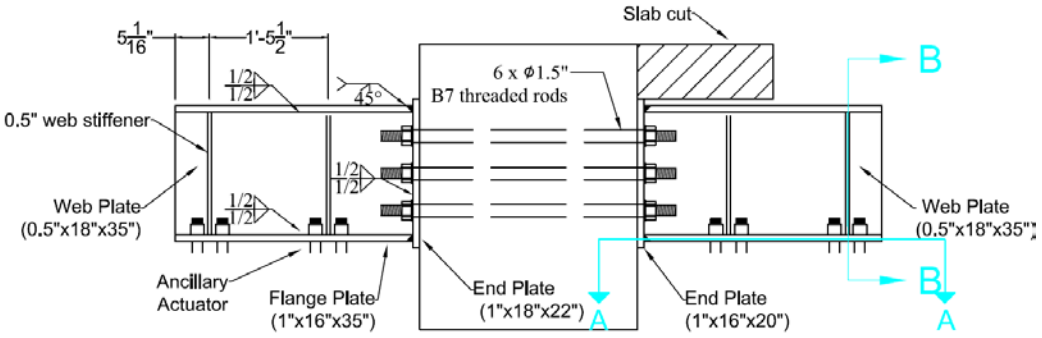

Figure 2.28 Details of transverse beam

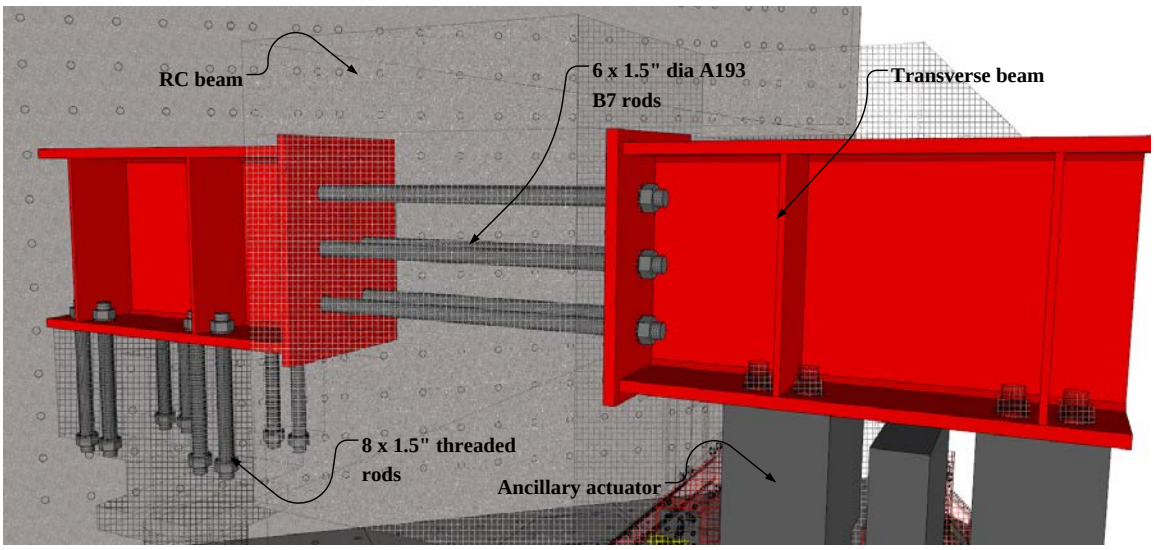

Figure 2.29 Connection details between transverse beam and beams

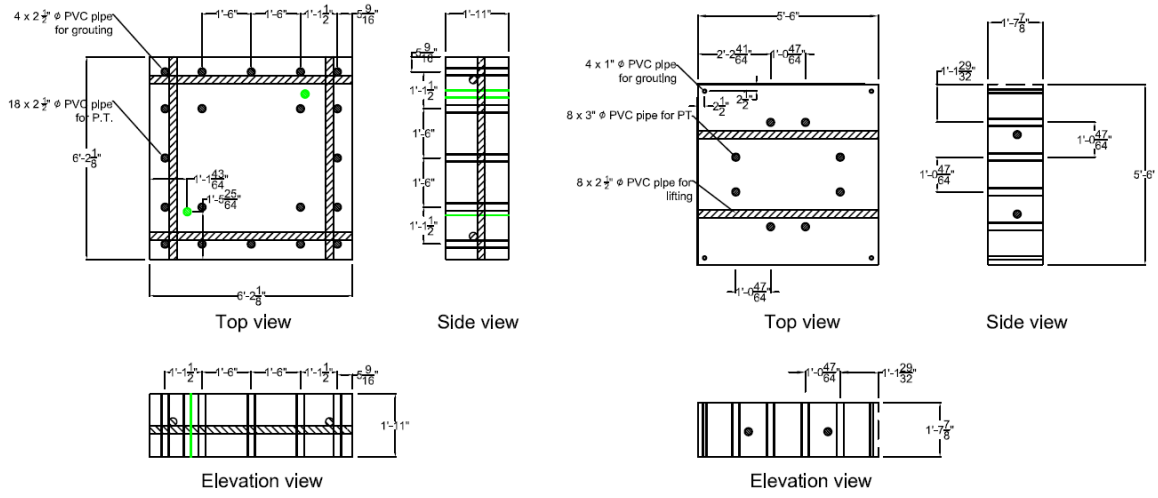

Figure 2.30 Details of loading and bottom block

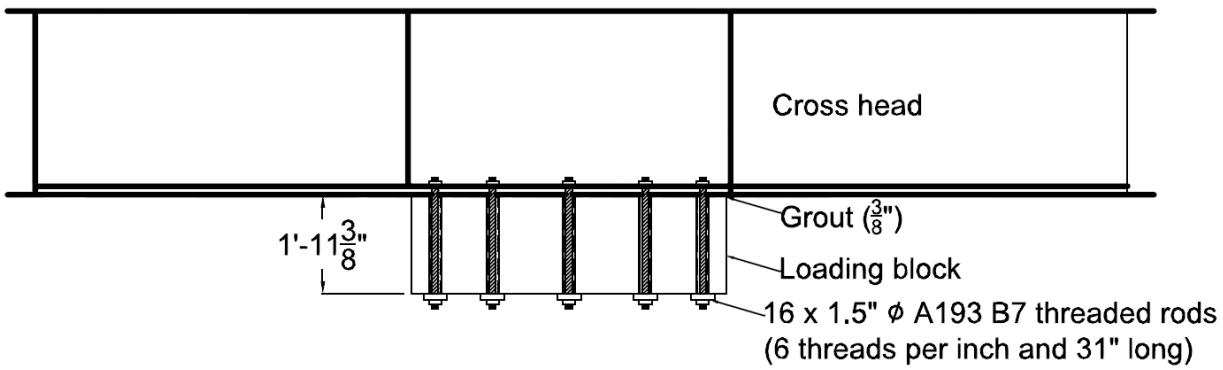

Figure 2.31 Connections details between loading block and crosshead

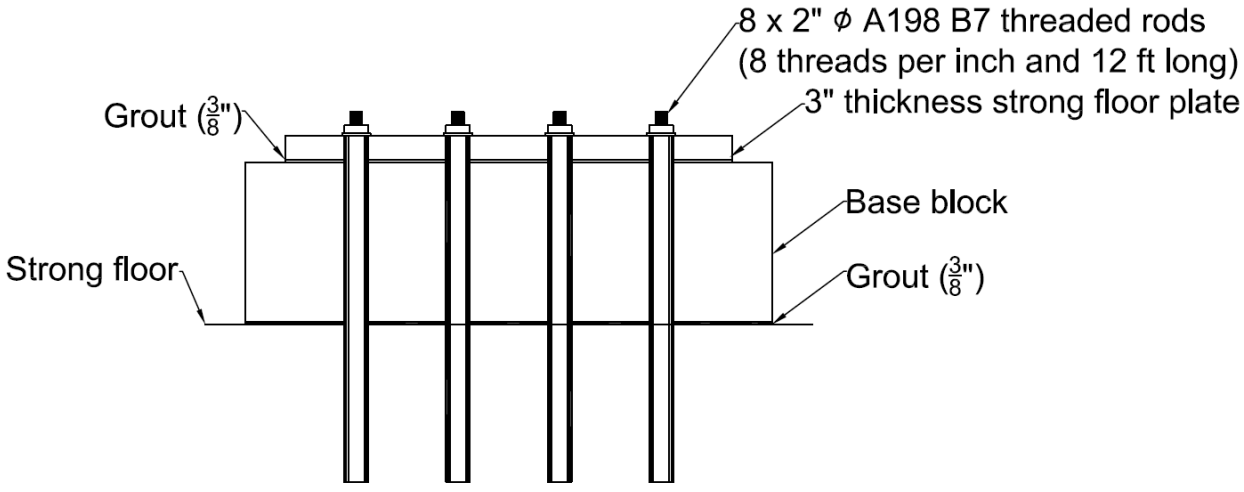

Figure 2.32 Connection details between base block and strong floor

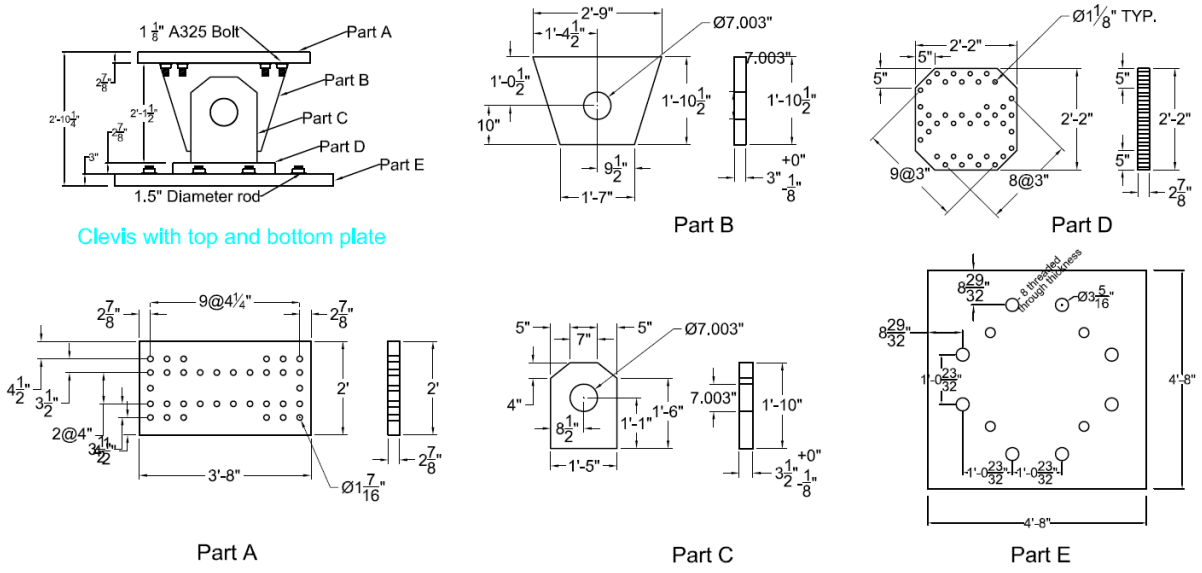

Figure 2.33 Details of clevis

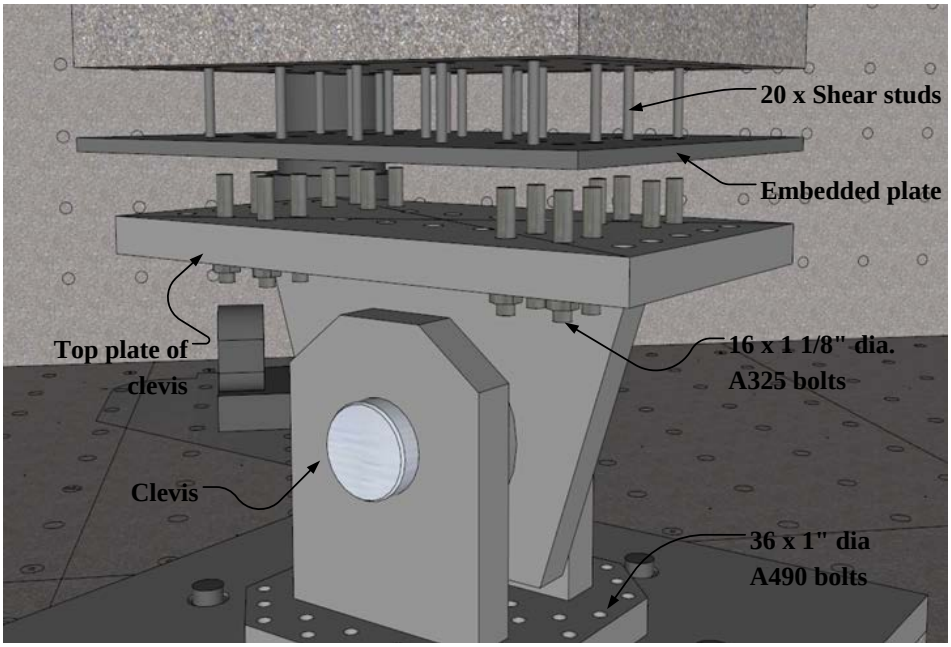

Figure 2.34 Connection details between clevis and lower column

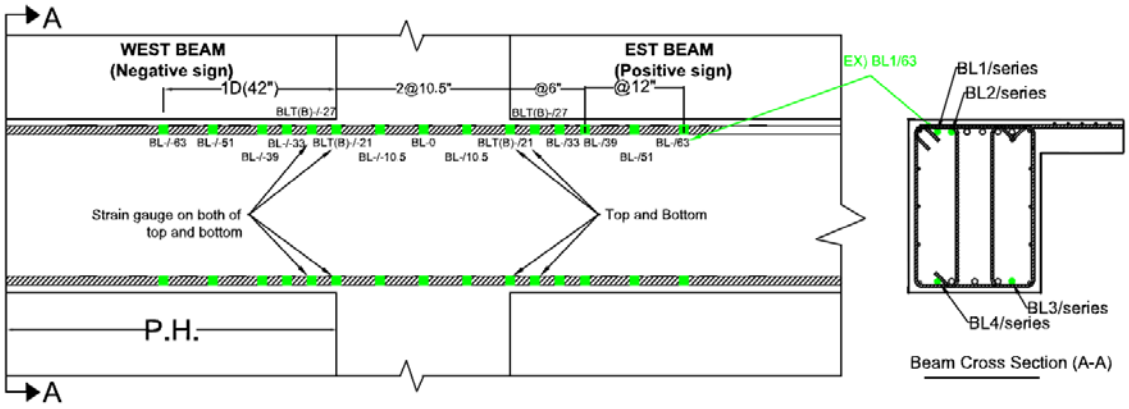

Figure 2.35 Locations of strain gauges on beam longitudinal reinforcement

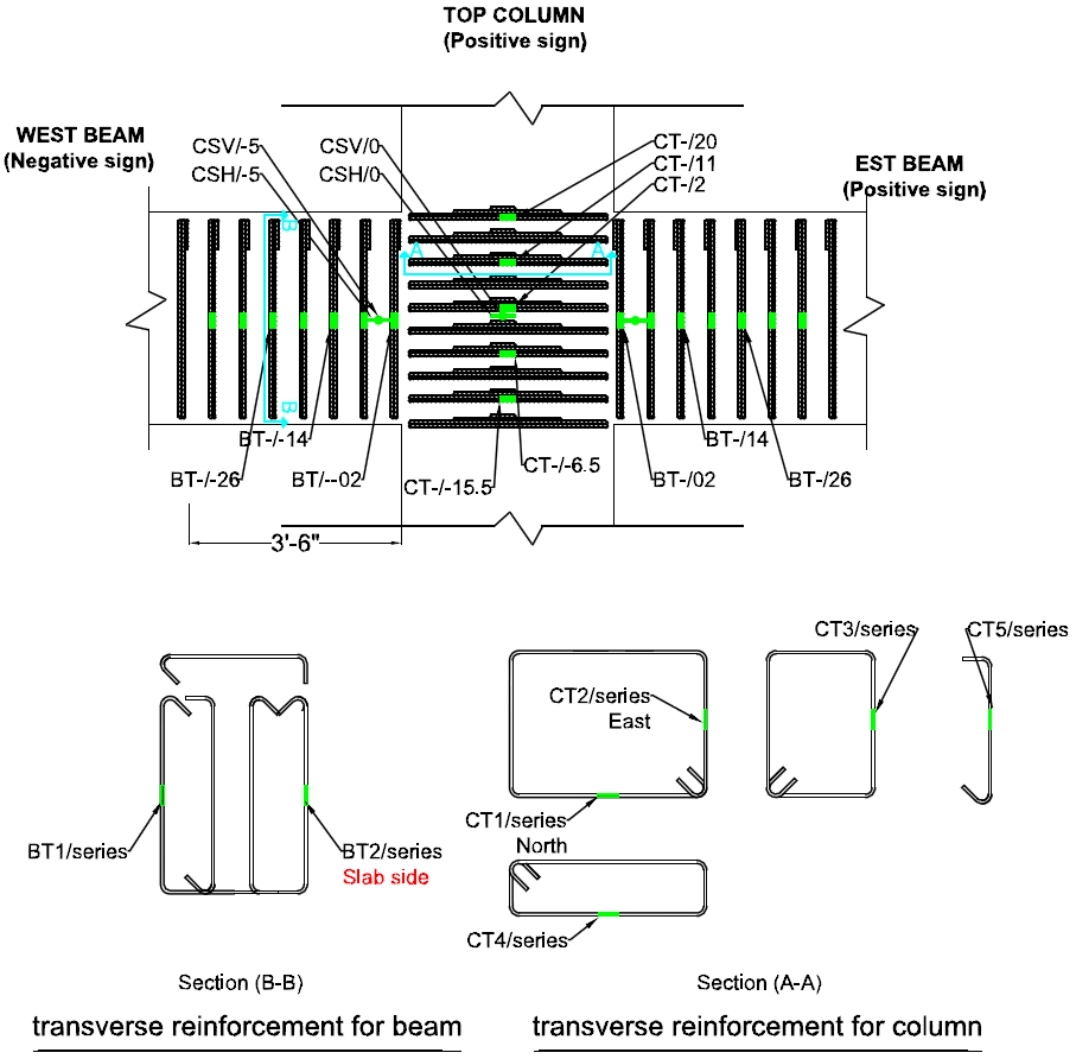

Figure 2.36 Locations of strain gauges on transverse reinforcement

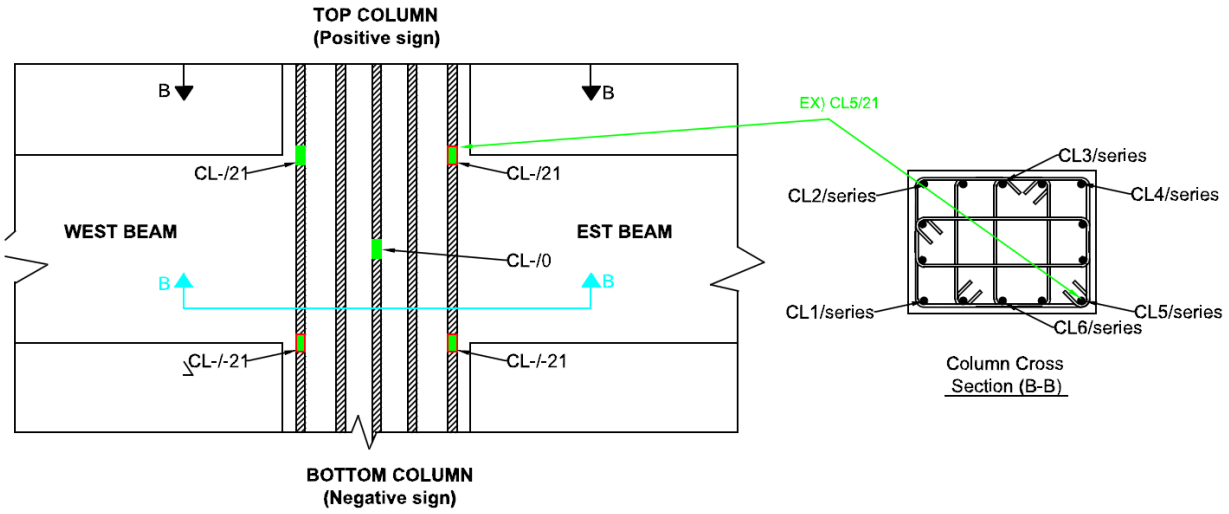

Figure 2.37 Locations of strain gauges on column longitudinal reinforcement

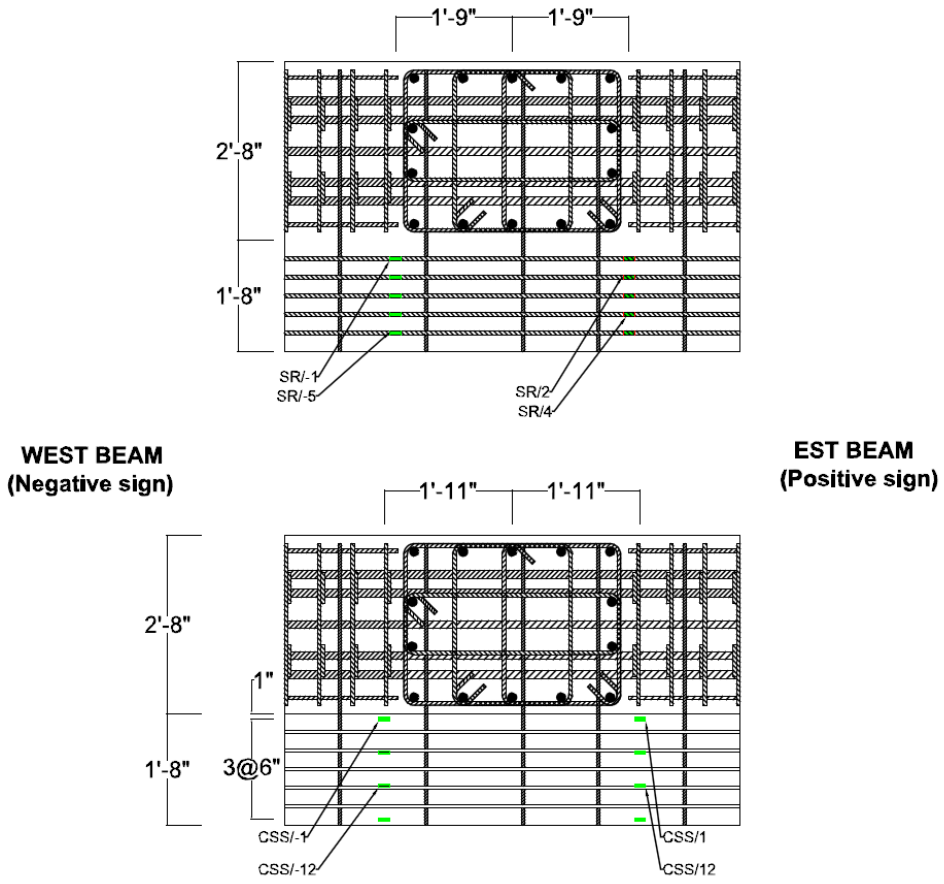

Figure 2.38 Locations of strain gauges on slab longitudinal reinforcement

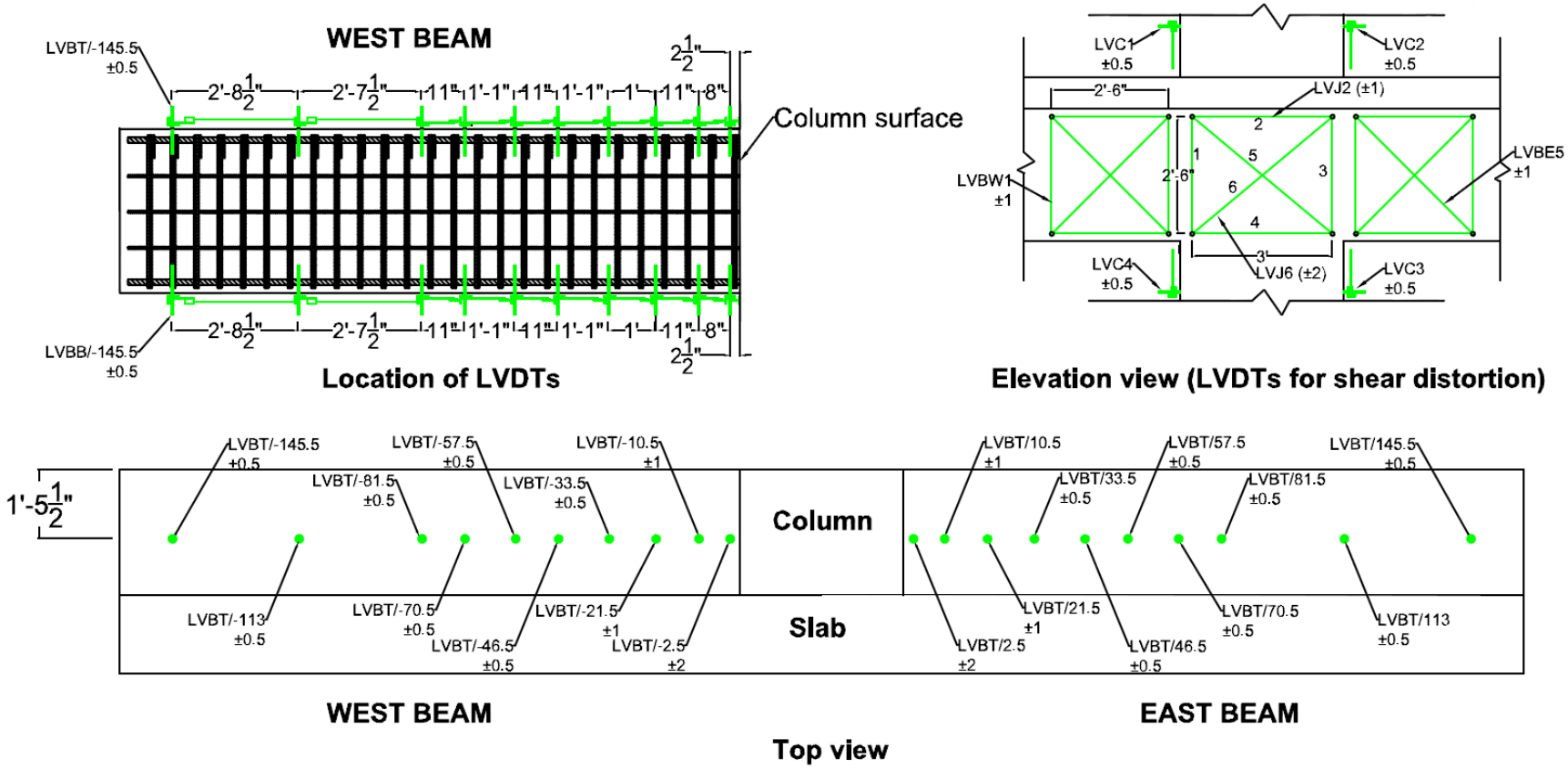

Figure 2.39 Locations of LVTDs and string pots

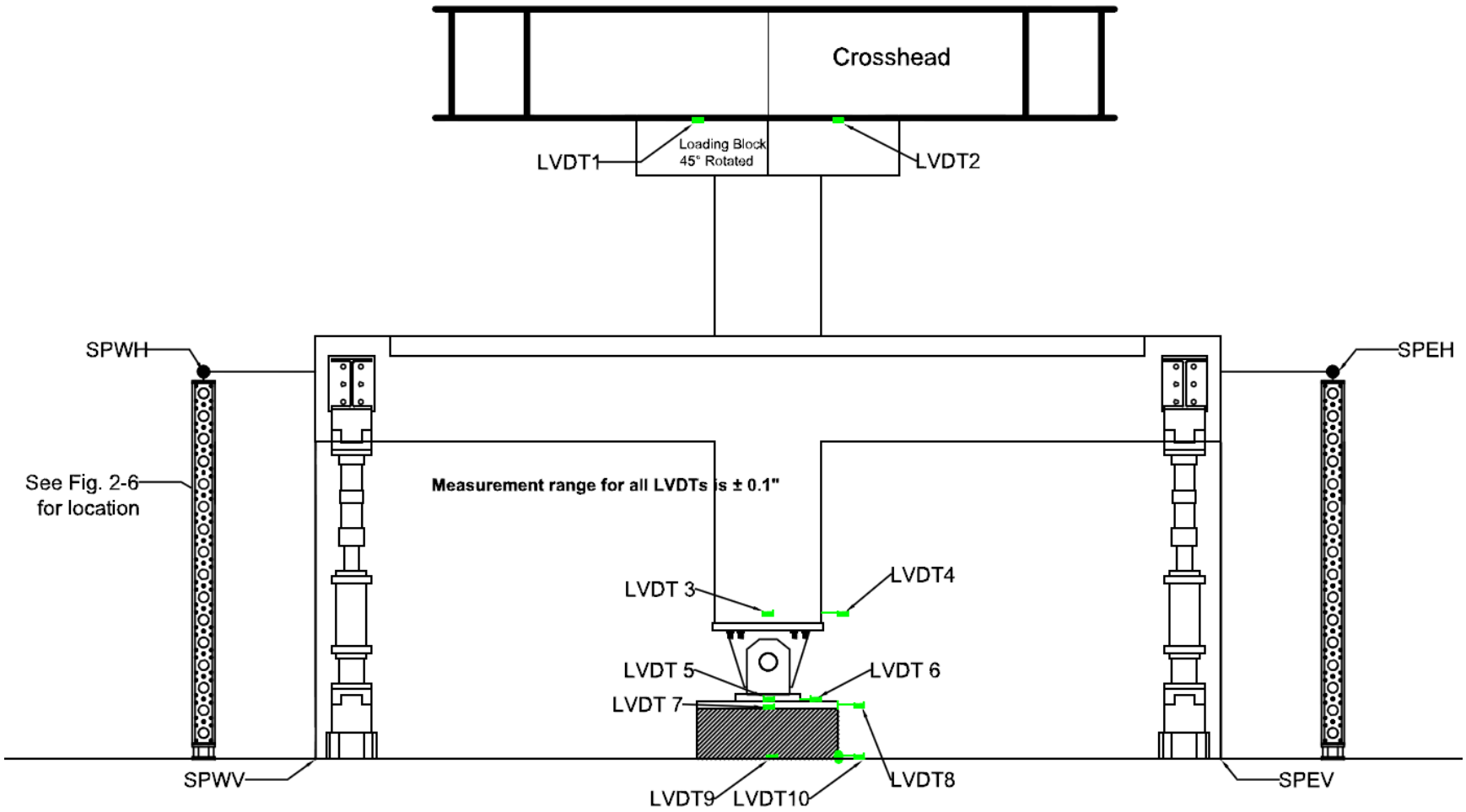

Figure 2.40 Locations of strain gauges around specimen

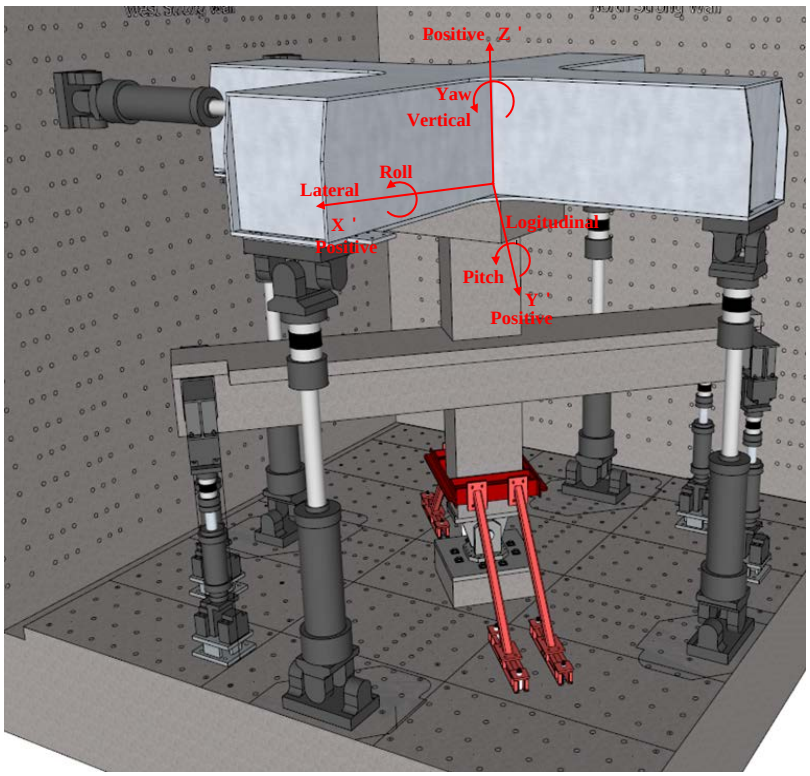

Figure 2.41 Overview of the test setup with the rotated MAST control coordinate system

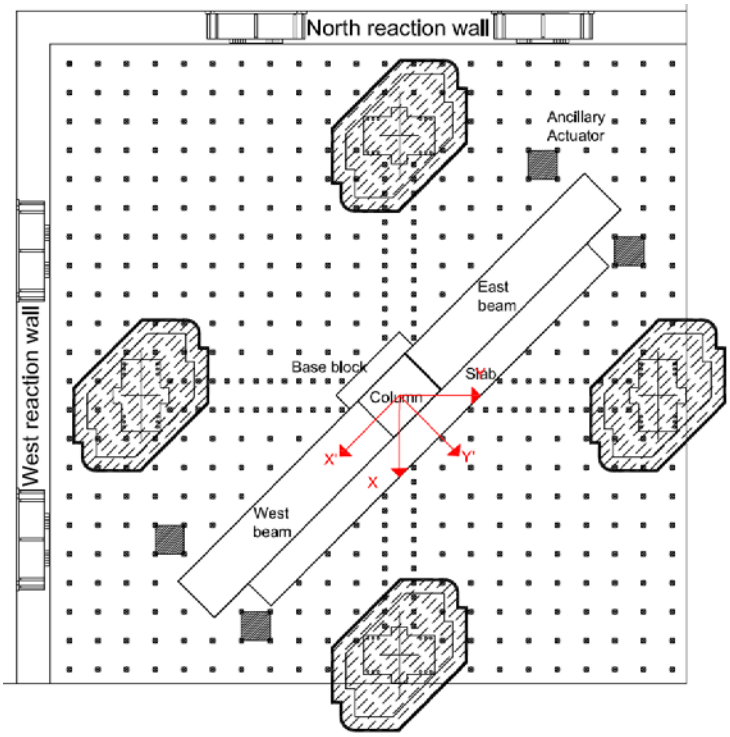

Figure 2.42 Cross section orientation of the slab-beam-column specimen

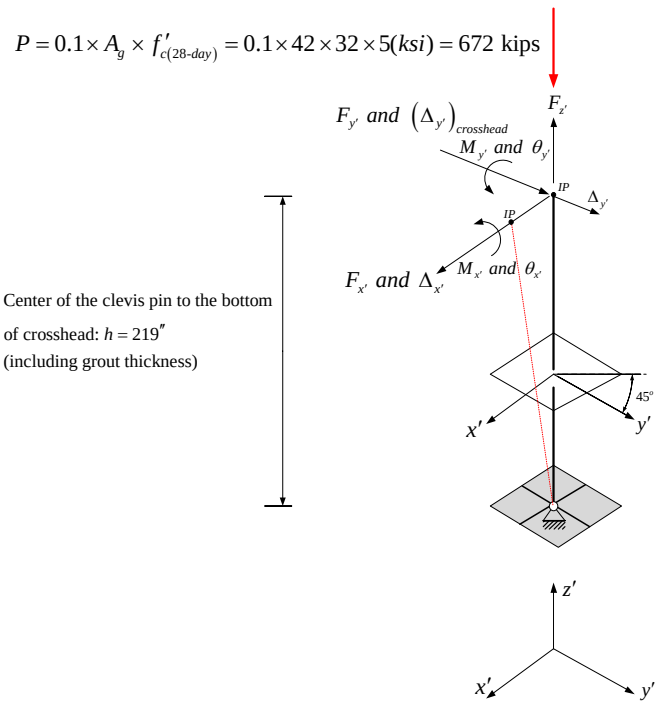

Figure 2.43 Notations of the Loading and displacement components

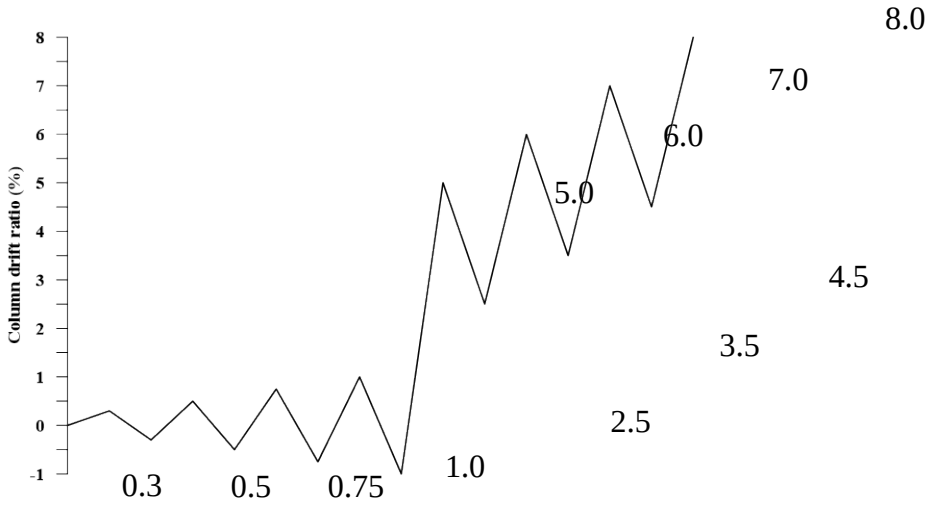

Figure 2.44 Loading protocol for RC-SP-NL

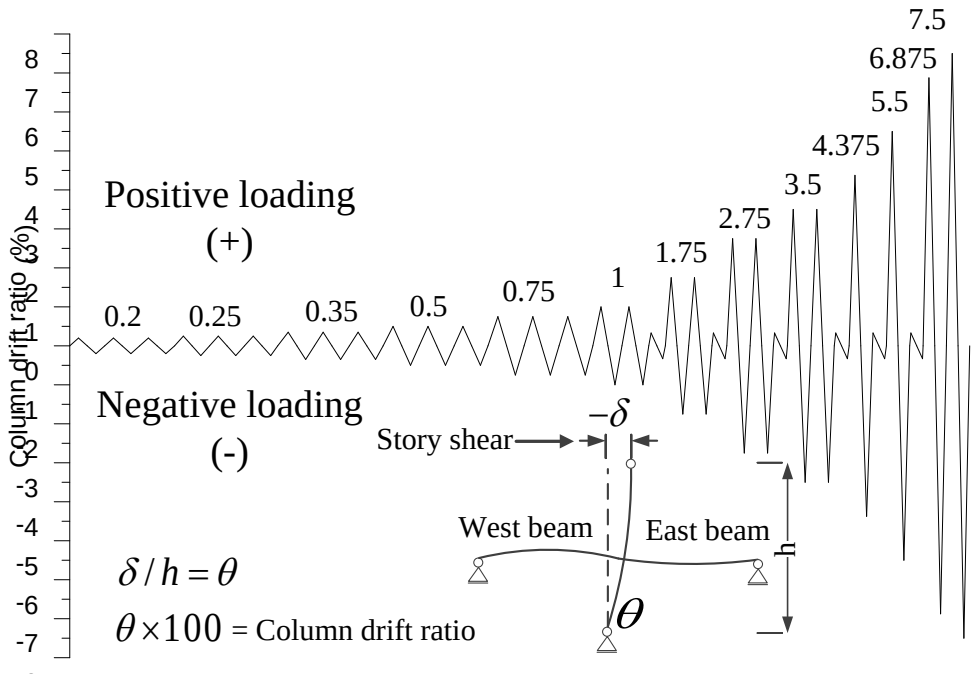

Figure 2.45 Loading protocol for RC-SP-CL and HPFRC-SP-CL

Chapter 3

EXPERIMENTAL RESULTS AND DISCUSSION

3.1 Cracking and Damage Pattern

Figure 3.1 through 3.6 show the cracking and damage patterns of all specimens. The photos show entire specimens at the end of the test of each specimen and show closely the slab-beam-column connections, which include beam-column joints, beam plastic hinge regions and part of upper and lower columns, because the cracks and damage was predominantly occurred in those regions.

Figure 3.1 and 3.2 shows the cracks and damage of RC-SP-NL. This specimen was failed due to the buckling of beam longitudinal reinforcing reinforcement. Although some minor cracks were developed, no noticeable damage was found in the column during the test. In the joint, many diagonal cracks and some concrete spalling were observed. However no noticeable damage was observed throughout the test. The first crack appeared at 0.3% column drift ratio. It was a vertical flexure crack developed at a beam-column interface. As load reversed, a similar crack occurred at the opposite side of the column. At this point, no cracks were observed in the columns and joint. At 0.5% column drift level, the first crack in the joint appeared. It was a diagonal crack which developed from a corner to the opposite corner. A few flexure cracks were overserved, which were located away from the beam-column interfaces. No shear cracks were found in the beam plastic hinge regions. As load reversed, another diagonal shear crack was observed in the joint. This diagonal crack intersected previous one building a grid.

At 0.75% column drift level, the flexure crack at the beam-column interfaces kept progressing toward the top or bottom fibers of the beams. And another diagonal shear crack parallel to the previous ones appeared in the joint. The first shear crack developed away from the column faces. This was a flexure shear crack. That is, the vertical flexure crack became inclined. There was still no crack in the column at this column drift ratio, while the first flexure crack was observed in the slab near the beam-column interface.

At 1.0% column drift, the first flexure crack developed in the column, while the other cracks in the joint and beam plastic hinge regions became wider. After 1.0% column drift level, the specimen was displaced up to 5.0% column drift level without any reversed cyclic loading. During this loading, significant damage occurred at the beam-column interfaces. The vertical flexure cracks at the beam-column interfaces that developed at the beginning of the loading became very wide and separated the beams from the column. The sliding between the column and beams was observed. The concrete at the bottom of the east beam crushed. The shear cracks in the beams were evident at this drift level. The widths of shear cracks were visible. The flexure crack in the slab became so wide that it separated the slab. On the other hand, the damage in the joint was not severe. Only the width of the diagonal cracks became slightly wider. Also no notable damage or cracks in the column was observed. Therefore, most of damage concentrated in the beam plastic hinge regions.

Increasing drift only made the cracks and damage in the beam plastic hinge regions much more severe, while it does not cause any visible damage in the joint and columns. At this point there was no evident visible sign of the buckling of beams longitudinal reinforcement. After reaching up to 8.0% column drift ratio, the loading was

continued in a monotonic manner until the crosshead reached its stroke capacity. While this loading all the longitudinal reinforcement in compression zone were buckled out, perpendicular to the beam longitudinal axis. The cracks in the joint, column, and the beams away from the column faces became difficult to observe with bare eyes. Test was finished since the specimen was failed due to the buckling of beams longitudinal reinforcement.

The progressive cracking and damage patterns of RC-SP-CL are shown in Figure 3.3 and 3.4. In RC-SP-CL, most of cracking and damage occurred in the plastic hinge regions of the beams, leading to the buckling of beam longitudinal reinforcement and shear sliding at beam-column interfaces. Although some minor cracks were developed, no noticeable damage was found in the column during the test. In the joint, many diagonal cracks and some concrete spalling were observed. However joint maintained its strength throughout the test without significant damage.

The first vertical flexural crack of RC-SP-CL was observed at the beam-column interface during positive loading at the 0.2% column drift ratio followed by a similar crack at the same location on the opposite side of the column during negative loading. This type of vertical cracking started spreading away from the beam-column interface toward the beam plastic hinge regions at 0.35% column drift ratio. The vertical cracks, which developed at the beam-column interfaces, started interconnecting with other vertical cracks at the 0.5% column drift ratio. These cracks became wide enough at the 1.75% column drift ratio to eventually separate the beams from the joint at the 2.75% column drift ratio, while other flexure cracks (which started appearing at 0.35% column drift ratio) away from the column face maintained nearly the same width until the end of the test.

Concrete spalling started at the bottom of the beam at the 1.75% column drift ratio. At the 2.75% column drift ratio, sliding between the beams and column was observed, which was mainly due to the separation of the column and beams caused by the vertical flexural cracks at the beam-column interfaces. The sliding caused large dowel force in the longitudinal reinforcement of the beams which in turn created longitudinal cracks at the bottom of the beam. This can be observed from the spalled concrete at the bottom of the beams as shown in Figure 3.4. At this stage, the buckling of the longitudinal reinforcement in the beams was clearly seen in the region where the concrete spalled out . The flexural cracks in the beam plastic hinge region became inclined at 0.75% column drift ratio. At 2.75% column drift ratio, the shear cracks initiated from flexural cracks became much wider. However, beyond this stage, the width of the shear cracks remained in their original width up to the end of the test.

The first diagonal crack in the joint region appeared during the positive loading at 0.35% column drift ratio. This crack was located at the center of the joint. As the load reversed, another diagonal crack formed, which intersected with the previous diagonal crack. As the load increased, the diagonal cracks spread over a wider range making a grid all over the joint region. Their widths became wider and concrete eventually spalled in the center of the joint at 3.5% column drift ratio. The first flexure crack in the columns was observed at 0.75% column drift, followed by a few more cracks as the load increased. These cracks started inclining after 1% column drift ratio. However, no concrete spalling or notable damage in the column was observed during the test. The test for RC-SP-CL was stopped at 3.5% column drift ratio, where the strength degradation began and the entire SBC subassemblage started to twist due to significant damage at the beam-column interfaces because of the unsymmetrical geometry of the specimen.

Figure 3.5 and 3.6 show the crack and damage patterns of HPFRC-SP-CL, which can be compared to those of RC-SP-CL since they are subjected to the same cyclic loading. And this can be used to evaluate the performance of HPFRC on controlling the cracks and damage. The testing of HPFRC-SP-CL was able to continue up to 8.0% CDR because the damage in the beams was minimized by the balanced damage in the joint, thereby preventing any significant twisting of the sub-assemblage. The joint damage of HPFRC-SP-CL was not noticeable up to 1.75% column drift ratio compared with RC-SP-CL. However, it became much more severe after 2.75% column drift ratio. Some cracks were observed in the column, but no notable damage was found up to the end of the test. The first flexural crack at the bottom of the west beam-column interface developed during the first positive cycle at 0.25% column drift ratio followed by another flexural crack at the east beam-column interface during the first negative cycle at the 0.35% column drift ratio. Unlike RC-SP-CL, these flexural cracks at the bottom of the beam-column interfaces did not interconnect with other cracks from the top of the beam. Therefore, the beam and column did not separate until the end of the test.

At 1% column drift ratio, the lengths of the flexural cracks in HPFRC-SP-CL were much shorter than those in RC-SP-CL. This means that the strains of the beam longitudinal reinforcement in RC-SP-CL are much greater than that in HPFRC, resulting in a higher contribution of the beams to the total drift ratio. Also, the number of cracks and degree of damage in the beams of RC-SP-CL were more severe than those of HPFRC-SP-CL. The flexural cracks in the plastic hinge region started to incline at 1.75% of CDR, which was much later than in RC-SP-CL (0.75% column drift ratio). Note that in general, a code compliant moment frame experiences a maximum column drift ratio (interstory drift ratio) of approximately 1.0% under moderate earthquakes. Their widths

did not become wider until the end of the test. No severe concrete damage and bar buckling in beams occurred throughout the testing. Note that the east beam of HPFRC-SP-CL had no transverse reinforcement in the plastic region and a few transverse reinforcement were placed in the west beam.

The diagonal crack in the joint of HPFRC-SP-CL initiated at 0.35% column drift ratio at nearly the same location as RC-SP-CL. However, unlike RC-SP-CL, the diagonal cracks did not spread over the joint. At 1.0% column drift ratio, two major diagonal cracks appeared in the joint of HPFRC-SP-CL which originated from the corners of the joint to the opposite corners. Moreover, as the load increased, other fine cracks developed around the two major diagonal cracks. This implies that the force-transferring mechanism in the HPFRC-SP-CL joint could be different from the RC-SP-CL joint, which formed a grid of diagonal cracks. Note that although the amount of transverse reinforcement in the HPFRC-SP-CL joint was much less than that in RC-SP-CL, the RC-SP-CL joint had more damage than that of the HPFRC-SP-CL at 1.0% column drift ratio.

The width of the cracks in the HPFRC-SP-CL joint became wider after the 1.75% CDR, exhibiting an irregular crack progressive pattern. After this stage, the joint started bulging out as seen in Fig. 3.5, eventually leading to noticeable joint damage. Despite the observed damage in the joint, no concrete spalling had occurred by the time the 3.5% CDR was reached. The first flexural crack in the column was noticed at the 0.75% CDR, which was at the same drift level as RC-SP-CL. A few flexural cracks followed and inclined as the load increased, but no noticeable damage in the column was observed during the test.

To sum up, Both RC specimens had localized damage in their beams adjacent to the column faces, as intended in the design and displayed very similar cracking and damage patterns during the tests regardless of the difference in loading. However, the buckling of the longitudinal reinforcements in the beams seems to depend on loading types. The buckling was more vulnerable to the cyclic loading rather than the near collapse loading. It was the vertical crack that caused the early buckling of RC-SP-CL. This vertical crack eventually separated the beams from the column and caused the sliding between the beams and column. This activated the dowel action, weakened the concrete in the compression zone near the column faces, and crushed the concrete. Consequently, the compression force that was resisted by the concrete transferred to the longitudinal reinforcement. This additional compression force may be the cause for early buckling of the longitudinal reinforcement since the sliding was more obvious for the specimens which was subjected to the cyclic loading.

For HPFRC-RC-CL, the vertical cracks were prevented by the fiber and skin reinforcement that passed through the beam column joint. Also, this specimen showed shared damage between the beams and joint up to 2.75% column drift ration. The less rotation of the beams due to the shared damage can be also the reason that prevented the vertical cracks. As a result, no sliding and concrete crushing was observed in the beams. Although failure occurred in the joint, it is worthy to mentioned that using HPFRC with the balanced concept can prevent or delay the buckling of the longitudinal reinforcement in the beam.

3.2 Column Shear vs. Column Drift Ratio Response

Figure 3.7 through 3.10 plot column shear force against column drift ratio for all specimens. The column shear force is the force measured from the crosshead. The column drift ratio is the result of displacement measured from the crosshead divided by the distance between the bottom of the crosshead and the center of the clevis. The calculated column shear force, V_i, which are shown as dashed lines in the plots was determined by Equation 3.1 through 3.3 (Figure 3.11).

$$V_{column} = \frac{[(M_{pr}^{+} + M_{pr}^{-}) + (V_{pr}^{+} + V_{pr}^{-})2/h]}{\ell_1} \quad 3.1$$

$$V_i = V_{column} + \frac{P \cdot \Delta_{crosshead}}{\ell_1} \quad 3.2$$

As seen in Figure 3.7, RC-SP-CL showed a stable response up to 8% column drift ratio without significant loss in strength and the response of this specimen was controlled by the flexure mechanism. The calculated column shear force was slightly less than the maximum measured column shear force. The column shear force of RC-SP-CL at 8% column drift ratio was 94% of the maximum column shear force. It needs to be mentioned that although significant damage at the beam-column interfaces occurred, no significant strength loss was observed. Strength degradation began at 5% column drift ratio when the concrete in the compression zone started spalling. Part of the reason for the strength loss is believed due to a decreased moment arms that resulted from the concrete spalling. The maximum column shear force during the monotonic loading was 245 kips, which was 84% of the maximum column shear force. The loss in strength

during the monotonic loading resulted from the buckling of the longitudinal reinforcement in the beams

The column shear force versus column drift ratio response of both RC-SP-CL and HPFRC-SP-CL up to the 3.5% column drift ratio is shown in Figure 3.8 and 3.9. For comparison, both specimens are discussed simultaneously. Although HPFRC-SP-CL was loaded up to 8% column drift ratio, the plot only shows the response up to 3.5% because the testing of RC-SP-CL stopped at 3.5% column drift ratio. However, the full response of HPFRC-SP-CL is shown in Figure 3.10. As seen in Figure 3.8 and 3.9**,** both specimens showed stable hysteretic responses up to 3.5% column drift ratio without significant strength degradation and the measured column shear force was close to the calculated column shear force for both specimens.

The response of RC-SP-CL was controlled by the beam flexural mechanism, while the response of HPFRC-SP-CL was controlled by the flexural mechanism up to 1.75% column drift ratio and changed into joint shear mechanism after 1.75% drift ratio (as indicated by the pinched-shape in Figure 3.9). The strength at the first cycle of the 3.5% column drift ratio, where strength degradation began, was 95% and 87% of the peak strengths for RC-SP-CL and HPFRC-SP-CL, respectively. The strength degradation of RC-SP-CL started after 2.75% column drift ratio, where the sliding shear at beam to column interfaces and the buckling of the beam longitudinal reinforcement were observed. The strength loss of the HPFRC-SP-CL after 2.75% column drift ratio was due to the damage in the joint as seen in Figure 3.6. However, the strength degradation of HPFRC-SP-CL was gradual up to the end of the test.

As mentioned before, the performance of the specimens is evaluated by ACI Committee 374 criteria. Considering the cracking, damage patterns, and hysteresis responses, all specimens satisfy the criteria. Therefore, the balanced design concept together with HPFRC can be used when considering performance level.

3.3 Stiffness

Measured lateral secant stiffness of all specimens at each cycle of each column drift ratio is listed in Table 3.1**.** The stiffness of each specimen for a given loading cycle is defined as an average of the story shear divided by the story displacement at each positive and negative peak drift ratio. The calculation of the secant stiffness is shown in Figure 3.12. All specimens experienced stiffness degradation. The stiffness loss is the results from significant cracking, damage, and loss of bond. The stiffness of RC-SP-NL, which was subjected to the near collapse loading, was nearly the same as the stiffness of the other specimens that were subjected to sever cyclic loading. The stiffness of both RC-SP-CL and HPFRC-SP-CL up to 1.0% of column drift ratio is nearly the same. However, beyond 1.75% column drift ratio, HPFRC-SP-CL became stiffer than RC-SP-CL even after the severe damage in the joint. The stiffness of the first cycle at any drift level was greater than the stiffness of subsequent cycles. Therefore, the maximum column shear force for the sequent cycles at the same drift was always less than that of previous cycles.

The secant stiffness of all specimens was very similar to all specimens with the largest stiffness in HPFRC-SP-CL. It does mean that the different damage pattern and

force resisting mechanism in HPFRC-RC-CL does not affect the stiffness. On the other hand, it is straightforward to recognize that the tangent stiffness of HPFRC-RC-CL during the unloading was much less than that of the other specimens. This is due to the shear mechanism of the joint of HPFRC-SP-CL. This can lead to less amount of the total dissipated energy for HPFRC-SP-CL.

Table 3-1 Stiffness

Column Drift Ratio (%)	RC-SP-NL	RC-SP-CL	HPFRC-SP-CL
0.2-1/0.2-2/0.2-3	-	238/229/225 (k/in.)	227/226/221 (k/in.)
0.25-1/0.25-2/0.25-3	-	211/203/201 (k/in.)	210/200/198 (k/in.)
0.35-1/0.35-2/0.35-3	192 (k/in.)	182/175/174 (k/in.)	182/175/173 (k/in.)
0.5-1/0.5-2/0.5-3	154 (k/in.)	155/151/150 (k/in.)	155/150/148 (k/in.)
0.75-1/0.75-2/0.75-3	129 (k/in.)	132/127/126 (k/in.)	128/123/123 (k/in.)
1.0-1/1.0-2	110 (k/in.)	112/109 (k/in.)	112/108 (k/in.)
1.75-1/1.75-2	68 (k/in.)	71/68 (k/in.)	80/74 (k/in.)
2.75-1/2.75-2	47 (k/in.)	47/44 (k/in.)	51/44 (k/in.)
3.5-1/3.5-2	38 (k/in.)	35 (k/in.)	35/30 (k/in.)
4.375-1/4.375-2	30 (k/in.)	-	30/24 (k/in.)
5.0	26 (k/in.)	-	-

3.4 Contribution of Each Member to Total Dissipated Energy

The contribution of each component to the total dissipated energy only for RC-SP-CL and HPFRC-SP-CL (for a direct comparison since both specimens were subjected to the same cyclic loading) are illustrated in Figure 3.13 and 3.14**,** which was calculated by using the Equation 3.3 to 3.6 (Figure 3.15). To calculate the component contribution, there are some assumptions, which are as follows:

1. The very top and bottom of the column represent points of inflection.
2. Point of inflection in beam does not deflect vertically
3. Beam length ℓ_2 is a distance between inflection points of the beams.
4. Important deformation components are: (1) flexure deformation in column outside beam-column joint, (2) flexure deformations in beams outside beam-column joint and outside rigid beams portion, and (3) shear distortion in beam-column joint.
5. Plastic deformation may occur at the following plastic hinge locations: (1) in column just outside joint, (2) in beam just outside joint, and (3) in joint.

$$\delta_{b,e} = \frac{(\ell_2 - e_b)^3}{3EI_b}\frac{\ell_1}{\ell_2}(F_1 + F_2) \qquad 3.3$$

$$\delta_{b,p} = \frac{\ell_1(\ell_2 - e_b)}{\ell_2}\theta_{pl} \qquad 3.4$$

$$\delta_j = (\ell_1 - 2e_c)\gamma_j \qquad 3.5$$

$$\delta_c = \delta_{total} - \delta_{b,e} - \delta_{b,p} - \delta_j \qquad 3.6$$

Equation 3.3 shows the contribution of beam elastic deformation, $\delta_{b,e}$. L is the distance between the loading points of the beams (i.e., distance between the vertical actuators). h_c is the depth of the column. E and I_b are the elastic modulus of concrete and the moment of inertia of the beam section, respectively. h is the story height and F is the measured force from the ancillary actuators attached at the ends of the beams. The contribution of beam plastic deformation, $\delta_{b,p}$, was calculated by Equation. 3.4. θ_{pl}, which is the plastic rotation of the beams and was computed based on the measurement obtained from LVDTs attached on the top and bottom of each beam subtracting the beam elastic rotation computed based on Equation 3.3. δ_j is the lateral deformation due to the shear deformation of joint (Equation 3.5). h_b is the depth of the beams and γ_j is joint shear distortion calculated based on data from the string potentiometers attached on the face of the joint. The joint shear distortion is calculated by Equation 3.7 (Figure 3.16). Finally, the column contribution to the drift ratio, δ_c, is the difference between the total deformation, δ_{total}, and the sum of $\delta_{b,e}$, $\delta_{b,p}$, *and* δ_j.

$$\gamma_{avg} = \frac{(D_1 - d_1)d_1 - (D_2 - d_2)d_2}{2HL} \qquad 3.7$$

For RC-SP-CL, at column drift ratio of 2.75%, the dissipated energy by the beams' flexural deformation accounts for 80% of total dissipated energy. The contribution of the joint was nearly maintained at 26% up to 1% column drift ratio with a decrease starting at 1.75% column drift ratio (16%) down to 11% at the 2.75% column drift ratio. The energy-dissipation contribution of the column increased from 10% to 15% at 0.75% column drift ratio where the first crack of the column was observed. However, the contribution of the column decreased after 1.0% column drift ratio when beams started

yielding, showing only 9% contribution at 2.75% column drift ratio. Referring to the shear story vs. column drift ratio and damage patterns of this specimen, beam flexural mode clearly dominated the response with most damage concentrating in the beams.

In the case of HPFRC-SP-CL, at 0.5% column drift ratio, the beam produced 61% of the total dissipated energy, while the joint accounted for 36%. At 1.0% column drift ratio, the contribution of the beams and joint were 55% and 36% of the total dissipated energy, respectively, with the increasing contribution of the column. At this moment, the story shear vs. column drift ratio response was still similar to that of RC-SP-CL although the joint contribution was higher than RC-SP-CL. The shape of the hysteresis curve was pinched at 2.75% column drift ratio where the contribution of the joint increased up to 46%, which was nearly the same as that of the beams. The contribution of the column started decreasing after 1.75% column drift ratio where the beams and joint of this specimen experienced yielding. Considering the percent contribution of each component, damage pattern, and story shear vs. column drift ratio of HPFRC-SP-CL, it is seen that flexural mode dominated up to 1.75% column drift ratio and then joint shear mode controlled.

As seen in Figure 3.13 and 3.14, total dissipated energy of RC-SP-CL at 2.75% column drift ratio was 1.28 times greater than that of HPFRC-SP-CL. The gradually pinched shape of the hysteresis loop is due to the joint shear mechanism in HPFRC-SP-CL. However, up to 1.75% column drift ratio, both specimens dissipated a similar amount of energy. As discussed earlier, this study used a very low transverse reinforcement ratio for HPFRC-SP-CL. An improved performance can be achieved with an optimized amount transverse reinforcement.

The reduction in total dissipated energy for HPFRC-SP-CL was due to the pinching. The pinching occurs during reloading after unloading, mainly due to the cracks. The stiffness decrease while the cracks close and it recovers after the closure of the cracks. While it is inevitable to avoid this pinching, the level of which depends on the characteristic of the structures. The shear mechanism in the joint of HPFRC-SP-CL led to much more pinched-shape in it hysteresis curve. However, previous works show that the pinching and the degradation in stiffness barely affect peak displacement for the systems with moderate and long period. In addition, The systems with 50% reduction in total dissipated energy due to the pinching had similar peak displacement to those of structures with elasto-plastic or bilinear strength-hardening hysteretic behavior (Otani, 1981; Nassar and Krawinkler 1991; Rahnama and Krawinkler, 1993; Shi and Foutch, 1997; Foutch and Shi, 1998; Gupta and FEMA P440A 2: Background Concepts 2-7 Krawinkler, 1998; Gupta and Kunnath, 1998; Medina 2002; Medina and Krawinkler, 2004; Ruiz-Garcia and Miranda, 2005). Also, the balanced dissipated energy between the beams and joint confirms the success of the balanced damage concept. Therefore, the balanced damage concept can be used for structures with moderate and long period.

3.5 Beam Behavior

3.5.1 Strain in Beam Longitudinal Reinforcement

The locations of strain gauges and strain of the beam longitudinal reinforcement are shown in Figure 3.17 to 3.19**. The** strain was measured within the plastic hinge region (42 in. away from the beam-column interface). The yield strain was indicated with dashed lines in the figures. For RC-SP-NC, the first yielding in a longitudinal reinforcement was

measured at 0.75% column drift ratio. After this point, the longitudinal reinforcement experienced large elongation forming a plastic hinge near a column face. This plastic hinge spread away from the column face as load or column drift ratio increases. The plastic hinge length was about 42 in. (height of beam) distance away from the column face.

The first yielding of one of the beam longitudinal reinforcement for RC-SP-CL was at 0.75% column drift ratio. This means that the Initiation of the yielding of longitudinal reinforcement was not affected by the number of cycle. Similar to RC-SP-CL, the longitudinal reinforcement went through large elongation after the first yielding. The yielding eventually spread to one effective-beam-depth from the beam-column interface. Figure 3.20 also shows that no significant beam reinforcement yielding in HPFRC-SP-CL until 1.75% column drift ratio, and the strains were approximately half of that in RC-SP-CL. The yielding penetration of beam reinforcement was much delayed in HPFRC-SP-CL.

The reduction in area of longitudinal steel reinforcement, which resulted from the large elongation of the reinforcement is one of the reason to the reduced bond strength between concrete and the steel reinforcement. This can affect the stiffness of structures. As discussed in section 3.3, the stiffness of RC-SP-CL was less than that of HPFRC-SP-CL after 1.0% column drift ratio where large elongation in the longitudinal reinforcement occurred. The decrease in the stiffness of HPFRC-SP-CL is mainly due to the damage in the joint. This can be improved by adding more transverse reinforcement in the joint (this will be explained later on). In addition, due to the large elongation of the longitudinal reinforcement under cyclic loading, the stress-strain relation under tensile loading

becomes nonlinear under stresses below the specified yield stress. This can affect the performance of structures for service loads after even moderate earthquake. The balanced damage concept can resolve this issue since the contribution of the beam is much less.

3.5.2 Flexure and Shear Strength

Table 3.2 shows the measured yield moment strength and calculated nominal moment strength of the beams for all specimens. The measured yield strength was determined when the first yielding in any longitudinal reinforcement occurred. And the nominal moment strength was calculated without considering any over-strength in materials. Table 3.3 shows the peak measured moment strength and probable moment strength for all specimens. The peak measured moment strength was calculated based on the force measured from the ancillary vertical actuators. Table 3.4 and Figure 3.20 through 3.22 illustrate the beam rotation in plastic hinge regions. The beam rotation was calculated by using Equation 3.8. Here, Δ is top or bottom relative displacement measured by LVDTs attached on the top and bottom of each beam.

$$\theta_{ph} = \frac{\Delta_{top\ or\ bottom} + \Delta_{bottom\ or\ top}}{h_{ph}} \qquad 3.8$$

The measured positive and negative yield moment strength for RC-SP-NL were 19,863 k-in and 20,907 respectively. The measured positive yield moment strength was 1.11 times higher than calculated nominal moment. On the other hand, the measured

Table 3-2 Measured yield and calculated nominal moment

Specimens	M_y^+, k-in.	M_n^+	$\frac{M_y^+}{M_n^+}$	M_y^-, k-in.	M_n^-	$\frac{M_y^-}{M_n^-}$
RC-SP-NL	19,863	17,863	1.11	20,907	20,840	1.00
RC-SP-CL	20,289	17,863	1.13	20,907	20,684	1.01
HPFRC-SP-CL	22,657	21,269	1.06	2,3172	24,276	1.04

Table 3-3 Measured peak and calculated probable moment

Specimens	M_b^+, k-in.	M_{pr}^+	$\frac{M_b^+}{M_{pr,b}^+}$ [1]	M_b^-, k-in.	M_{pr}^-	$\frac{M_b^-}{M_{pr,b}^-}$
RC-SP-NL	27,259	22,139	1.23	30,450	25,659	1.19
RC-SP-CL	27,021	22,139	1.22	29,482	25,659	1.15
HPFRC-SP-CL	29,916	26,677	1.12	30,925	29,350	1.05

Note: [1] M_b: maximum measured moment of beams, $M_{pr,b}$: calculated probable moment of beams.

negative moment was close to the calculated nominal moment. Corresponding beam rotations in plastic hinge regions were 0.004 for the west beam and 0.0067 for the east beam with average rotation of 0.0053. As seen in Figure 3.21, after the yielding of a longitudinal steel reinforcement, the beam rotation in the plastic hinge regions increased visibly with increasing column shear force. The peak measured positive and negative moments were 27,259 k-in. and 30,450 k-in, which were 1.23 and 1.11 times greater than calculated probable positive and negative moment strengths. Unlike the measured positive and negative yield moment strength, The difference between the calculated probable moment strength and peak measured moment strength resulted from the actual

material properties and the p-delta effect. After 4% column drift ratio, the strength of the beams in RC-SP-NL began dropping. The average beam rotation at this time was 0.036. The strength loss was partially due to the concrete crushing at compression zones as explained before.

Similar to RC-SP-NL, the measured positive yield moment strength for RC-SP-CL was greater than the calculated positive moment strength, while the negative measured and calculated yield moment strengths were similar. On the other hand, the measured negative and positive yield moment strength for HPFRC-SP-CL were close to the calculated yield moment strengths. The measured peak moment strength of RC-SP-CL was similar to those of RC-SP-NL since they have the same reinforcement details. The measured negative peak moment strength was 1.1 times higher than that of positive peak moment strength, which means the longitudinal reinforcement in the slab increase the negative moment. Also, the peak moment strengths of HPFRC-SP-CL were greater than that of RC-SP-CL. This was because the skin and construction reinforcement increased the moment strength. The difference between the peak negative and positive moment strengths and calculated probable moment strengths for HPFRC-SP-CL was less than the differences in RC specimens. This is because the longitudinal reinforcement in HPFRC-SP-CL did not elongate as much as RC specimens so that the strength increase that resulted from the strain hardening was less.

As seen in Figure 3.22 and 3.23, the average beam rotation at the first yield of beam longitudinal reinforcement for both RC-SP-CL and HPFRC-SP-CL were 0.0064 and 0.0058. There was not much difference at this time. However, after the first yielding in the longitudinal reinforcement of RC-SP-CL occurred, the difference in the rotation between

two specimens increased. The beam rotations in the plastic hinge regions at 1.75% column drift ratio were 0.0145 and 0.0098 for both specimens. The rotation of RC-SP-CL was 1.48 times greater than that of HPFRC-SP-CL. This means the beams of RC-SP-CL deformed much more than HPFRC-SP-CL. The rotation dramatically increased after 2.75% column drift ratio for both specimens. This is due to the increased relative displacement of LVDTs for the buckling of beams longitudinal reinforcement for RC-SP-CL. Also, the increase of rotation of east beam for HPFRC-SP-CL is contributed to bond failure in the joint (this will be explained later).

Table 3-4 Beam rotation in plastic hinge region

Drift ratio	RC-SP-NL (West/East beam)	RC-SP-CL (West/East beam)	HPFRC-SP-CL (West/East beam)
0.2	-	0.0015/0.0011	0.0015/0.0013
0.25	-	0.002/0.0017	0.0018/0.0016
0.3	0.0011/0.0024	-	-
0.35	-	0.0027/0.0023	0.0024/0.0022
0.5	0.002/0.0037	0.0037/0.0031	0.0034/0.0032
0.75	0.0029/0.0049	0.0052/0.0047	0.0046/0.0046
1	0.004/0.0067	0.007/0.0058	0.0056/0.0060
1.75	-	0.016/0.013	0.0096/0.010
2	0.015/0.018	-	-
2.75	-	0.024/0.023	0.015/0.016
3	0.024/0.029	-	-
3.5	-	0.055/-	0.016/-
4.375	-	-	-
4	0.034/0.040	-	0.018/-
5	0.044/0.051	-	-

3.5.3 Effective Stiffness

Effective stiffness, I_{eff}, is used to estimate building periods such that accurate internal forces can be achieved for buildings. A definition of the effective stiffness is shown in Figure 3.24 and it is calculated by using Equation 3.10. Here, E_c is Young's modulus of concrete and it is determined by Equation 3.11. ℓ_n is the length of the beam, and Δ_y is obtained from Equation 3.12, where $\theta_{y,pl}$ is beam rotation in the plastic hinge region at yielding and $\ell_{n,el}$ is the length of the beam except the plastic hinge region. The effective stiffness of the beams for RC-SP-NL, RC-SP-CL, and HPFRC-SP-CL is 0.3 $E_c I_g$, 0.26 $E_c I_g$, and 0.28 $E_c I_g$, respectively.

$$I_{eff} = \frac{V\ell_n^{\,3}}{3E_c\Delta_y} \tag{3.10}$$

$$E_c = 57{,}000\sqrt{f_c'} \tag{3.11}$$

$$\Delta_y = \theta_{y,ph} / \ell_n + \frac{V\ell_{n,el}^{3}}{3E_c I_g} \tag{3.12}$$

3.5.4 Beam Fixed End Rotation

The fixed end rotation of the beams for all specimens are shown in Figure 3.26 to 3.28, which was calculated by the measurements of LVDTs at the top and bottom of the beam ends (Equation 3.13). As the LVDTs were fixed to the beam only 1.5 in. from the

$$\theta_f = \frac{\Delta_{top\ or\ bottom} - \Delta_{bottom\ or\ top}}{h_b} \quad 3.13$$

column face, the deformation from the beam was negligible and the measurement mainly came from the fixed end rotation of the beam, which is the result of the bond failure either in the joint and/or beam plastic hinge regions. The bond failure of the joint will be dealt with later on in this report.

Figure 3.29 illustrate the increment of the contribution of the beam fixed end rotation to total column drift ratio for RC-SP-NL. As seen in Figure 3.29, the contribution of the fixed end rotation for RC-SP-NL increases as column drift ration increases. It was almost 60% at 6.0% column drift ration. As seen in Figure 3.30**,** the fixed end rotation of both RC-SP-CL and HPFRC-SP-CL is almost the same up to 1% column drift ratio. However, at 1.75% column drift ratio, the fixed end rotation of RC-SP-CL increased much faster than HPFRC-SP-CL. This can be explained by the strains of the beam's longitudinal reinforcement in the plastic hinge region of RC-SP-CL. As shown in Figure 3.19, the strain at the beam column interface of RC-SP-CL dramatically increased at 1.0% column drift ratio, spreading into both the beam plastic hinge region and the joint. The yielding penetration into the beam plastic hinge regions can cause bond deterioration due to the decreased area of reinforcement. On the other hand, the fixed end rotation of HPFRC-SP-CL is due to the bond failure in the joint only (this will be discussed later on). The fixed end rotation from beams is much smaller due to the lower strains in the beam longitudinal reinforcement of the plastic hinge region of HPFRC beams.

3.5.5 Buckling of Beam Longitudinal Reinforcement

As explained in the previous section, a major cause of the strength loss for RC-SP-NL and RC-SP-CL was the buckling of beam longitudinal reinforcements. The buckling arose during the monotonic loading in RC-SP-NL. During the loading to 8% column drift ratio, the longitudinal reinforcements experienced large elongation, then the stretched longitudinal reinforcements were compressed during the monotonic loading, making the longitudinal reinforcements buckled. The buckling occurred about 11 in. away from the beam-column interface, spanning two hoop sets. The hoops completely yielded, making arches. Figure 3.31 shows the buckling of the beam longitudinal reinforcements for RC-SP-NL.

Although the longitudinal reinforcements of RC-SP-NL did not buckle up to 8% column drift ratio, the buckling of the longitudinal reinforcements in the beams of RC-SP-CL was observed at 2.75% column drift ratio. This can be detected by LVDTs reading. The arch shape of the buckled reinforcements increases the LVDTs reading and the measurement of the strain gauges attached on the top and bottom of the longitudinal reinforcements gives different gauge readings. Therefore, it is believed that the buckling of longitudinal reinforcements are greatly affected by the number of cycles (strain history). The location of the buckling for RC-SP-CL was the same as that of RC-SP-NL. It was about 11 in. away from a beam-column interface (Figure 3.32). A buckling did not occur for HPFRC-SP-CL.

3.4.6 Shear Stress and Strain in Hoops

The purpose of placing transverse reinforcements in plastic hinge regions is: 1) to resist shear force, 2) to confine concrete and 3) to prevent or delay the buckling of beams longitudinal reinforcements. Unlike the longitudinal reinforcement in the beams in plastic hinge area, any yielding in transverse reinforcement (Hoops and crossties) may lead to a shear failure. The shear failure must be prevented, since loss of strength and stiffness can be rapid and the failure is brittle. Figure 3.33 through 3.43 show the strain in transverse reinforcements in plastic hinge regions for all specimens. In general, the strain in hoops on the slab side was smaller than the strain in the opposite side where no slab exists. This was because slab resists shear as well. The strain in the hoops and crossties for all specimens were stable. However, only one strain gauge shows yield strain during the loading to 3.5% column drift ratio for RC-SP-NL. For RC-SP-CL, although all of strain gauge shows elastic response, the strains of a few of hoops were close to yield strain. Note that although HPFRC-SP-CL had no hoops and crossties in its east beam, no significant shear damage occurred. This was attributed to both the high shear resistance provided by HPFRC and the balanced damage between the beams and joint. Strain gauge data also showed that the four sets of transverse reinforcement in the left-side beam of the HPFRC specimen had a maximum strain of only 0.06%, while the maximum strain in the transverse reinforcement of RC-SP-RC was greater than the yielding strain 0.22%.

Table 3.5 provides the maximum measured shear and normalized shear stress. And, the shear resistance provided by the steel transverse reinforcement (hoops and crossties) is given in Table 3.5 as well. According to ACI 318-14, contribution of concrete

to resist shear force is zero if earthquake-induced shear force is larger than the maximum required shear strength within plastic hinge regions. If the construction reinforcements were not placed, only one hoop and one crosstie were to be placed in the plastic hinge regions. However, one more crosstie was provided to comply with ACI 318-14 section 25.7.2.3. It needs to be noted that even if the additional confinement or shear resistance were provided by one more crosstie, one hoop experienced yielding for RC-SP-NL, a few hoops were close to the yielding strain and the buckling of the longitudinal reinforcement still occurred.

Table 3-5 Measured shear stress

Specimens	V_b^+, k-in.	Normalized shear stress for V_b^+ [1],psi	V_b^-,	Normalized shear stress for V_b^-, [1] psi	V_s kips
RC-SP-NL	189	1.44$\sqrt{f'_c}$	-216	1.65$\sqrt{f'_c}$	486
RC-SP-CL	187	1.64$\sqrt{f'_c}$	204	1.79$\sqrt{f'_c}$	486
HPFRC-SP-CL	207	1.83$\sqrt{f'_c}$	214	1.95$\sqrt{f'_c}$	0

Note: [1] V_b divided by $\sqrt{f'_c}\, b_w h$ and measured concrete strength has been used, here V_b is measured shear force in beams

3.6 Joint Behavior

3.6.1 Joint Shear Stress vs. Joint Shear Distortion Response

Joint shear stress versus joint distortion responses for all specimens are shown in Figure 3.44 through 3.46. The joint shear stress was results of the difference between the horizontal shear force caused by the beams and column shear force. The horizontal shear force caused by the beams were determined by dividing end moments of the beams by design moment arms. As can be seen, the responses for both RC specimens remained in elastic domain while, the response of HPFRC-SP-CL was non-linear. The joint of HPFRC-SP-CL experienced yielding during the positive loading to 1.75 column drift ration and corresponding joint stress was $11.9\sqrt{f_c'}$ psi, which was slightly greater than the normalized maximum joint shear stress of RC-SP-CL.

Figure 3.47 shows a summary of prior research results regarding joint shear stress as a faction of measured concrete strength for interior joints without transverse beams (Kurose et al. 1988). The curve of $15\sqrt{f_c'}$ psi ($1.25\sqrt{f_c'}$ MPa) in the plot represents the ACI nominal joint shear strength for joints confined by beams on two opposite faces (ACI 318-14). Figure 3.44 shows that the joints with a joint strength close to the ACI nominal joint shear strength and a concrete compressive strength greater than 5 ksi (35.5 MPa) experienced yielding in both joints and beams. As indicated in Fig. 3.44, the design of specimen HPFRC-SP-CL in general meets these two conditions. The testing also shows that both the joint and beams in HPFRC-SP-CL had yielded. On the other hand, the joint of RC-SP-NL and RC-SP-CL did not yield due to relatively lower joint shear stress.

3.6.2 Strain in Hoops and Crossties

According to ACI 318-14, the role of transvers reinforcement is to confine the core concrete in beam-column joints for ductility. Figure 3.48 through 3.54 show the strains in hoops and crossties in the joints for all specimens. For all specimens, the highest yielding was measured at the mid-height of the joint. And the small hoops placed at the mid-height were yielded first and then, the strain of the big hoops at the same location started increasing. Although the big hoop did not yield for RC-SP-NL, measured strains of the big hoops for both RC-SP-CL and HPFRC-SPCL were beyond yield strain. It needs to be noted that rapid increase of the strain in small hoops coincided with the large increase of the strain gauge which were placed at the center of the joint for all specimens.

Although the hoops in the joint of RC-SP-CL yielded, the joint did not yield. This is because limited joint shear stress. For, HPFRC-SP-CL, yielding of the instrumented transverse reinforcement, placed at the center of the joint, coincided with the yielding of the HPFRC-SP-CL joint. The yielding occurred during the positive loading to 1.75% column drift ratio where the concrete strain gauge show dramatic increase in strain. After yielding of the transverse reinforcement, the HPFRC-SP2 joint started bulging in the direction perpendicular to the beam axis. Not that although the locations of strain gauges are different from the other specimens, it need to be noted that all the hoops in the joint of HPFRC-SP-CL experienced yielding.

3.6.3 Bond stress

The average bond stresses in the joints of both RC-SP-CL and HPFRC-CL are shown in Figure 3.55 through 3.68. The average bond stresses were obtained from Equation 3.16, where $\Delta\sigma_s$ is the difference in steel reinforcement stress over a distance Δ_x, A_s is the cross sectional area of the steel reinforcement, and $\sum_o$ is the perimeter of the steel reinforcement.

$$\frac{\Delta\sigma_s \cdot A_s}{\sum_0 \cdot \Delta_x} \qquad 3.16$$

Steel reinforcement stresses in Equation 3.16 was obtained from modified Menegotto-Pinto model (Sakai and Kawashima, 2003). This model accurately captures the cyclic stress-strain behavior of a steel reinforcement. In order to plot the average bond stresses, the strain data from the strain gauges on beam longitudinal reinforcement was inputted to a program that implements the Menegotto-Pinto algorithm, then the hysteretic stress-strain response of the steel reinforcement at a particular location is derived. As can be seen in Figure 3.69, average bond stress along the joint of RC-SP-CL is much higher than that of HPFRC-CP-CL. The average bond stress was 1056 psi for RC-SP-CL and 605 psi for HPFRC-SP-CL.

The bond efficiency parameter shown in Equation 3.17 can be utilized to evaluate the bond strength development of longitudinal beam bars in a beam-column joint (Leon, 1989; Parra-Montesinos, 2000). where Δf_s is the difference in steel reinforcement stress which was obtained from two different strain gauges located at each

beam-column interfaces in a joint. f_y is the yield stress of the steel reinforcement obtained from the monotonic tensile test.

$$\text{Bond Efficiency} = \frac{\Delta f_s}{f_y} \qquad 3.17$$

During load reversals, beam-column joints should be able to develop a tensile stress (with or without strain-hardening) on one side of the joints and a compression stress on the opposite side of the joints. If the joints had tensile stress on both sides, it means significant reduction in bond strength and it can decrease stiffness and strength of structures. Bond efficiency which is less than 1.0 indicates bond deterioration in a joint since it means that longitudinal reinforcement on both sides of the joint in tension. On the other hand, bond efficiency equal to 1.0 indicates that the steel reinforcement in the joints can develop a tensile stress without strain-hardening on one side and a compression stress on the other side of the joints. Bond efficiency larger than 1 represents the steel reinforcement on one side may develop strain-hardening while the opposite side is under compression. Figure 3.69 shows plots of bond efficiency versus column drift ratio for the steel reinforcement in the joints of RC-SP-CL and HPFRC-SP-CL. As can be seen, peak bond efficiency values for HPFRC-SP-CL was less than 1.0 while RC-SP-CL shows the peak bond efficiency larger than 1.0 as high as 2. Despite that the average bond stress in the joint of HPFRC-SP-CL was much less than RC-SP-CL, the bond efficiency for HPFRC-SP-CL indicates significant bond deterioration in its joint. The bond deterioration is due to severe damage in the joint.

3.7 Slab and Column Behavior

Behavior of RC beam-column connections can be quite different with the presence of slabs (ACI, 2014; French and Moehle, 1991). Previous research shows that when SBC subassemblages are subjected to large drifts, the longitudinal reinforcements across the entire slab width may contribute to the increase of the negative moment of the beams (ACI 352, 2002; French and Moehle, 1991). Current ACI 318 Section 18.7.3.2 considers slab participation up to a story drift ratio of approximately 2% (ACI, 2014; French and Moehle, 1991) by considering the contribution of longitudinal reinforcement within the effective flange width of the slab.

The contribution of slab longitudinal reinforcement was monitored by strains from a series of four strain gauges mounted at the beam-column interface. For all specimens, the longitudinal reinforcement strain became greater as the column drift ratio increased. Furthermore, the strain decreased with increased distance from the beams. The strains in the slab of RC-SP-CL(NL) were much greater than those in the HPRC-SP-CL slab. In RC-SP-CL(NL), all slab longitudinal reinforcement experienced yielding after 1.0% column drift ratio, while all longitudinal reinforcement yielded or was close to yielding at 1.75% column drift ratio in HPFRC-SP-CL. Because 2% column drift ratio is a typical upper bound for a well-designed SMF subjected to a design-basis earthquake, it is reasonable to consider all the longitudinal reinforcement in the slab as available for negative moment calculations for both specimens although the strain in HPFRC-SP-CL was much lower than that in RC-SP-CL(NL).

As discussed earlier, the columns in both specimens did not have significant damage up to 3.5% column drift ratio, which satisfied the design criterion of SCWB. The strain of column longitudinal reinforcement was measured at the bottom of top columns for both specimens. RC-SP-CL(NL) did not experience significant yielding up to 3.5% CDR. On the other hand, for HPRC-SP-CL, the reinforcement started yielding at 2.75% column drift ratio where significant yielding of the joint occurred. The yielding of the column reinforcement is believed to be a result of local kinking by the excessive distortion in the joint. Nevertheless, no negative effect on the performance of HPFRC-SP-CL was observed due to the local bar kinking.

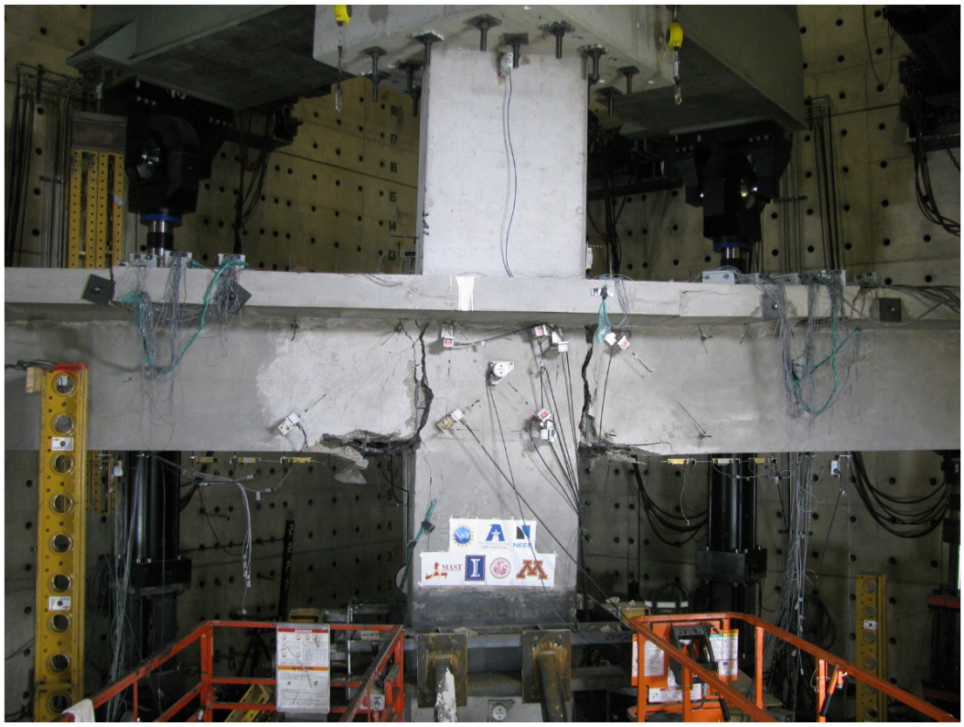

Figure 3.1 RC-SP-NL after test

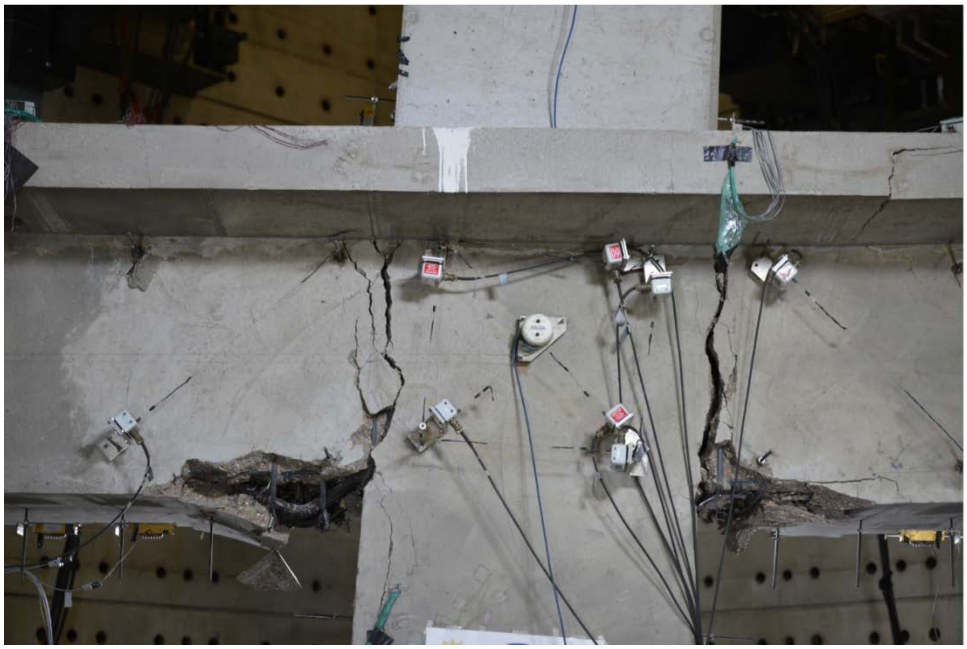

Figure 3.2 Cracks and damage pattern of RC-SP-NL after test

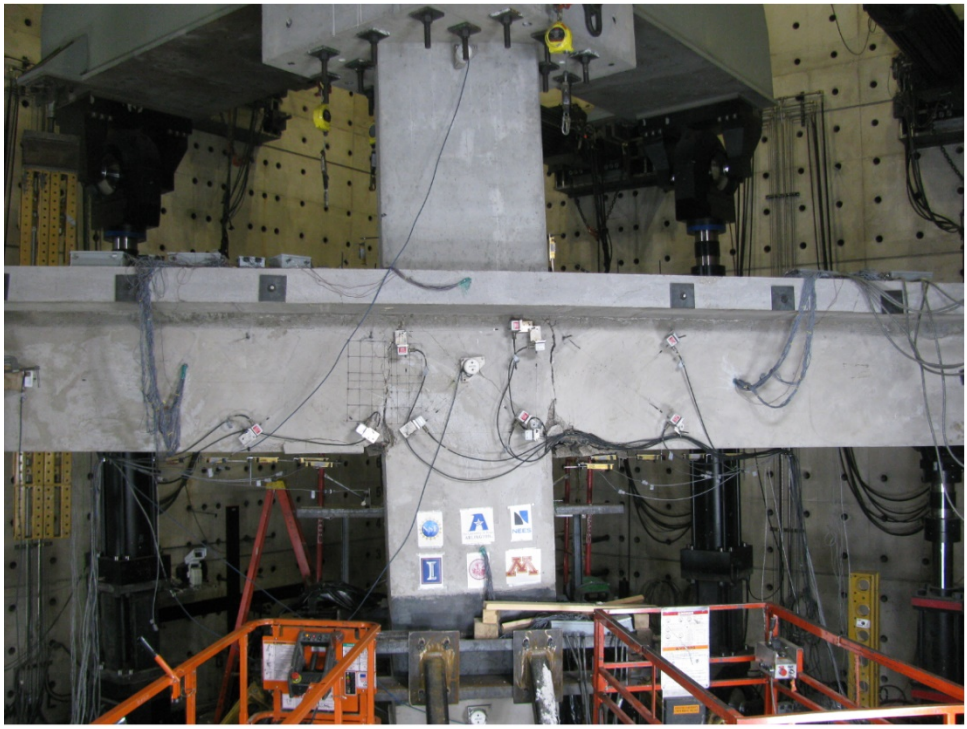

Figure 3.3 RC-SP-CL after test

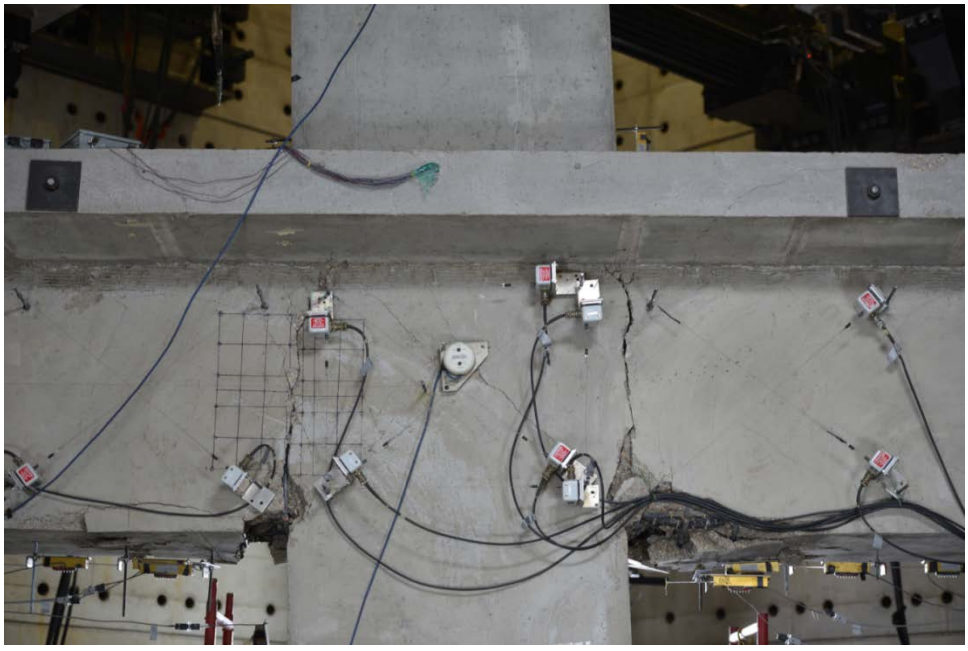

Figure 3.4 Cracks and damage of RC-SP-CL after test

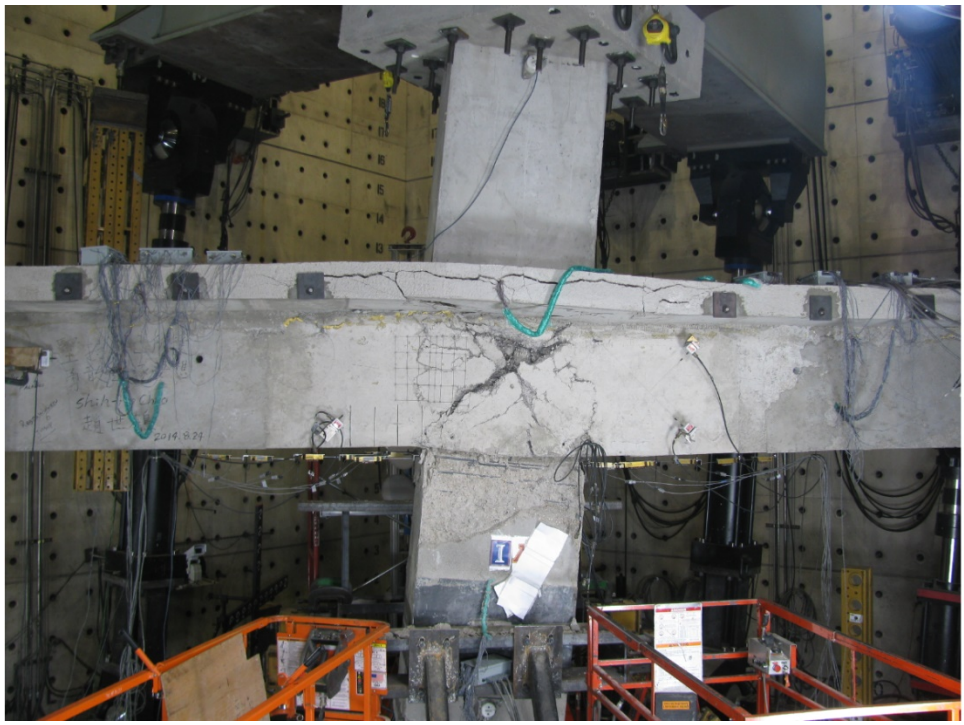

Figure 3.5 HPFRC-SP-CL after test

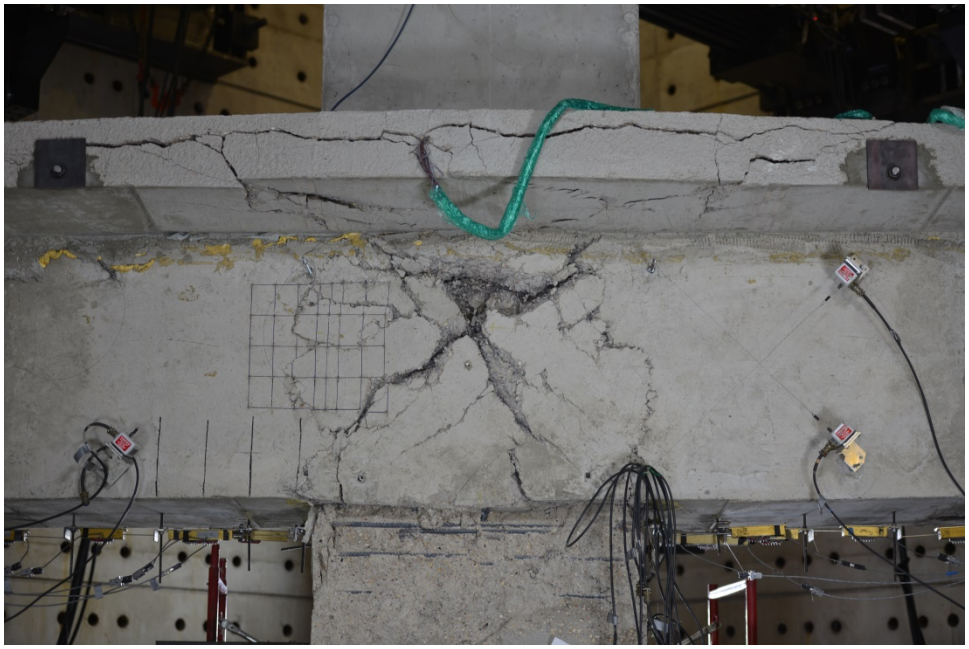

Figure 3.6 Cracks and damage of RC-SP-CL after test

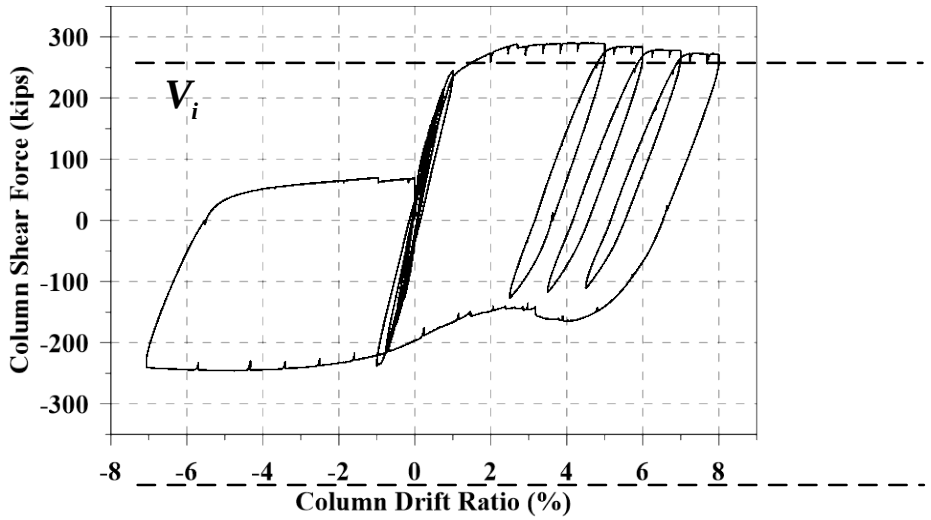

Figure 3.7 Column shear force vs. column drift ratio response of RC-SP-NL

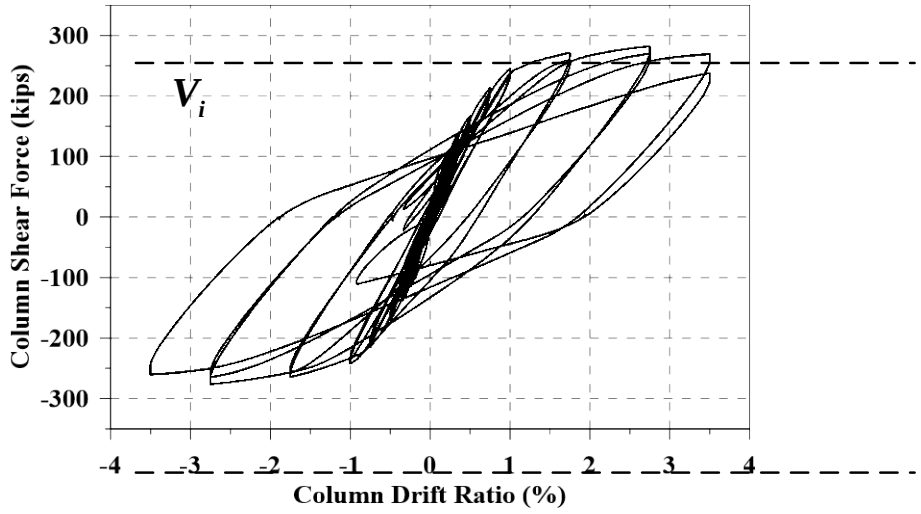

Figure 3.8 Column shear force vs. column drift ratio response of RC-SP-CL

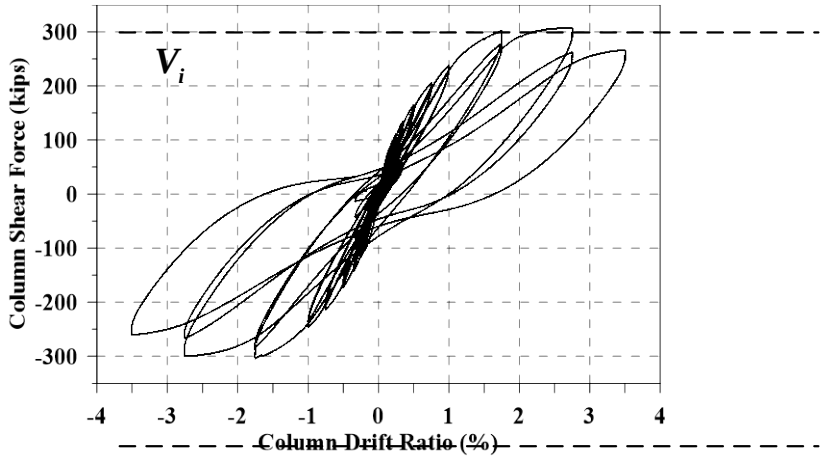

Figure 3.9 Column shear force vs. column drift ratio response of HPFRC-SP-CL up to 3.5%

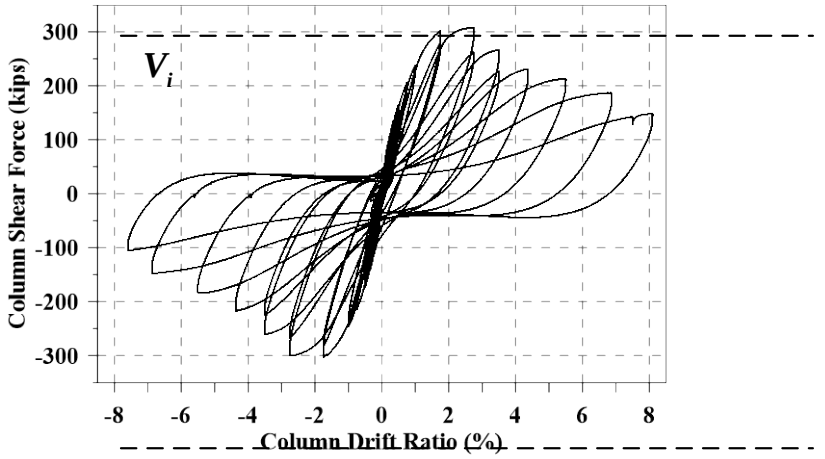

Figure 3.10 Column shear forces vs. column drift ratio response of HPFRC-SP-CL up to end of test

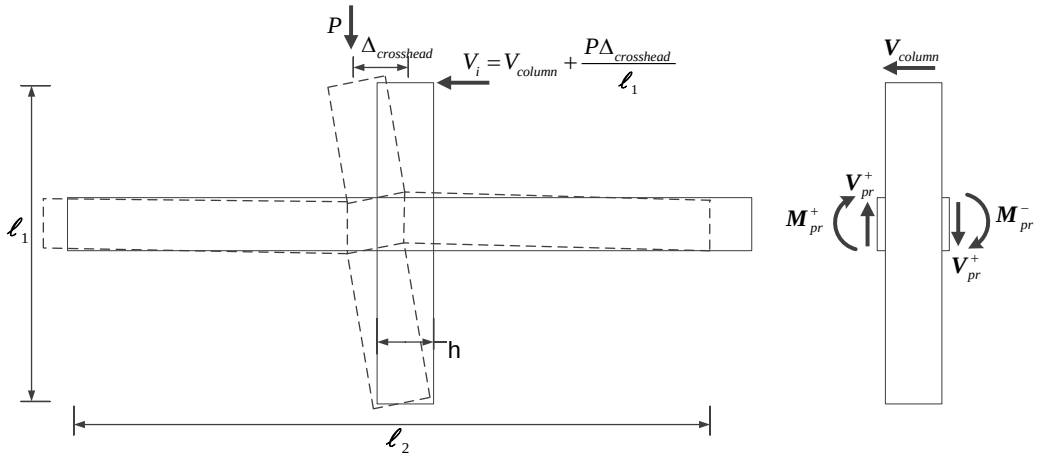

Figure 3.11 (a) Calculation of crosshead shear force and (b) Calculation of column shear force

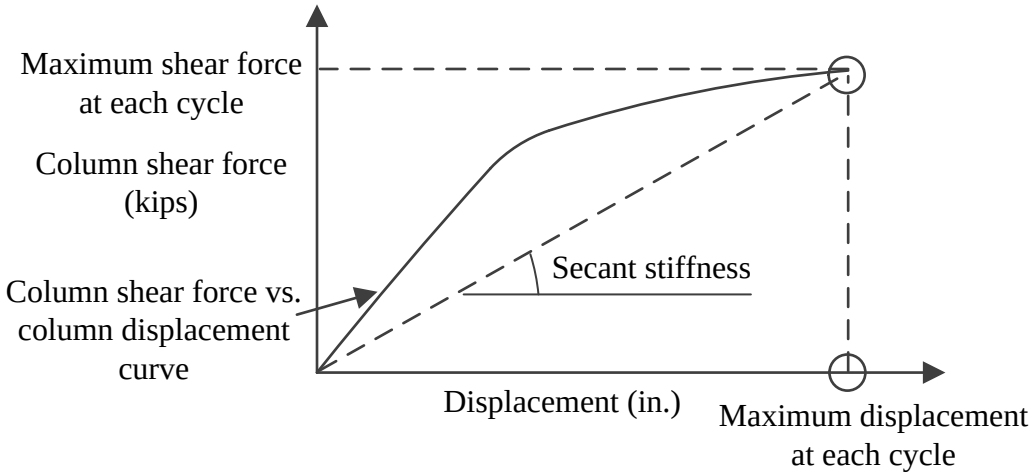

Figure 3.12 Calculation of secant stiffness

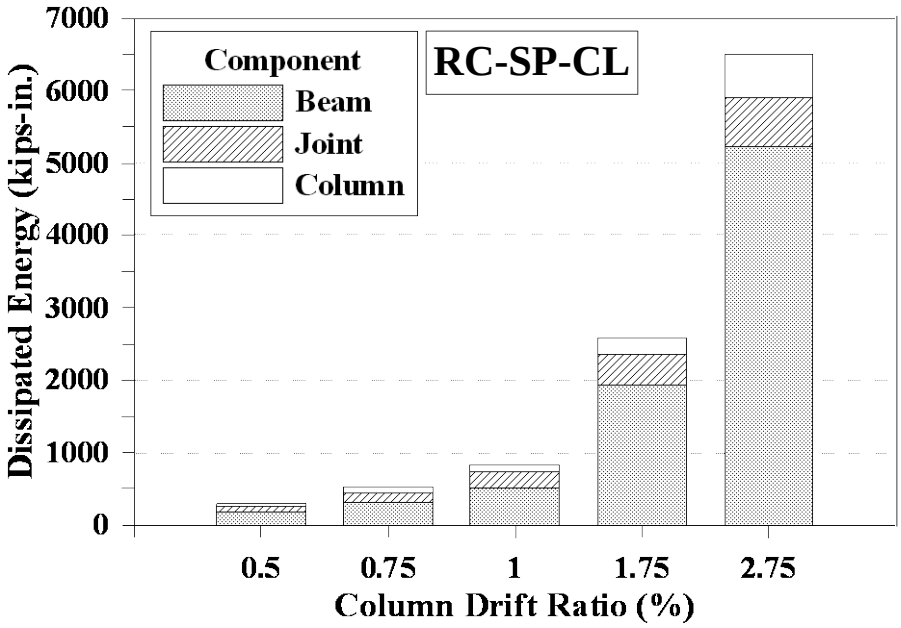

Figure 3.13 Dissipated energy by each component of RC-SP-CL

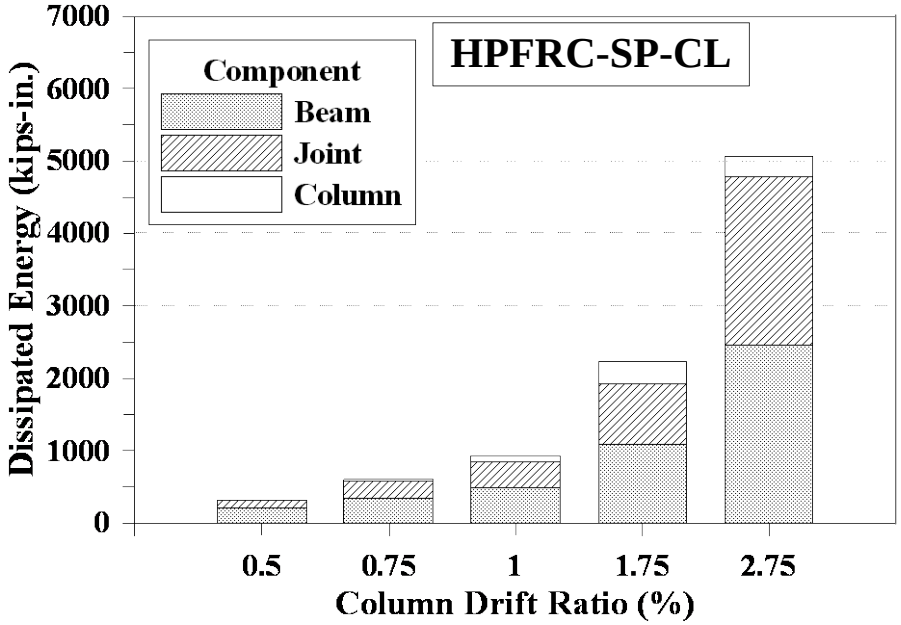

Figure 3.14 Dissipated energy by each component of HPFRC-SP-CL

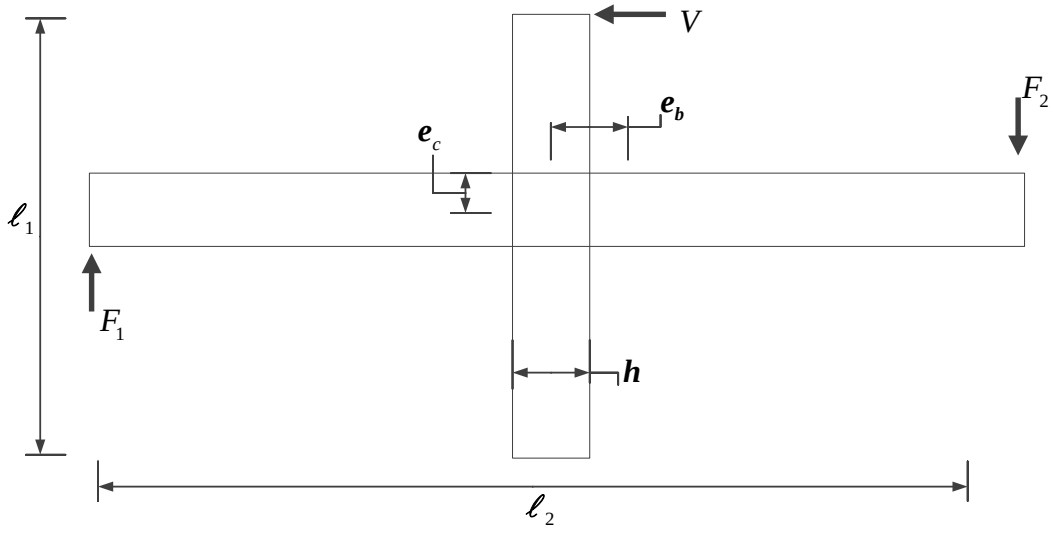

Figure 3.15 Geometry of specimen for deformation calculation

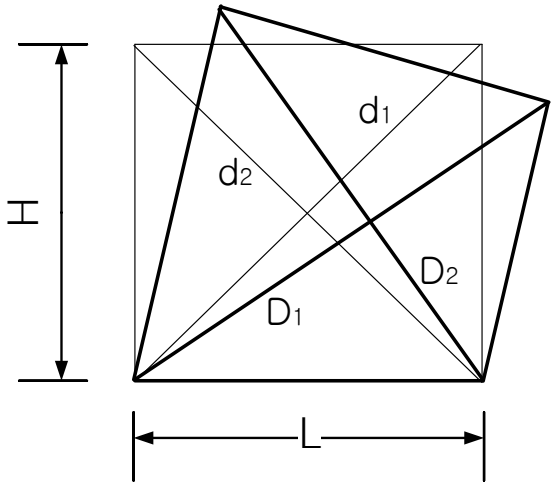

Figure 3.16 Calculation of joint shear distortion

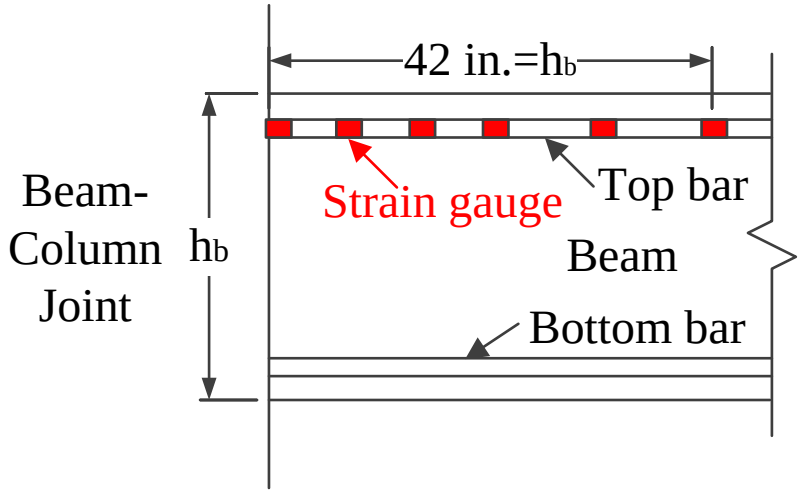

Figure 3.17 Strain gauge locations

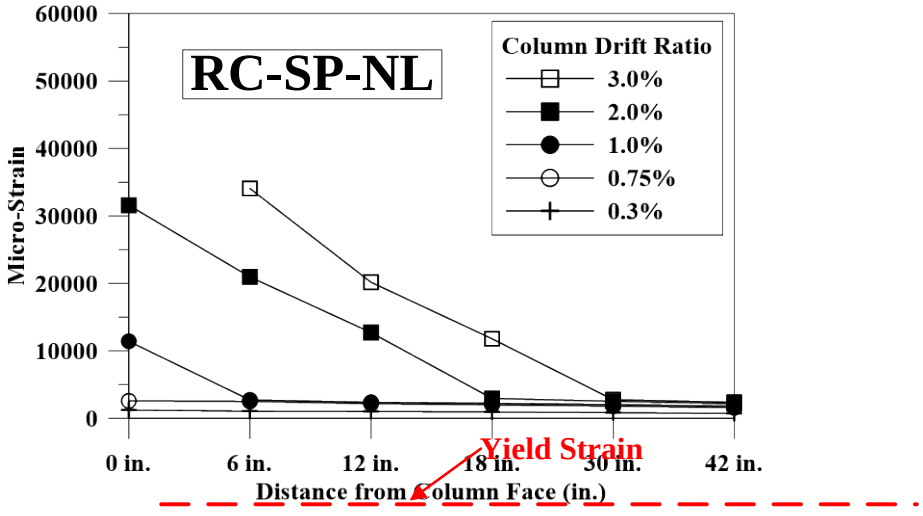

Figure 3.18 Strain of beam longitudinal reinforcement in beam plastic hinge region (RC-SP-NL)

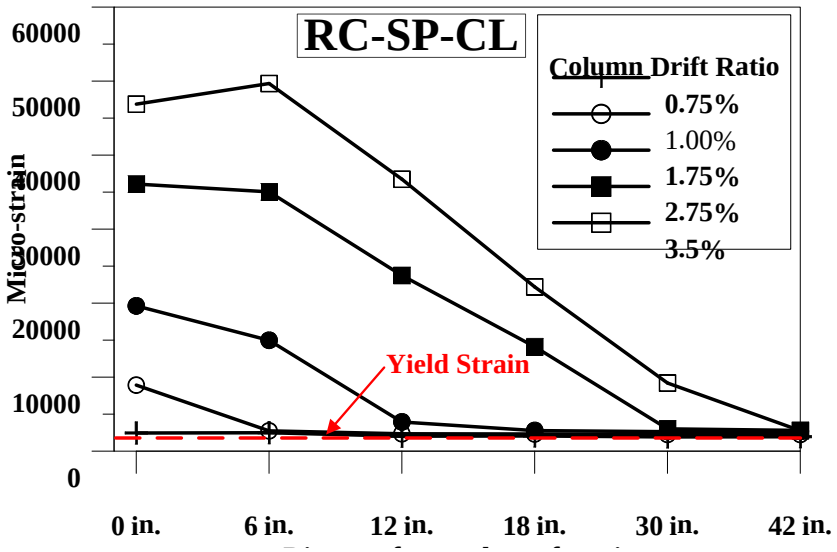

Figure 3.19 Strain of beam longitudinal reinforcement in beam plastic hinge region (RC-SP-CL)

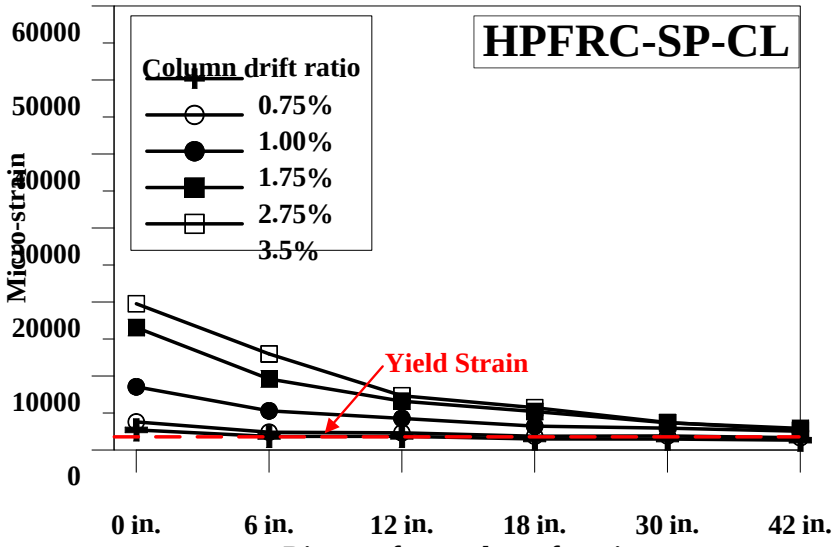

Figure 3.20 Strain of beam longitudinal reinforcement in beam plastic hinge region (HPFRC-SP-CL)

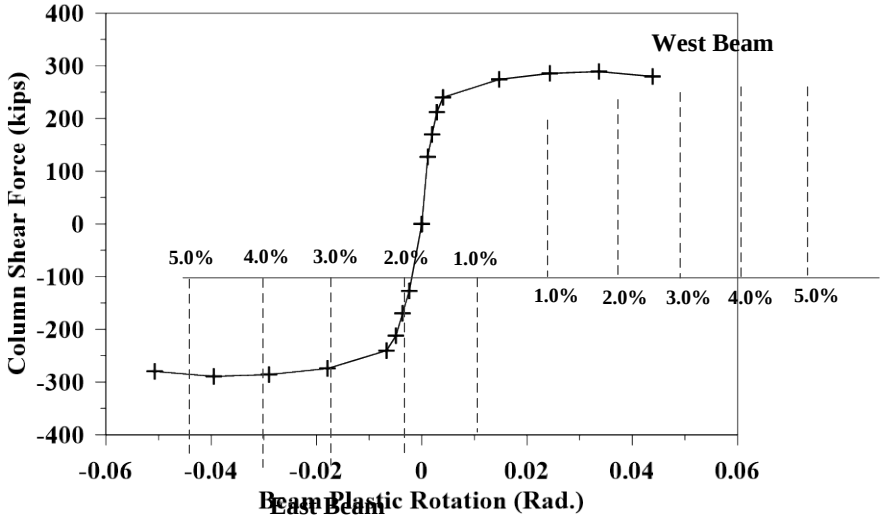

Figure 3.21 Beam plastic rotation of RC-SP-NL

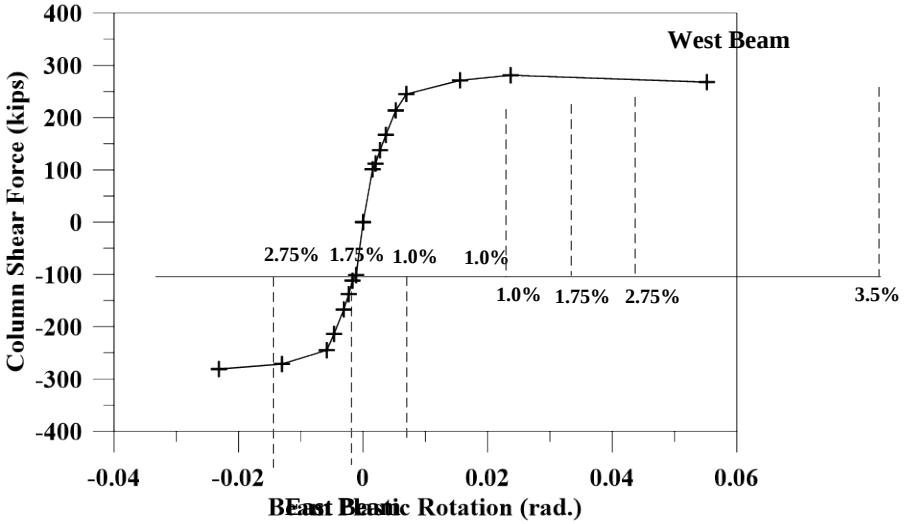

Figure 3.22 Beam plastic rotation of RC-SP-CL

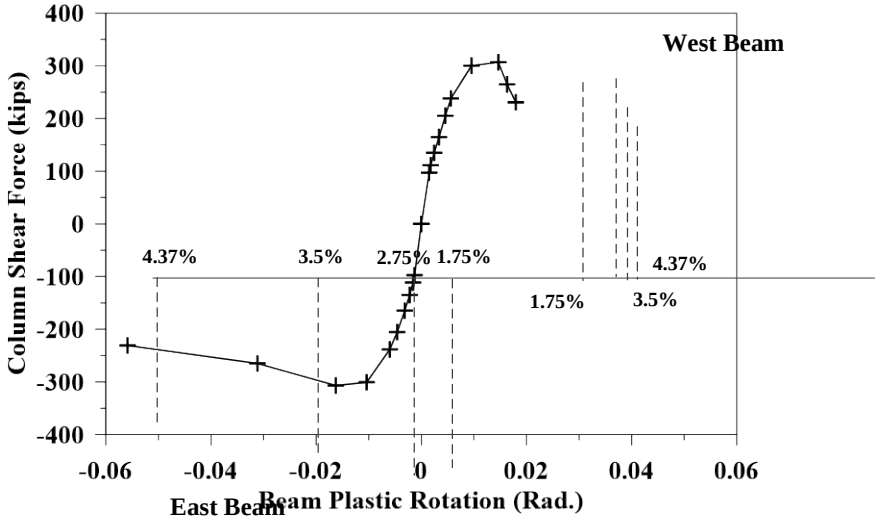

Figure 3.23 Beam plastic rotation of HPFRC-SP-CL

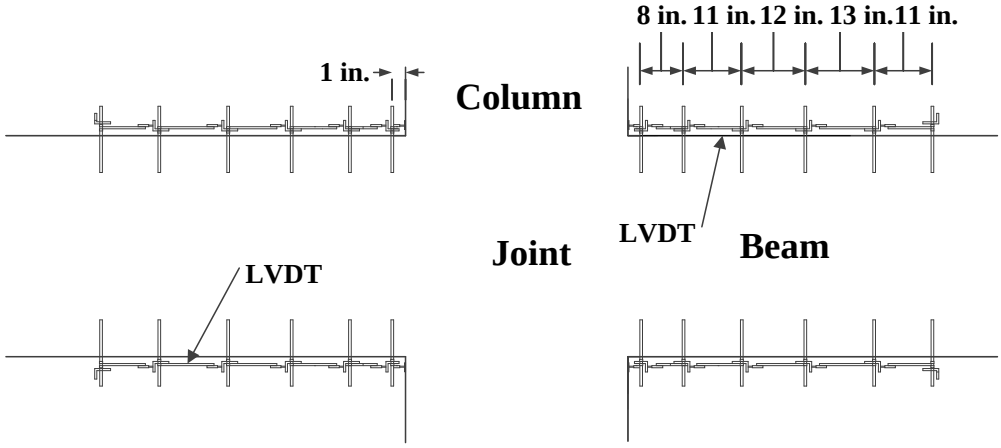

Figure 3.24 Locations of LVDTs

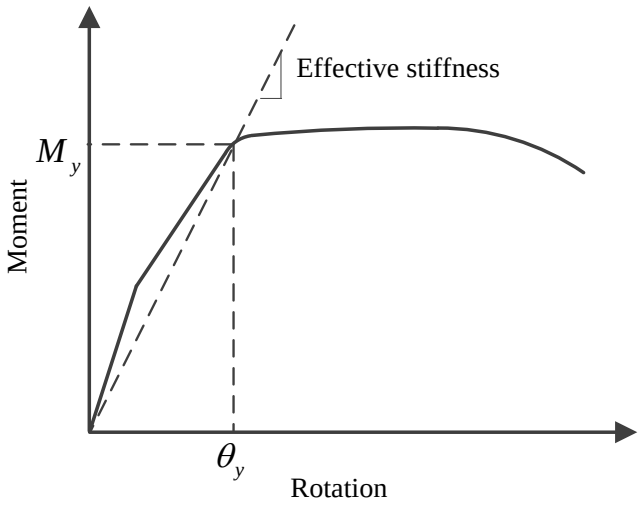

Figure 3.25 Effective stiffness for yielding member

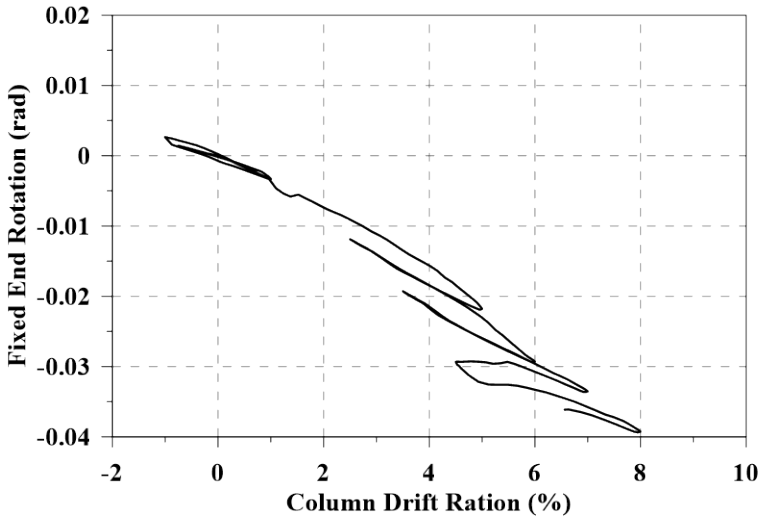

Figure 3.26 Fixed end rotation of RC-SP-NL

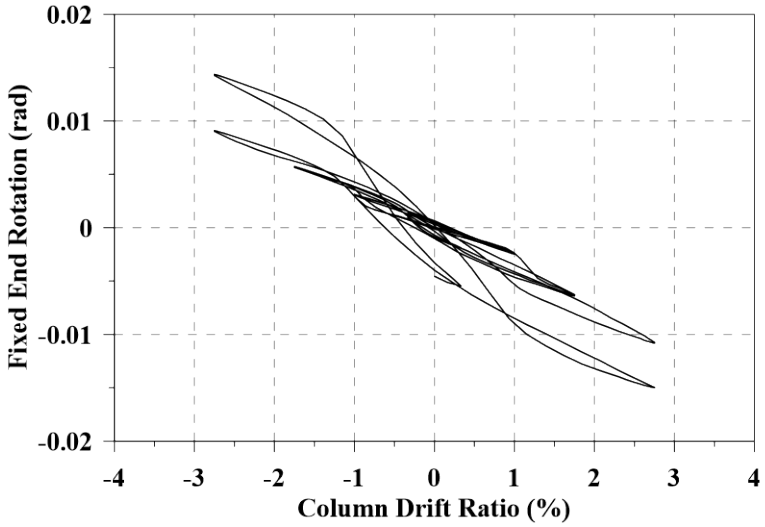

Figure 3.27 Fixed end rotation of RC-SP-CL

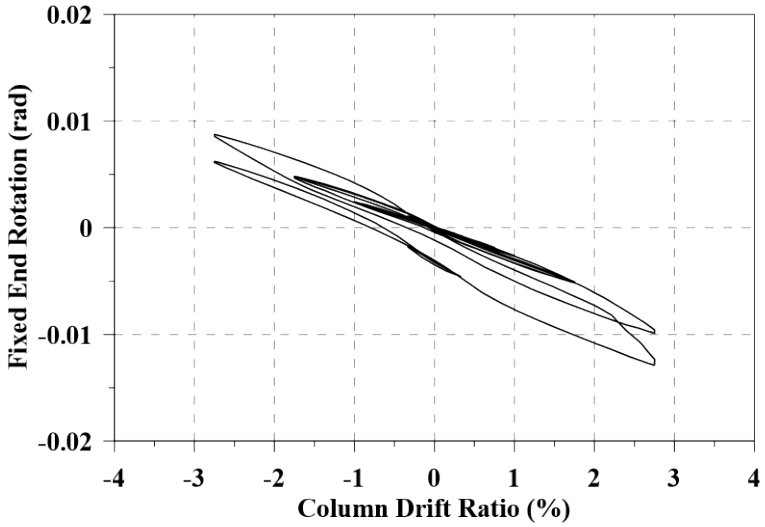

Figure 3.28 Fixed end rotation of HPFRC-SP-CL

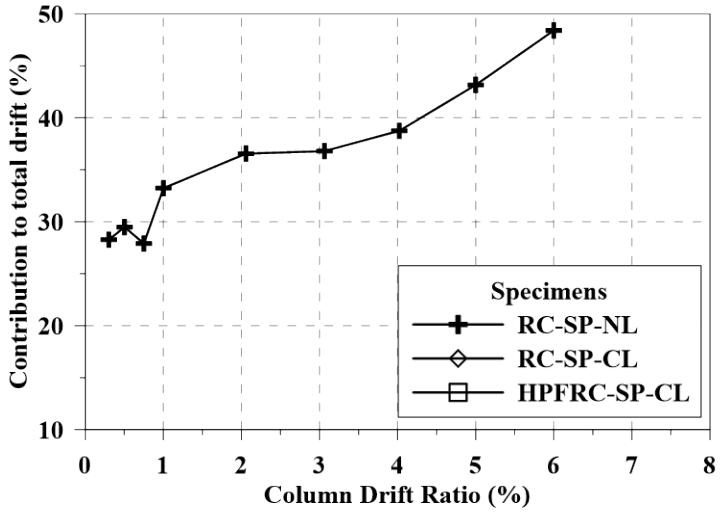

Figure 3.29 Contribution of fixed end rotation to total column drift of RC-SP-NL

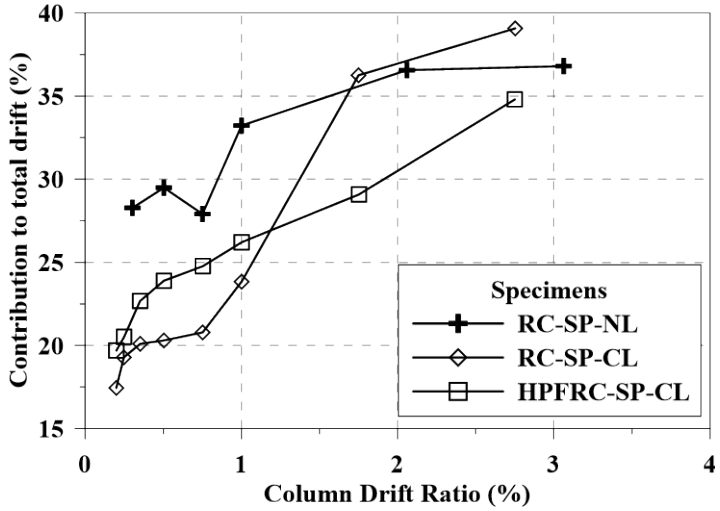

Figure 3.30 Contribution of fixed end rotation to total column drift

Figure 3.31 Buckled longitudinal reinforcement for RC-SP-NL

Figure 3.32 Buckled longitudinal reinforcement for RC-SP-CL

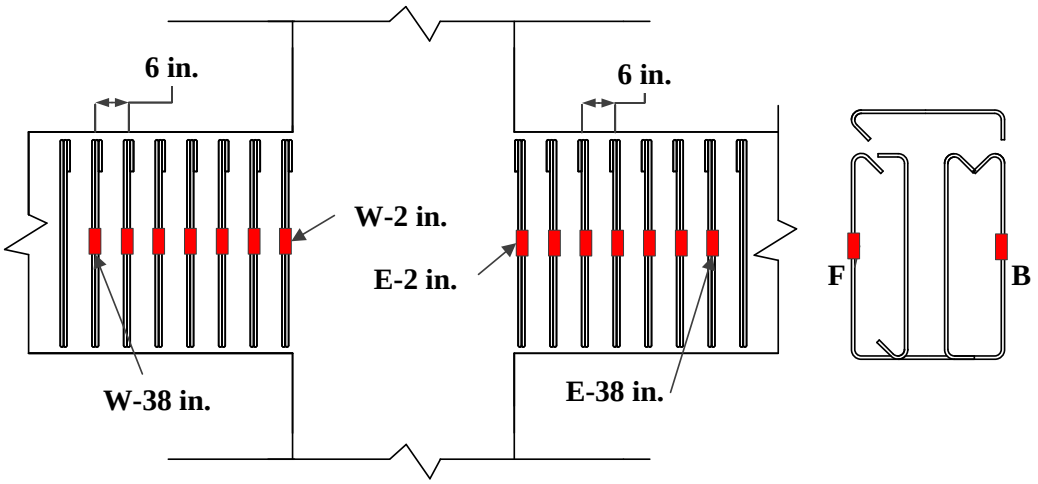

(a) Locations of strain gauge on hoops and crossties in beams

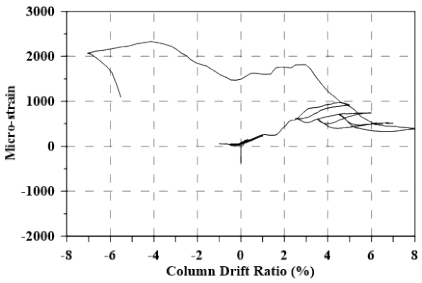

(b) W-F-8

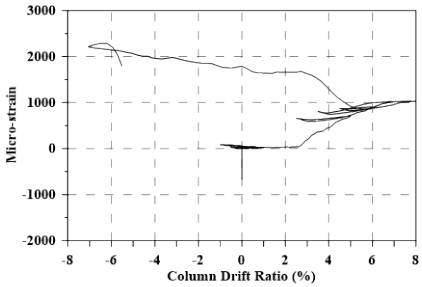

(c) W-F-14

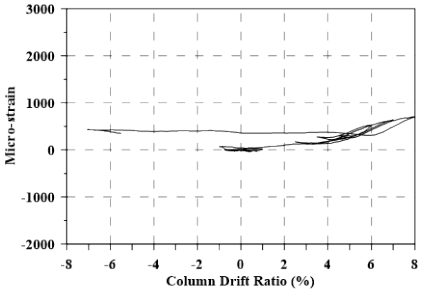

(d) W-F-8

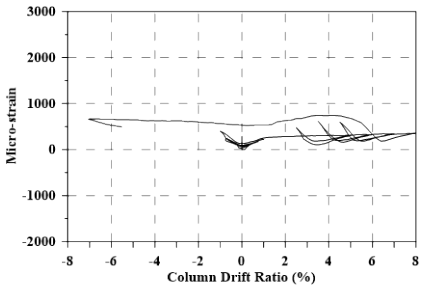

(e) W-F-14

Figure 3.33 Strain in hoops and crossties of RC-SP-NL

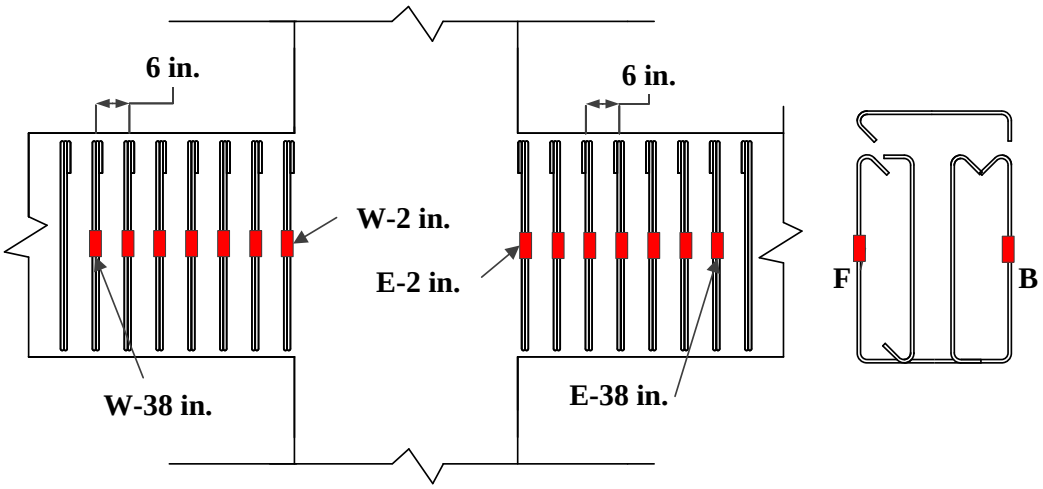

(a) Locations of strain gauge on hoops and crossties in beams

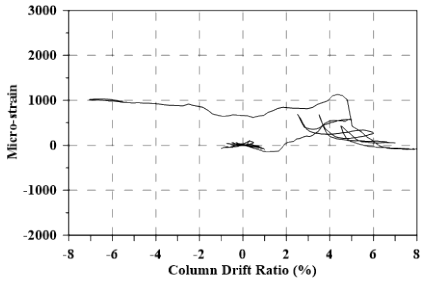

(b) E-F-2

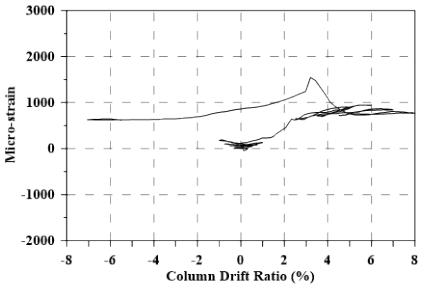

(c) E-F-8

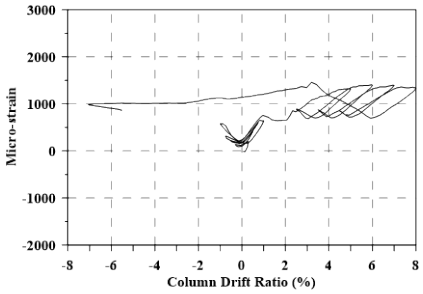

(d) E-F-14

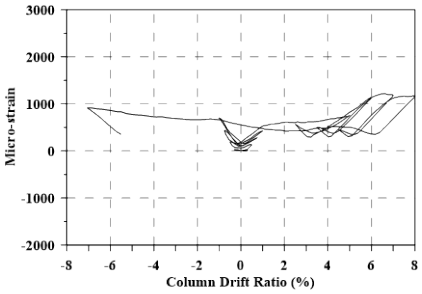

(e) E-F-32

Figure 3.34 Strain in hoops and crossties of RC-SP-NL

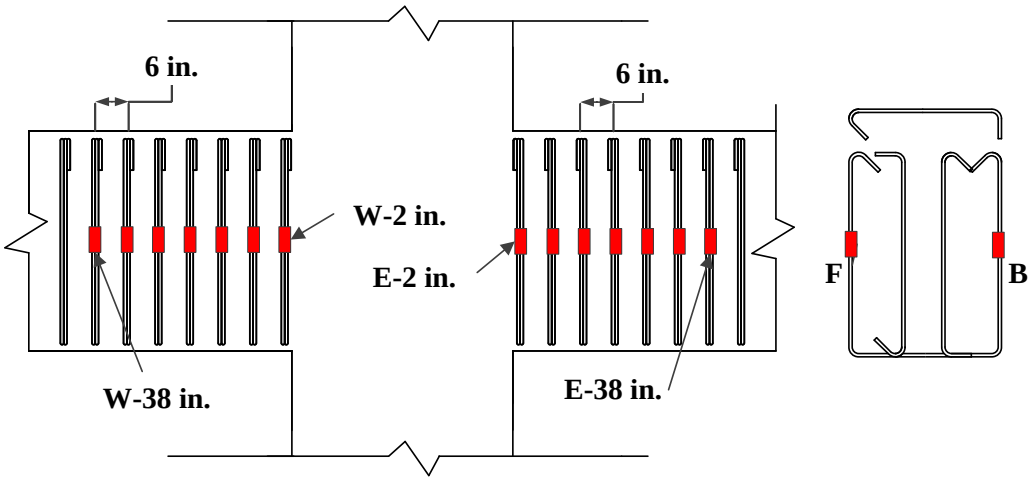

(a) Locations of strain gauge on hoops and crossties in beams

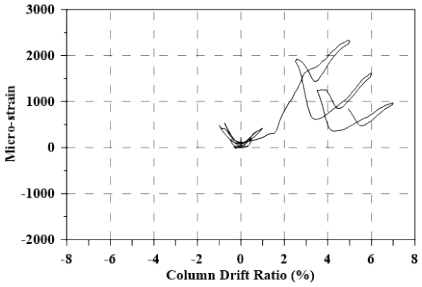

(b) W-B-2

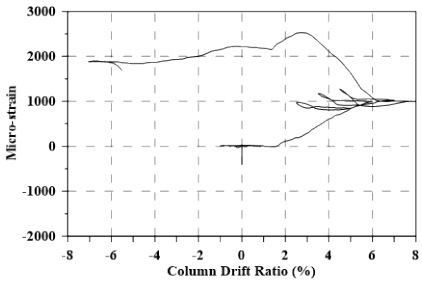

(c) W-B-8

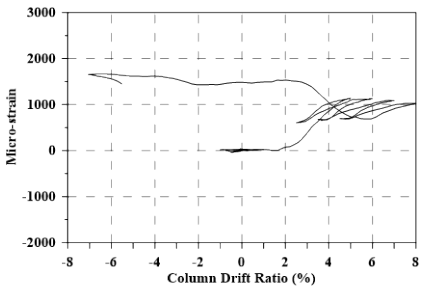

(d) W-B-14

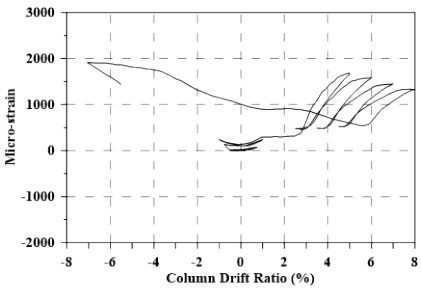

(e) W-B-20

Figure 3.35 Strain in hoops and crossties of RC-SP-NL

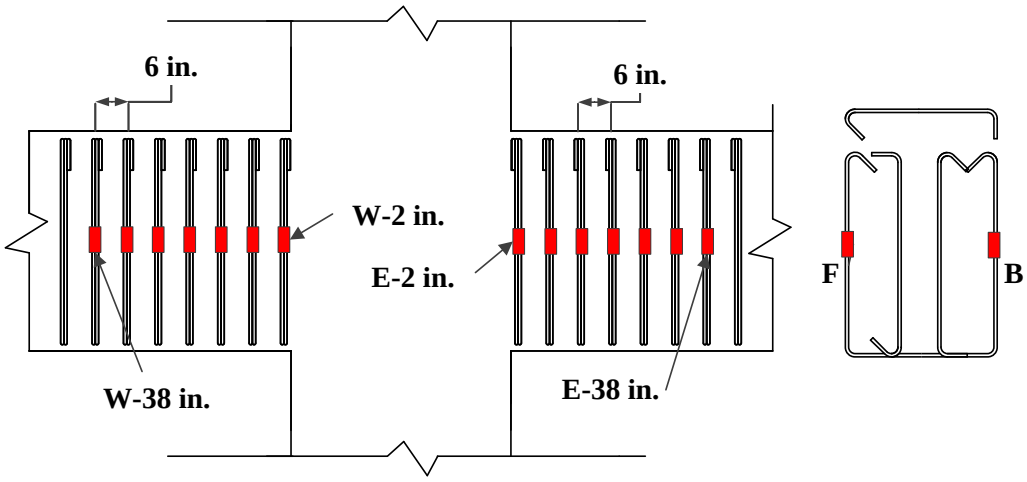

(a) Locations of strain gauge on hoops and crossties in beams

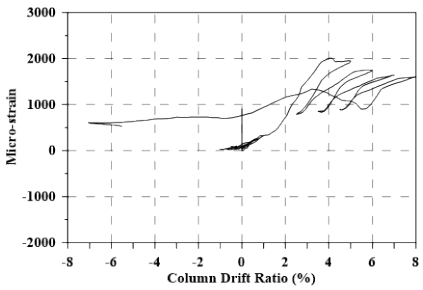

(b) E-B-8

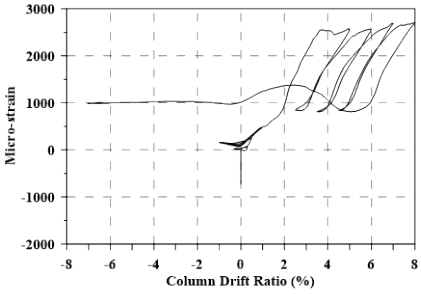

(c) E-B-14

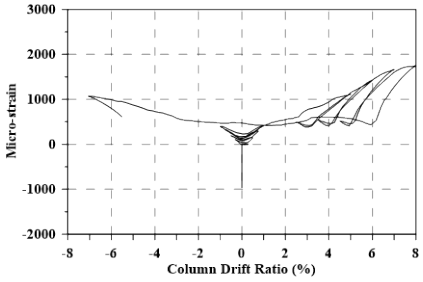

(d) E-B-26

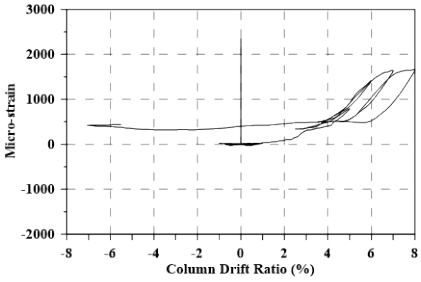

(e) E-B-20

Figure 3.36 Strain in hoops and crossties of RC-SP-NL

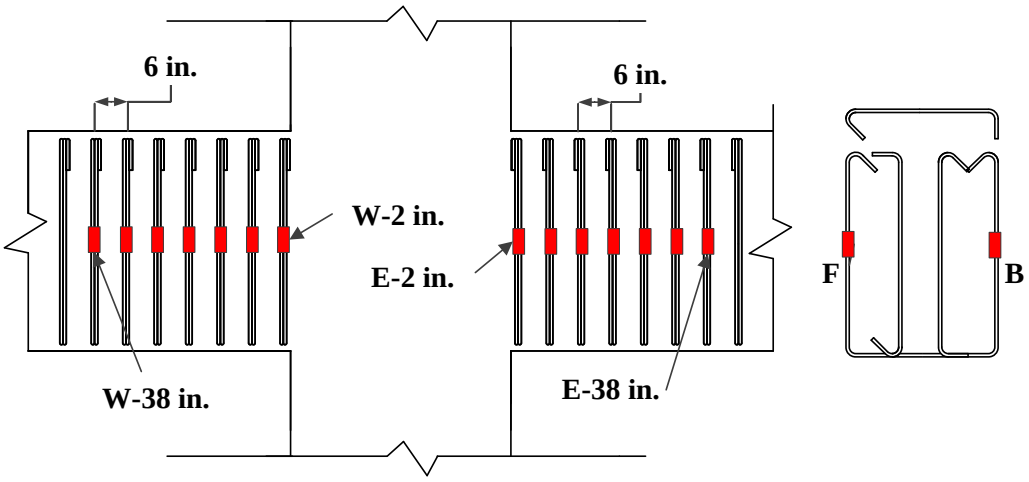

(a) Locations of strain gauge on hoops and crossties in beams

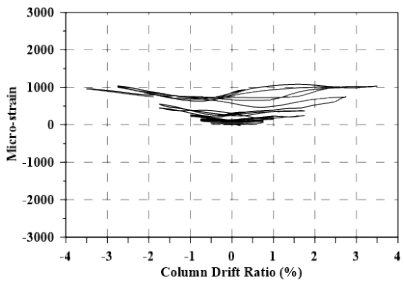

(b) W-F-8

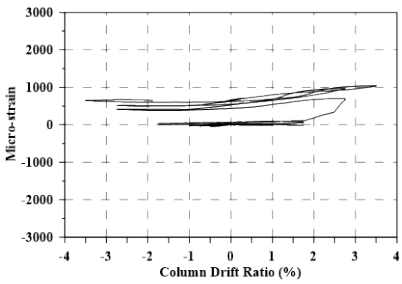

(c) W-F-14

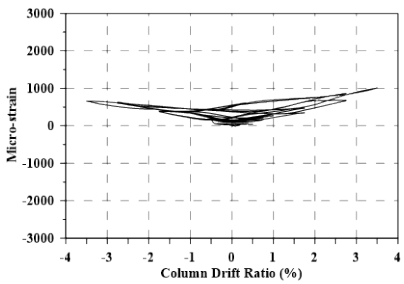

(d) W-F-20

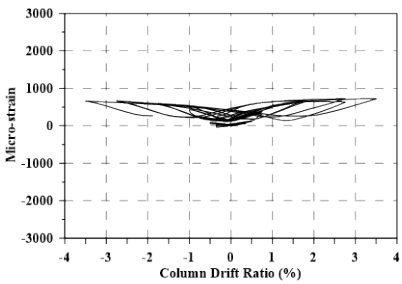

(e) W-F-132

Figure 3.37 Strain in hoops and crossties of RC-SP-CL

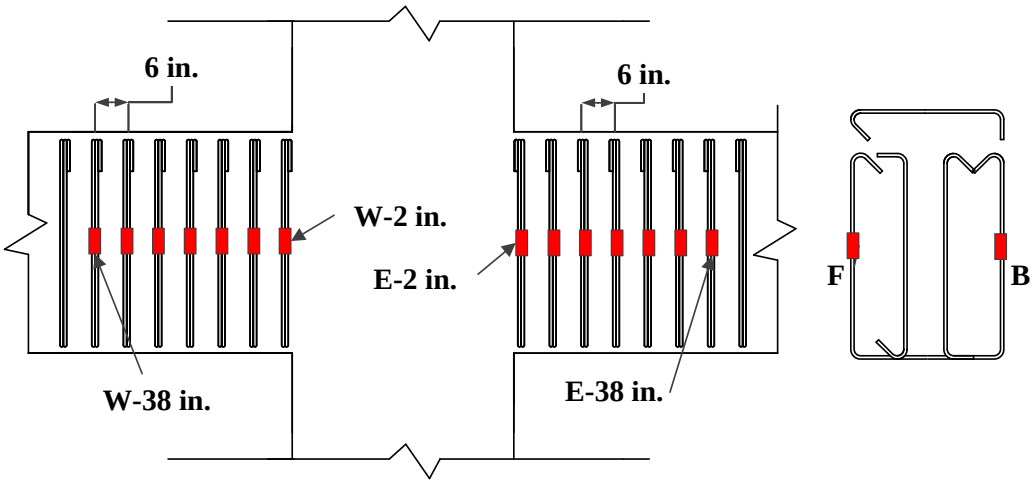

(a) Locations of strain gauge on hoops and crossties in beams

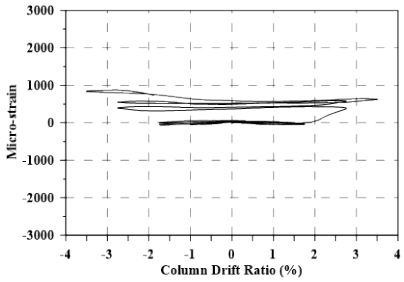

(b) E-F-8

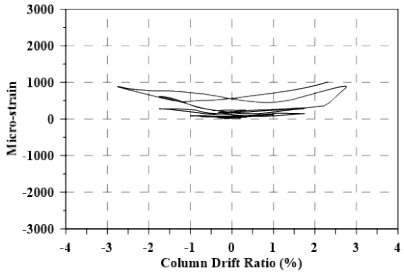

(c) E-F14

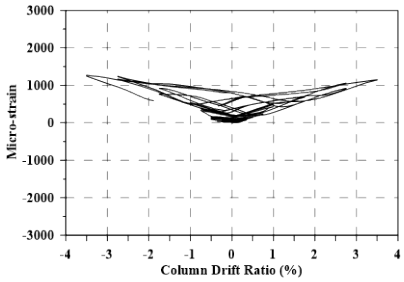

(d) E-F14

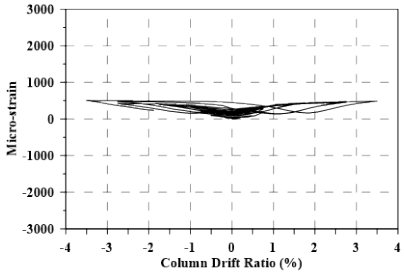

(e) E-F-38

Figure 3.38 Strain in hoops and crossties of RC-SP-CL

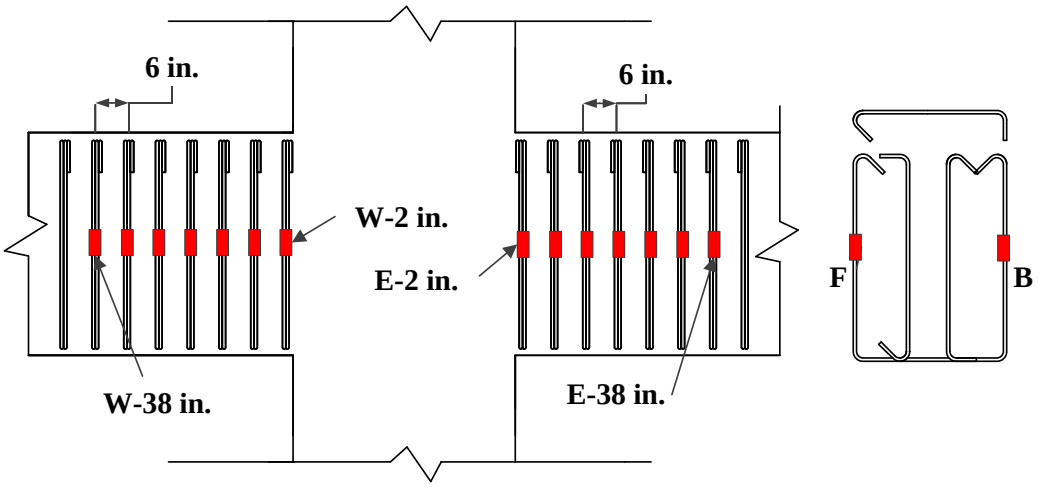

(a) Locations of strain gauge on hoops and crossties in beams

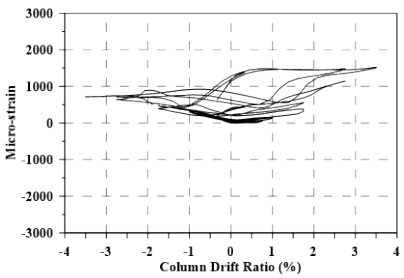

(b) W-B-8

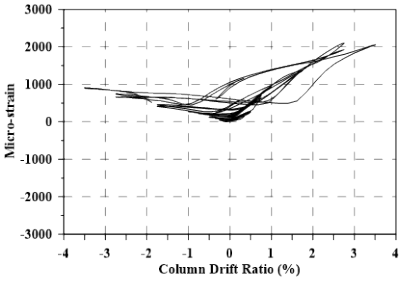

(c) W-B-20

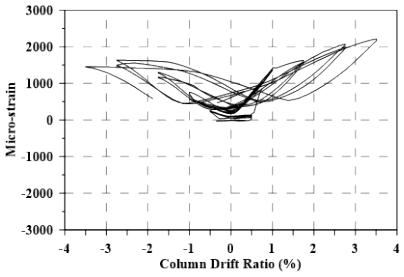

(d) W-B-32

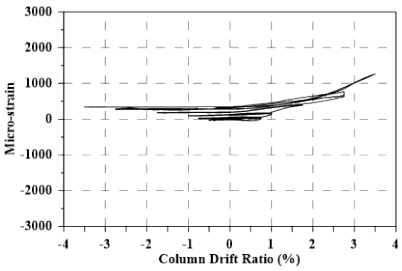

(e) W-B-38

Figure 3.39 Strain in hoops and crossties of RC-SP-CL

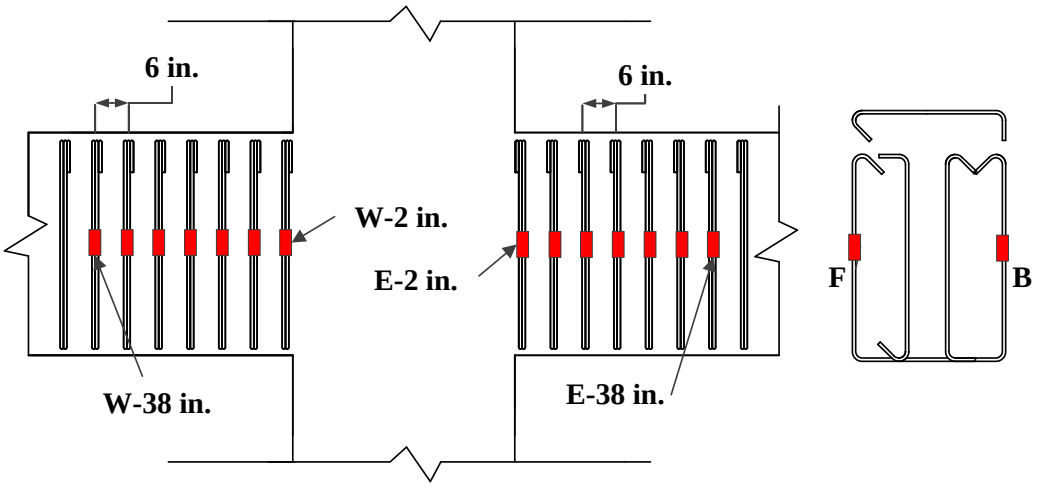

(a) Locations of strain gauge on hoops and crossties in beams

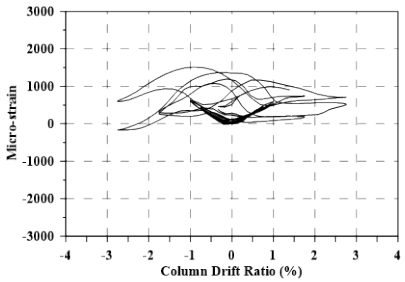

(b) E-B-2

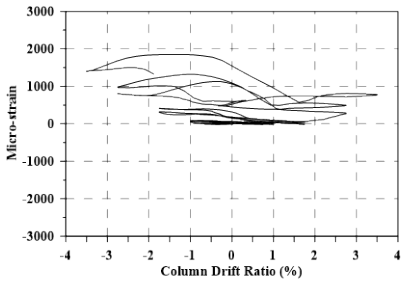

(c) E-B-8

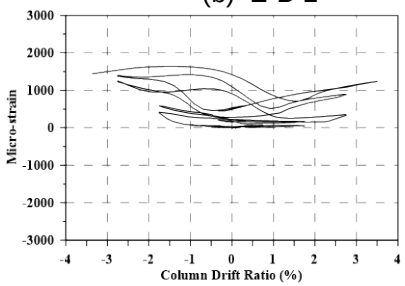

(d) E-B-14

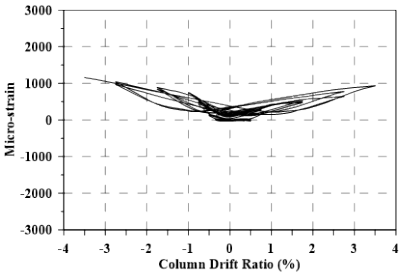

(e) E-B-38

Figure 3.40 Strain in hoops and crossties of RC-SP-CL

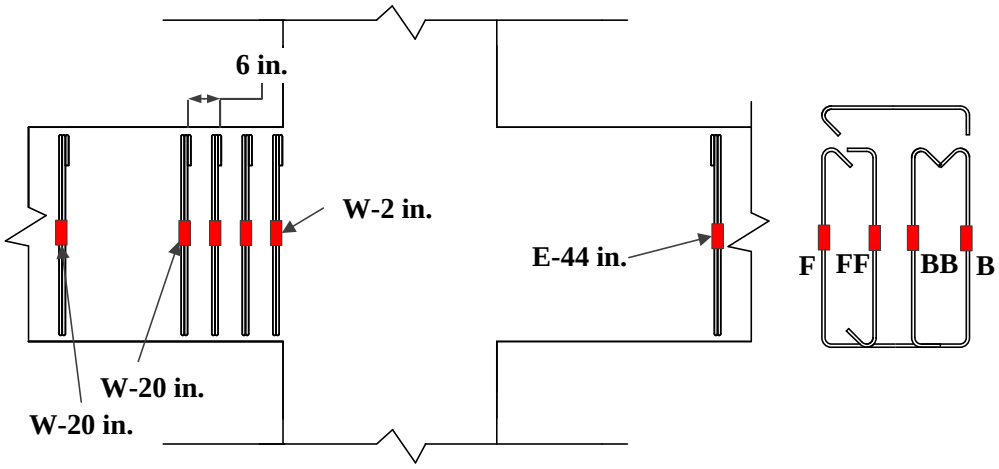

(a) Locations of strain gauge on hoops and crossties in beams

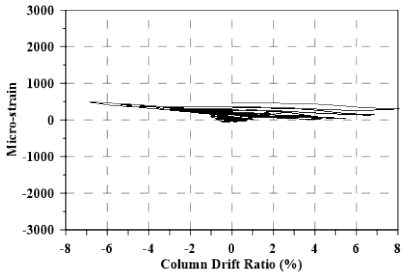

(b) W-F-8

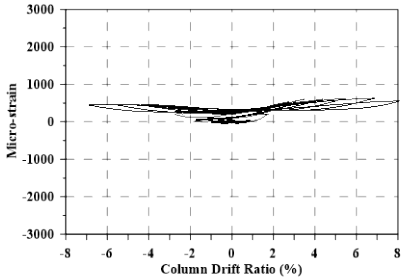

(c) W-F-14

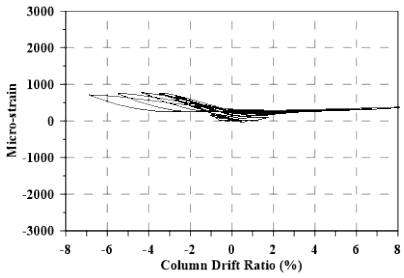

(d) W-F-20

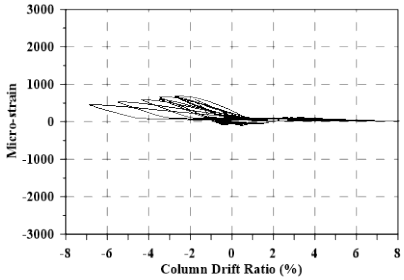

(e) W-F-132

Figure 3.41 Strain in hoops and crossties of HPFRC-SP-CL

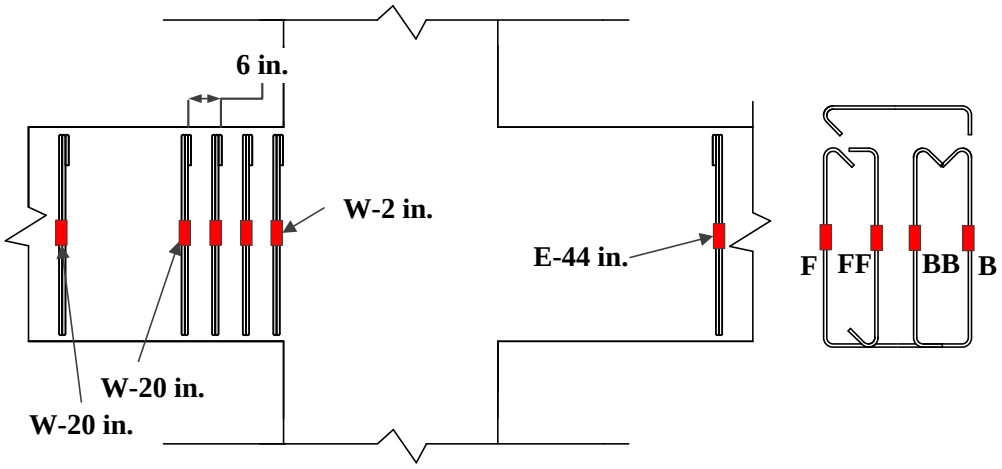

(a) Locations of strain gauge on hoops and crossties in beams

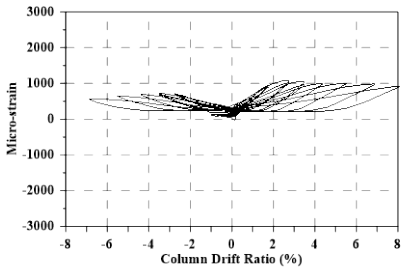

(b) E-F-44

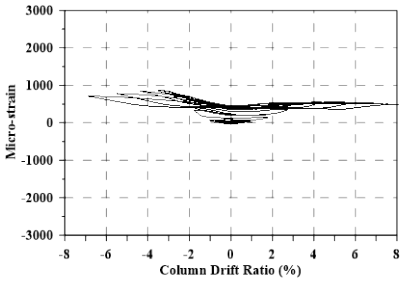

(c) W-FF-8

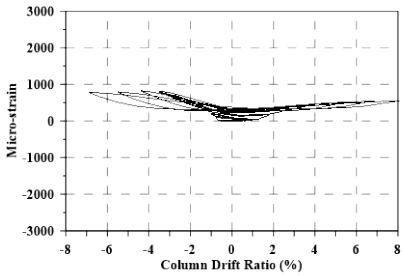

(d) W-FF-14

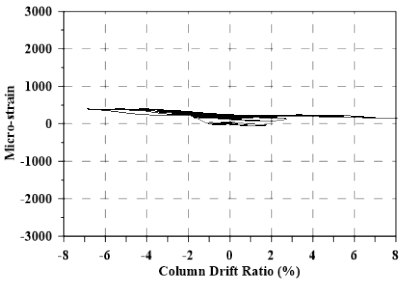

(e) W-BB-8

Figure 3.42 Strain in hoops and crossties of HPFRC-SP-CL

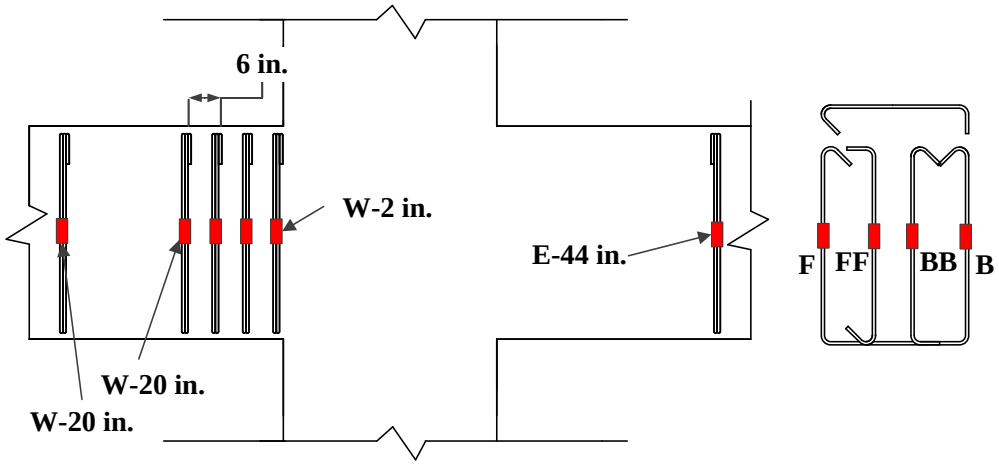

(a) Locations of strain gauge on hoops and crossties in beams

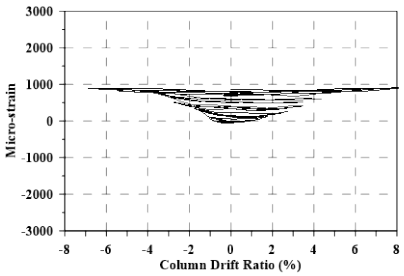

(b) E-B-2

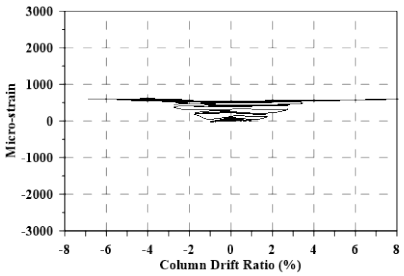

(c) E-B-8

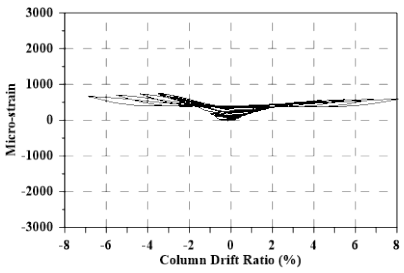

(d) E-B-20

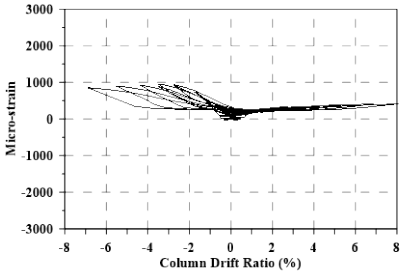

(e) E-B-44

Figure 3.43 Strain in hoops and crossties of HPFRC-SP-CL

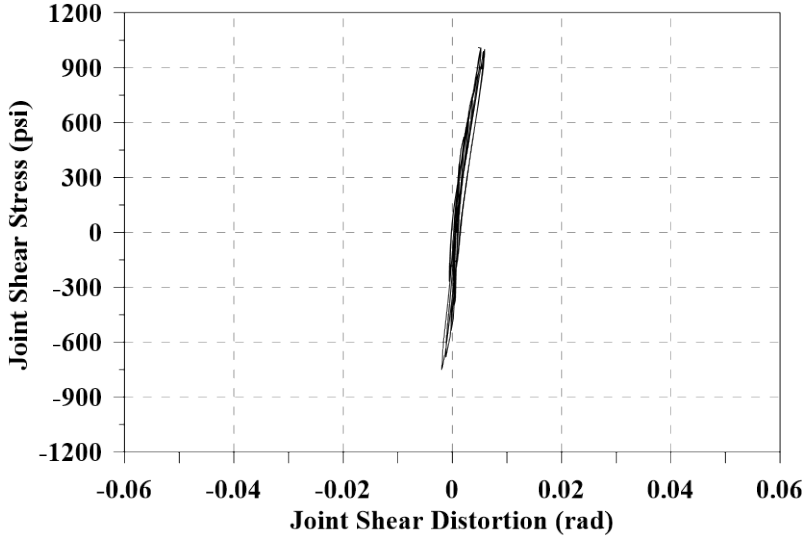

Figure 3.44 Joint shear stress vs. joint shear distortion response of RC-SP-NL

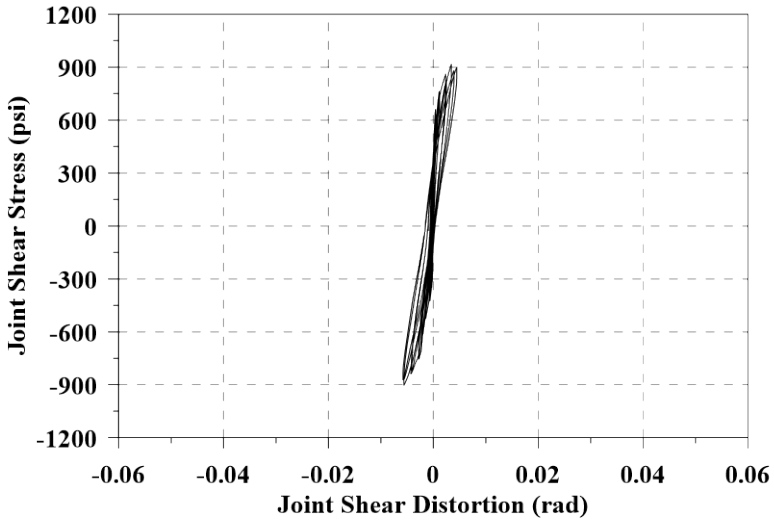

Figure 3.45 Joint shear stress vs. joint shear distortion response of RC-SP-CL

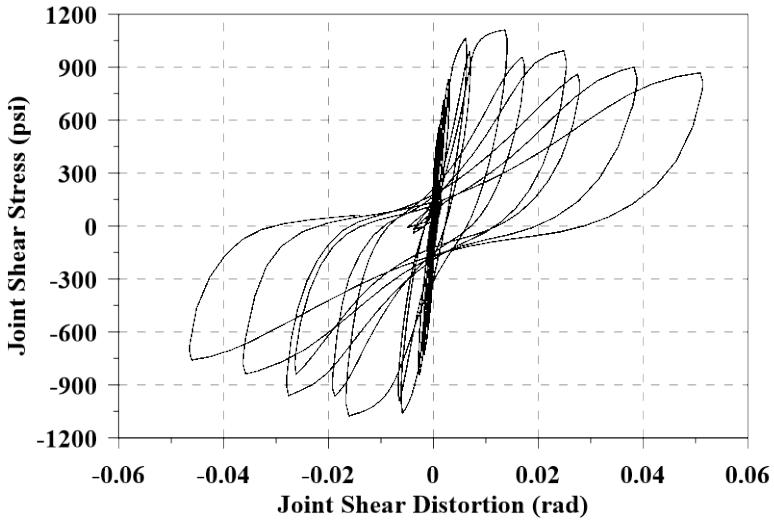

Figure 3.46 Joint shear stress vs. joint shear distortion response of HPFRC-SP-CL

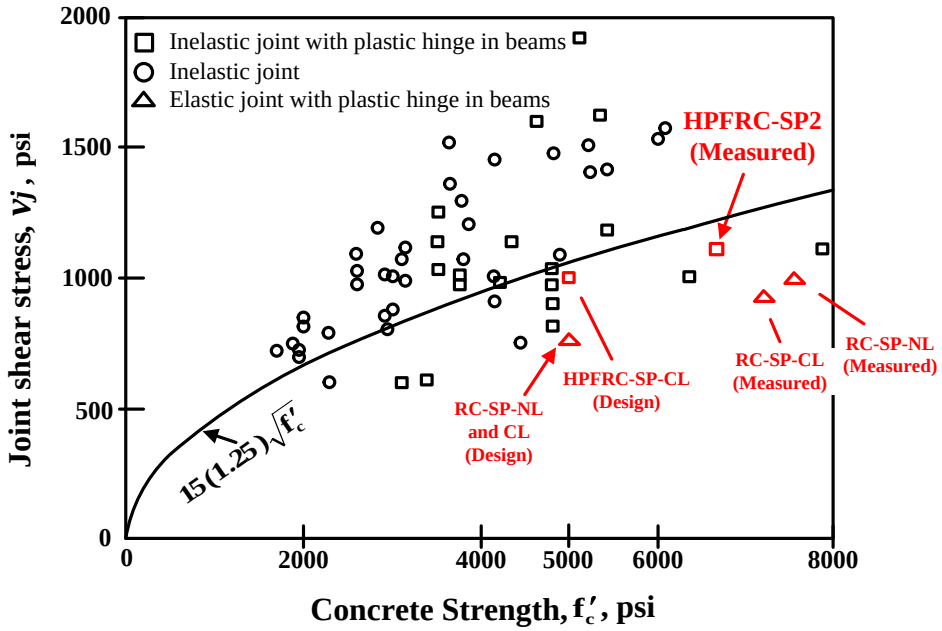

Figure 3.47 Strength of interior joints without transverse beams

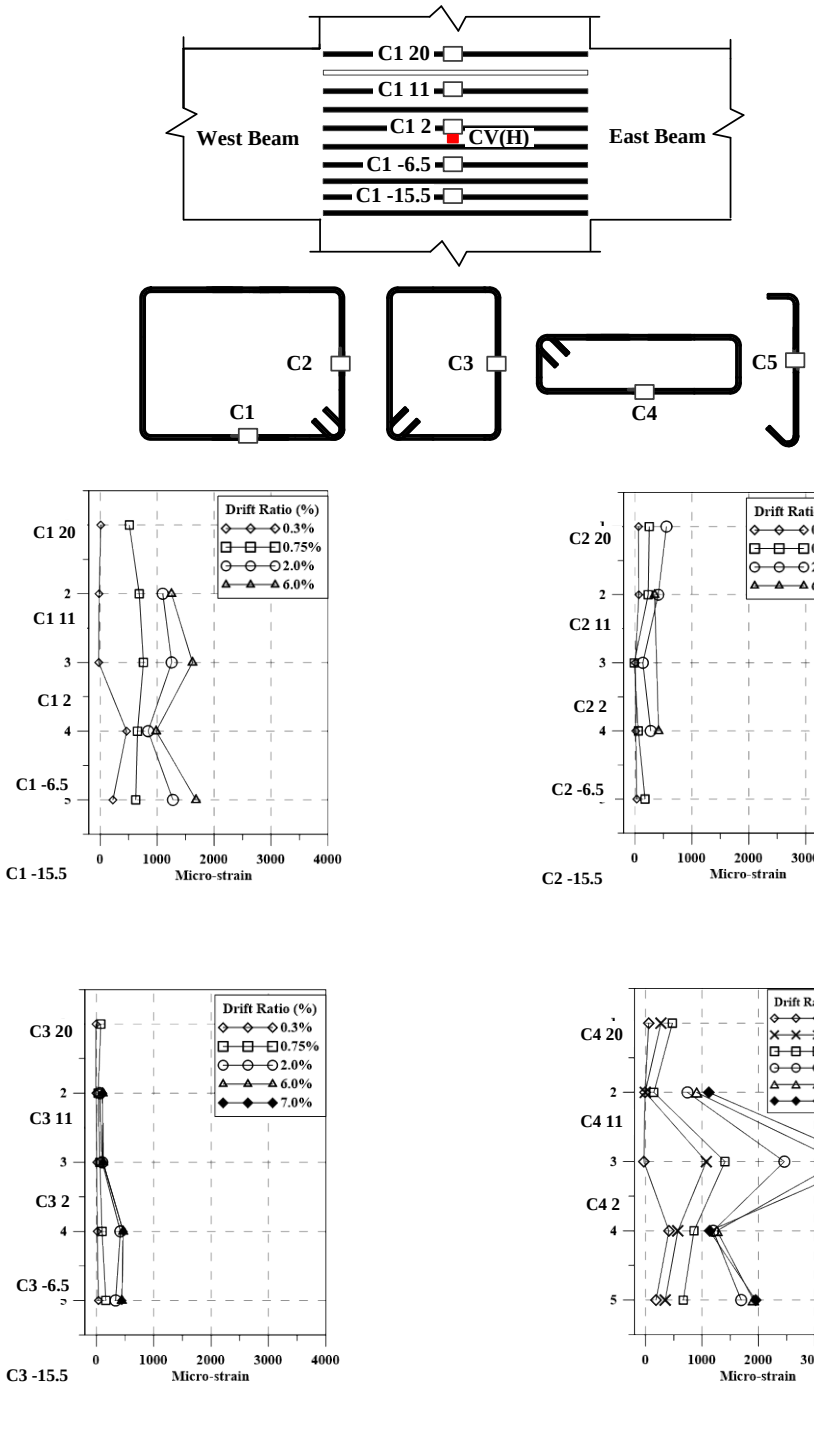

Figure 3.48 Steel strain in joint of RC-SP-NL

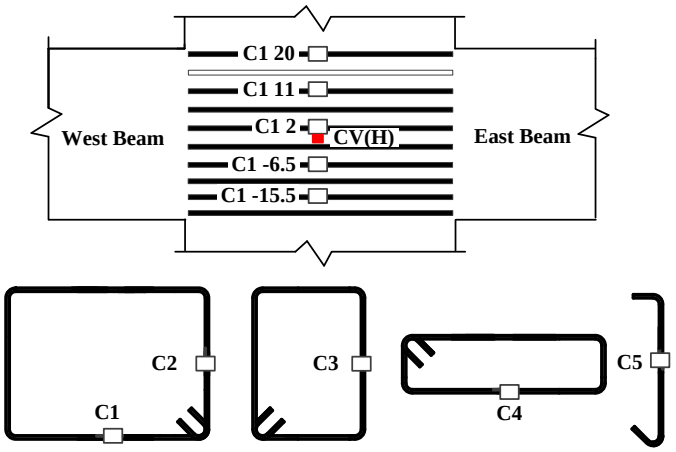

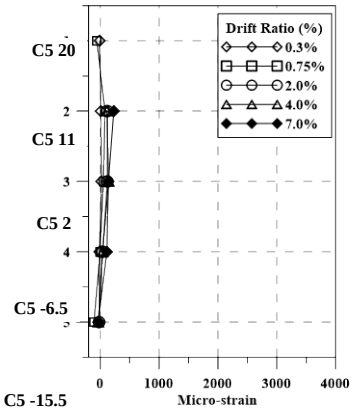

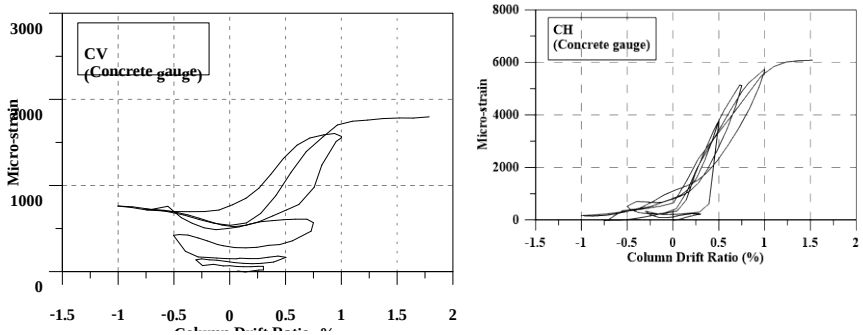

Figure 3.49 Steel and concrete strain in joint of RC-SP-NL

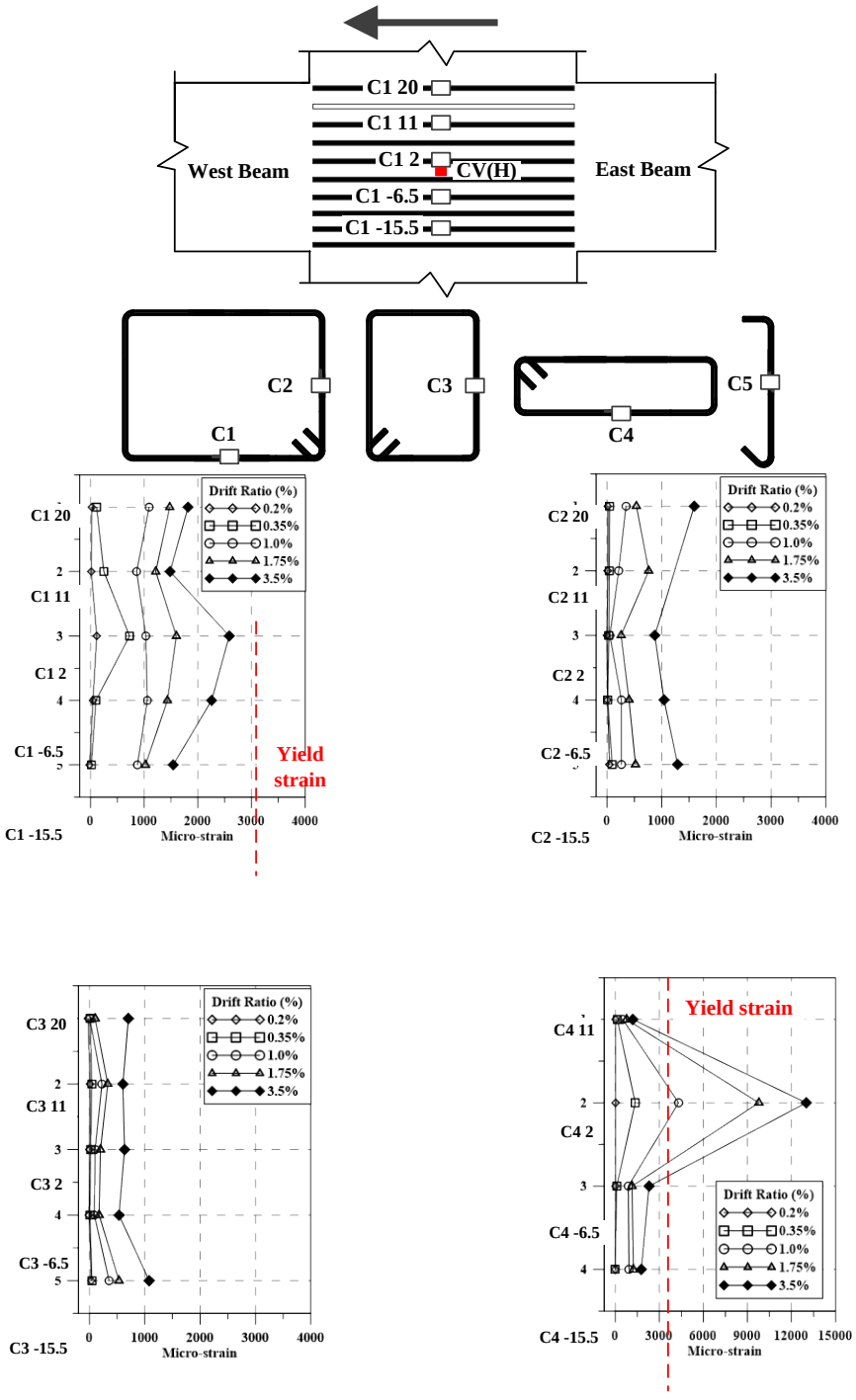

Figure 3.50 Steel strain in joint of RC-SP-CL

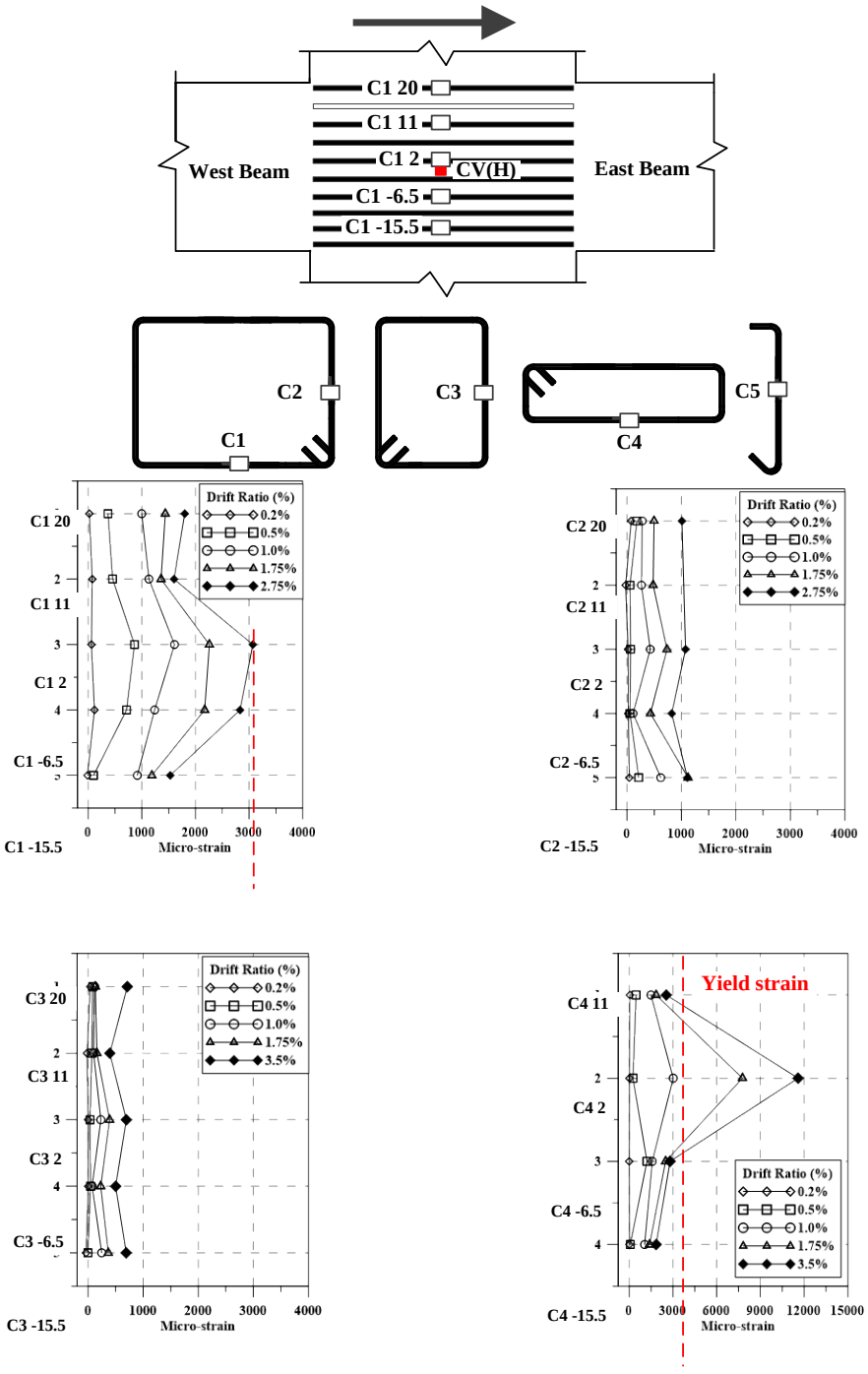

Figure 3.51 Steel strain in joint of RC-SP-CL

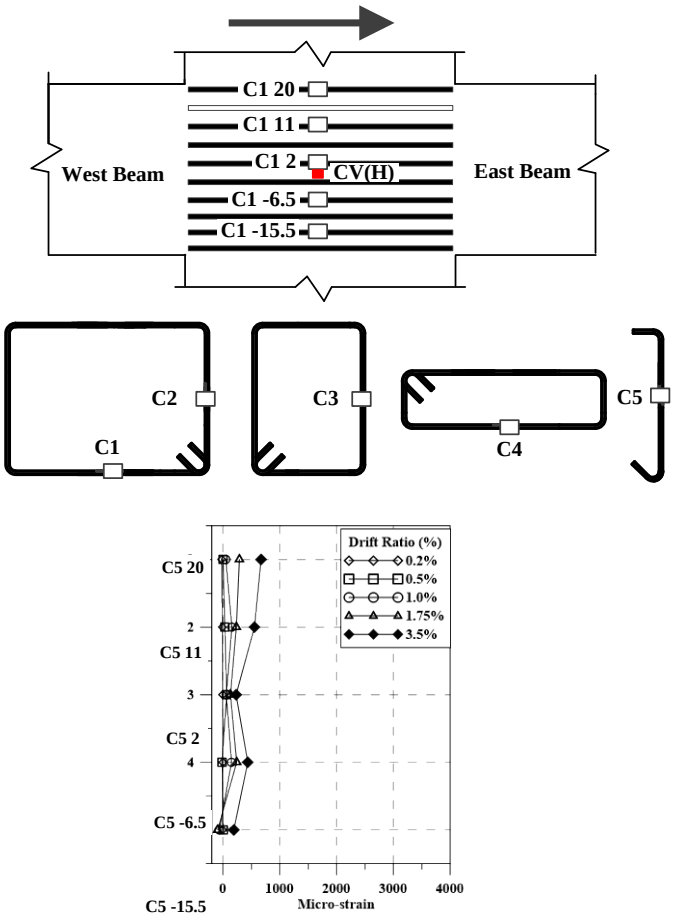

Figure 3.52 Steel and concrete strain in joint of RC-SP-CL

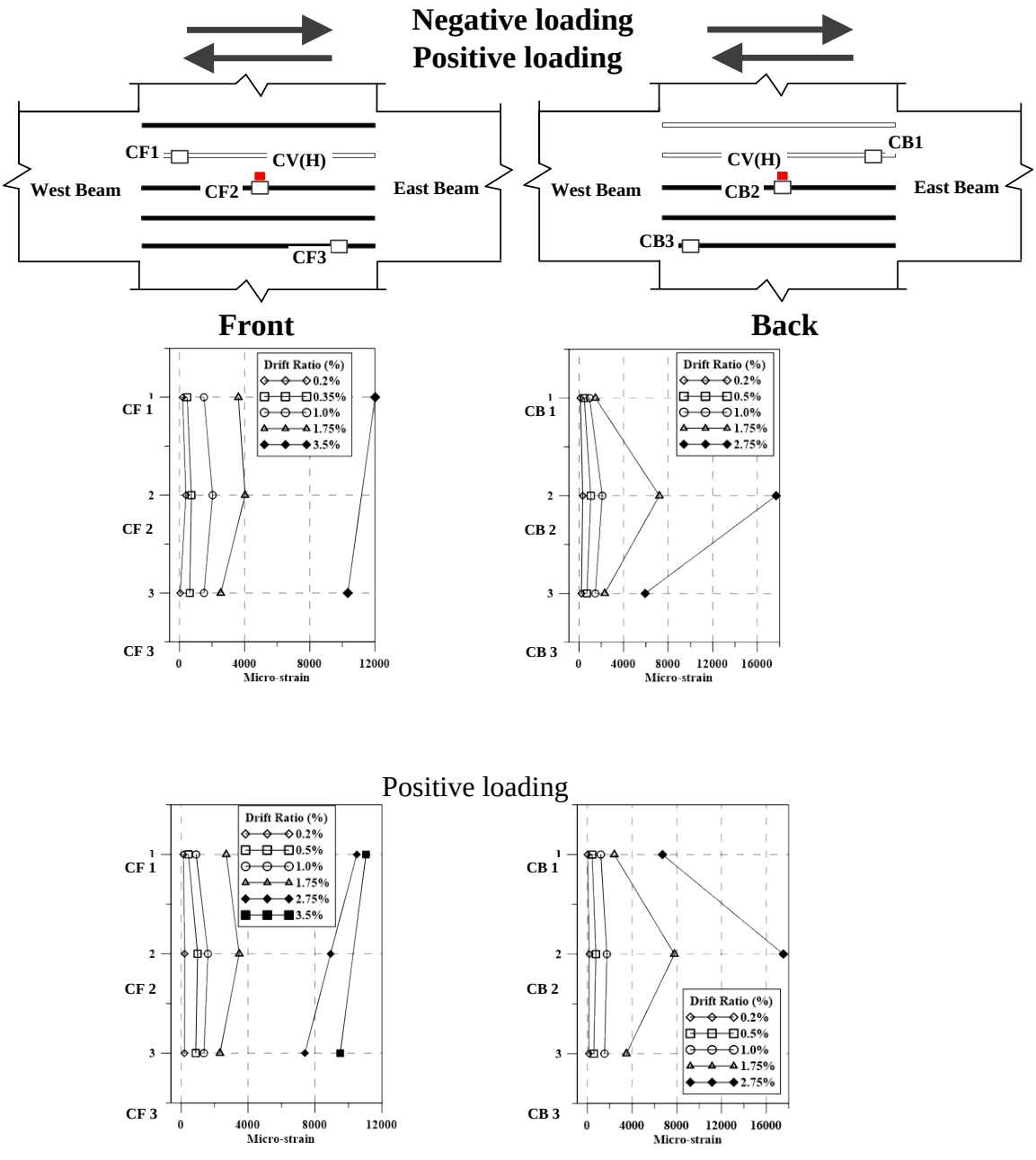

Positive loading

Negative loading

Figure 3.53 Steel strains in the joint of RC-SP-CL

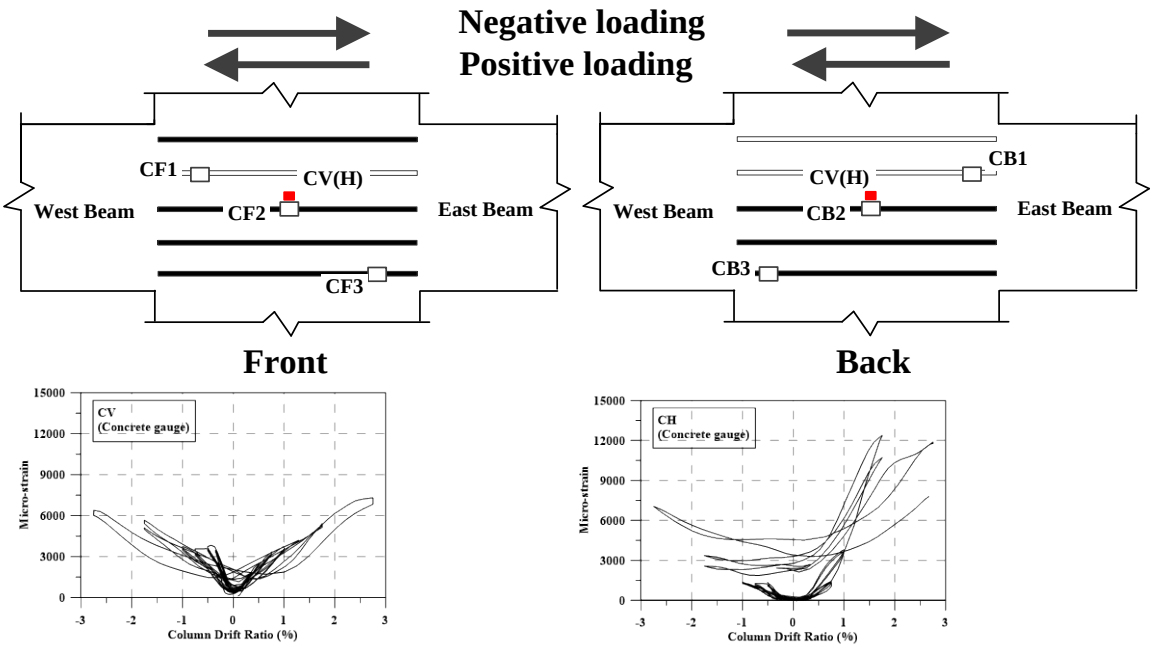

Figure 3.54 Concrete strains in the joint of RC-SP-CL

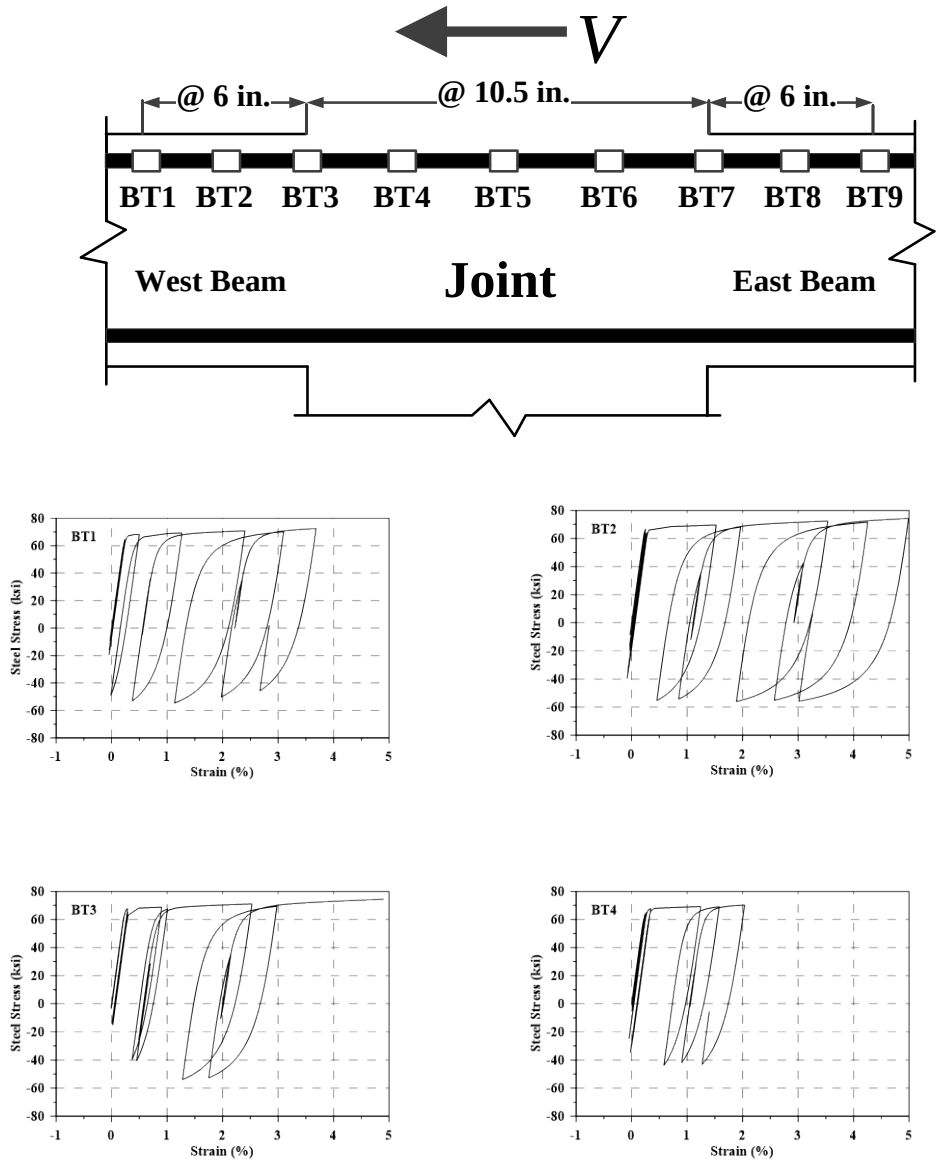

Figure 3.55 Hysteretic stress-strain responses of beam longitudinal reinforcement (BL1 series, RC-SP-CL)

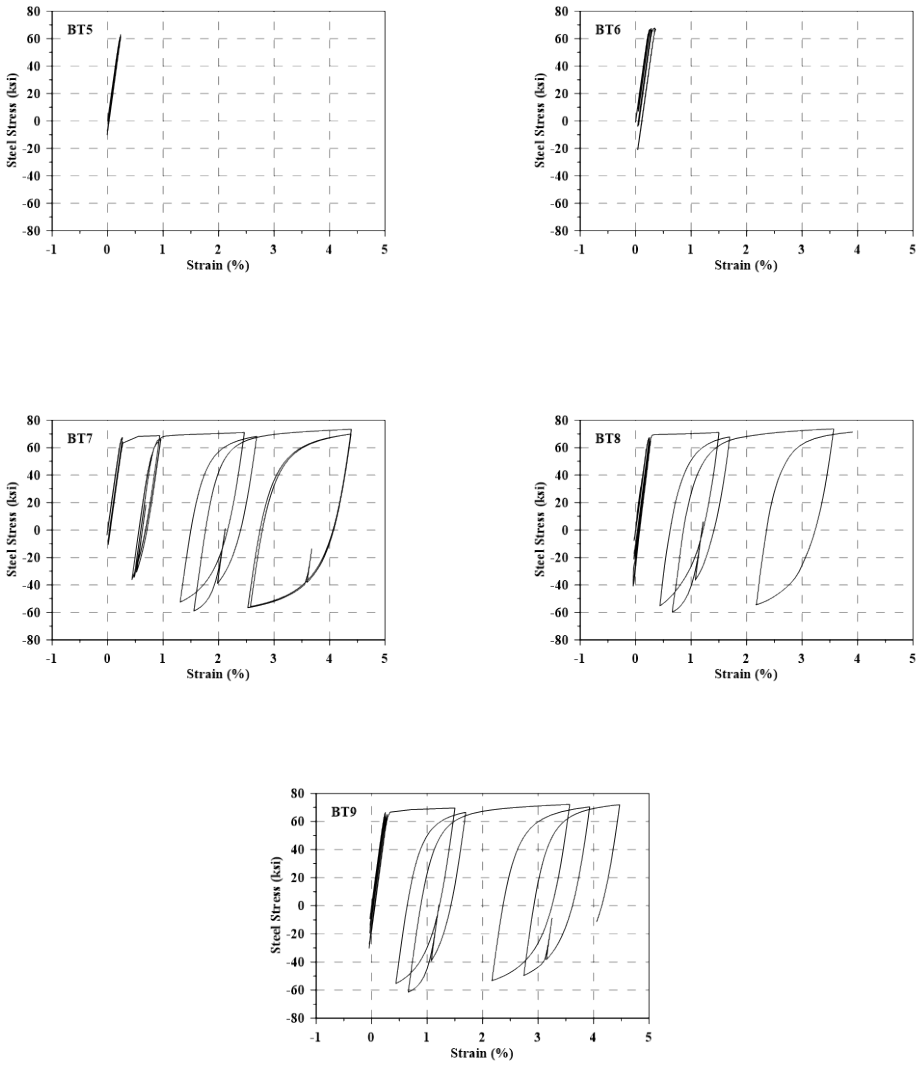

Figure 3.56 Hysteretic stress-strain responses of beam longitudinal reinforcement (BL1 series, RC-SP-CL)

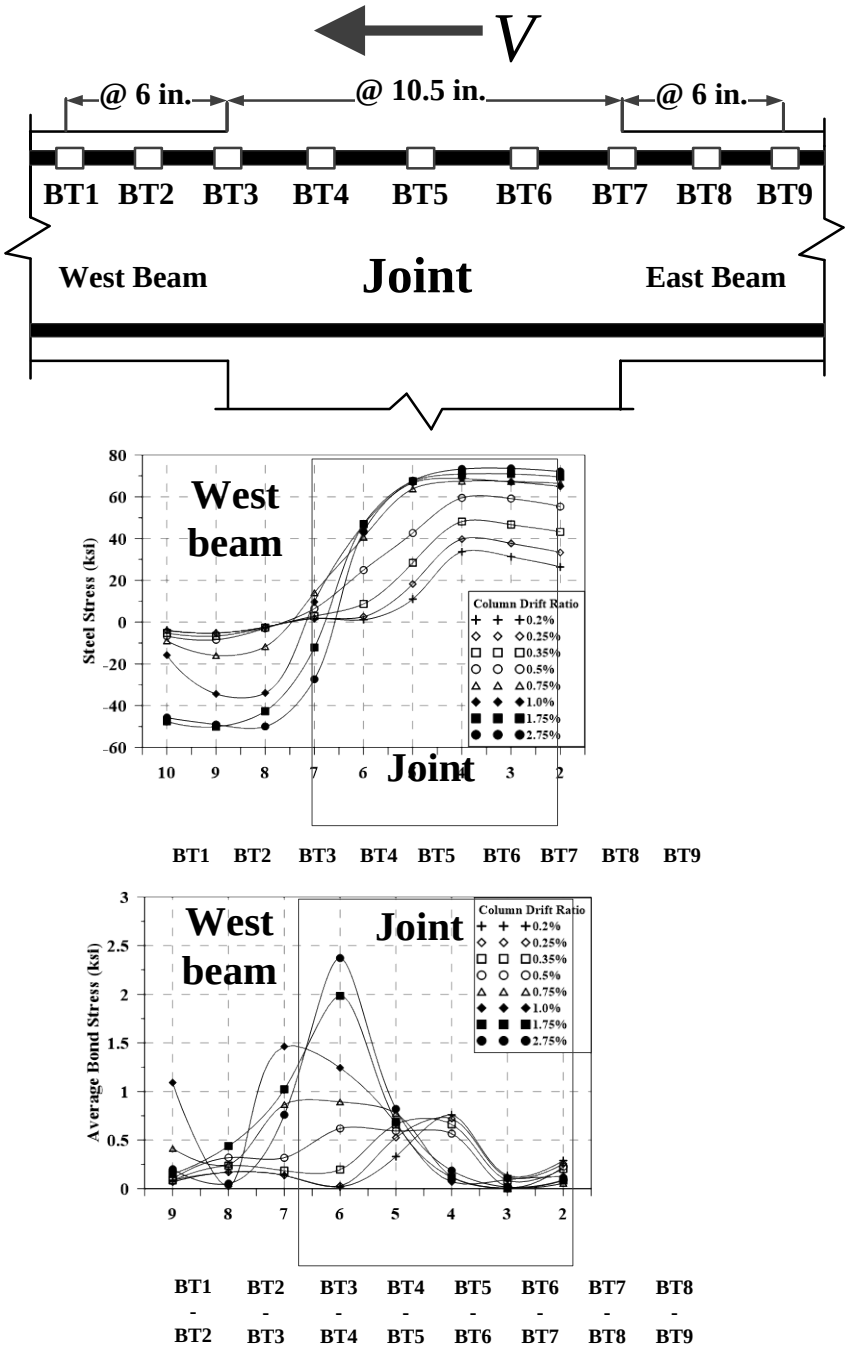

Figure 3.57 Steel stress and average bond stress distribution in beam longitudinal reinforcement (BL1 series, RC-SPCL)

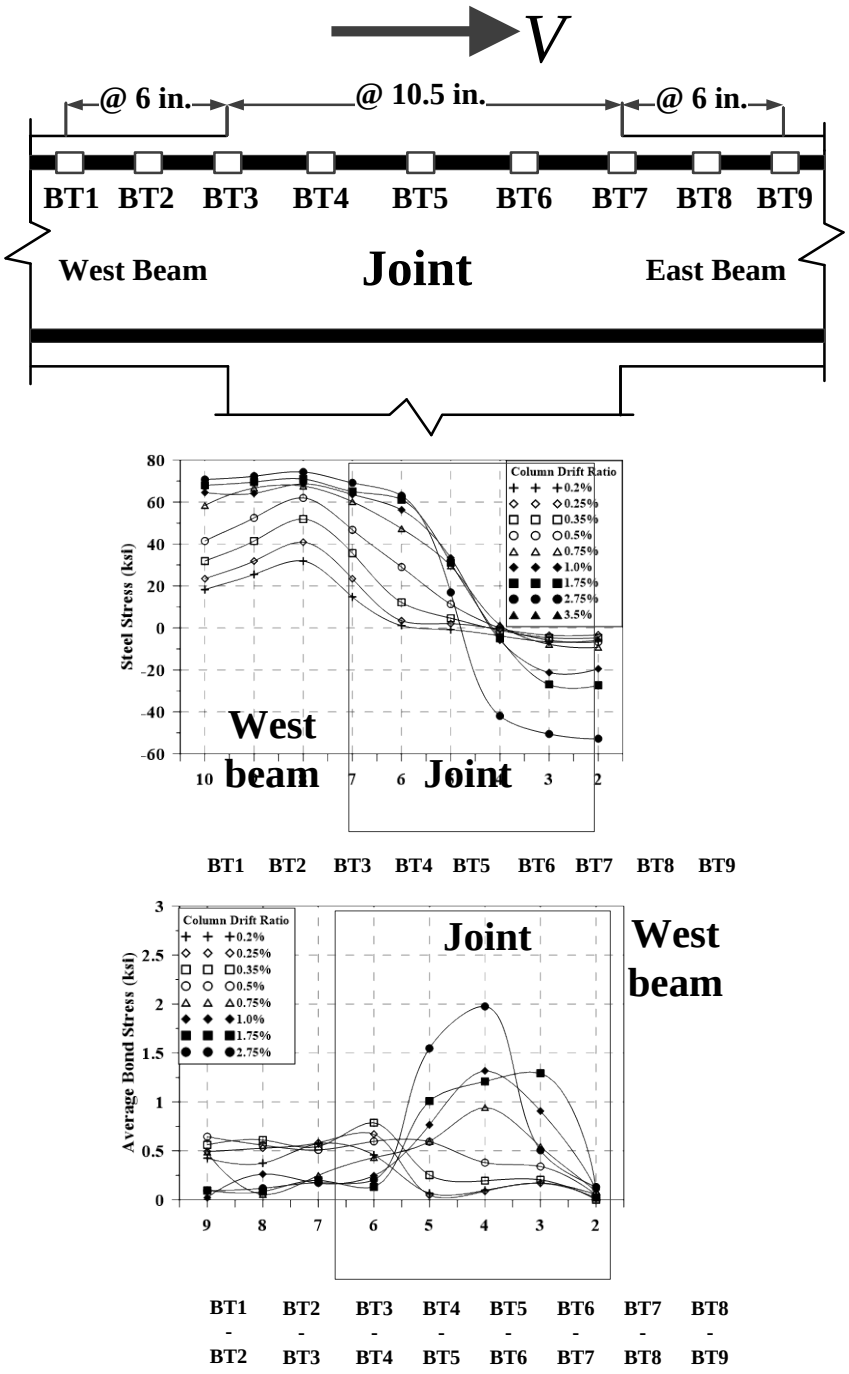

Figure 3.58 Steel stress and average bond stress distribution in beam longitudinal reinforcement (BL1 series, RC-SPCL)

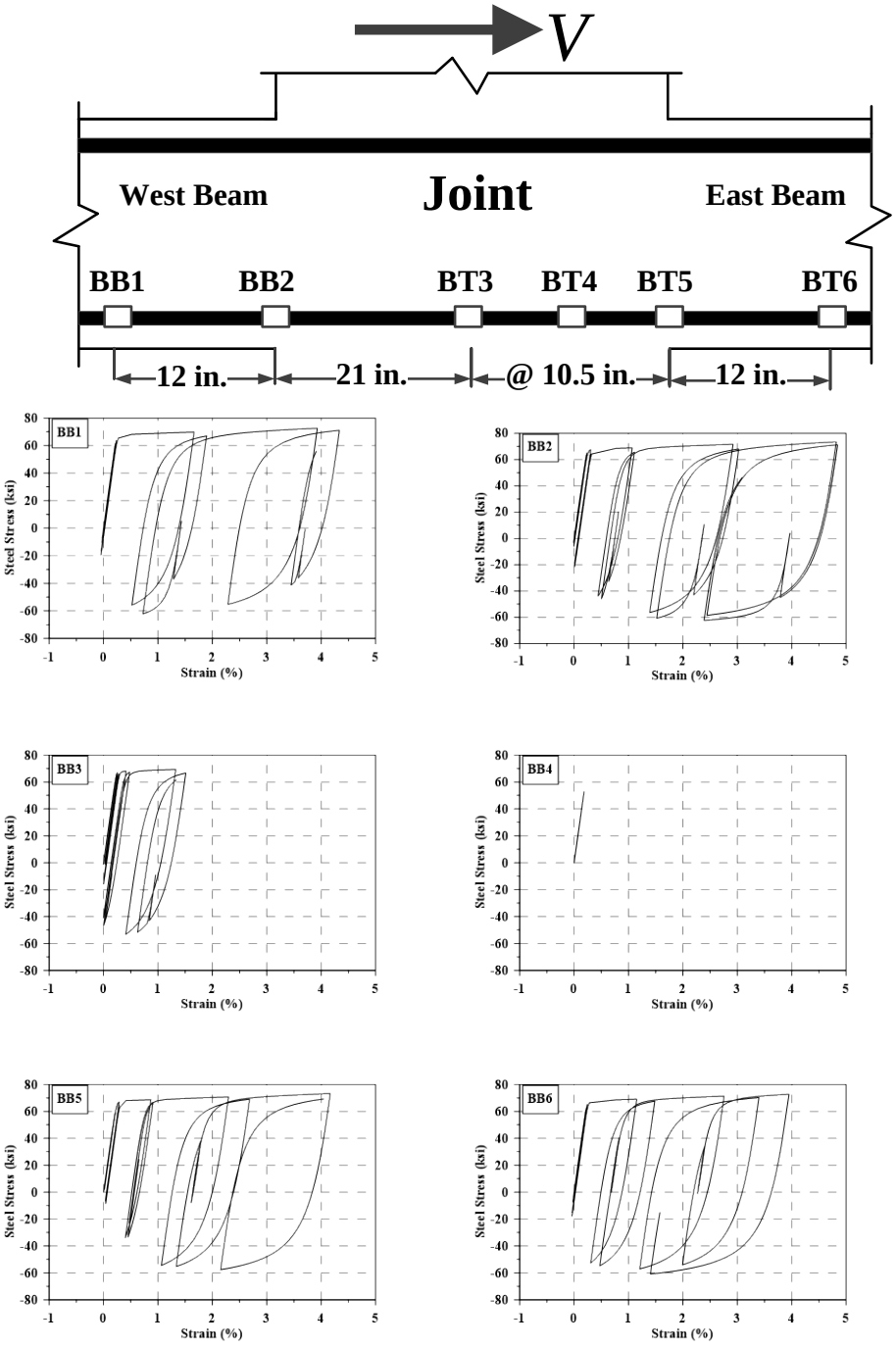

Figure 3.59 Hysteretic stress-strain responses of beam longitudinal reinforcement (BL4 series, RC-SP-CL)

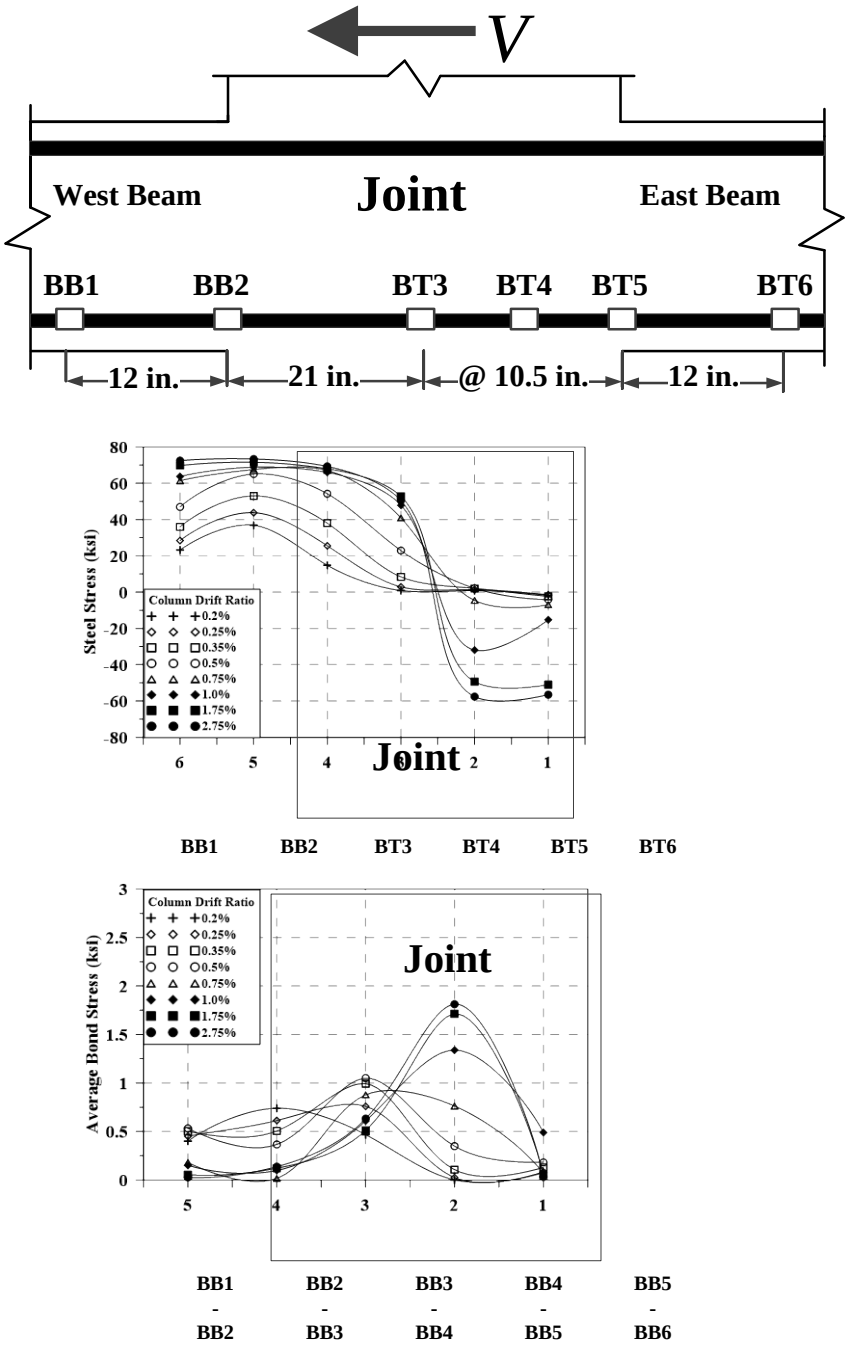

Figure 3.60 Steel stress and average bond stress distribution in beam longitudinal reinforcement (BL4 series, RC-SPCL)

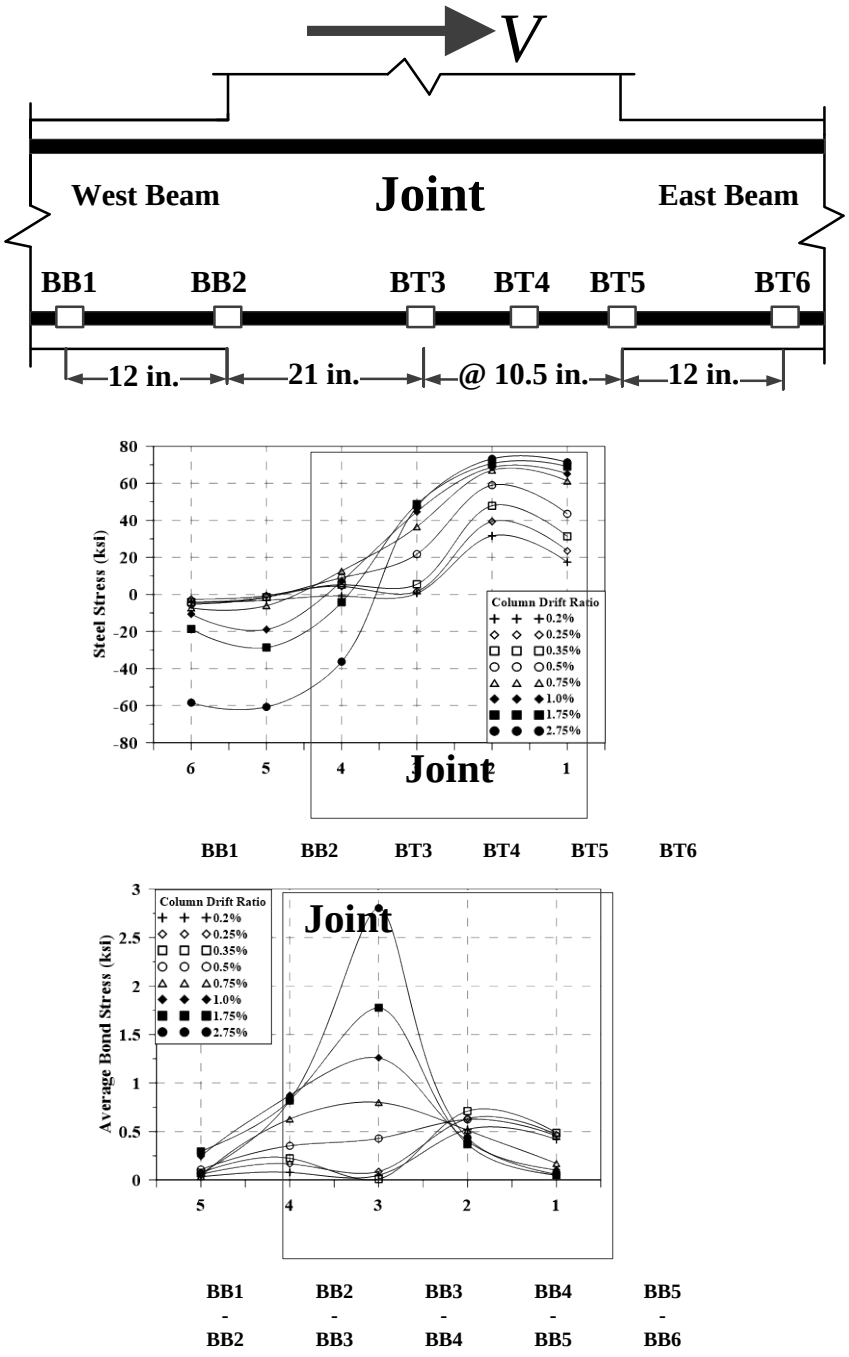

Figure 3.61 Steel stress and average bond stress distribution in beam longitudinal reinforcement (BL4 series, RC-SPCL)

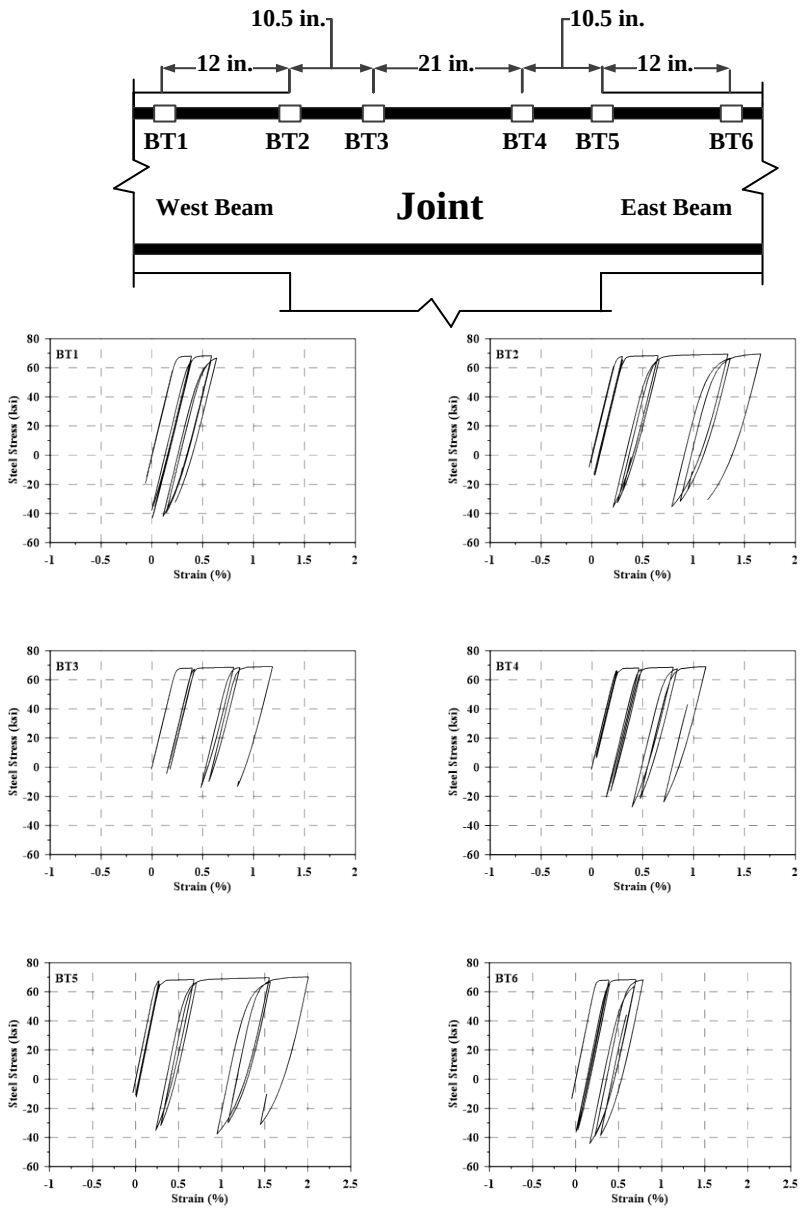

Figure 3.62 Hysteretic stress-strain responses of beam longitudinal reinforcement (BL1 series, HPFRC-SP-CL)

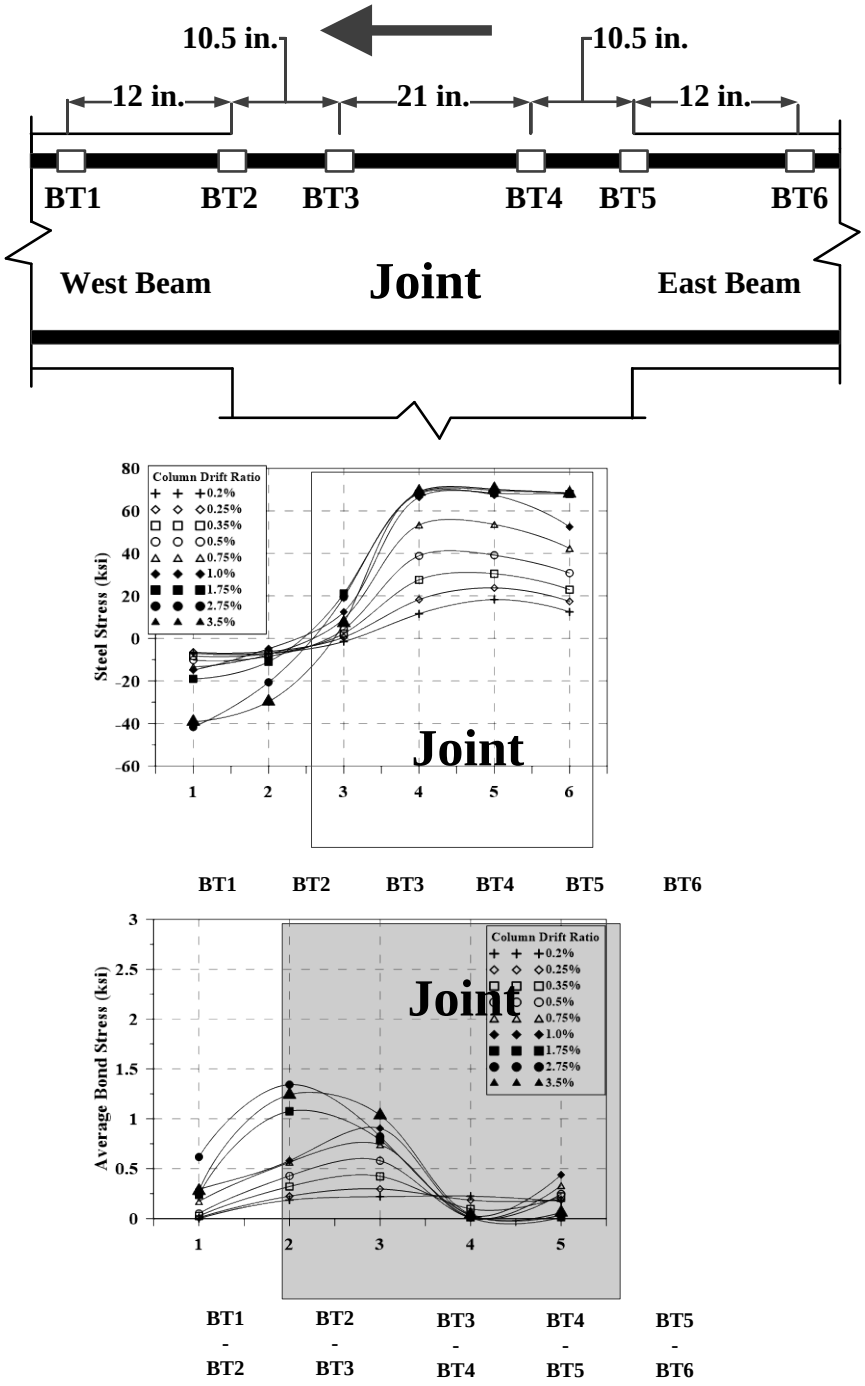

Figure 3.63 Steel stress and average bond stress distribution in beam longitudinal reinforcement (BL1 series, HPFRC-SP-CL)

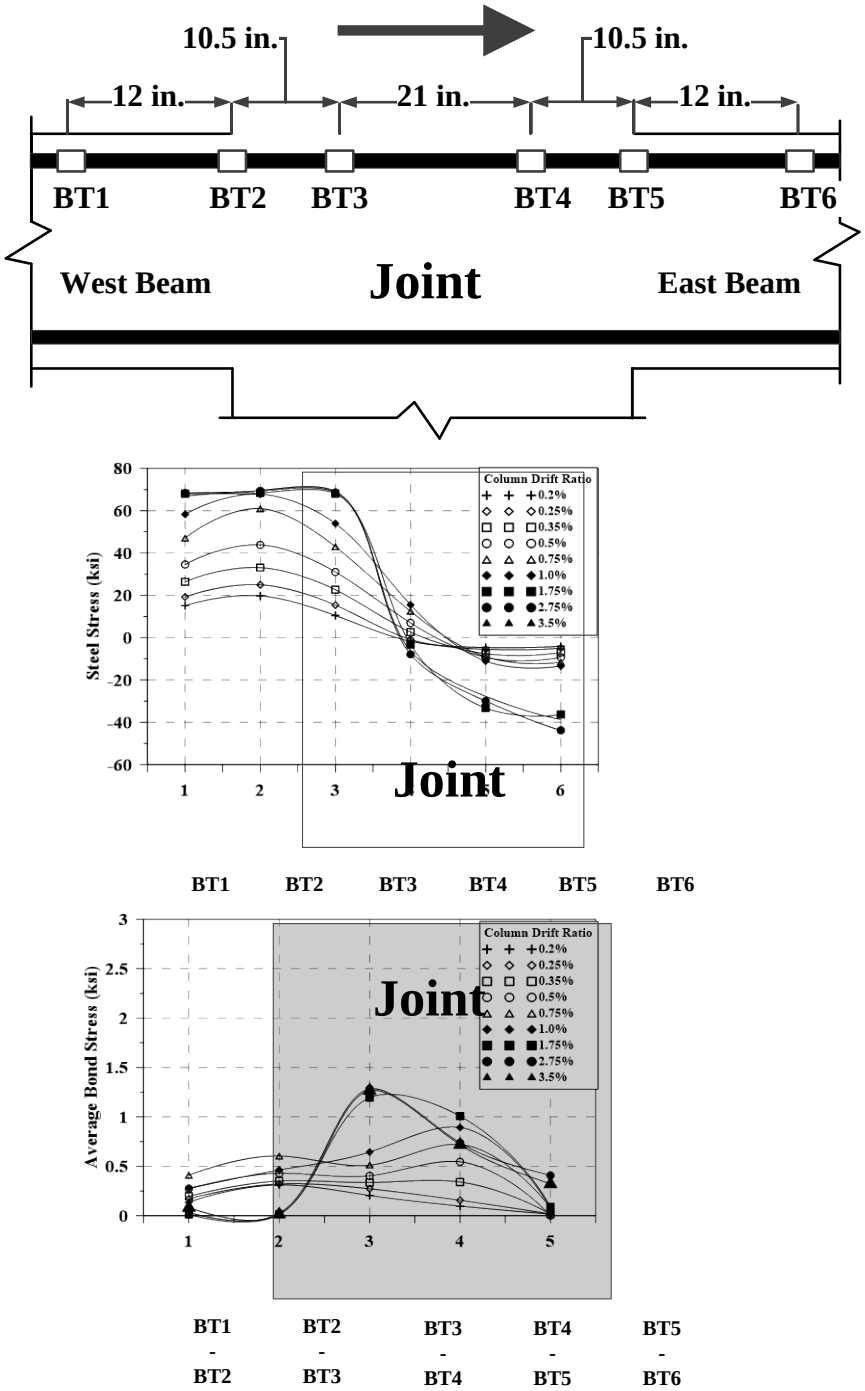

Figure 3.64 Steel stress and average bond stress distribution in beam longitudinal reinforcement (BL1 series, HPFRC-SP-CL)

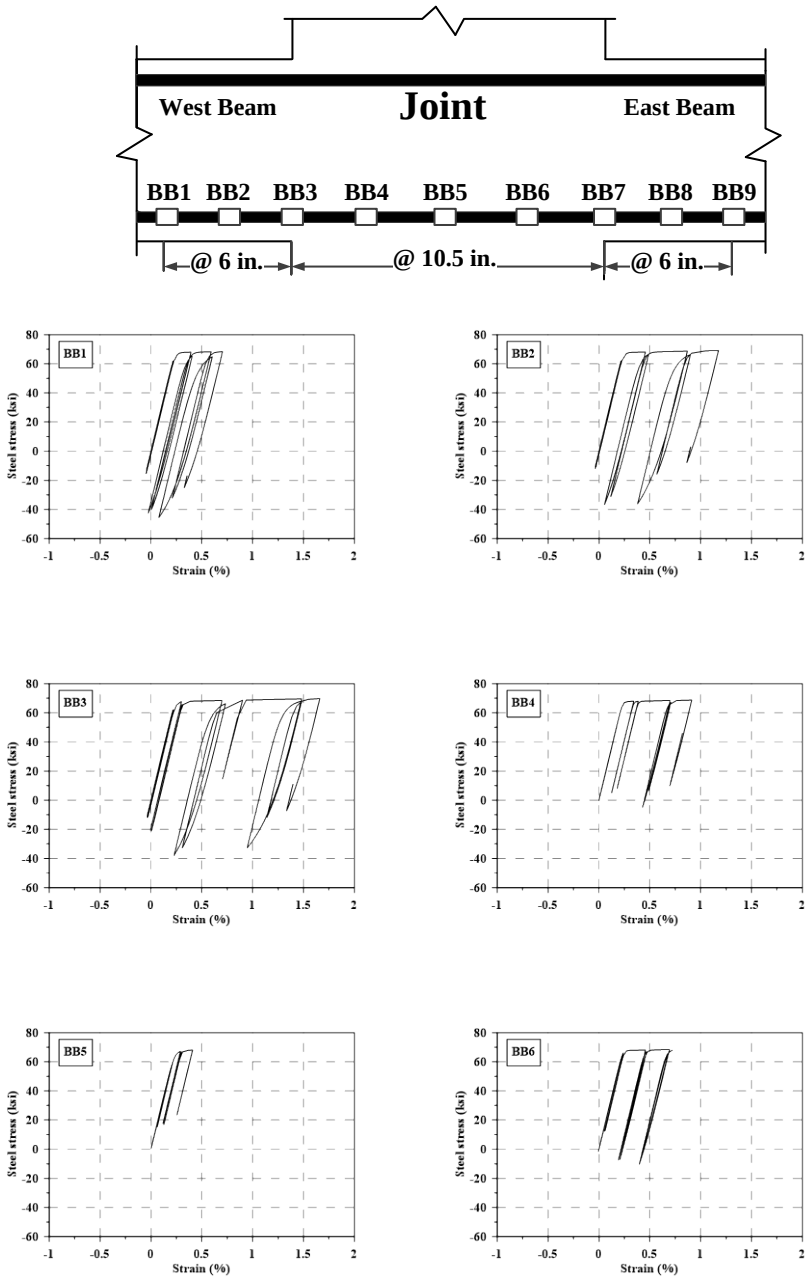

Figure 3.65 Hysteretic stress-strain responses of beam longitudinal reinforcement (BL4 series, HPFRC-SP-CL)

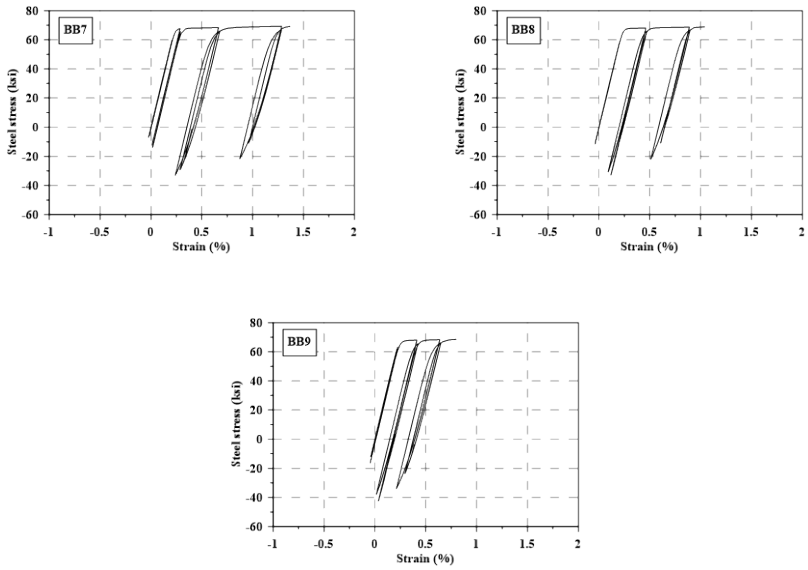

Figure 3.66 Hysteretic stress-strain responses of beam longitudinal reinforcement (BL4 series, HPFRC-SP-CL)

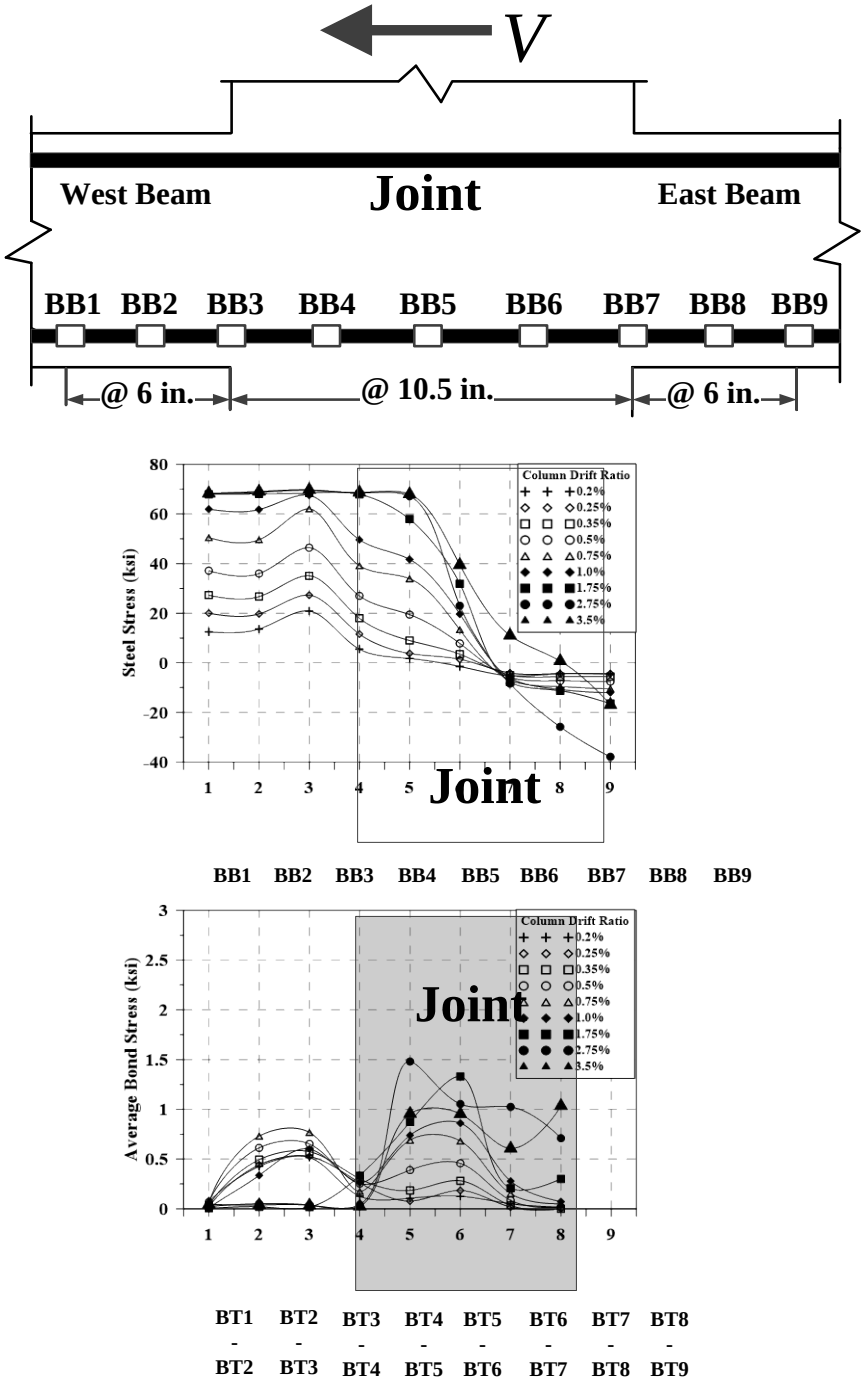

Figure 3.67 Steel stress and average bond stress distribution in beam longitudinal reinforcement (BL4 series, HPFRC-SP-CL)

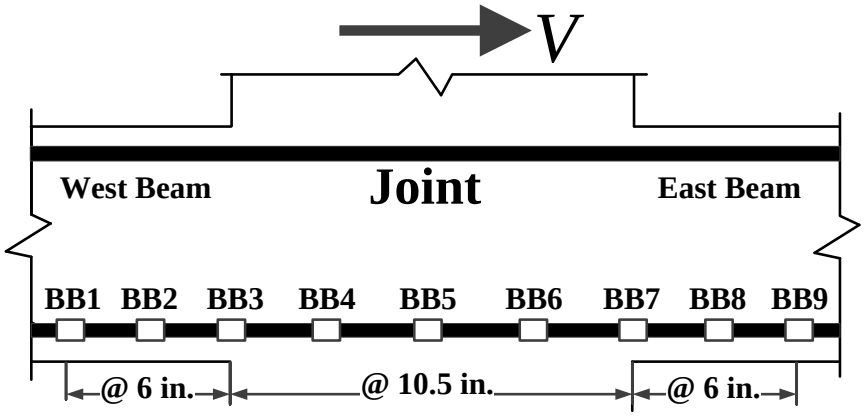

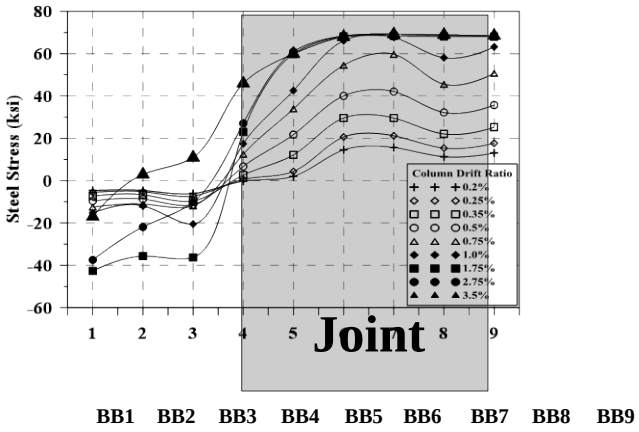

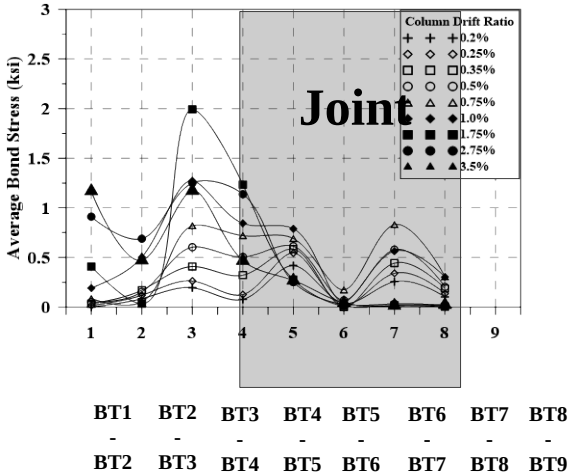

Figure 3.68 Steel stress and average bond stress distribution in beam longitudinal reinforcement (BL4 series, HPFRC-SP-CL)

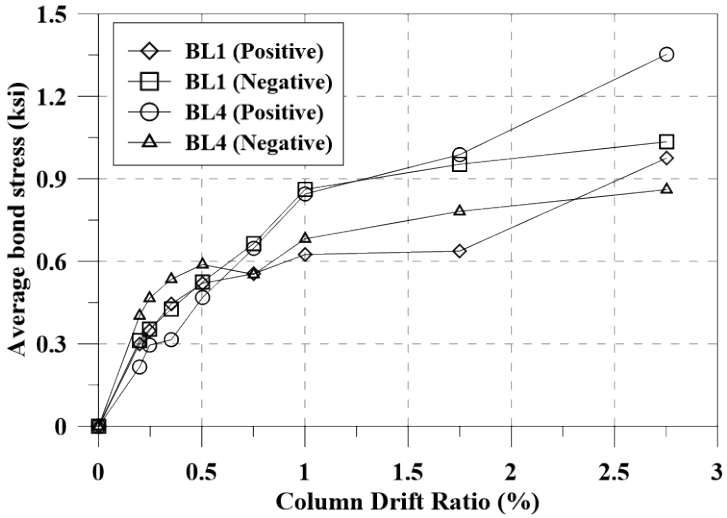

(a) RC-SP-CL

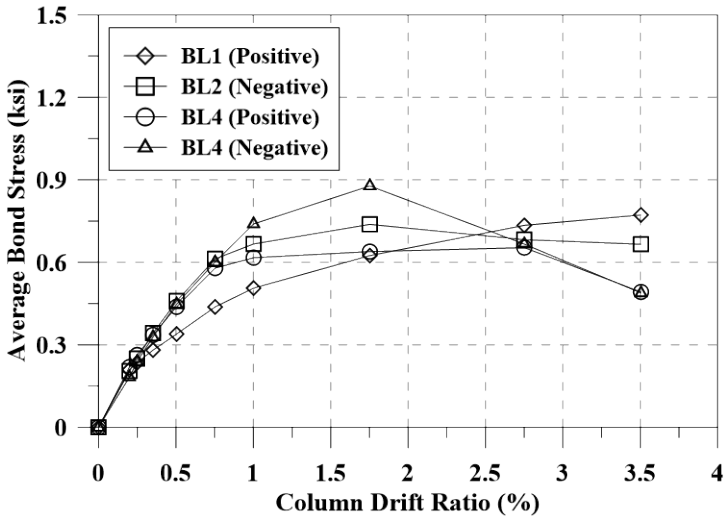

(b) HPFRC-SP-CL

Figure 3.69 Average bond stresses of beam longitudinal bars in joints

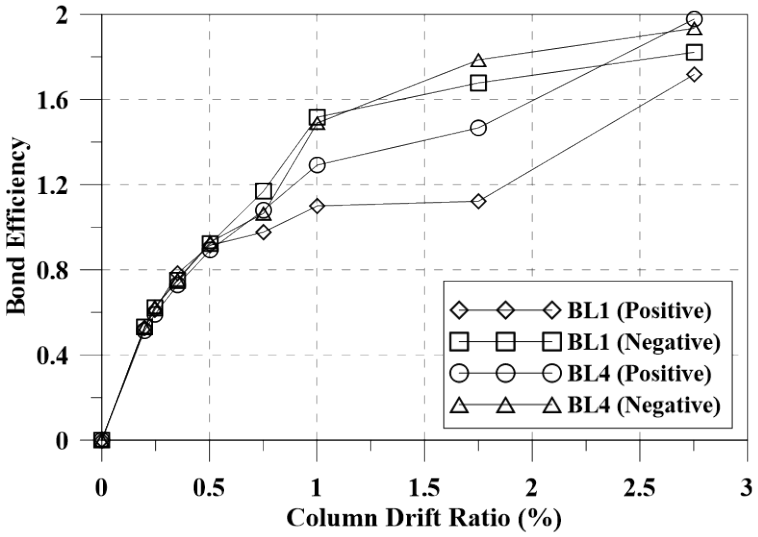

(a) RC-SP-CL

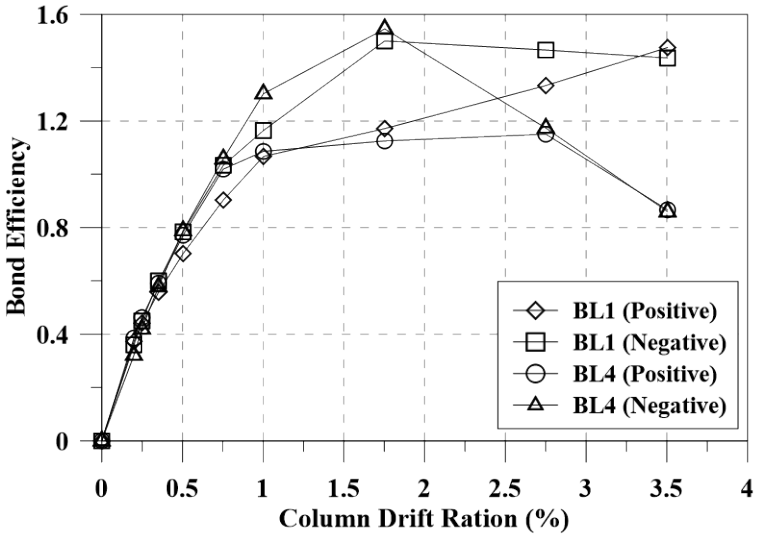

(b) HPFRC-SP-CL

Figure 3.70 Bond efficiency of beam longitudinal bars in joints

Chapter 4

SUMMARY AND CONCLUSION FROM THE FIRST PHASE

Two full-scale RC perimeter SMF slab-beam-column subassemblages, designated as RC-SP-CL(NL) and one HPFRC-SP-CL, were tested to investigate a balanced damage concept in an attempt to reduce construction difficulties and minimize damage and repair work after earthquakes. RC-SP-CL(NL) had a “strong joint” and was compliant with ACI 318-14. HPFRC-SP-CL was designed to allow large joint inelastic deformation. Nearly 80% of the transverse reinforcement in its joint was eliminated as compared to RC-SP-CL(NL). Furthermore, for HPFRC-SP-CL test results conclude that if shear stress in beam plastic hinge regions are kept below $1.95\sqrt{f'_c}$ psi ($0.16\sqrt{f'_c}$ MPa), no hoops in the plastic hinge regions are needed. The following conclusions are drawn from this research:

1. Seismic behavior of RC-SP-CL and RC-SP-NL were very similar to each other even if they were subjected two different types of loading protocols. The performance of both specimens clearly satisfied ACI 374 criterion.

2. Both RC-SP-CL and HPFRC-SP-CL showed stable hysteretic responses up to 3.5% CDR without significant strength degradation, which meets the collapse prevention structural performance according to ACI 374 criterion. The response of RC-SP-CL was controlled by a flexural mode with the formation of plastic hinges in the beams. The main source of strength decay was due to the buckling of beam reinforcement and sliding shear at the beam-column interface. HPFRC-SP-CL responded in a flexural mode up to 1.75% column drift ratio and afterwards it changed to joint shear mechanism. The

HPFRC-SP-CL's joint and beams yielded at 1.75% column drift ratio. The main source of strength degradation was due to the significant shear distortion in the joint.

3. Severe bond deterioration occurred in the HPFRC-SP-CL joint. However, the consequential negative effect of the large drift ratio resulting from the bond failure was not as serious as expected compared to RC-SP-CL. This is because the excessive yielding in the beam longitudinal reinforcement of RC-SP-CL also led to severe bond deterioration in the beam plastic hinge region which in turn contributed to large story drift ratio.

4. The pilot full-scale test proved the balanced damage concept to be feasible as indicated by the considerably reduced damage in beams and the nearly equal energy dissipation in the beams and joint in Specimen HPFRC-SP-CL.

5. Although the overall performance of HPFRC-SP-CL is satisfactory, the small amount of transverse reinforcement (about 20% of that used in a typical RC joint) placed in the joint leads to major damage in the joint at larger drift ratio. It is expected that this pilot specimen can serve as a baseline design for future study with an optimal amount of transverse reinforcement or a further enhanced HPFRC material to delay the deterioration of the HPFRC joint and thereby lead to a further optimized damage balance.

Chapter 5

INTRODUCTION FOR THE SECOND PHASE

5.1 Background

Reinforced concrete (RC) structural walls are used commonly as the primary seismic force resisting system in RC buildings. Based on the architectural requirements, these walls often have numerous openings for entities such as elevators, windows, and doors, which divide a single wall into more slender (cantilever) walls connected by substantial beams (Figure 5.1). This system is known as coupled walls and the beams are called coupling beams. The target mechanism of a coupled wall is shown in Figure 5.2. In the coupled wall, the coupling beams must yield before the wall piers for the coupled wall to behave as a single cantilever wall and the desirable behavior of the coupled wall demands all the coupling beams to experience yielding. Properly designed coupled wall can have many benefits compared to isolated walls (structural walls without opening).

First, since all coupling beams are participated to the stiffness and strength of the coupled walls, the stiffness and strength of the coupled wall is much greater than those of isolated walls. Second, as seen in Figure 5.3, shear forces that is generated due to the frame actions of the coupling beams are transferred to the wall piers which generates axial tension and compression force. These axial forces can resist part of the overturning moment at the base, making the foundation restraint much easier. Third, the coupling beams and wall piers in a coupled wall are the major source of energy and the coupling

beams are required to be subjected to large load reversals during a strong earthquake. This allows the coupled wall to dissipate energy over its height.

During a strong earthquake, the coupling beams are subjected to double curvature, which results in the chord rotation of the coupling beams much greater than the story or global drift ratio. As a result, In order for the coupled wall to survive multiple displacement cycles during a strong earthquake, it is required that the coupling beams need to possess large rotational capability with adequate stiffness, and strength.

5.2 Previous Works

Two types of coupling beams are allowed by ACI code (ACI, 2014) for coupled wall system (Figure 5.4 and 5.5). They are conventional and diagonally reinforced coupling beams, and their application depends on the span-to-depth ratio (or aspect ratio, l_n/h) and shear demands. Prior studies (Barney et al., 1980; Naish at el., 2013; Lim et al., 2016) have shown that conventionally reinforced coupling beams (reinforced with vertical and longitudinal reinforcing bars), with span-to-depth ratios between 2.5 and 4 and maximum shear stress between $3.4\sqrt{f'c}$ and $7.9\sqrt{f'c}$, exhibited fast strength degradation after approximately 4% beam chord rotation. The major source of the strength degradation was the sliding shear at the beam-to-wall interface.

Another important factor when considering strength degradation is rotational capacity. Prior nonlinear time-history analyses (Harries et al., 2006) indicated that coupling beams would need average rotational capacities of approximate 3% and 6% for

design basis earthquakes (DBE) and maximum considered earthquakes (MCE), respectively. These rotational capacities help maintain the integrity of a coupled wall system. Note that DBE has a 10% probability of exceedance in 50 years corresponding to Life Safety Performance Level and MCE has a 2% probability of exceedance in 50 years corresponding to Collapse Prevention Performance Level.

Based on the shear resistance and adverse failure mechanisms of conventional coupling beams, Paulay and Binney (1974) proposed diagonally reinforced coupling beams (DCBs) with reinforcement detailing consisting of two intersecting diagonal reinforcement groups combined with closely spaced transverse reinforcement (Figure 5.6). In this reinforcement detail, the diagonal bars need to be well confined by transverse reinforcement and carefully anchored in the walls. In a design using this type of coupling beam, the whole shear transfer mechanism is resisted by heavily reinforced diagonal cages. Experimental results have shown that diagonal reinforcement detailing can significantly improve deformation and energy dissipation capacity compared to conventional detailing for coupling beams subjected to reverse cyclic loading (Barney et al., 1980; Galano and Vignoli, 2000; Naish et al., 2009; Paulay and Binney, 1974).

For coupling beams with a span-to-depth ratio approximately 1.0, diagonal reinforcement placed with a large inclination has proven to be the most efficient solution (Harries et al., 2005). On the other hand, modern architectural specifications typically require span-to-depth ratios between 2.4 and 4. Prior research shows that for DCBs with span-to-depth ratios between 2.4 and 3.3, the majority of damage occurred at the beam-to-wall interface due to slip of the diagonal reinforcing bars from adjacent walls (Naish et al., 2013). This type of bond failure is typically difficult to repair (Engindeniz et al., 2005).

In addition to the slip, damage at the ends of DCBs revealed full depth cracking, which leads to separation of the beam and wall (Paulay, 1977). In addition, coupling beams with span-to depth ratios between 2.4 and 4 lead to a very shallow angle of inclination for the diagonal reinforcement (can be as low as approximately 10 degrees). The lower angles of inclination, combined with the detailing requirements specified in ACI 318 (2014), can cause several major issues for both design and construction (Harries et al., 2005; Moehle et al., 2011; Naish et al., 2009; Moehle, 2015):

1. A small angle of inclination significantly decreases the efficiency of diagonal reinforcement in resisting shear forces, which in turn requires an even smaller angle to accommodate the reinforcing bars; thus, more reinforcing bars are needed, which ultimately increases the difficulty of construction. There is significant difficulty in placing the diagonal reinforcing bars because they can be easily obstructed by transverse reinforcement used to confine the diagonal bars (Figure 5.5, option 1). Additional reinforcement detailing is also required when the extension of the diagonal bars are bent at the top of the wall or at openings in the wall.

2. Although ACI 318-14, Sect. 18.10.7.4(d), allows alternative full beam section confinement to reduce congestion issues, there is still the obvious difficulty of passing the diagonal bars through the hoops and crossties (Figure 5.5, option2).

3. It can be very challenging and time-consuming to thread the diagonal reinforcement through the congested vertical and horizontal bars in the wall's boundary elements (Figure 5.5).

4. The minimum width requirement for diagonal elements causes interlock of the two diagonal elements. This in turn demands an increased clear distance between reinforcing bars in order for one diagonal element to pass through the other. Often, the diagonal reinforcing bars need additional space to prevent the conflict with the boundary element reinforcement of the wall pier. The minimum dimensions and required reinforcement clearances can make the coupling beam very wide, which controls the wall width.

5. Modern construction also calls for the additional architectural requirement of having utility ducts go through the coupling beams (Hooper, 2014). This is generally a difficult task when using diagonally reinforced coupling beams (DCBs) due to reinforcement congestion or the concern of weakening the local region when ducts are present.

Other alternative reinforcement schemes have been investigated (Tassios et al., 1996), such as the addition of dowels at the ends of the coupling beams or a diagonal reinforcement located only at the beam-wall interface. However, it was experimentally demonstrated that coupling beams with these alternative reinforcement details did not exhibit satisfactory seismic behavior, and/or they posed construction difficulties (Tassios et al., 1996).

5.3 Research Objectives and Scope

The above-mentioned construction and design issues with DCBs can be considerably minimized by utilizing an innovative and simplistic reinforcing scheme investigated in this study as illustrated in Figure 5.6. This new coupling beam, double-beam coupling beam (DBCB), consists of two separate cages similar to those used for beams in RC special moment frames. The new coupling beam acts like a conventional coupling beam under small displacements. With larger displacements, cracks begin developing at the beam's mid-span and mid-height where the narrow unreinforced concrete strip is located, gradually propagating towards the ends. The cracks eventually separate the beam into two relatively slender beams (ACI 318 section 18.6.2.1 define a beam with clear span, $l_{n,}$ at least four times of the effective depth as relatively slender member) where each has nearly twice the aspect ratio of the original coupling beam.

This essentially transforms the shear-dominated behavior into flexure-dominated behavior common to conventional beams. Because damage initiates from the center of the beam, then spreads towards the ends, the beam's ends maintain their integrity even under very large displacements, thereby eliminating the sliding shear failure at the beam-to-wall interface, as is commonly seen in conventional beams (Aktan and Bertero, 1981; Aristizabal-Ochoa, 1987). In addition, because the cracks always initiate at mid-span and mid-height, the damage location can be easily predicted, which makes repair work, if needed, much easier after moderate earthquakes. Furthermore, the gap between the two cages allows for utility ducts through the beam without affecting the beam's seismic behavior.

For performance-based design, a structural component's damage at various performance levels needs to be investigated in order to evaluate its potential impact on

life and economic loss, downtime, and occupancy. Post-earthquake damage states at various performance levels for RC coupling beams outlined by ACI 374 (2013) and ASCE/SEI 41 (2014) are used to evaluate the performance of DBCBs:

1. Immediate Occupancy Performance Level (defined as the post-earthquake damage state in which a structure remains safe to occupy and essentially retains its pre-earthquake strength and stiffness): coupling beams experience diagonal cracking.

2. Life Safety Performance Level (defined as the post-earthquake damage state in which a structure has damaged components but retains a margin against the onset of partial or total collapse): coupling beams have extensive shear and flexural cracks; some crushing, but concrete generally remains in place.

3. Collapse Prevention Performance Level (defined as the post-earthquake damage state in which the building is on the verge of partial or total collapse. Substantial damage to the structure has occurred, potentially including significant degradation in the stiffness and strength of the lateral-force-resisting system): coupling beams are shattered and virtually disintegrated.

5.4 Research Significance

This research investigated the seismic performance of reinforced concrete (RC) double-beam coupling beams (DBCBs) used in RC coupled core walls (CCWs) using innovative configurations, which can significantly improve and simplify constructability,

design, and repair work, while exhibiting excellent strength, stiffness, and ductility under large displacement reversals. The reinforcement layout of the new DBCBs is similar to that used for typical beams in reinforced concrete special moment frames. Results from this research show how the new detailing approach provides simplified construction while having equivalent seismic behavior as that provided by the diagonally reinforced coupling beams with span-to-depth ratios between 2.4 and 3.3.

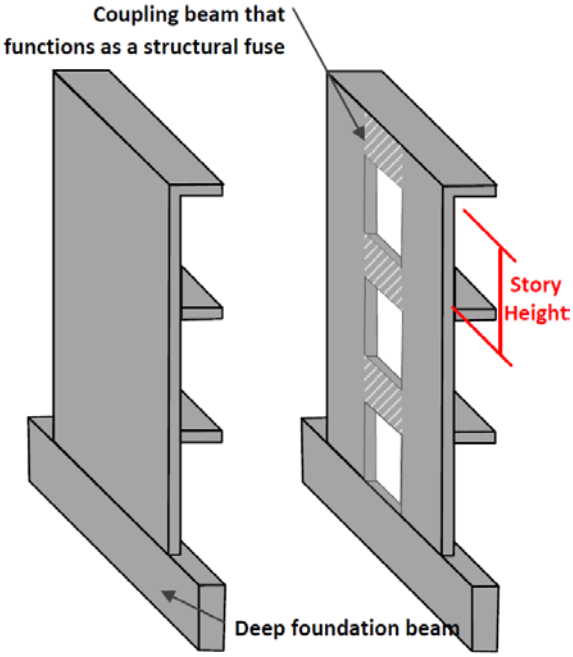

5.1 Configuration of coupled wall

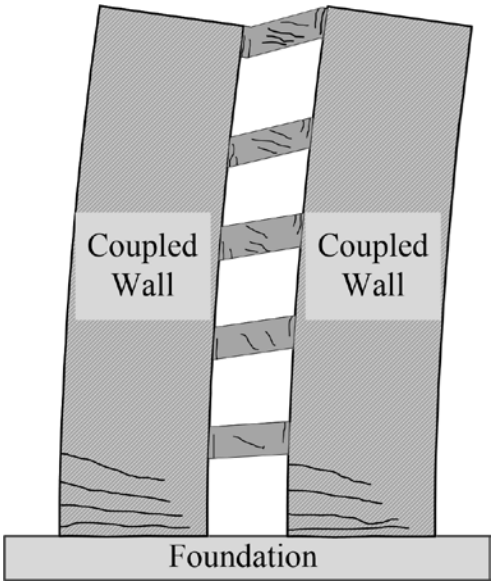

5.2 Coupled wall yield mechanism

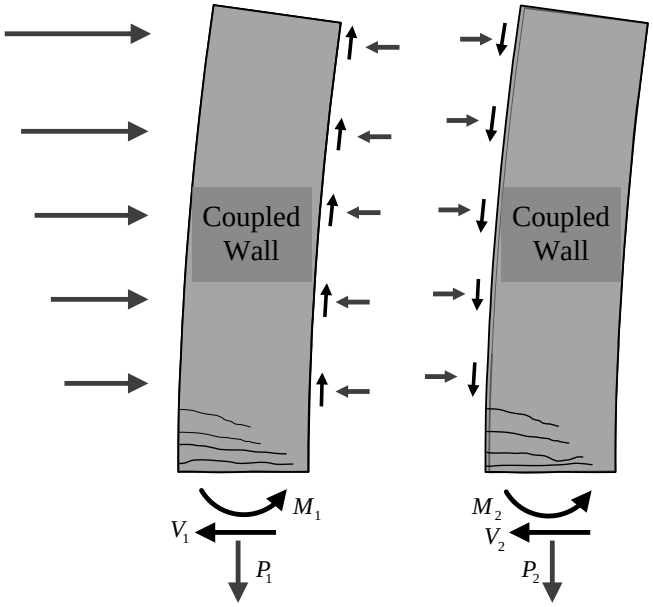

5.3 Internal forces in Coupled wall system

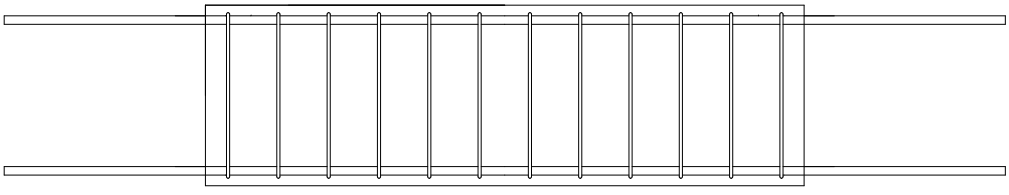

5.4 Conventionally reinforced coupling beam

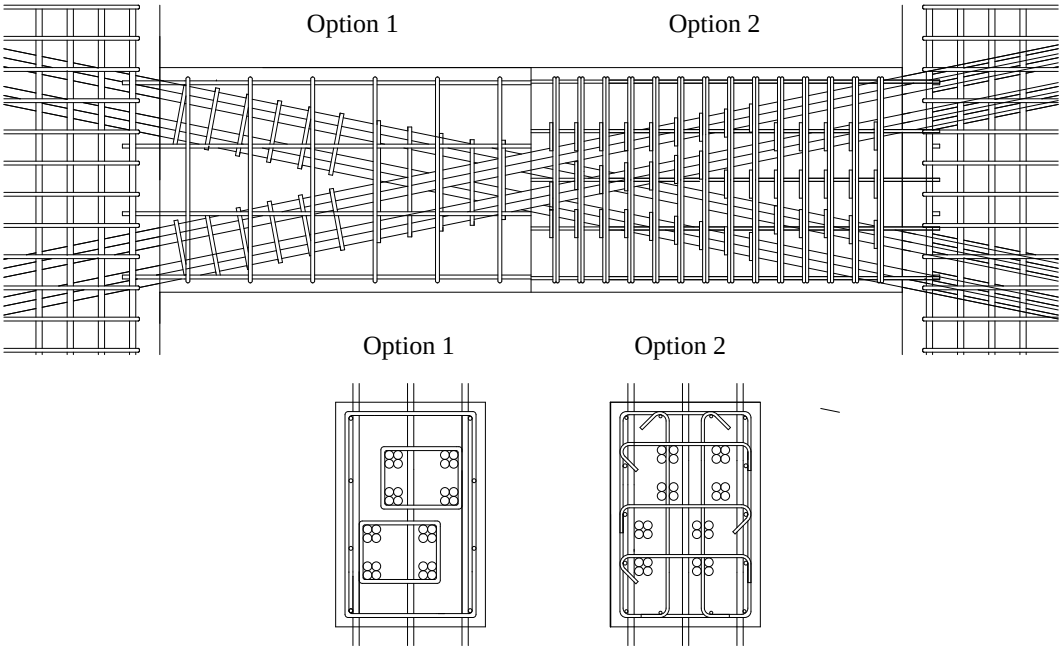

5.5 Diagonally reinforced coupling beam

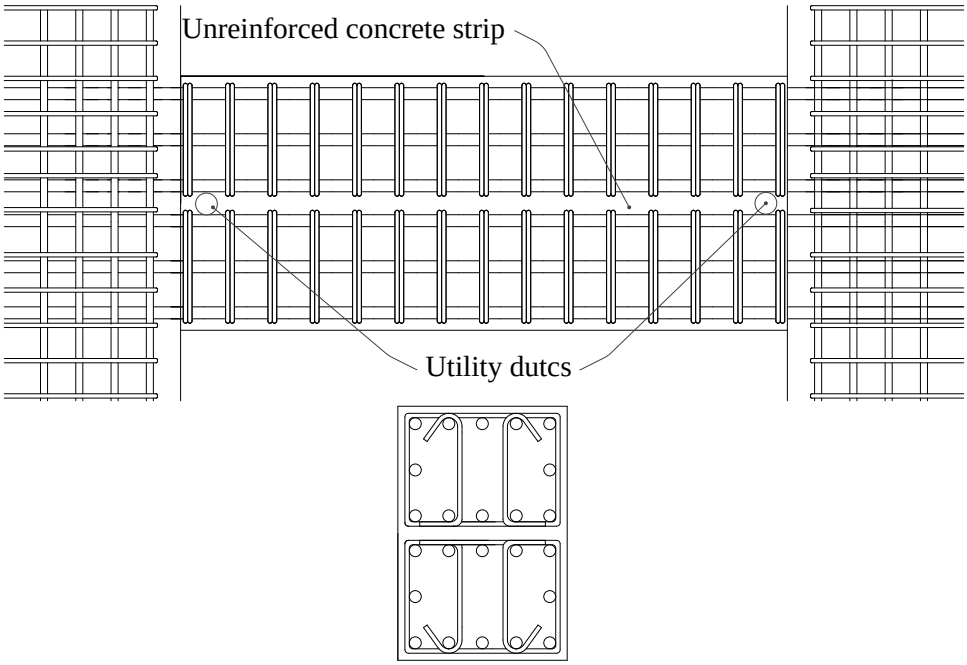

5.6 Double beam coupling beam

Chapter 6

EXPERIMENTAL PROGRAM

6.1 Reinforcement Details

Reinforcement details of the test DBCBs are illustrated in Figure 6.1 through 6.7. Each DBCB has two separate steel cages, and each consists of three layers of vertically distributed longitudinal reinforcing bars. Each steel cage is confined by closed transverse reinforcing bars. The advantages of using distributed longitudinal reinforcing bars are: 1) They delay the propagation of flexure-shear cracks from becoming the dominating cracks before the gap opens and separates the DBCB. The diagonal cracks resulting from cyclic shear forces can rapidly diminish the concrete's shear resistance (Park and Paulay, 1975); 2) vertically distributed longitudinal reinforcing bars form a pattern of multiple finer cracks, which helps in the development of a more uniform distribution of stresses along the transverse reinforcement (Paulay, 1969); 3) vertically distributed longitudinal reinforcing bars can prevent sliding shear failure near the beam-to-wall boundaries (Xiao et al., 1999); 4) a beam section with vertically distributed longitudinal reinforcing bars can add additional flexural strength and ductility(Wong et al., 1990). Therefore, the width of the coupling beam can be reduced and wider spacing between rebars can be used in the top of the beam for placing and controlling vibration of concrete during construction.

6.2 Specimen Design

Six half-scale and one full-scale DBCBs were fabricated and tested under reversed cyclic loads. The information of each DBCB is shown in Table 6.1. The name of each specimen was designated according to test variables. Primary test variables were span-to-depth ratios, displacement (loading) protocol, the size of the unreinforced concrete strip, and existence of construction pipes in the strip. For instance, Specimen R2.4-SC-2-PE represents a DBCB with a span-to-depth ratio of 2.4 (R2.4) and a one-inch unreinforced concrete strip (2), tested under symmetrical cyclic (SC) displacement protocol Specimen, utility pipes at the ends of the beam (PE). R3.3-SC-1 had a span-to-depth ratio of 3.3.

The ratios were selected to reflect modern architectural specifications, which typically require coupling beams with span-to-depth ratios of approximately 2.4 for residential buildings and 3.3 for office buildings. Ratios were also selected to compare the test results of DBCB specimens with previous research on DCBs with the same span-to-depth ratios (Naish et al., 2009). However, instead of using a beam width of 12 in. as in the DCB specimens (Naish et al., 2009), the width of DBCBs was reduced by fifty percent because this width is sufficient to accommodate the longitudinal reinforcement. Also, this smaller width is able to impose high shear stress on the DBCBs. The In addition, The ratio for R2.15-SC-1.5-PM was 2.15. This to accommodate the available holes in the strong floor, since it was full-scale. the development length of the longitudinal reinforcement is only about 50% (for No. 7 bars) to 60% (for No. 6 bars) of that required by ACI 318-14 Sect. 18.8.5.3(b), due to the fact that the beam-to-wall boundary did not suffer severe damage (discussed later). This is opposite to DCBs where the major damage is at the beam-to-wall boundary as a result of the slip and extension of the diagonal reinforcing bars (Naish et al., 2013).

Table 6-1 Specimen information

Specimen	l_n/h	l_n/d	Unreinforced concrete strip, in.	$V_{normalized}$ [1]	Transverse Reinforcement [2]		ρ_l,% [3] (main bar, intermediate bar)	f_{cm} [4] ksi
					$\rho_{plastic\ hinging}$,% (bar size, spacing)	$\rho_{non-plastic\ hinging}$, % (bar size, spacing)		
R2.4-SC-1	2.4	5.76	1	8.34	4.9 (#4, 1.5 in.)	2.9 (#4, 2.5 in.)	2.4 (#6, #6)	5.7
R2.4-NC-1	2.4	5.76	1	8.34	4.9 (#4, 1.5 in.)	2.9 (#4, 2.5 in.)	2.4 (#6, #6)	6.3
R3.3-SC-1	3.3	7.98	1	7.47	4.9 (#4, 1.5 in.)	1.8 (#4, 4.0 in.)	3.2 (#7, #7)	5.7
R2.4-SC-0.25	2.4	5.49	0.25	10.1	4.9 (#4, 1.5 in.)	2.9 (#4, 2.5 in.)	3.0 (#7, #6)	6.0
R2.4-SC-2-PE	2.4	6.33	2	9.43	3.7 (#3, 1.0 in.)	2.6 (#3, 1.4 in.)	3.5 (#7, #6)	4.0
R2.4-SC-2-W	2.4	6.33	2	8.6	1.7 (#3, 1.5 in.)	1.7 (#3, 1.5 in.)	2.4 (#7, #6)	4.4
R2.15-SC-1.5-PM	2.15	4.95	1.5	6.3	1.9 (#5, 3.0 in.)	1.5 (#5, 3.0 in.)	2.4 (#8, #6)	5.1

[1]: Normalized shear stress: $V_{normalized} = V_{design} / \sqrt{f_c'} h b_w$, where f_c' = 5 ksi (design compressive strength).

[2]: Transverse reinforcement ratio, ρ, is calculated by $A_v/(sb_w)$. Here, A_v is the total transverse reinforcement area within the transverse reinforcement spacing, s; b_w is the width of the beam. Note that the hoops for R2.4-C-1, R2.4-NC-1, and R2.4-SC-0.25 are overlapped by two C-shaped stirrups, so the area of one leg is two times the original area of the No. 3 stirrup.

[3]: ρ_l is the reinforcement ratio of either top or bottom longitudinal bars of each individual beam, $\rho_l = A_s/(b_w d)$. Intermediate bars are not included in the ratio.

[4]: f_{cm} is measured concrete compressive strength.

The sizes of the unreinforced concrete strip were selected based on preliminary sizes taken from a nonlinear finite element analysis conducted by VecTor2 (2002), which is explained later in this paper. The analysis shows that a wide unreinforced concrete strip could lead to a reduced moment arm for each cage; consequently, its moment capacity as well as the overall shear strength of the DBCBs is reduced. On the other hand, if the unreinforced concrete strip is too narrow, the beam might not completely separate into two beams before the major shear cracks dominate the behavior as in conventionally reinforced coupling beams (using only vertical and longitudinal reinforcement) and can lead to early strength degradation. The first three specimens have a 1 in. unreinforced concrete strip (clear distance between the ends of the transverse reinforcing bars) at the mid-height, next specimen have 0.25 in. to investigate the effect of a narrow width of the unreinforced concrete strip, next two specimens with 2 in. width to investigate the effect of a wide width, and finally last specimens with 1.5 in. width.

When a DBCB separates into two relatively slender beams, the individual beams will have a span-to-depth ratio which meets ACI code criteria for beams in special moment frames; i.e., the span of the beam shall be at least four times greater than that of the effective depth of the beam (ACI 318 Section 18.6.2.1). Therefore, each half of the DBCB specimens were designed according to ACI code except when enforcing the requirement for longitudinal reinforcement ratio which is limited up to 2.5% for beams of special moment frame. The top or bottom reinforcement ratio of each separated beam was slightly higher than 2.5% (Table 6.1). This was done to increase the shear stress of the specimens. As shown in Figure 6.1 through 6.7**,** reinforcement details of Specimens R2.4-SC-1 and R2.4-NC-1 were identical, and the only difference between these two

specimens was the applied loading protocols. For these two specimens, No. 6 bars were used for both the main and intermediate longitudinal reinforcement. In Specimen R3.3-SC-1, because this specimen had greater span length, No. 7 bars were used for longitudinal reinforcement to increase the shear stress as much as that in Specimens R2.4-SC-1 and R2.4-NC-1.

A pilot analytical study using VecTor2 indicated that if the unreinforced concrete strip is too narrow the beam might not completely separate into two beams. To verify the analysis result, Specimen R2.4-SC-0.25 was fabricated with a 0.25 in. unreinforced concrete strip. This specimen was also used to gauge the maximum shear stress and rotation a DBCB can carry when it is not separated. No. 7 bars and No. 6 bars were used as the beam's main and intermediate longitudinal reinforcement, respectively. Specimen R2.4-SC-2-PE used the same bars as used in R2.4-SC-0.25. However, the nominal shear strength of Specimen R2.4-SC-2-PE was lower than that of Specimen R2.4-SC-0.25. This is because of the decreased moment arm caused by using the two-inch unreinforced concrete strip. Specimen R2.4-SC-2-PE aimed at reaching a shear stress demand of about $9.5\sqrt{f'c}$ (psi), which is slightly lower than the ACI limit on the maximum nominal shear strength of DCBs. R.24-SC-2-W has a 2 in. wide unreinforced concrete strip. However, a shear stress demand was much lower than that of R2.4-SC-2-PE. This was done by widening the beam width. The full-scale specimens, R2.15-SC-1.5-PC have a 1.5 in. strip and consists of 8 No. 8 main bars with 2 No. 6 intermediate bars.

The required transverse reinforcement was calculated based on the maximum probable moment at beam ends. An overstrength factor of 1.25 was multiplied to the specified yield strength of steel reinforcing bars when calculating the probable moment of

all specimens. Note that following ACI 318's assumption with a maximum useable concrete strain of 0.003 would lead to a small compressive stress in the compression steel, which in turn leads to a smaller probable beam end moment and shear demand. It was observed in our preliminary testing that the maximum compression reinforcement strain reached 0.008 without concrete crushing. This is due to the fact that a large amount of confinement is provided by closely placed transverse and longitudinal reinforcement. Therefore, a maximum usable concrete strain of 0.008 was used for the calculation of the moment capacity of DBCBs, which leads to a higher maximum probable moment. It should be also noted that the restraint from the adjacent walls can provide non-negligible compression, which in turn increases the bending strength of the beam.

Then, the expected peak shear stress (design shear stress, $V_{design)}$ can be calculated from the sum of maximum probable beam end moments divided by the beam's span. The normalized peak shear stress of each specimen is calculated using the expected peak shear stress divided by square root of design concrete compressive strength (5 ksi [34.4 MPa]). These shear stress calculation results are listed in Table 6.1**.** However, the required transverse reinforcement of each specimen was controlled by ACI 318's confinement requirements rather than by shear demand. Except for Specimen R2.4-SC-2-PE and R2.4-SC-2-W, all specimens (except R2.15-SC-1.5-PM which used No. 5) used No. 3 transverse reinforcement at a spacing of 1.5 in. in the plastic hinging region which was assumed to have a length equal to the height of the DBCB. The first two hoops from the beam-to-wall interfaces were placed with a spacing of 1.0 in except the last two specimens. This was done to increase confinement to the concrete where the maximum moments occurred. The last two specimen had their first hoops at interfaces of beam-to-walls. Beyond the plastic hinging region, the spacing of transverse

reinforcement varied with specimens. A wider spacing in Specimen R3.3-SC-1 was used considering the less shear demand due to the slender aspect ratio. Except for Specimen R2.4-SC-2-PE, R.2.4-SC-2-W, and R2.15-SC-1.5-PC, the closed hoops were made of two overlapping U-shaped stirrups by welding. Therefore, clear spacing of the transverse reinforcement was less than using one single No. 3 hoop. For the other specimens, No. 3 or No. 5 hoops with a 135 degree hook were spaced. Design of transverse reinforcing bars for R2.4-SC-2.PE was controlled by shear strength. On the other hand, the design of R2.4-SC-2-W was done such that the amount of transverse reinforcing bars was much less than the other specimens. This was to gauge the minimum amount of the bars that DBCBs need for a satisfactory performance.

6.3 Specimen Construction

Each specimen consisted of a coupling beam, and a pair of big and small reinforced concrete blocks representing adjacent structural walls. Laying on one side on the strong floor, concrete was placed for all specimens. Formworks were made of plywood reinforced with 2 in. by 4 in. lumber. DBCB formwork was inserted in between the formworks for the blocks. Top and bottom cages of the DBCB were built separately and were easily slid into the cage of the blocks (Figure 6.8). This construction process was much easier than that for DCBs. Ready-mix concrete was used to cast all the specimens. The specified concrete compressive and steel yield strength was 5000 (34.5 MPa) and 60,000 psi (414 MPa), respectively. The measured average concrete compressive strengths, f_{cm}, obtained on the testing dates are listed in Table 6.1.

6.5 Test Setup

The specimens were cast horizontally, then rotated and placed in the test setup, with the big block fixed to the strong floor (Figure 6.9). Displacement reversals were applied via a vertical actuator, with the line of action of the actuator forces passing through the mid-span of the test specimen to produce an anti-symmetrical moment pattern in the coupling beam and zero moment at the beam's mid-span. The actuator was connected to the small block through a wide flange steel section. The load was transferred to the small block by means of direct bearing and unbonded threaded bars passing through the small block. Two steel links were used to provide some moderate axial restraints for the beams because, in reality, the adjacent structural walls and surrounding slab would provide non-negligible resistance to beam expansion upon cracking (Lequesne, 2011; Teshigawara et al., 1998).

Each steel link consisted of two channel sections and was pin-connected to a T-stub. The T-stub was tightened to each block by four high-strength threaded rods. To determine the shear force carried by the links, one of the coupling beam specimens was cut in the middle after testing and the loading block was displaced 4-in. (102 mm) upward. It was found that the maximum shear force carried by the links was 44 pounds (195 N), which is negligible as compared with the peak strength of the coupling beams. The coupling beam specimens were subjected to cyclic loading in a displacement control mode, which produced predefined reversed cyclic displacement patterns. Two loading protocols were used, starting from a coupling beam chord rotation of 0.25% and reaching a maximum rotation of 12%. The first loading protocol consisted of symmetric cyclic (SC) loading utilizing 2–3 cycles per deformation level (Figure 6.10, a). However, this type of

loading is not representative of near-collapse (NC) earthquake response, which would be unsymmetrical and would contain fewer cycles of loading; hence, the loading protocol should contain displacements which are representative of the ratcheting effect that leads to structural collapse (Figure 6.10, b). Such a protocol was developed based on preliminary nonlinear analyses. Linear variable differential transformers (LVDTs) were placed at the boundary of the DBCB and the small block to measure beam chord rotations and at the outer face of the big block to gauge its rotation and movement. Strains of transverse and longitudinal reinforcement were measured by strain gauges attached to the reinforcement.

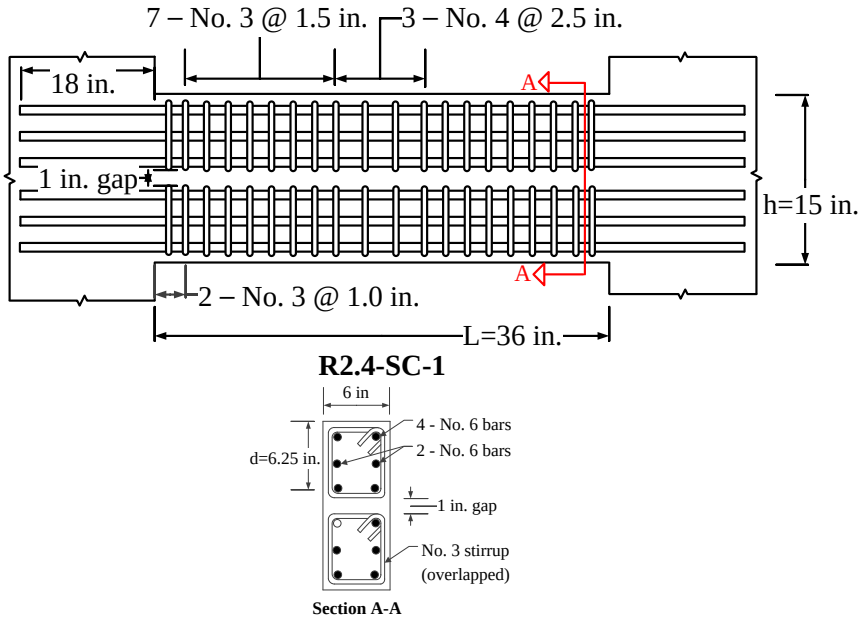

Figure 6.1 Reinforcement details of R2.4-SC-1

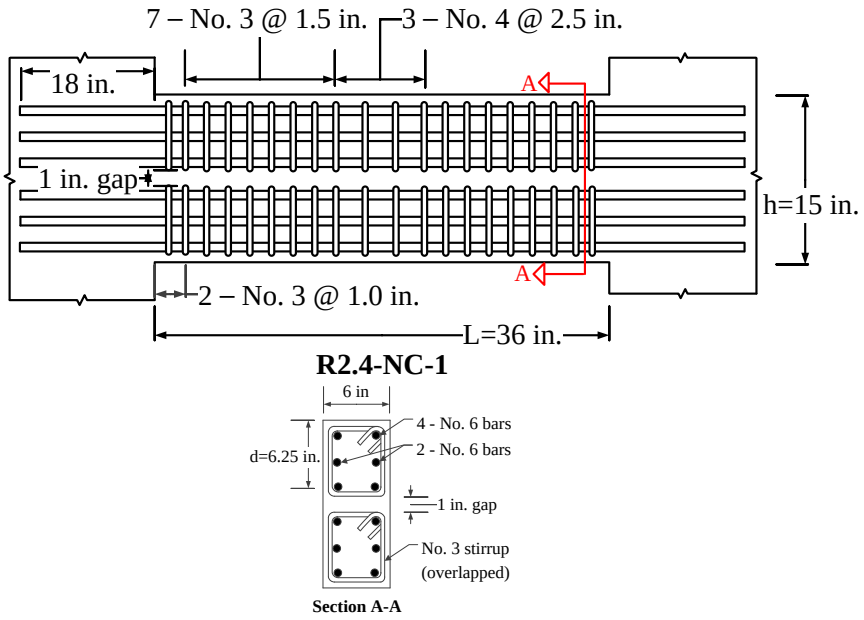

Figure 6.2 Reinforcement details of R2.4-NC-1

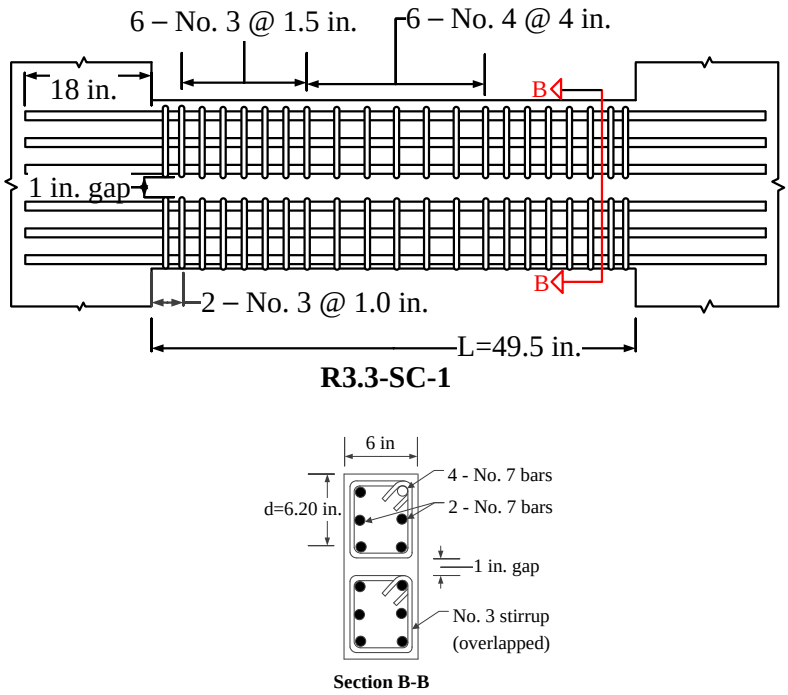

Figure 6.3 Reinforcement details of R3.3-SC-1

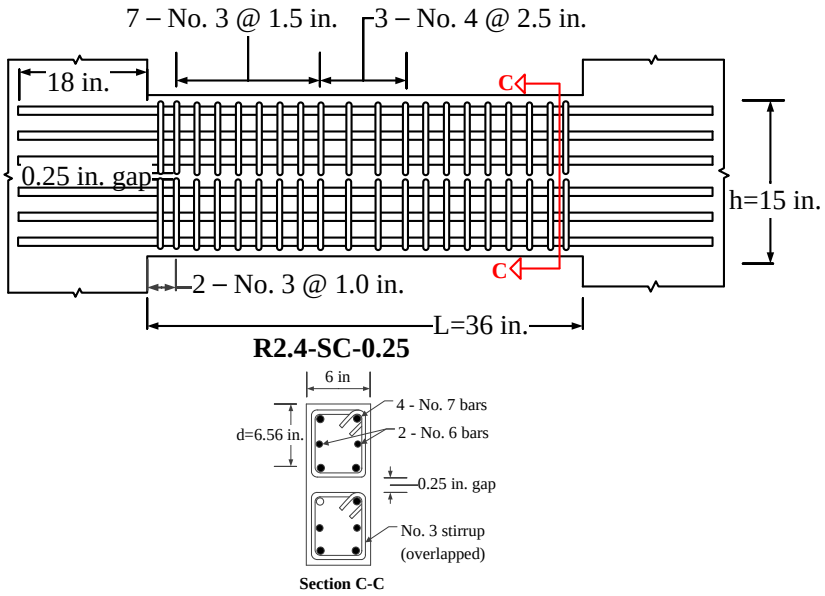

Figure 6.4 Reinforcement details of R2.4-SC-0.25

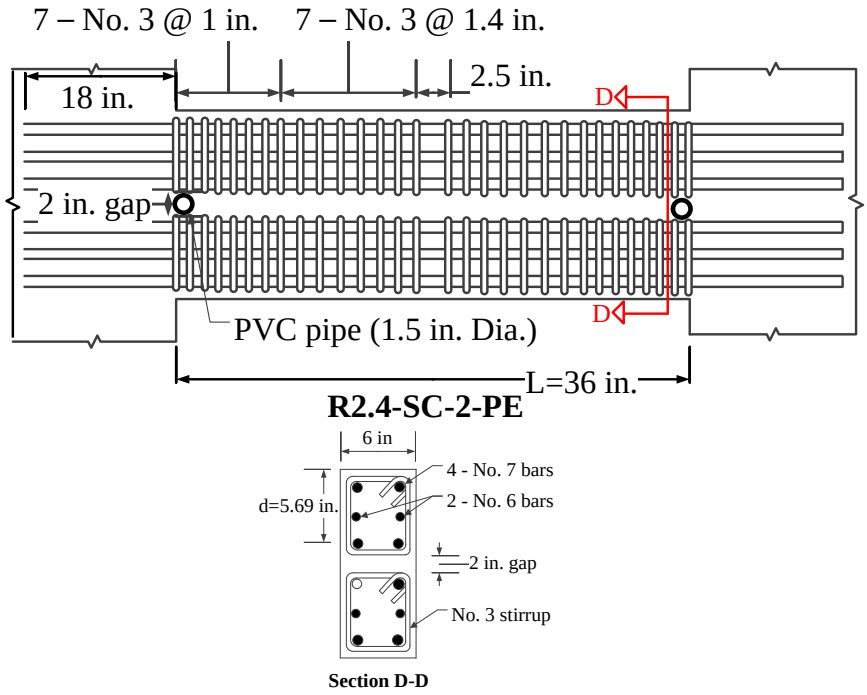

Figure 6.5 Reinforcement details of R2.4-SC-2-PE

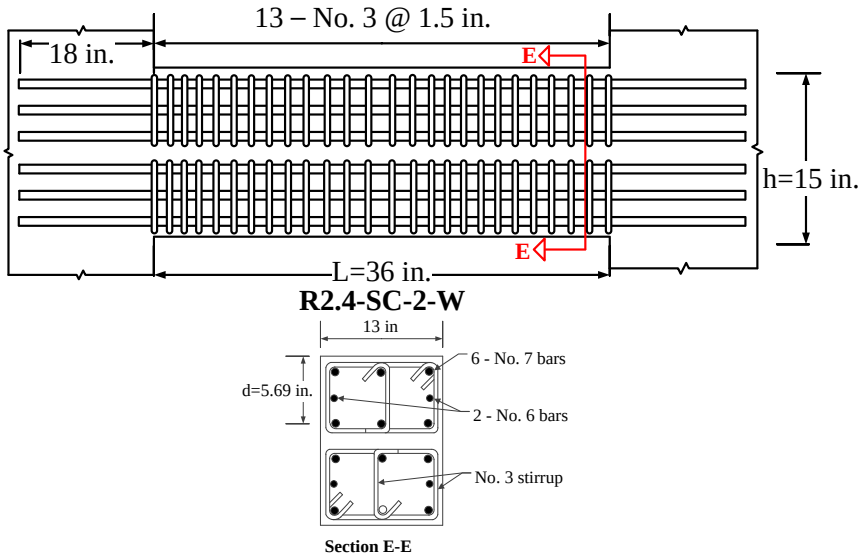

Figure 6.6 Reinforcement details of R2.4-SC-2-W

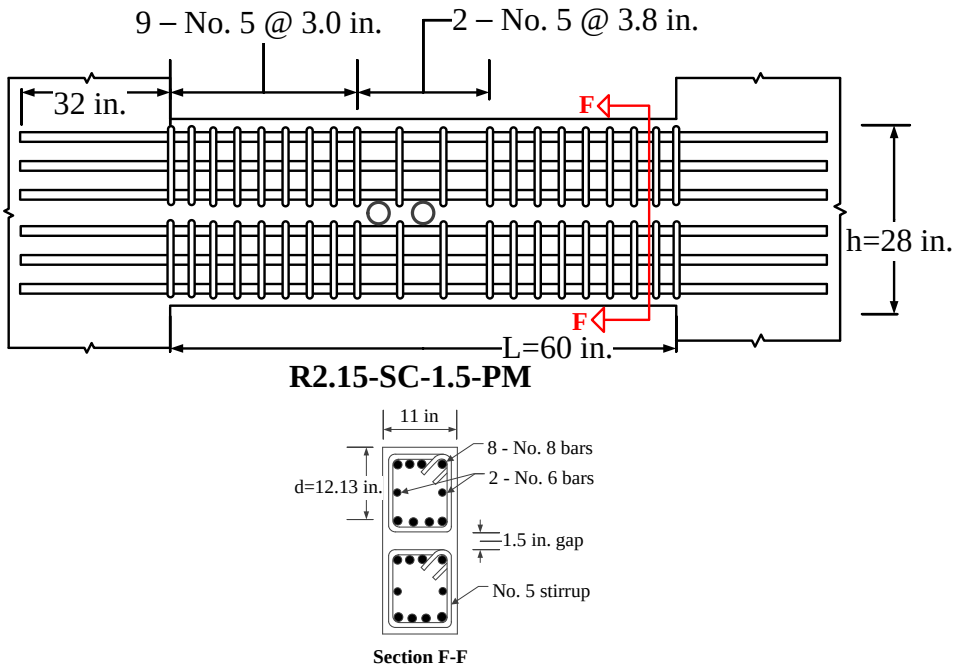

Figure 6.7 Reinforcement details of R2.15-SC-1.5-PM

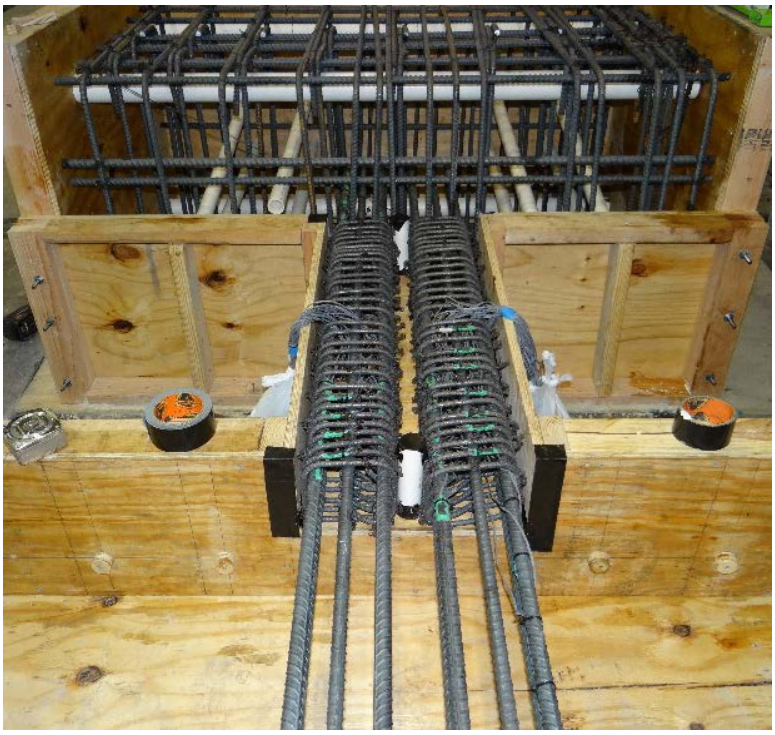

Figure 6.8 Construction photo of DBCB

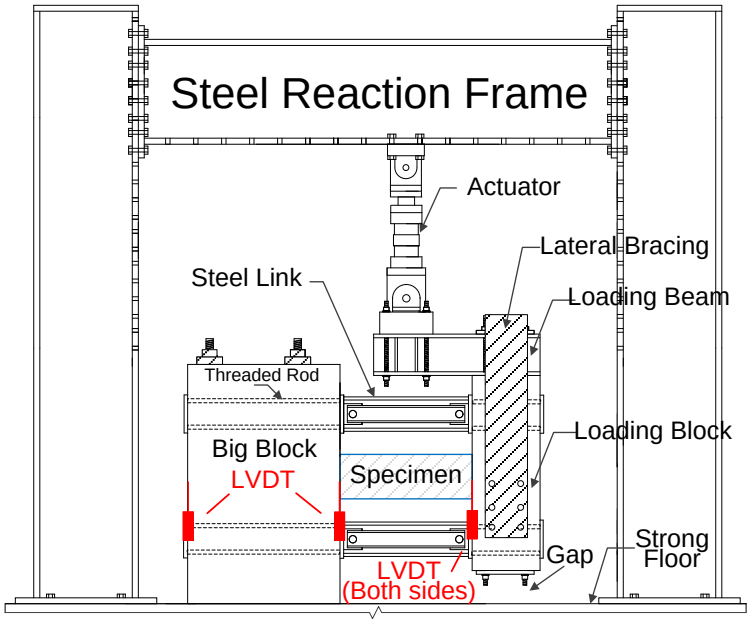

Figure 6.9 Test setup of DBCB

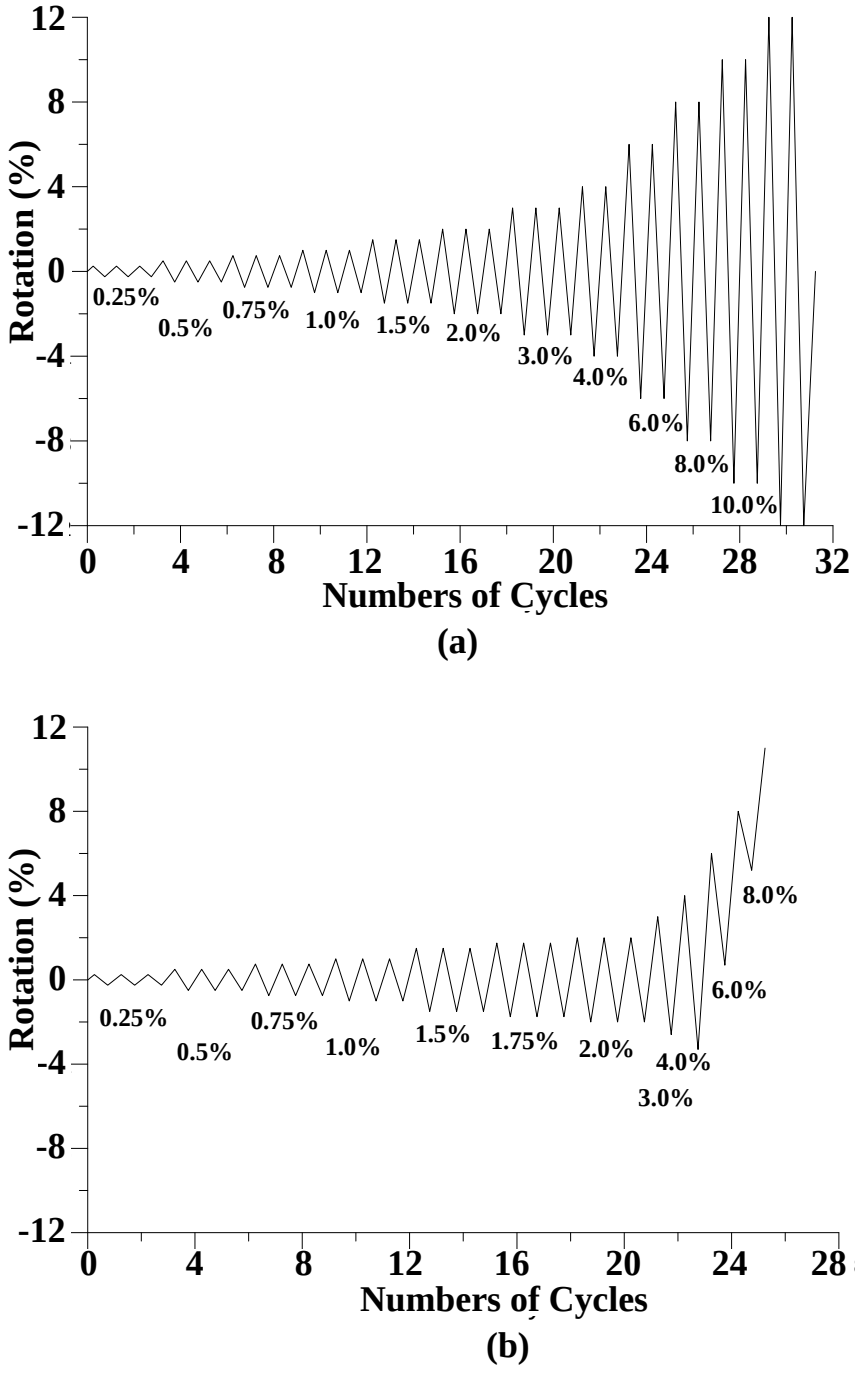

Figure 6.10 Loading protocols: (a) Symmetrical loading protocol and (b) near collapse loading protocol.

Chapter 7

EXPERIMENTAL RESULTS

7.1 Cracking and Damage Pattern

Table 7.1 summarizes experimental test results for all specimens. The progressive cracking patterns and the failure mechanisms for all specimens are shown in Figure 7.1 through 7.14. The specimens with a 1 in. and 2 in. unreinforced concrete strip separated into two beams which had nearly twice their original span-to-depth ratio. The cracking and the damage patterns of the specimens were very similar to one another.

For specimens with a 1 in. unreinforced concrete strip, during the first positive cycle loading, diagonal tension cracks (shear cracks) were observed at the mid-span and the mid-height of the specimens where the one-inch unreinforced concrete strip was located. As the load reversed, the same crack pattern appeared at the same location, producing diagonal grids of cracks crossing each other. No flexural cracks were observed at this time. As the load increased, those cracks spread toward both ends of the specimens. As cyclic loads continued increasing, concrete at the unreinforced concrete strip was crushed due to the abrasion resulting from the sliding of the top and bottom beams. This crushing initiated from mid-span, progressing toward the beam ends because the blocks provided the DBCBs with a confinement effect near the boundaries. The relative displacement of the top and bottom beams due to the horizontal sliding is clearly seen by a marked grid on the specimens.

At 1.5% chord rotation, diagonal cracks widened. Canbolat et al. (2005) reported that diagonal cracks were first observed during the cycles at 0.25% rotation for their DCB specimen, and the diagonal cracks widened up to 3 mm (0.12 in.) at 1.5% rotation. This indicated that the occurrence of initial cracks in DBCBs and their widths are similar to that of conventional DCBs.

Table 7-1 Test results

Specimen	θ_{yield} [1] %	$V_{\max}$ kip	$V_{\max}/V_{design}$	$\theta_{\max}$ %	$V_{normalized}$ [2]
R2.4-SC-1	2	68.5	1.29	8	10.1
R2.4-NC-1	2	89	1.68	11	12.5
R3.3-SC-1	2	68	1.43	8	10.0
R2.4-SC-0.25	4	68	0.97	2	9.75
R2.4-SC-2-P	2	63.5	1.06	6	11.16
R2.4-SC-2-W	1.5	111	1.28	6	8.58
R2.15-SC-PM	-	162	0.87	1.5	7.36

[1] θ_{yield} : Beam chord rotation when longitudinal bar yields.

[2] Normalized shear stress, $V_{normalized}$, is $V_{\max}/(\sqrt{f_{cm}}b_w h)$. Here, f_{cm} = measured compressive strength.

At 2% rotation, the end of the separation is about a few in. away from the beam-to-wall boundaries Except for R2.4-SC-2-PE, since this specimens had utility pipes at ends and it helped the separation (this will be explained later). Diagonal cracks at the end of the separation spread toward the boundaries in a fan-shape pattern. Concrete crushing at all corners of the specimens was initiated at approximately 2%–3% rotations. At this time, measured strain in longitudinal reinforcement at the corners showed yielding

in compression. Beyond 4% rotation, the concrete crushing at the corners caused all the cover concrete in the plastic region to come off. Beyond 6%–8% rotations, the core concrete crumbled due to the combined normal and shear stresses, leading to significant degradation in the shear resistance. This was the primary reason for the strength drop of the specimens with a 1 in. and 2 in. unreinforced concrete strip. For Specimen R2.4-NC-1, which was subjected to near-collapse protocol, the damage was not as severe as the damage observed in Specimen R2.4-SC-1. It has to be mentioned that all the specimens maintained their integrity at the beam-to-wall interfaces up to the end of the tests, which effectively eliminated the sliding shear failure.

The cracking pattern of Specimen R2.4-SC-0.25 (with smaller height of the unreinforced concrete strip) and R.215-SC-1.5-PC was similar to the other specimens in the early stage of loading. However, the concrete crushing in the unreinforced concrete strip progressed in a slower manner. Before the separation occurred, a considerable amount of flexural-shear cracks had propagated across the entire depth of the beam, leading to a drastically different shear stress distribution from that shown in Figure 7.8 and 7.14. In addition, horizontal cracks along the outermost longitudinal reinforcing bars developed after considerable shear cracks occurred. This is believed to be due to dowel failure as a large number of shear cracks developed causing loss of the aggregate interlock after the width of the cracks widened. Only the middle one-half of the unreinforced concrete strip separated which made the portions above and below the strip to behave like beams with very short span-to-depth ratio. This aggravated the shear dominated damage in the separated region. Cover concrete came off in this region and the specimen eventually failed by shear dominated behavior.

As shown in Figure 7.9 and 7.10, Specimen R2.4-SC-2-PE has a more complete separation toward the beam ends which was believed to be attributed to the presence of the utility pipes as well as the larger size unreinforced concrete strip. However, R2.4-SC-2-PE and R2.4-SC-2-W had more shear cracks because Specimen R2.4-SC-2-P had higher shear stress demand and Specimen R2.4-SC-2-W had much less the transverse reinforcement ratio than the other specimens. These results indicate that the separation of the unreinforced concrete strip is affected by the span-to-depth ratio, the size of the strip, and the transverse reinforcement rati.o Besides, placing the utility pipes at the ends of DBCBs seems to help the separation.

While a seismic resistant coupling beam is expected to experience severe damage at Life Safety and Collapse Prevention performance levels, it is expected to retain most of its pre-earthquake design strength with light damage (ACI 374, 2013; ASCE/SEI 41, 2014) at the Immediate Occupancy Performance Level. For the Immediate Occupancy Performance Level, the maximum accepted beam chord rotation for coupling beams is from 0.4 to 1% according to ACI 374 (2013). Figure 7.1 shows that at 1% rotation DBCBs only had cosmetic concrete cracking and the peak strengths had not been reached. Furthermore, the beam-to-wall interfaces were undamaged. Therefore, DBCBs can be easily repaired by patching with new concrete to regain the elastic stiffness after moderate earthquakes.

7.2 Shear versus Rotation Responses

Shear force (and stress) versus beam chord rotation responses for all specimens are illustrated in Figure 7.15 through 7.21. For comparison purposes, ACI 318's upper bound shear stress $V_u = \phi 10\sqrt{f'c}A_{cw}$ is also plotted as dashed lines in the figures. The beam chord rotation was obtained by using the net vertical displacements (measured between the two beam-to-wall interfaces and excluding the fixed-end rotation or displacement, if any) divided by the beam span.

It is seen in Figure 7.15 that Specimen R2.4-SC-1 was able to maintain a very high shear stress ($10.1\sqrt{f_{cm}}$; f_{cm} is the measured concrete compressive strength, or $10.8\sqrt{f'c}$; f'c is the design concrete compressive strength = 5 ksi) without significant strength degradation up to a rotation of 6% (approximate demand for MCE level ground motions). Also, it could still resist 80% of the peak stress at 8% rotation. In addition, Specimen R2.4-NC-1 showed no strength degradation up to 11% rotation while shear stress increased ($12.5\sqrt{f_{cm}}$ or $14\sqrt{f'c}$) when subjected to the near-collapse loading protocol as shown in Figure 7.12. Furthermore, the shear strength in Specimen R3.3-SC-1 did not drop until 8% rotation, maintaining shear stress of $10\sqrt{f_{cm}}$ (or $10.7\sqrt{f'c}$) (Figure 7.13). The shear stress of Specimen R2.4-SC-0.25 reached $9.75\sqrt{f_{cm}}$ (or $10.7\sqrt{f'c}$). However, it experienced significant shear strength degradation after 2% rotation due to the shear dominated behavior as discussed previously. Specimen R2.4-SC-2-P retained very high shear stress ($11.16\sqrt{f_{cm}}$ or $10\sqrt{f'c}$) up to 6% rotation without significant strength drop. However, after 6% rotation, its shear strength dropped rapidly. Specimen R2.4-SC-2-PE barely reached the factored ACI shear stress limit, maintaining ductility up to 6% rotation without significant strength loss. The maximum shear stress was $8.6\sqrt{f_{cm}}$ or $8.1\sqrt{f'c}$. The highest shear stress measured during the test of R2.15-SC-1.5-PM was $7.4\sqrt{f_{cm}}$ or $7.4\sqrt{f'c}$. This specimen failed at 2.5% beam chord rotation due to, shear since it did not separated.

7.3 Strain in Steel Reinforcement

The yielding in the top and bottom layers of the longitudinal reinforcing bars (rebars) of the two steel cages at the beam-to-wall interface indicates the separation of DBCBs and a mechanical behavior shifting from shear to flexure. For Specimens R2.4-RC-1, R2.4-NC-1, R2.4-SC-2-P, and R2.4-SC-2-PE, the complete yielding of longitudinal rebars commenced at 2% rotation, while it was 3% in Specimen R3.3-SC-1. For Specimen R2.4-SC-0.25, no yield in the longitudinal rebars was measured at the beam-to-wall interface at the rotation. In addition, strains in the top and bottom longitudinal rebars of each individual cage at the beam-to-wall interface showed opposite signs, indicating no residual tensile strains affecting the behavior of DBCBs. This is because the rebars in DBCBs do not experience large inelastic deformation even at large displacement. On the other hand, due to the residual tensile strains after the rebars experience large inelastic deformation, both the top and bottom rebars in conventionally reinforced coupling beams are usually subject to tension at large displacement. This does not allow the interface crack to be entirely closed when subject to compression, thereby causing degradation of shear-transfer mechanism and sliding shear failure. The strain gauges at the interfaces for R2.15-SC-2-PC did not work. However, the strain gauges near the interfaces did no show yield strain during the test.

Yielding in the longitudinal reinforcement spread up to about 7.5 in. (which is 50% of the height of DBCBs) away from the beam-to-wall interface for Specimens R2.4-SC-1, R-2.4-NC-1, and R2.4-SC-2-PE, about 9 in. for Specimen R2.4-SC-2-W, and about 15 in. for Specimen R3.3-SC-1. This indicates that the plastic hinging region of DBCBs may depend on the span-to-depth ratio. No yielding in transverse reinforcement was

recorded for Specimen R2.4-SC (NC)-1. However, only one hoop in the plastic hinge region of Specimens R3.3-SC-1 and R2.4-SC-2-PE experienced yielding at 4% and 6% rotation, respectively. A few more hoops yielded in R2.4-SC-W. This is because the transverse reinforcement ratio was much lower than the other specimens. In addition, all intermediate longitudinal reinforcement experienced yielding, thereby contributing toward the strength of the DBCBs.

7.4 Stiffness

Figure 7.22 illustrates the normalized shear stress versus beam chord rotation response for DBCBs with the symmetrical cycling load and DCBs tested in prior research (Naish, 2009). The normalized shear stress is the stress divided by the maximum shear stress of each specimen. These figures indicate that DBCBs have equivalent elastic stiffness and act like a conventional coupling beam before inelastic behavior occurs. In other words, DBCB's elastic stiffness is not affected by its unique separation mechanism. In any case, a beam's elastic stiffness can be easily adjusted by optimizing its dimensions.

7.5 Comparison Between DBCB and DCB

The performance of DBCBs was compared with that of DCBs tested by Naish et al. (2009). Both DCB and DBCB specimens were about one-half scale replicas of the coupling beams in typical residential and office buildings. The only major difference was that DBCBs were half the width of DCBs. The design of the DCBs followed current ACI

provisions (ACI 318, 2014). Their DCBs can be divided into two groups: one group had transverse reinforcement around diagonal bar groups (CB24D or CB33D), and the other group had transverse reinforcement around the entire cross section (CB24F or CB33F). Since the performance of the latter group, in terms of strength and ductility, was slightly better (Naish et al., 2009), the performance of DBCBs is compared to CB24F and CB33F in Figure 7.23a and 23b.

The shear stress, normalized by the square root of measured concrete compressive strength, f_{cm}, was used for comparison because the specimens have different concrete compressive strengths and cross-sectional areas. Two beam chord rotations, 3% and 6%, are highlighted in the figures because they represent approximately the upper bound rotational demands of coupling beams for the DBE (Life Safety) and MCE (Collapse Prevention) level ground motions (Harries et al., 2006). The specimens with the span-to-depth ratio of 2.4 for both the DCBs and DBCBs exceeded a shear stress level of $10\sqrt{f_{cm}}$ (psi), which is the unfactored shear strength limited by the ACI provision. Although the strength in DBCB R2.4-SC-1 slightly decreased after 3% beam rotation, the overall ductility and strength of DBCB R2.4-SC-1 were similar to that of the DCB specimen (CB24F) up to a beam rotation of 6% (MCE). For the specimens with a span-to-depth ratio of 3.3, CB3.3F has a shear strength of $6.6\sqrt{f_{cm}}$ (psi) and its shear strength degradation begins after 3% beam rotation. On the other hand, DBCB R3.3-SC-1 was able to sustain much higher shear stress ($10\sqrt{f_{cm}}$, psi)) with no strength degradation up to 8% beam rotation. This shows that DBCBs are able to provide higher safety by maintaining a stable global response of the structure without loss of coupling between walls due to the high plastic rotational capacity (Harries et al., 2006).

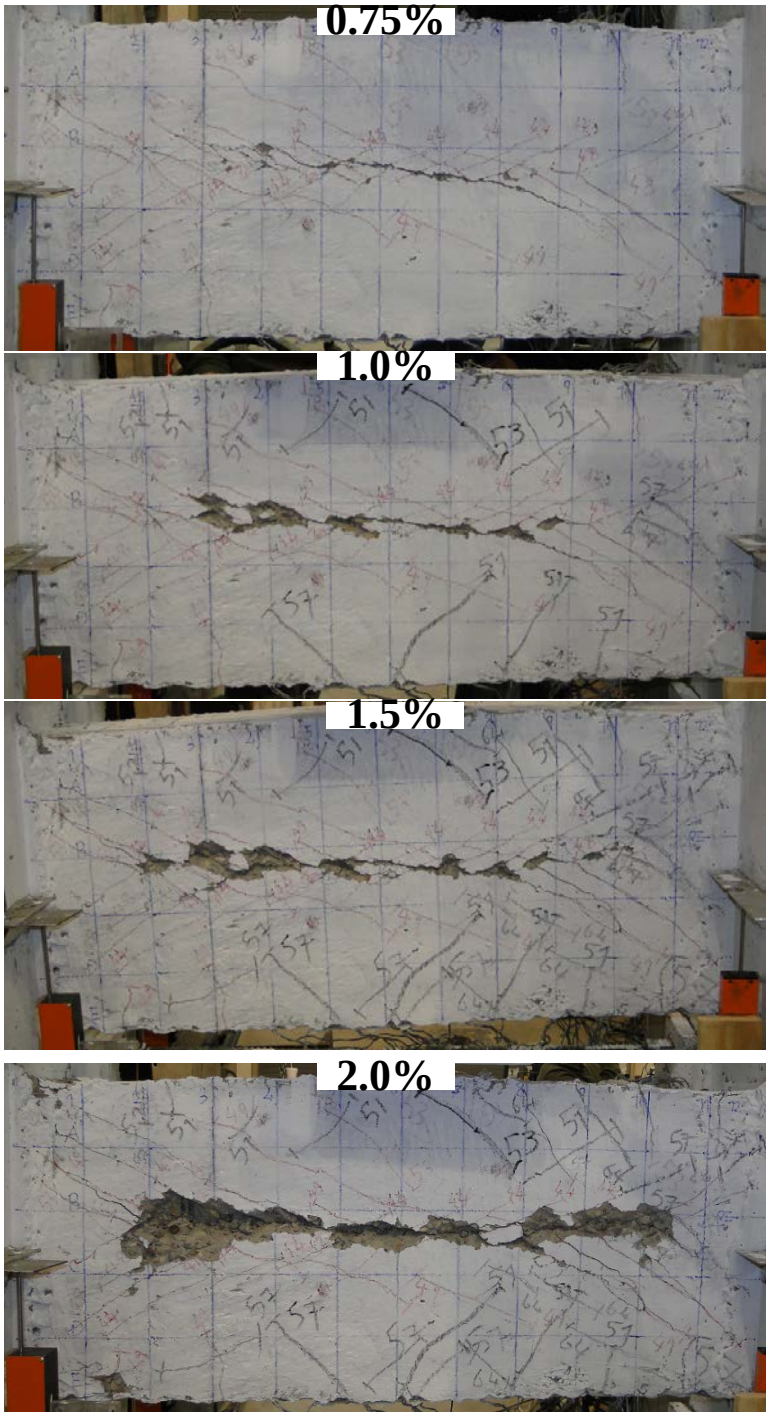

7.1 Cracks and damage patterns of RC-2.4-SC-1 (1)

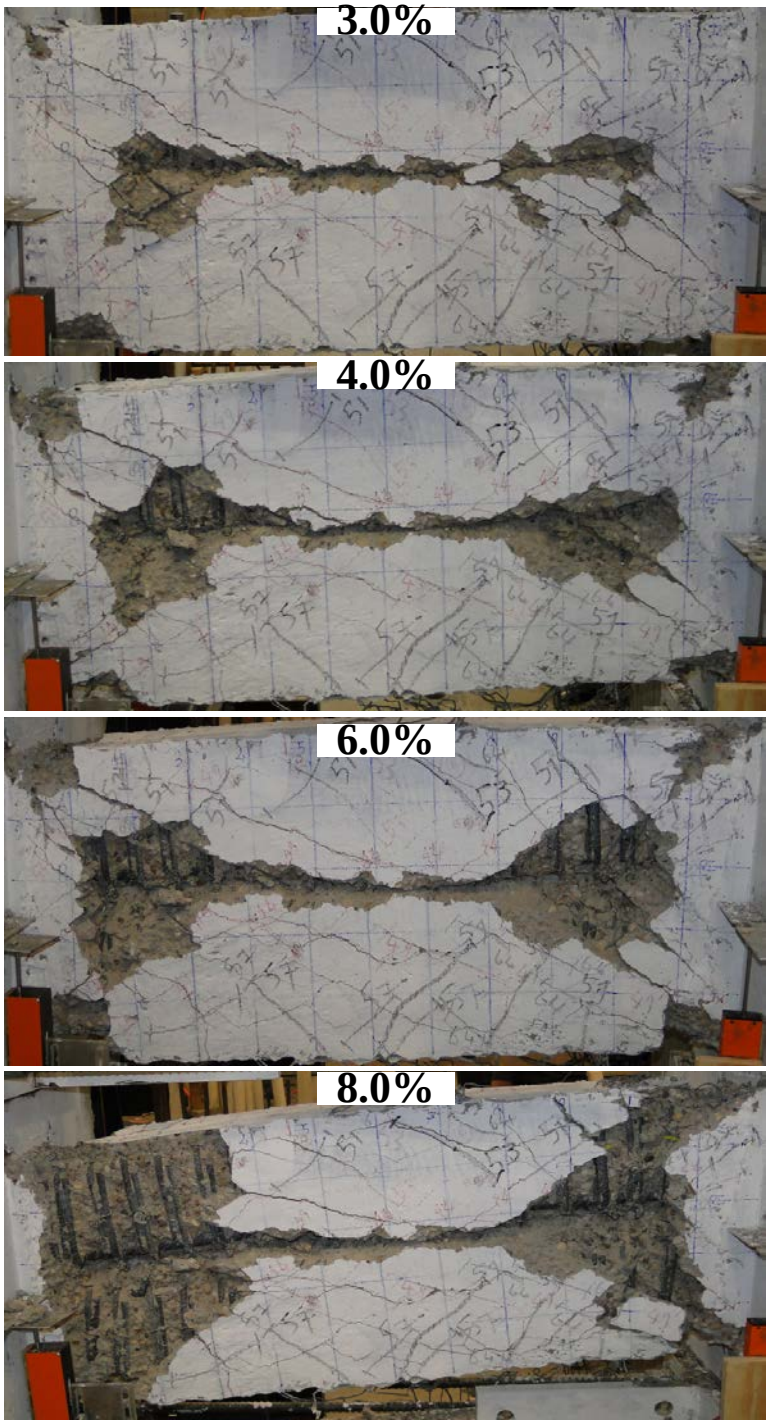

7.2 Cracks and damage patterns of RC-2.4-SC-1 (2)

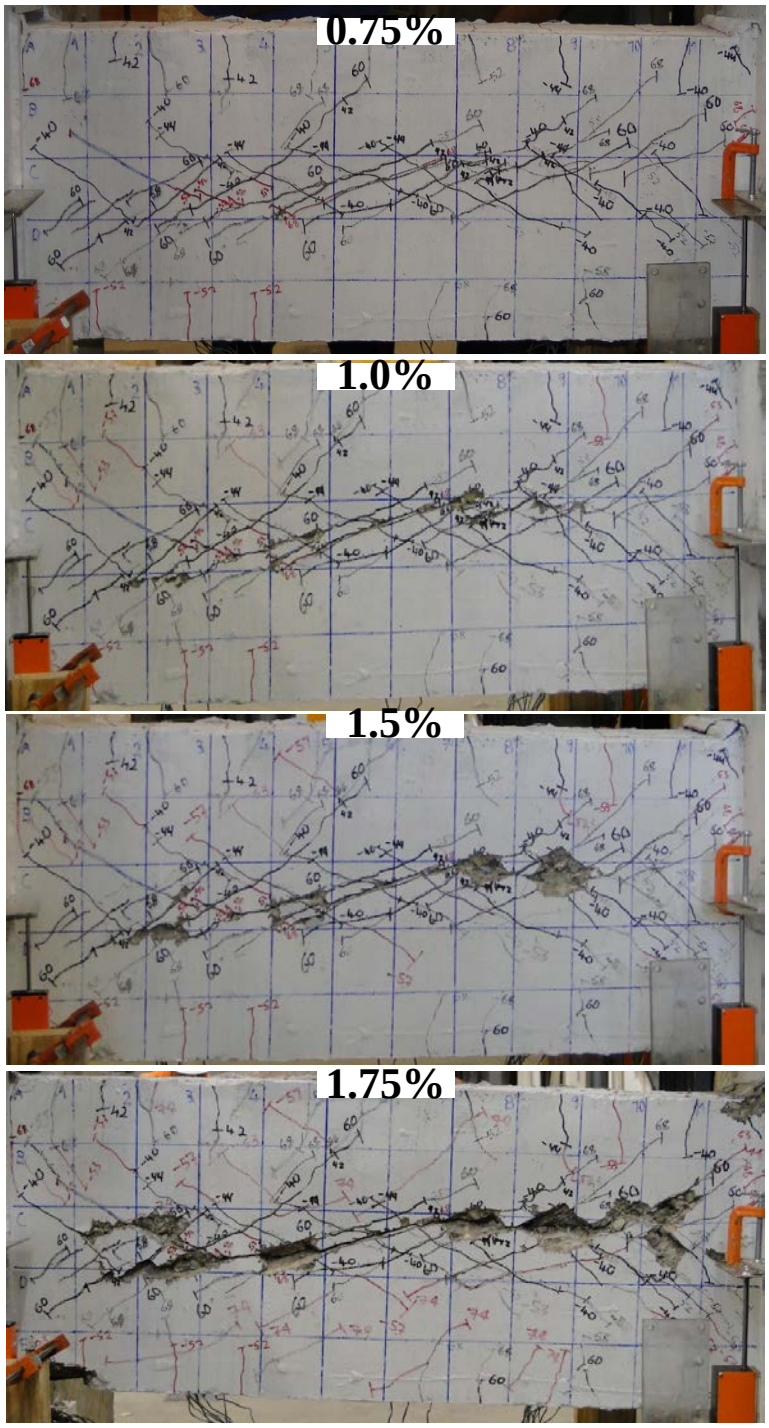

7.3 Cracks and damage patterns of RC-2.4-NC-1 (1)

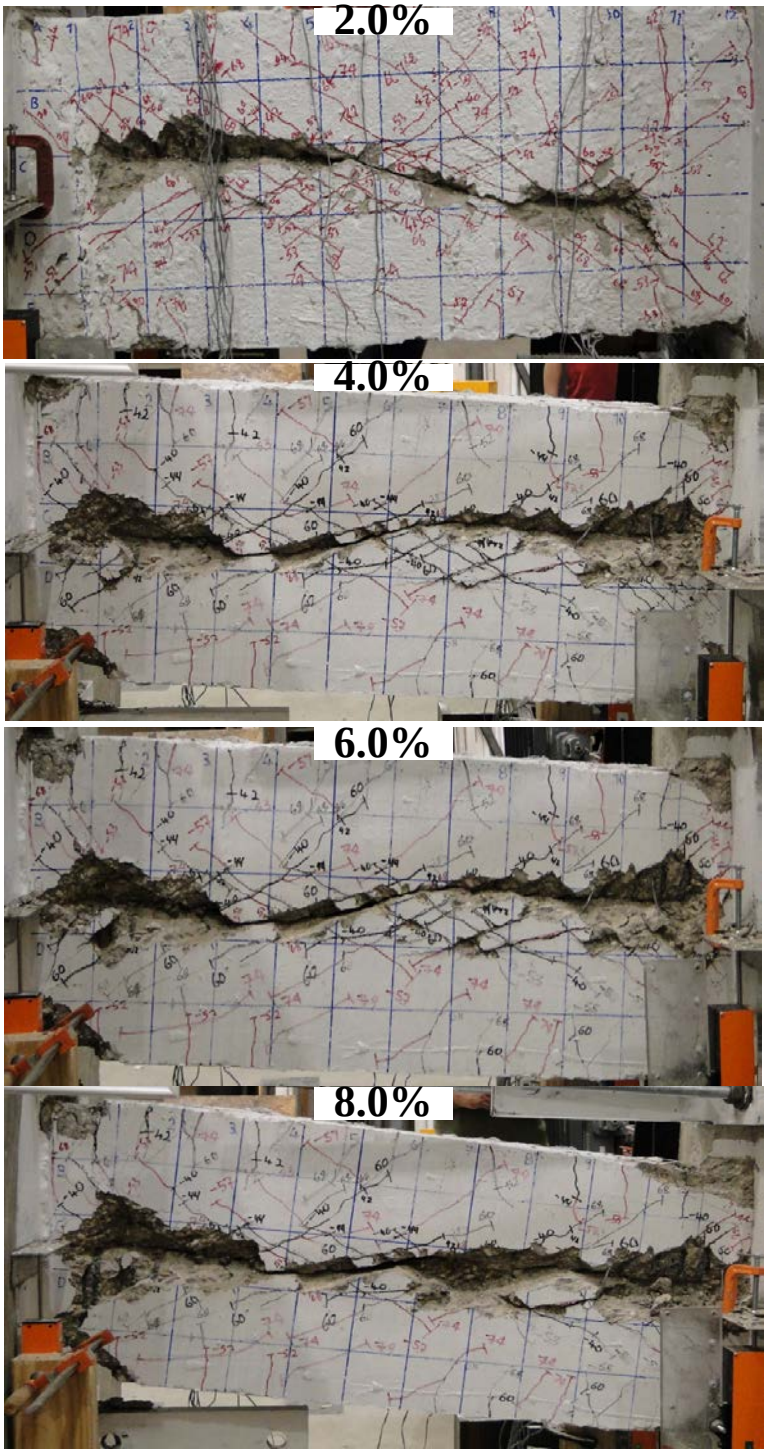

7.4 Cracks and damage patterns of RC-2.4-NC-1 (2)

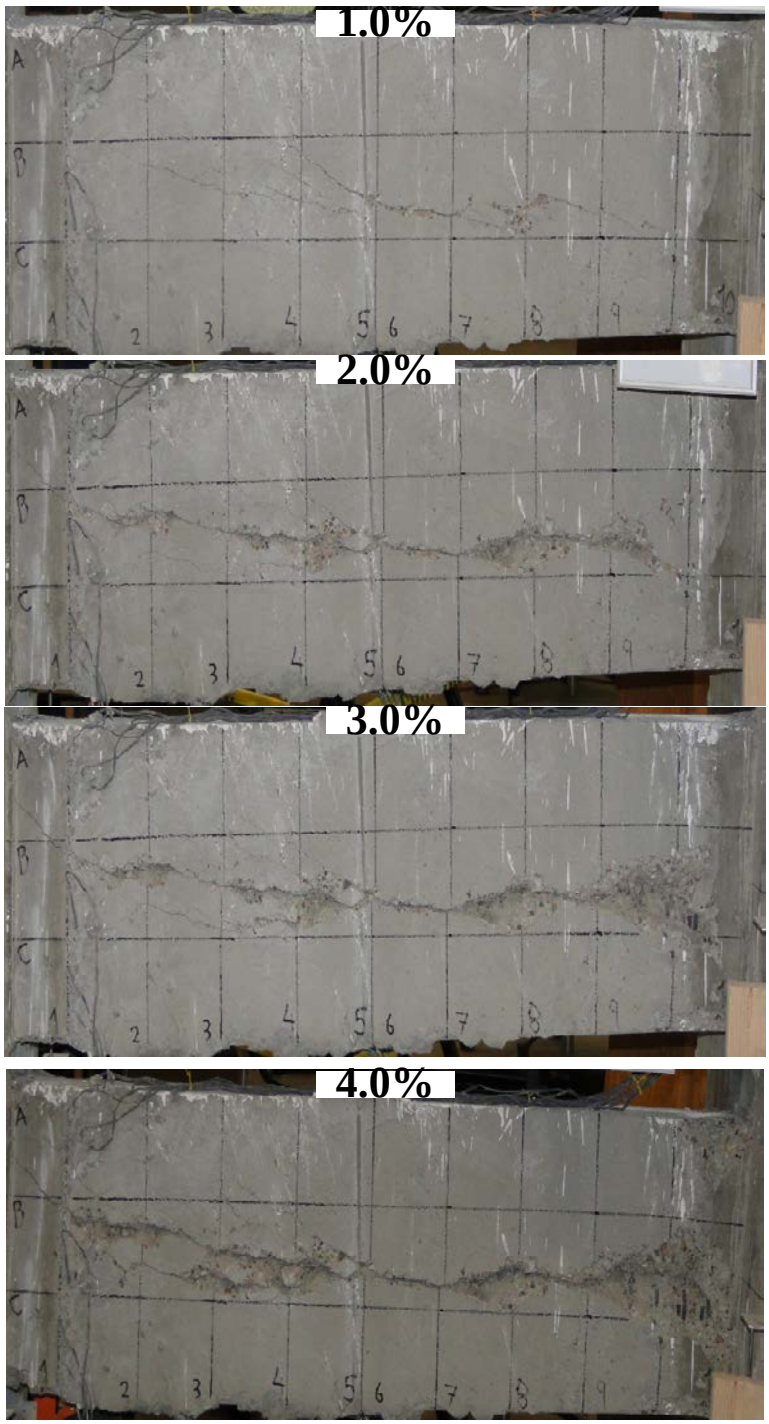

7.5 Cracks and damage patterns of RC-3.3-SC-1 (1)

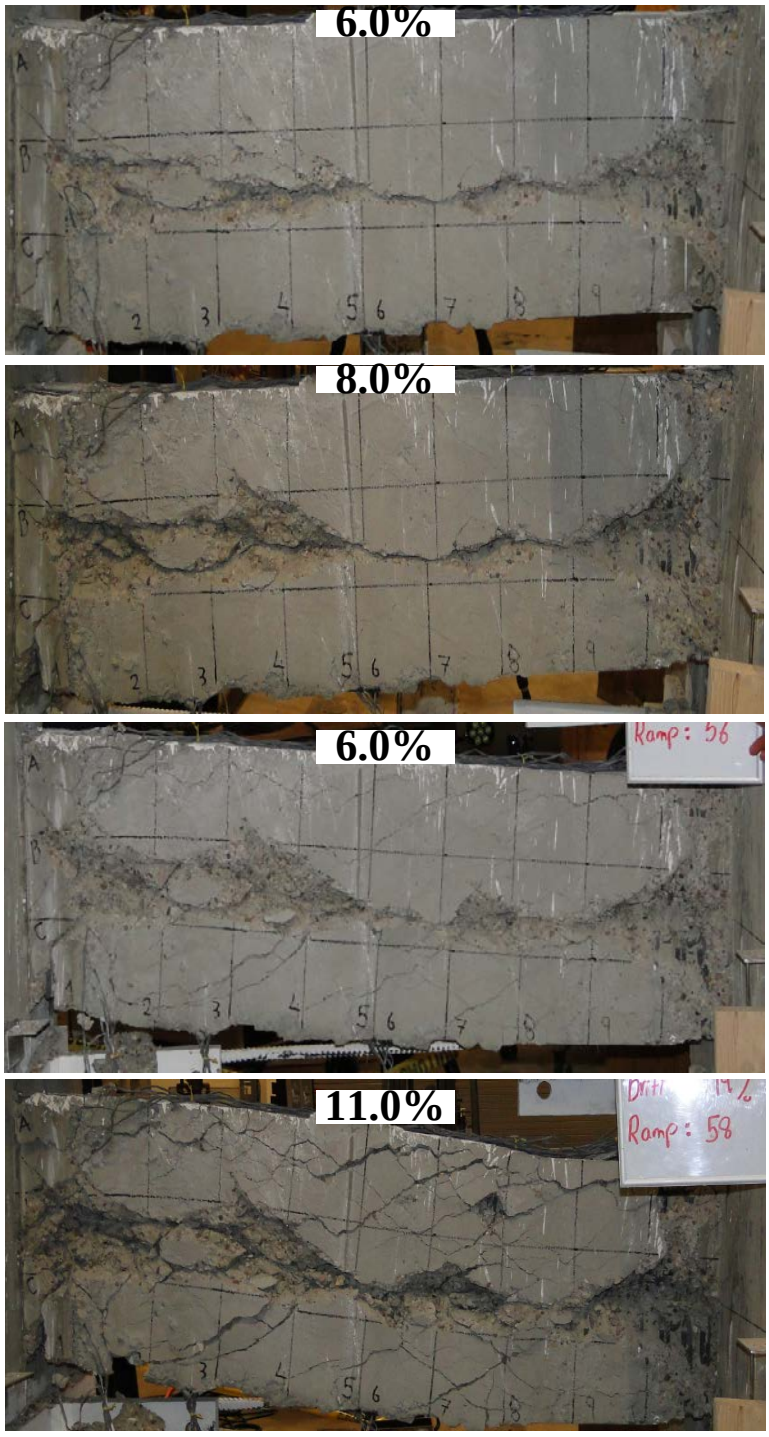

7.6 Cracks and damage patterns of RC-3.3-SC-1 (2)

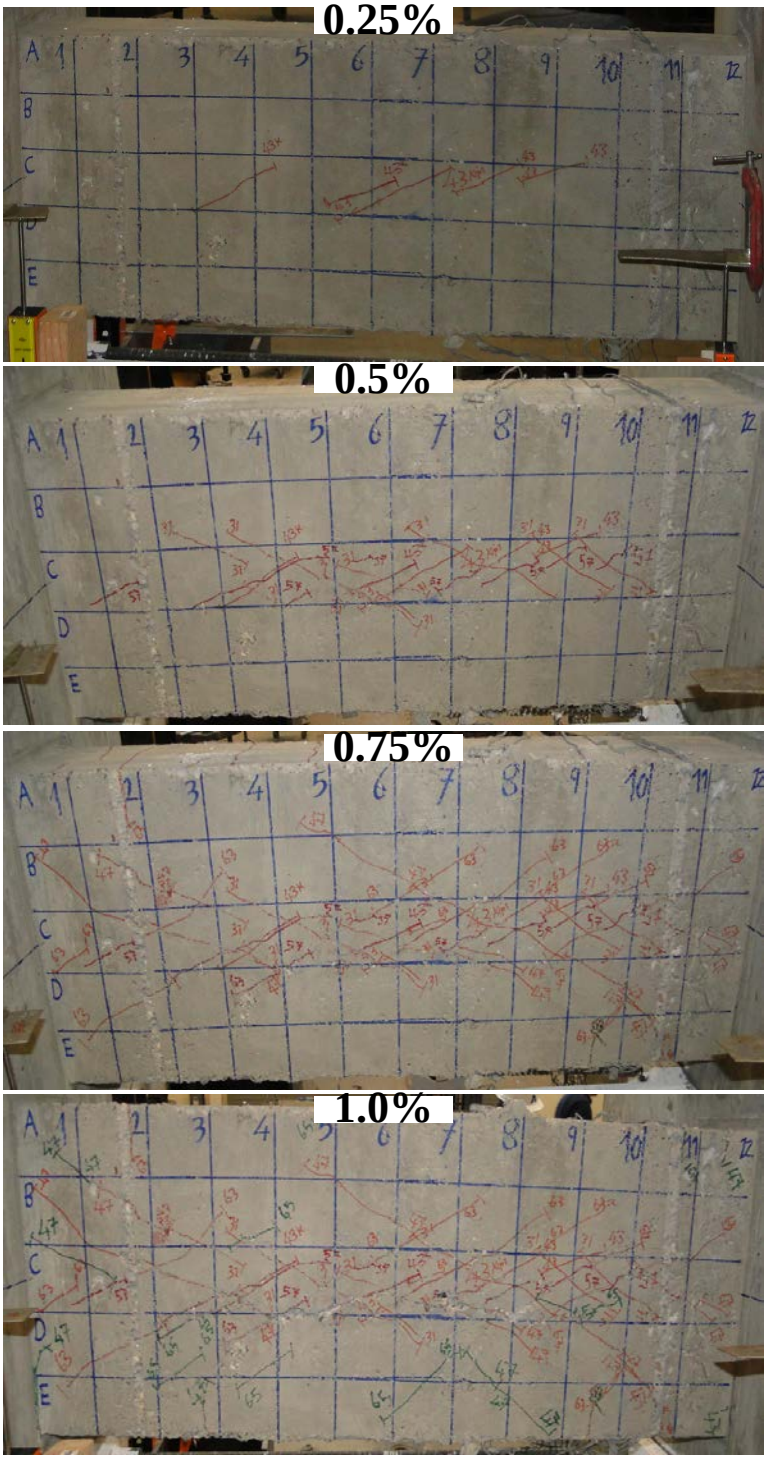

7.7 Cracks and damage patterns of RC-2.4-SC-0.25 (1)

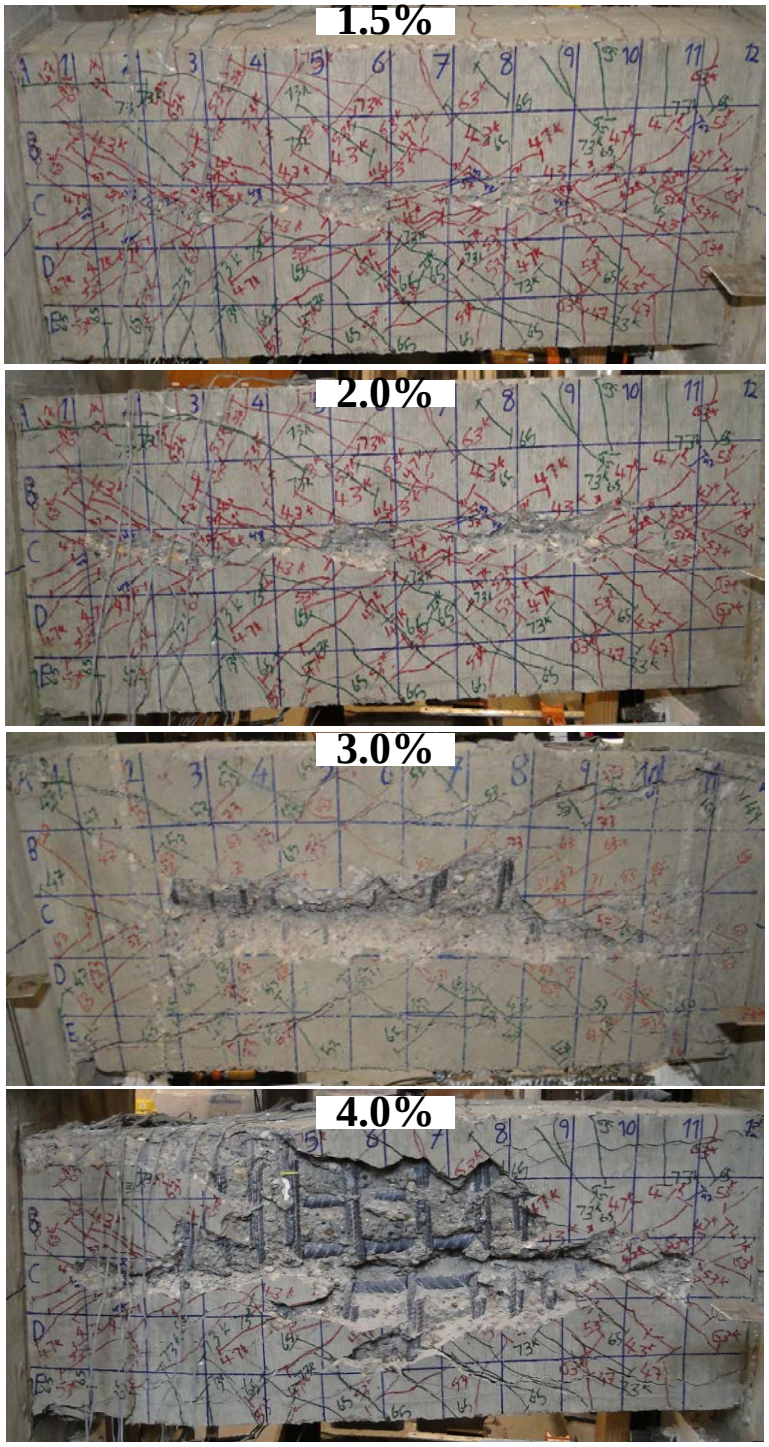

7.8 Cracks and damage patterns of RC-2.4-SC-0.25 (2)

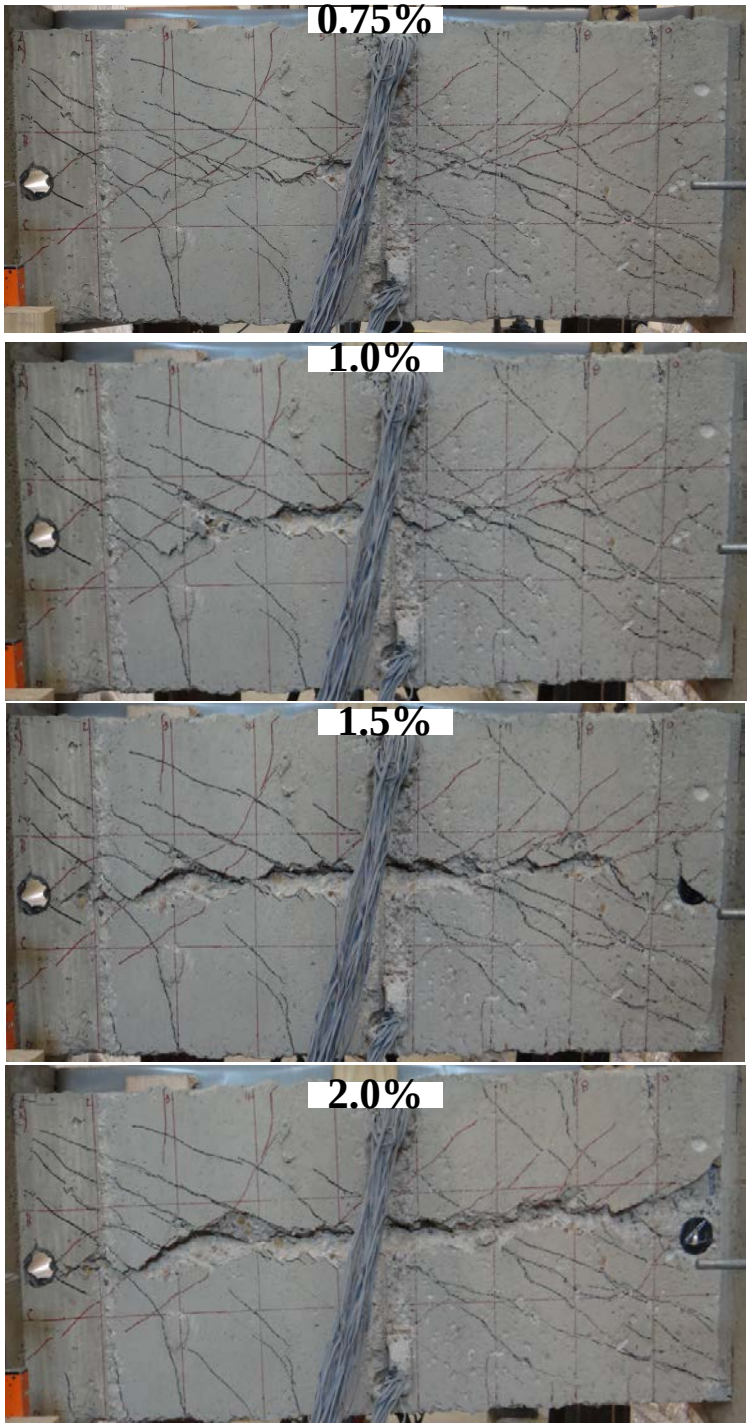

7.9 Cracks and damage patterns of RC-2.4-SC-2 (1)

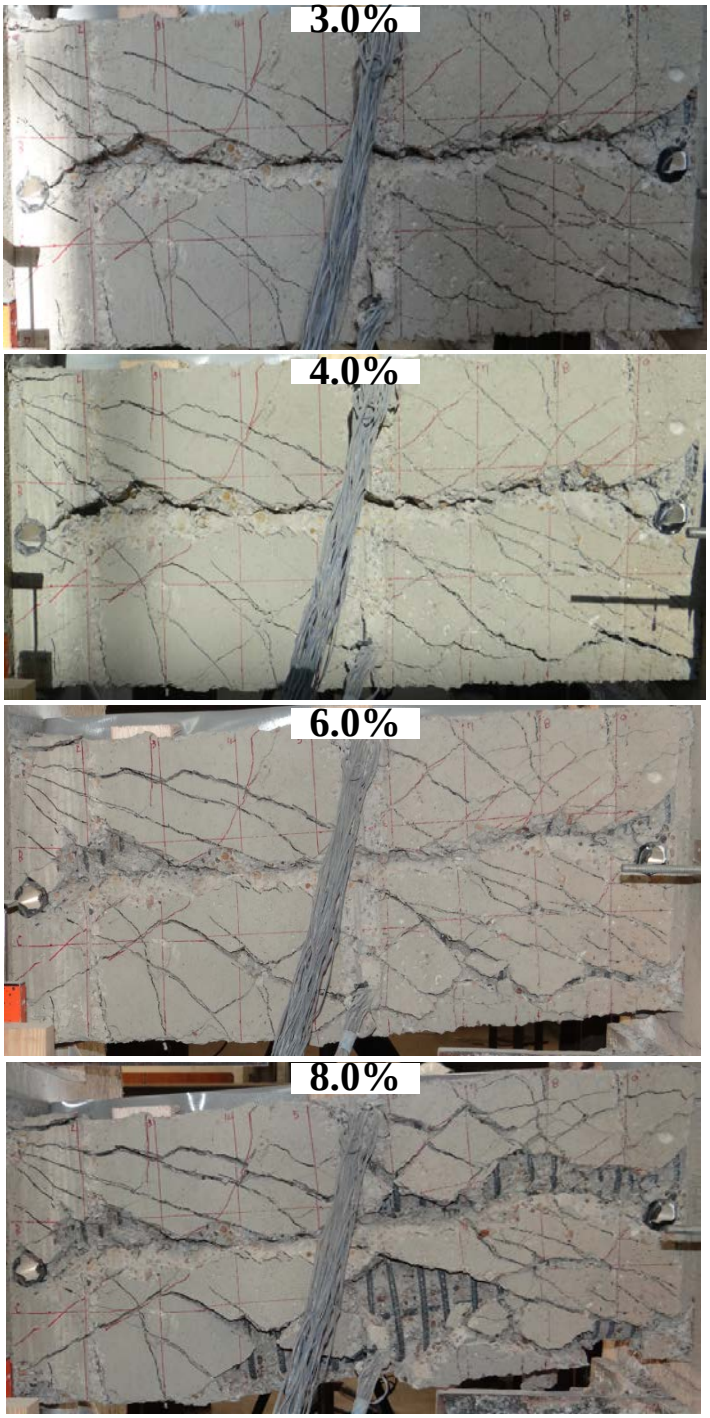

7.10 Cracks and damage patterns of RC-2.4-SC-2 (2)

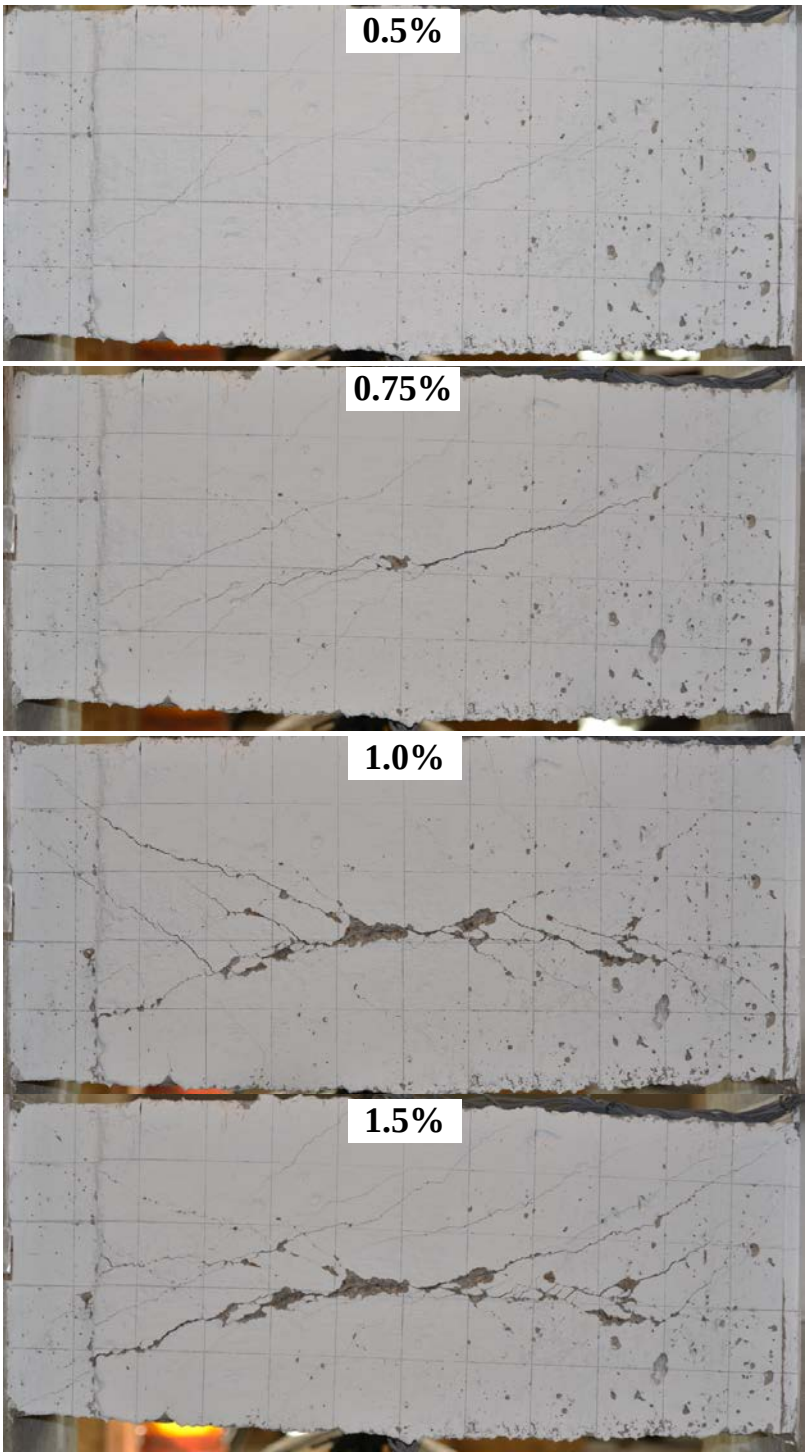

Figure 7.11 Crack and damage pattern of R2.4-SC-2-W (1)

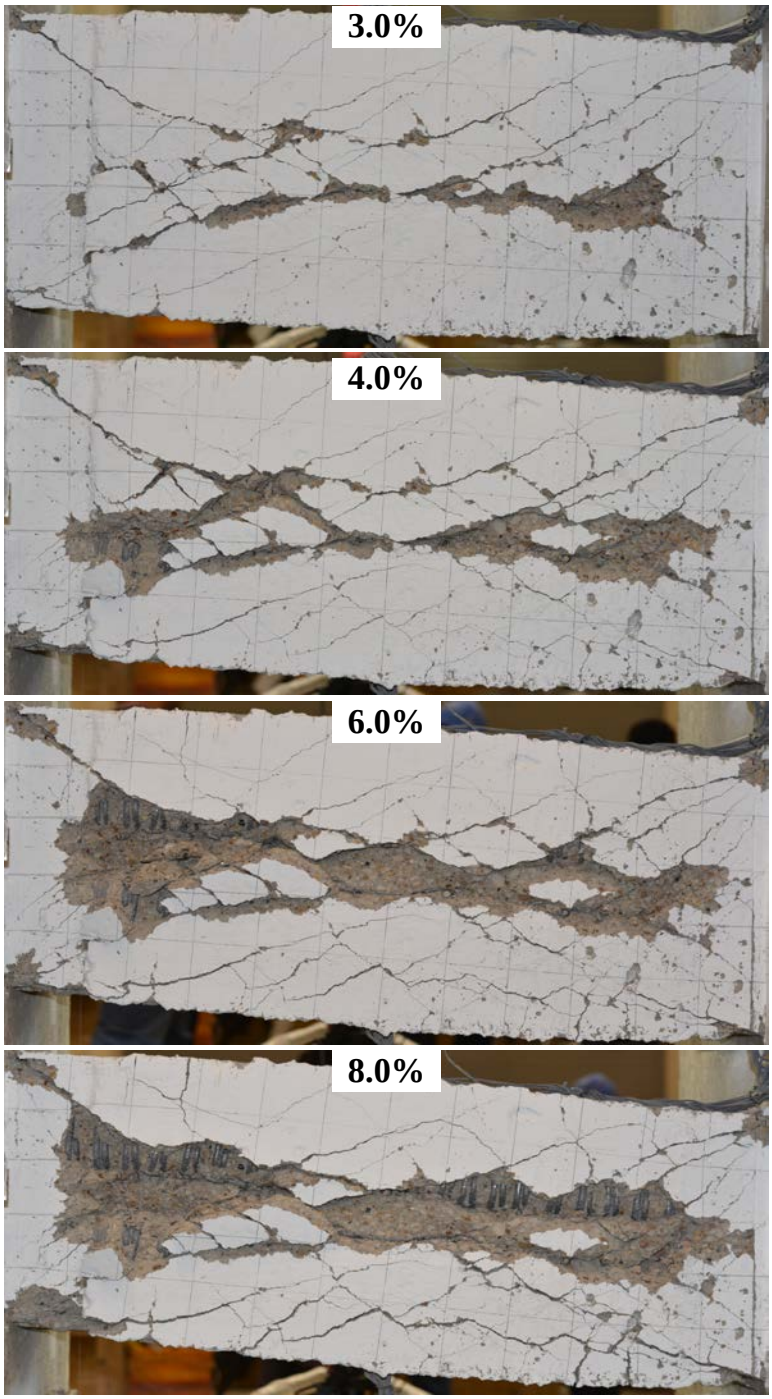

Figure 7.12 Crack and damage pattern of R2.4-SC-2-W (2)

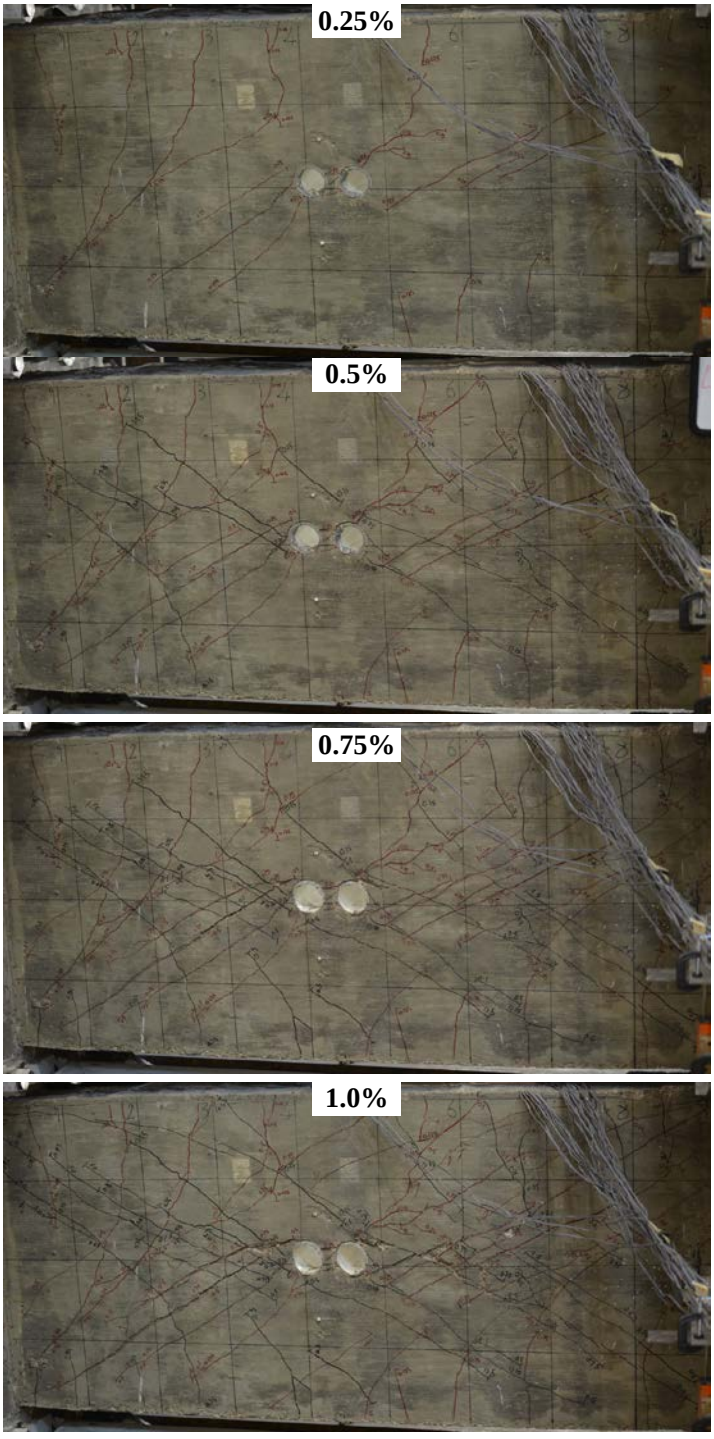

Figure 7.13 Crack and damage pattern of R2.15-SC-1.5-PM (1)

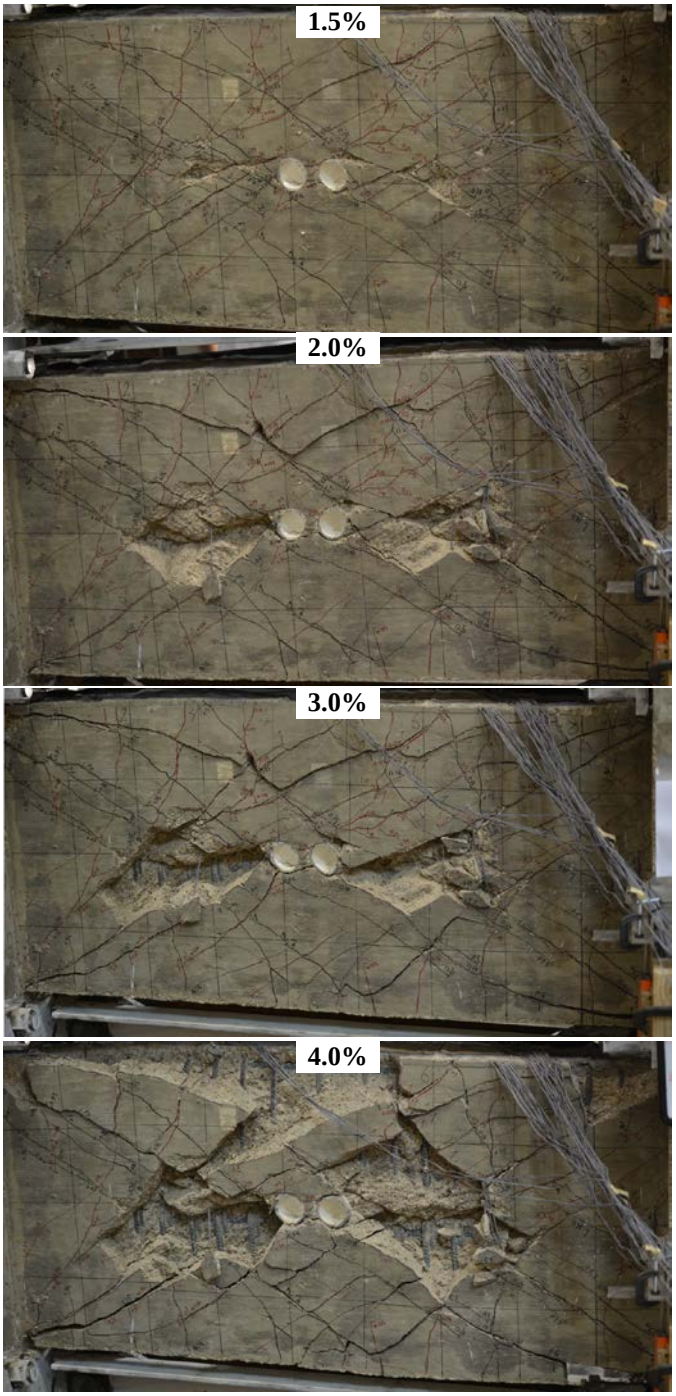

Figure 7.14 Crack and damage pattern of R2.15-SC-1.5-PM (2)

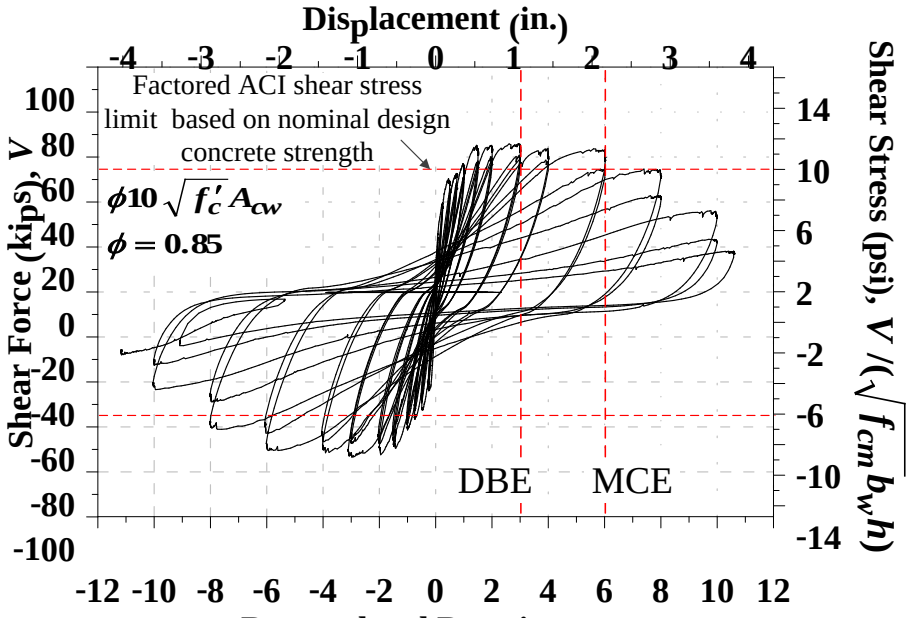

7.15 Hysteresis curves of RC-2.4-SC-1

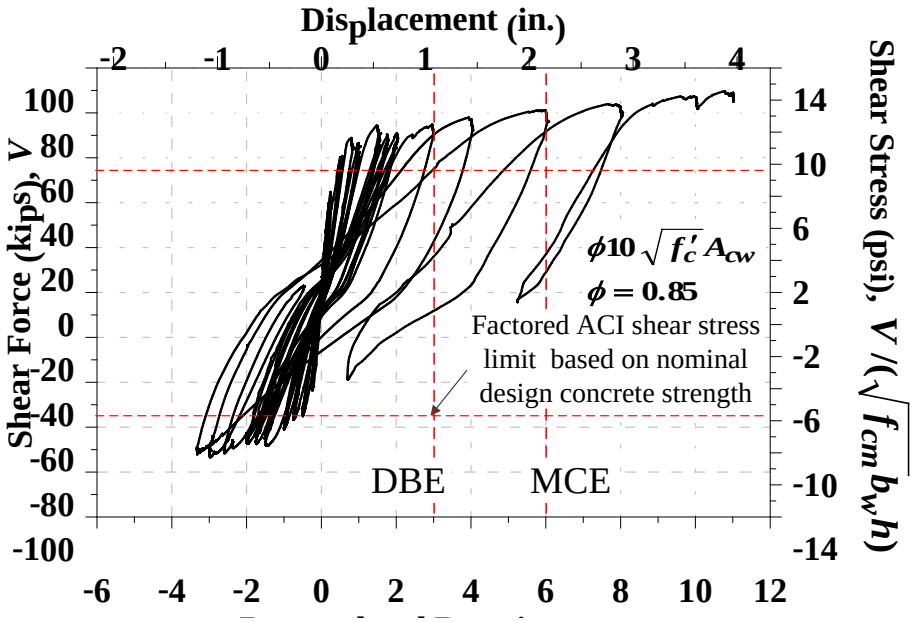

7.16 Hysteresis curves of RC-2.4-NC-1

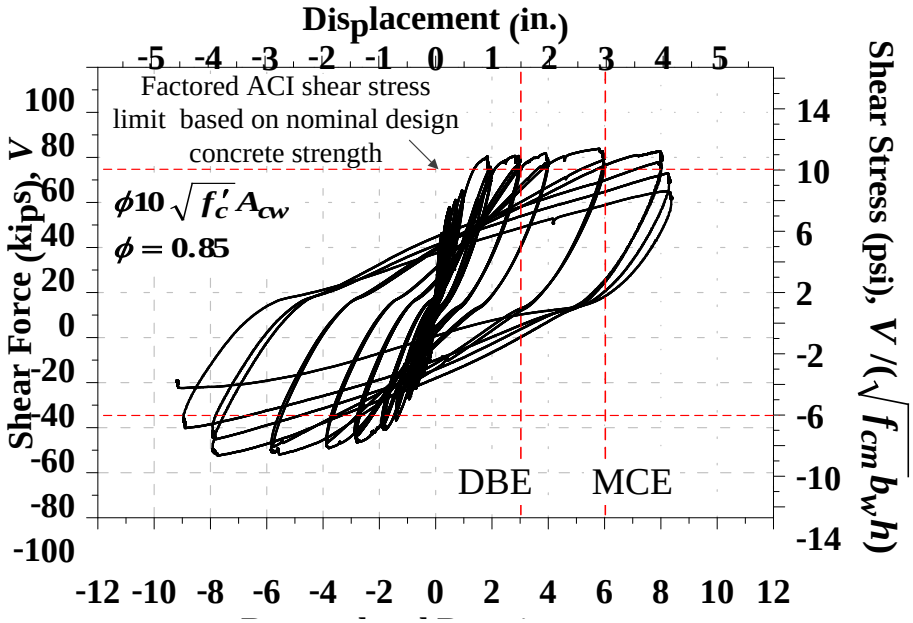

7.17 Hysteresis curves of RC-3.3-SC-1

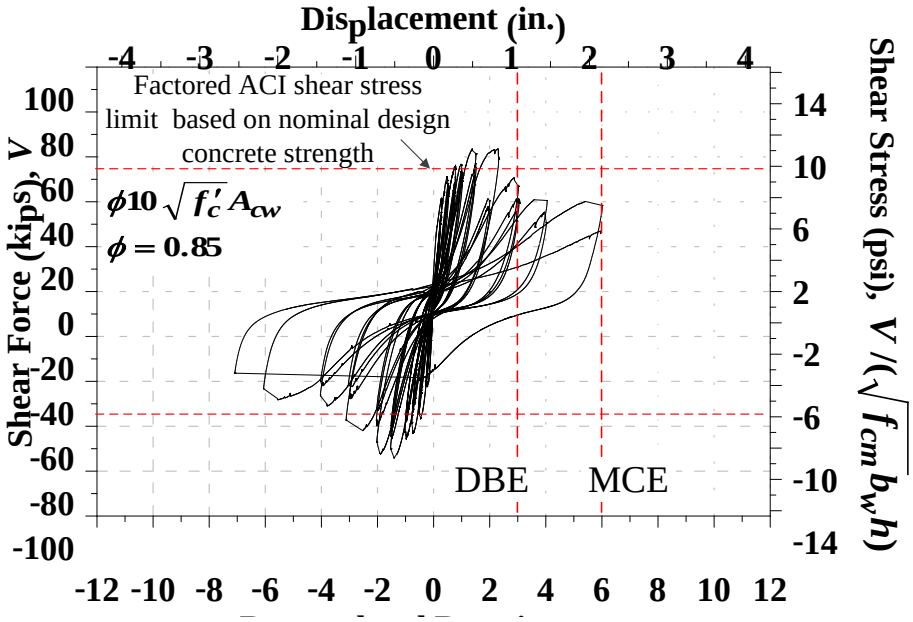

7.18 Hysteresis curves of RC-2.4-SC-0.25

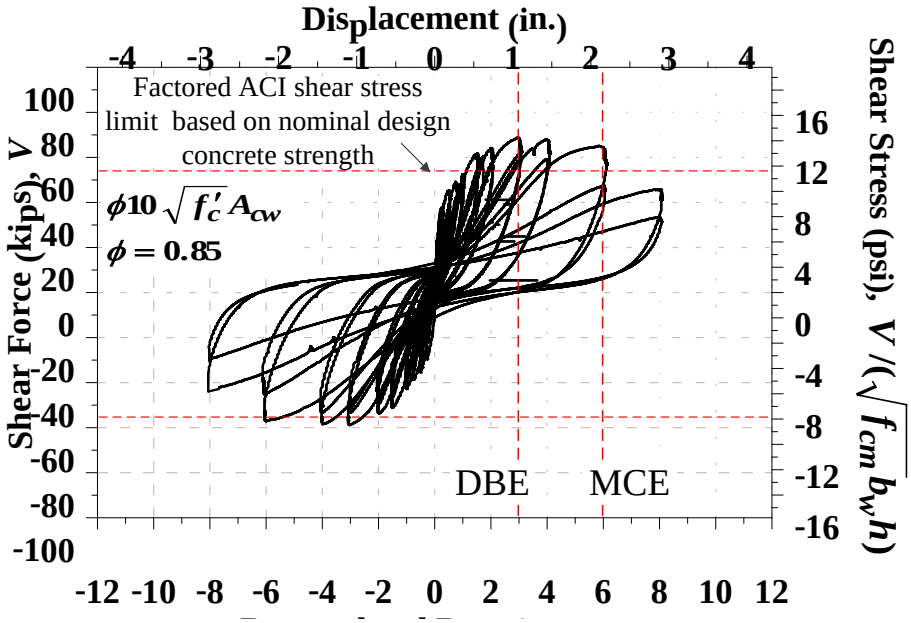

7.19 Hysteresis curves of RC-2.4-SC-2

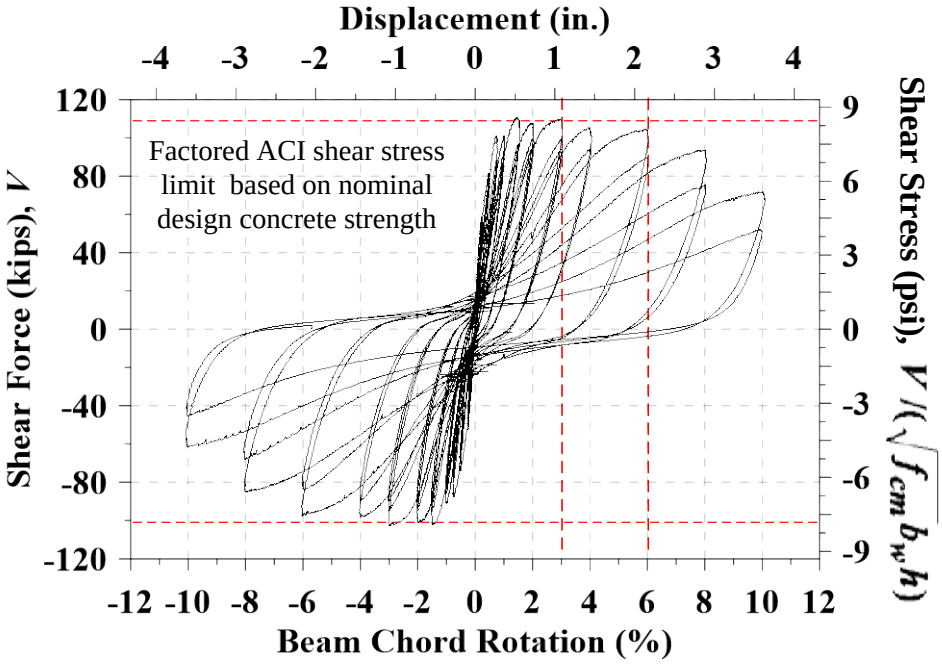

Figure 7.20 Hysteresis curves of R2.4-SC-2-W

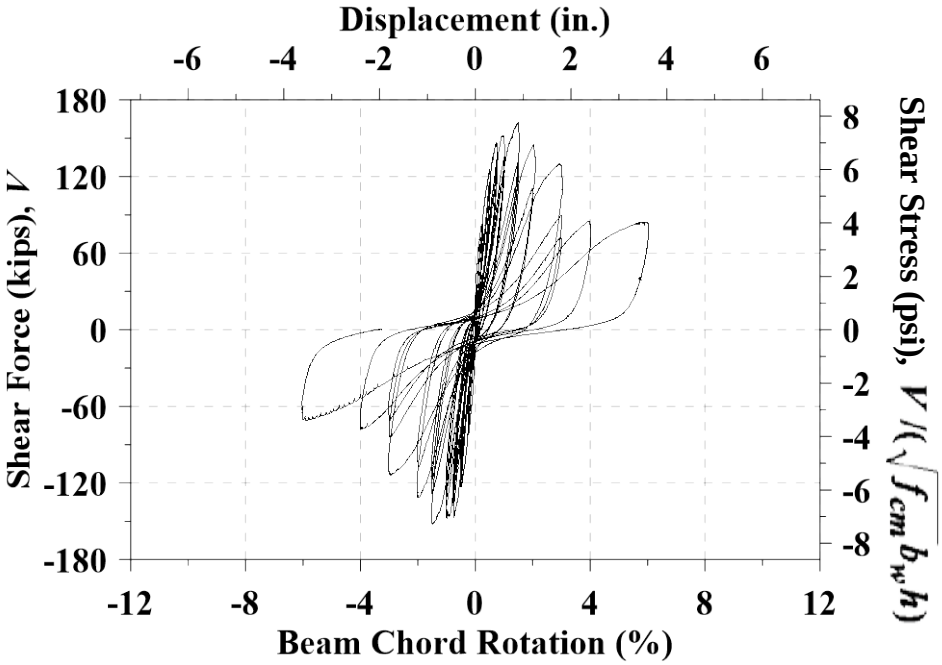

Figure 7.21 Hysteresis curves of R2.15-SC-1.5-PM

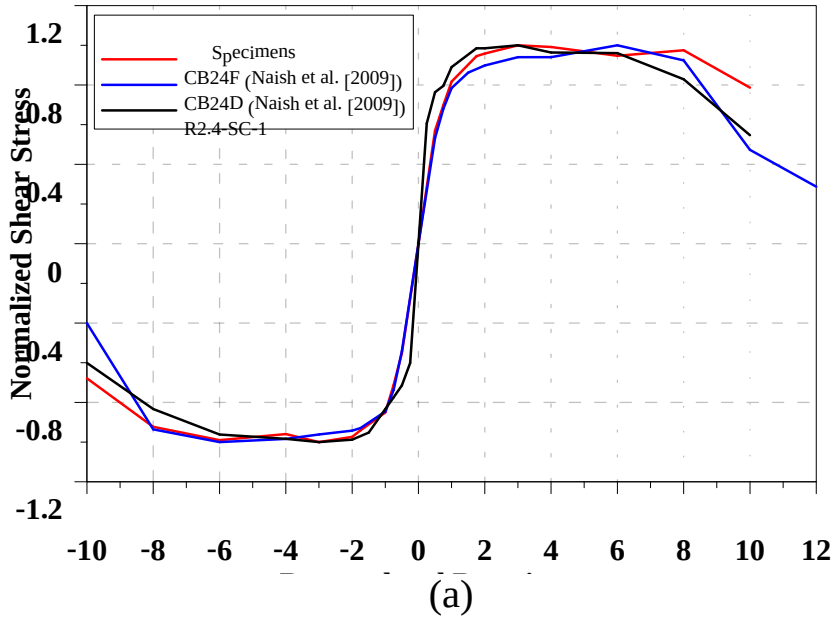

(a)

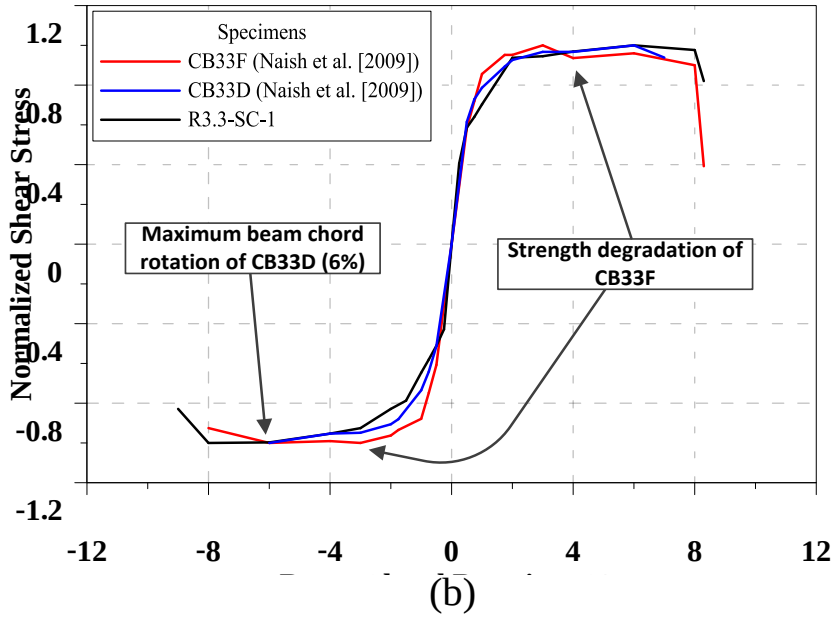

(b)

Figure 7.22 Normalized shear stress versus beam chord rotation: (a) span-to-depth ratio of 2.4 and (b) span-to-depth ratio of 3.3 (Note: Normalized shear stress is the shear stress normalized by the maximum shear stress of each specimen).

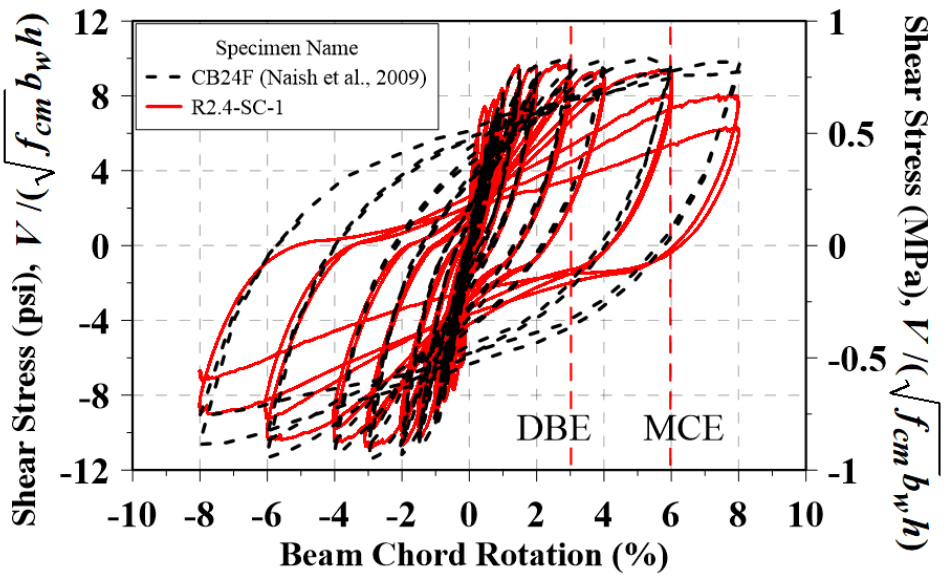

(a)

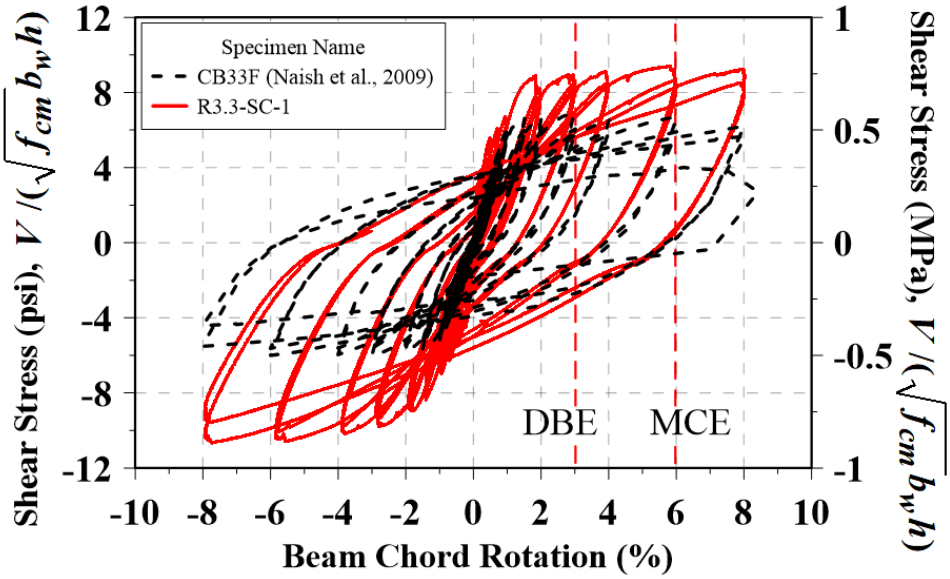

(b)

Figure 7.23 Comparison of DBCBs with DCBs: (a) span-to-depth ratio of 2.4 and (b) span-to-depth ratio of 3.3. (Note: Normalized shear stress is $V_{test} / \sqrt{f_{cm}} h b_w$. Here, f_{cm} = measured concrete compressive strength.)

Chapter 8

SEPARATION MECHANISM AND DESIGN RECOMENDATIONS

8.1 Force-Resisting Mechanism of DBCBs .

When a DBCB is subjected to small shear force, the vertical shear stress distribution along the beam height follows that predicted by elastic theory. Associated horizontal shear stress also acts along the longitudinal axis of the beam. Both stresses are the highest at the mid-height of the beam. As a consequence, maximum shear strain takes place at mid-height. Since there is no shear reinforcement along the mid-height of the beam, concrete at this location becomes soft. Note that although the shear stress is theoretically the same at beam ends (Section A in Figure 8.1), the restraint imposed by the adjacent walls prevents the DBCB from the sftening at the ends. Therefore, the softening starts at mid-span (Section B in Figure 8.1), then propagates toward both ends as displacement increases.

Strain in longitudinal reinforcing bars at the beam-to-wall interface after the softening in DBCBs are illustrated in Figure 8.2 (a) and 8.2 (b). The strain is shown up to 1.0% beam chord rotation. The reinforcing bars did not yield at 1.0% rotation. From the strain, it is clear that top and bottom beam act separately, since L3 shows compression strain, while L4 exhibits tension strain. Stress resultants based on the strain are shown in Figure 8.2 (c). As can be seen, the bottom reinforcing bar of the top beam is under tension, while the top reinforcing bar of the bottom beam is under compression. These tension and compression stresses cause the top and bottom beam to slide relative to

each other, generating sliding force, V_s. It is also worthy to mention that while the tension strain for both the top and bottom beam were similar, the compression strain of the top beam was much higher than that of the bottom beam. It is believed that the tension stress of the bottom beam made the unreinforced concrete strip very soft such that the compression force that was supposed to be taken by concrete was resisted by the longitudinal reinforcing bars. This increases the compression strain in the bottom reinforcing bars of the top beam.

The sliding force, V_s, is transferred to the unreinforced concrete strip by transverse reinforement as can be seen in Figure 8.3. When the unreinforced concrete strip is wide the sliding force is resisted by the concrete between the two adjacent hoops and the sliding force readily shears the concrete, completely separating the top and bottom beams (8.3 a). The restraint imposed by the adjacent walls prevents the DBCB from separation at the ends. Therefore, the separation starts at mid-span, then propagates toward both ends as displacement increases. This damage process is opposite from that of conventionally reinforced coupling beams in which the damage starts from the beam-to-wall interface, thereby drastically reducing the ability of transferring shear to the walls and eventually leading to sliding shear failure or bond slip failure. On the other hand, when the width is very narrow, the resistance provided by the concrete becomes very high since the concrete resists the sliding force by compression (Figure 8.3, b). This, together with the restraint provided by the adjacent walls, detains the separation, which leads to a very short separated length of the unreinforced concrete strip (Figure 8.4 (a). As seen in Figure 8.4 (b), the unseparated part acts as adjacent walls and shortened the shear span, causing DBCBs a shear failure without a complete separation.

The unreinforced concrete strip also contributes to increasing shear strength. The first and second columns of Table 8.1 give the design shear and measured shear force during the tests. The differences between the design and measured shear forces are given in the third column of the table. For the specimens which successfully separated, it is believed that the additional strength resulted from the aggregate interlock due to the relative displacement between the top and bottom beam (Figure 8.5).

Table 8-1 Design shear force vs. measured shear force

Specimen	$V_{design\ (0.003)}$[1]	V_{test}	$V_{test}/V_{design\ (0.003)}$
R2.4-SC-1	44.7	68.5	1.53
R2.4-NC-1	44.7	89	2
R3.3-SC-1	41.2	68	1.65
R2.4-SC-0.25	58.13	68	1.17
R2.4-SC-2-P	49.3	63.5	1.29
R2.4-SC-2-W	79	111	1.41
R2.1-SC-PM	180	162	0.9

[1]: 0.003 was used as maximum usable concrete compressive strain

8.2 Nonlinear Finite Element Analysis

8.2.1 Modeling Overview

Nonlinear analysis using the finite element software, VecTor2, was conducted to predict the effects of the width of unreinforced concrete strip and the location of the utility pipes on the performance of DBCBs. A standard model built for this study is shown in

Figure 8.6. This model represents the R2.4-SC-1. To simulate steel rebars, truss elements were used rather than smeared reinforcement. Reinforcements are automatically placed based on the given area of reinforcement when using the smeared reinforcement. On the other hand, all the rebars can be placed at specific positions when truss elements are used. A perfect bond between reinforcement and concrete was assumed. Smoothed triangle mesh was used with a mesh size of 0.04 in. The loading block and the big block were assumed to be rigid elements. Since VecTor2 does not provide any type of hinge boundary, the steel links, which connect the loading block to the big block in order to restrain the rotation of the loading block, were omitted. Instead, to prevent the block from rotating, displacement restraint was imposed evenly on the top of the blocks. The material models used in this study are shown in Table 8.2. A detailed explanation of the models' properties and functions can be found in the VecTor2's User Manual (2002).

The results from an experimental test (R2.4-SC-1) were compared with those from the VecTor2 analysis to verify the accuracy of the simulation (Figure 8.7). Comparisons were made for the damage pattern and the hysteresis response of experiment and analysis results. Damage pattern from the analysis is very similar to the result of the experiment (both at about 4% beam chord rotation), showing the beam separation and plastic hinges at the two separated beams (Figure. 8.7a and 8.7b). Comparison for hysteresis response up to about 4% beam chord rotation is shown in Figure 8.7c. It is seen that although unloading stiffness of the specimen can be overestimated by VecTor2, the peak strengths and the beam rotations associated with the starting of strength degradation reasonably match the experimental results. It should be noted that VecTors2 stopped running when severe cracking occurred at the

unreinforced concrete strip, although the strength of the DBCB model did not drop significantly.

Table 8-2 Material models

Concrete Models		Concrete Models	
Compression Pre-Peak	Hogmestad (Parabpla)	Crack Width Check	Agg/2.5 Max Crack Width
Compression Post-Peak	Modified Park-Kent	Crack Slip Calculation	Walraven (Monotonic)
Compression Softening	Vecchio 1992-A	Creep and Relaxation	No Available
Tension Stiffening	Modified Bentz 2003	Hysteretic Response	Nonlinear w/ Plastic Offsets)
Tension Stiffening	Linear	Concrete Bond	Eligehausen
FRC Tension	Not Considered		
Confined Strength	Kupfer / Richart	Reinforcement	
Dilation	Variable – Kupfer	Hysteretic Response	Bauschinger Effect (Seckin)
Cracking Criteria	Mohr – Coulomb (Stress)	Dowel Action	Tassios (Crack Slip)
Crack Stress Calculation	Basic (DSFM/MCFT)	Buckling	Refined Dhakal-Maekawa

8.2.2 Effect of the Height of the Unreinforced Concrete Strip

The width of the unreinforced concrete strip can be a critical factor on the seismic performance of DBCBs. As explained before, whether the DBCB separates or remains unseparated highly depends on the width of the unreinforced concrete strip. A specimen with 0.25 in.-wide unreinforced concrete strip was tested. This specimen has the same dimension and reinforcement detailing as the R2.4-SC-1 specimens except for the width of the unreinforced concrete strip. It was tested using the symmetrical loading protocol. The specimen failed by shear-dominant behavior and only partially separated (as

explained before). Figure. 8.8a and 8.8b show the hysteresis response and the damage pattern of the specimen with a 0.25 in.-wide unreinforced concrete strip. To assess the impact of the unreinforced concrete strip width, five models were built in VecTor2. All models are the same in dimension and reinforcement detailing as the R2.4-SC-1 specimens, but have various widths of unreinforced concrete strip (Figure 8.9).

The model with a 0.25 in.-wide unreinforced concrete strip failed earlier than the others, exhibiting the highest strength but poor ductility. On the other hand, the model with a 2 in.-wide unreinforced concrete strip exhibited the highest ductility, but lowest strength (due to the reduced moment arm of each beam). It is observed for the analytical study that elastic stiffness of the beam did not depend on the size of the unreinforced concrete strip, but the strength of the models increased as the width of the unreinforced concrete strip decreased (Figure 8.10). In order to compensate for the loss of strength in this model, No. 6 longitudinal bars at the top and bottom of each cage were replaced by No. 7 bars, which effectively increased the strength while maintaining the high ductility. It should be noted that the test specimen with a 0.25 in.-wide unreinforced concrete strip failed by shear-dominant mechanism. On the other hand, the VecTor2 model with the same unreinforced concrete strip width failed mainly by flexure with severe damage at the ends of the beam (Figure 8.11). Further refinement of the model is warranted.

8.2.3 Utility Pipe in Unreinforced Concrete Strip

As mentioned earlier, modern construction design often requires utility ducts to pass through the coupling beams (Hooper, 2014). While these openings may not be easily implemented in DCBs, the unreinforced concrete strips between two cages in the DBCBs potentially allow such openings to be easily placed. In order to study the effect of the openings, a specimen with two 1.5 in. diameter PVC pipes placed in the mid-span of the specimen was tested (R.2.15-SC-1.5-PC). Figure 8.12 shows that it did not completely separate and, hence, failed by shear-dominant behavior. The reason for this failure was attributed to the PVC pipes providing horizontal shear resistance at the critical location thereby preventing the intended separation from happening.

When PVC or other types of pipes are place in the mid-span, the sliding fore is are resisted by the pipes rather than the concrete, which prevents the separation of the unreinforced concrete strip from happening, thus allowing the diagonal cracks to develop and degrade the strength of the beam. One option is to place the pipes at the ends of the beam where the shear deformation caused by the horizontal shear stresses has already restrained the blocks. The ends typically remain unseparated until large displacement is imposed on the beam.

To investigate the effect of the utility pipe location, three models were built. All models have a 2 in.-wide unreinforced concrete strip and the same reinforcement detailing. No. 7 bars were used at the top and bottom of each cage. Table 8.2 gives the differences among the models. A rigid pipe model was assumed with a rectangular shape because of the difficulty in generating a circular shape in VecTor2.

Table 8-3 Details of models

Model name	width	Pipe size	Pipe location
DBCB-PM	2 in.	1.5 in.	Mid-span
DBCB-PS	2 in.	1.5 in.	Both Sides
DBCB	2 in.	-	-

The analysis results of all models are shown in Fig. 8.12. For the DBCB-PM, strength degradation began after 1.3% beam chord rotation and failed at 5.3% beam chord rotation. On the other hand, high ductility was maintained in both DBCB-PS and DBCB until 5.3% beam chord rotation occurred. Figure 8.14 compares the damage patterns of the three models. The strength of the DBCB-PM was higher than that of DBCB-PS and DBCB. This is because the additional shear resistance was provided by the pipes in the middle of the beam. This is indirectly verified by the strains in the vertical reinforcement near the mid-span. Figure 8.15 shows the strains in the reinforcements in DBCB-PM and DBCB-PS. The vertical reinforcement near the pipes were subject to very high strains in DBCB-PM. This is because the pipes strengthen the shear resistance, which induced greater shear near the mid-span, and led to an overall increase in the strength of DBCB-PM. For the other models, strains in the transverse reinforcements were much smaller. Since DBCB-PM was not completely separated, damage concentrated at the ends of the beam causing strength degradation earlier than DBCB-PS and DBCB (Figure 8.14). On the other hand, DBCB-PS and DBCB completely separated and exhibited a very similar damage pattern and shear force vs. rotation response. As a result, this study implies that placing the pipes at both sides of the beam has little or no effect on the behavior of DBCBs.

8.3 Design Recommendations

8.3.1 Width of Unreinforced Concrete Strip

Span-to-depth ratios of RC coupling beams can highly affect the performance of the coupling beams. As experimentally proven, DBCBs can be great alternative to DCBs for the range of the span-to-depth ratio of 2.4 to 3.3. The performance of the DBCBs with the span-to-depth ratio of 2.4 to 3.3 highly depends on the width of the unreinforced concrete strip. Experimental tests showed that if the width is more than 1 in. the separation is guaranteed. However, it also can be affected by the size of coupling beams. If the size of DBCBs were large, 1 in. unreinforced concrete strip may not be enough for the separation. Therefore, it is recommended to used span-to-effective depth ratio of each beam (top or bottom beam) such that the width of the unreinforced concrete strip can depend on the size of coupling beams.

8.3.1 Flexure Design

DBCBs' design basically follows the design of beams of special moment frames with some exceptions. The nominal or probable moment of DBCBs can be obtained by summing the moments of each beam at ends as shown in Figure 8.16. For the calculation, deciding the cover thickness of the side, where facing the unreinforced concrete strip, is to assume it as the same as the concrete cover thickness of the opposite side (Fig. 8.17). With the maximum usable concrete strain of 0.003, the successfully tested DBCB specimens have transition-zone sections with the

reinforcement tensile strain between 0.002 and 0.005 in the extreme layer. For the transition-zone section, the strength reduction factor varies linearly between 0.65 and 0.9. However, as seen from the test results, the behavior of DBCBs is highly ductile. Therefore, using 0.9 as strength reduction factor will be appropriate.

In addition, ACI 318-14, Sect. 18.6.3.1 specifies the ratio of longitudinal reinforcement does not exceed 0.025. This is due to the construction difficulty resulted from reinforcement congestions and indirectly not to increase shear stress in the beams. This limit on the amount of longitudinal reinforcement can be relaxed for DBCBs due to the following reasons: 1) although DBCB is designed based primarily on the beams of special moment frames, DBCBs are coupling beam. Therefore, their construction needs to be compared with the construction of current coupling beams in the provision. When comparing with diagonally reinforced coupling beams (DCBs), construction of DBCBs is much easier and 2) ACI 318 (2014) allows maximum shear stress for coupling beams to be up to $10\sqrt{f'c}$ psi ($0.83\sqrt{f'c}$ MPa) and it has been proved by experimental tests that DBCBs can withstand such high shear stress. Therefore, the longitudinal reinforcement ratio of 0.025 can be relaxed.

8.3.2 Shear Design

Damage statues of the specimens, before separation occurs, for different transverse reinforcement ratios are shown in Figure 8.18. As seen, the specimen with less transverse reinforcement developed a wide shear crack, the width of which was much wider than the specimens with greater reinforcement ratio. Furthermore, the length

of separated part was longer as the reinforcement ratio is greater. And, the relative displacement between the top and bottom beam was greater with high reinforcement ratio. The role of transverse reinforcement before the separation is to hold the width of shear crack so that DBCBs can successfully separate without shear failure. This is because when transverse reinforcement ratio is low, the relative displacement between the top and bottom beam can be taken by the width of the shear crack. This detains the separation and may cause shear failure before the separation.

The failure of all DBCB specimens was due to shear. The spalling of concrete cover and destruction of concrete along the inclined cracks, due to the abrasion, are all related to shear cracks developed during the cyclic loading and those led to the strength decay of the specimens. As can be seen in Figure 8.19, degree of damage depends on the transverse reinforcement ratio. The specimens with a high ratio had less damage, while Damage of the specimens with a low ratio was severe. The specimens with less transverse reinforcement ratio experienced strength loss earlier than the specimens with high ratio. Therefore, the role of transverse reinforcement in DBCBs after the separation is to resist shear and provide confinement so as to delay the beginning of the strength degradation.

The shear design of R2.4-SC-2-P was done according to ACI 318-14. While the specimens with 1 in. concrete strip were heavily reinforced, specimen R2.4-SC-2-W was lightly reinforced. Although all the specimens successfully separated and showed satisfactory performance, it is recommended to use current ACI provision for shear design of DBCBs, since the lightly reinforced specimen suffered from severe damage by shear and it is common practice to err on the conservative side.

8.3.3 Development Length

Figure 8.20 illustrates the strain distribution from four strain gauges on a longitudinal rebar inside the concrete block (representing the wall pier) of Specimen R2.4-SC-2-P. All specimens which separated successfully showed similar strain distribution inside the concrete block. As shown in the figure, strains in the rebars at the interface and at 4-in. inside the block increased by a similar amount up to a 2% beam rotation. However, after separation, only the strain at the interface showed dramatic increase. Although the specimen was subjected to many large displacement reversals yielding did not penetrate beyond about 4-in. inside the wall pier. The embedded length of the longitudinal rebars in Specimen R2.4-SC-2-P is 18 in., which is only 50% of that required by ACI 318-14, Sect. 18.8.5.3(b), which is 37 in. The minor yielding or complete elastic strain beyond 4-in. inside the wall pier indicates that DBCBs did not suffer bond deterioration as commonly seen in DCBs (Naish et al., 2013).

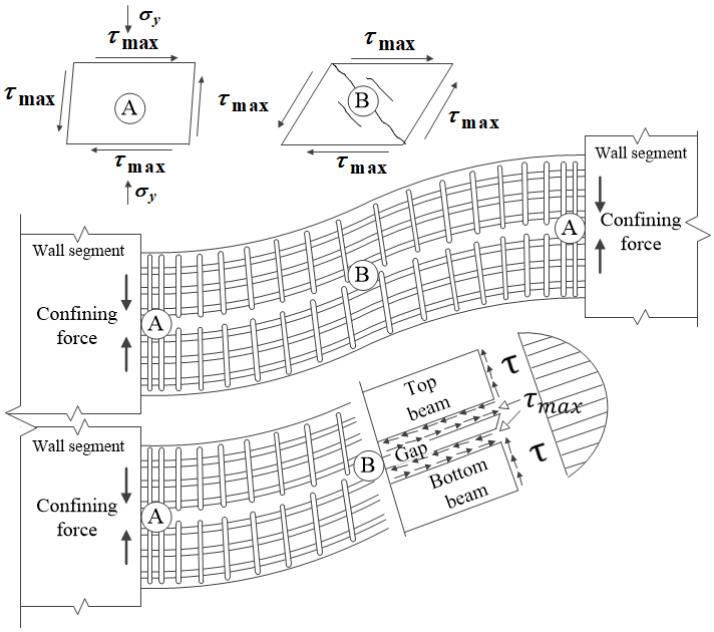

8.1 Force-resisting mechanism of DBCBs before softening of unreinforced concrete strip

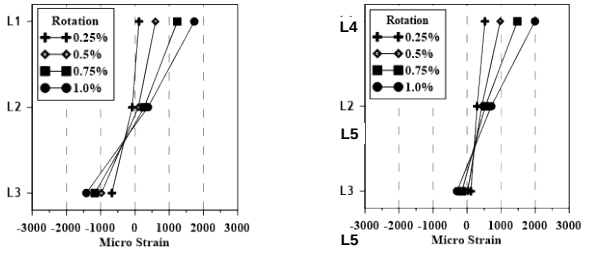

(a) **(b)**

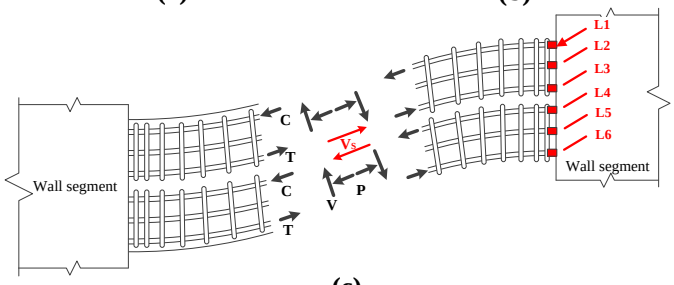

(c)

Figure 8.2 (a) Stress resultants in DBCBs and (b) longitudinal reinforcing bars strain at beam-wall interface

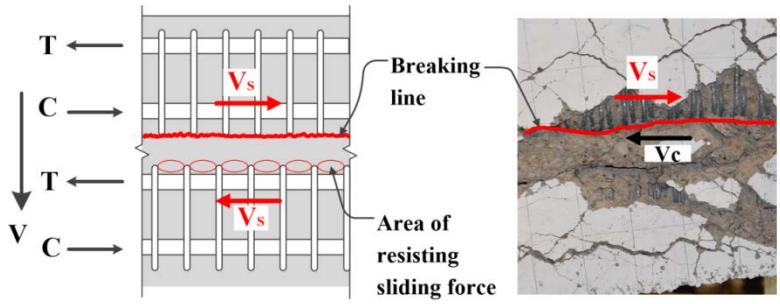

(a)

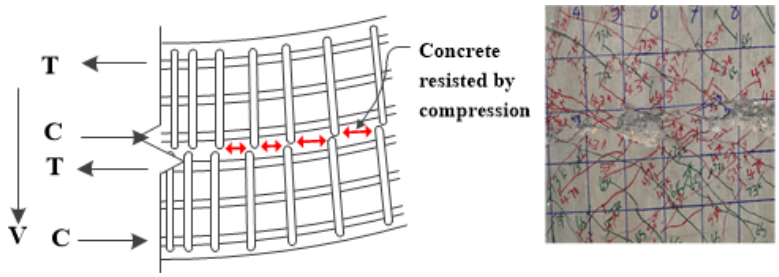

(b)

Figure 8.3 (a) Force-resisting mechanism by wide unreinforced concrete strip and (b) force-resisting mechanism by narrow unreinforced concrete strip

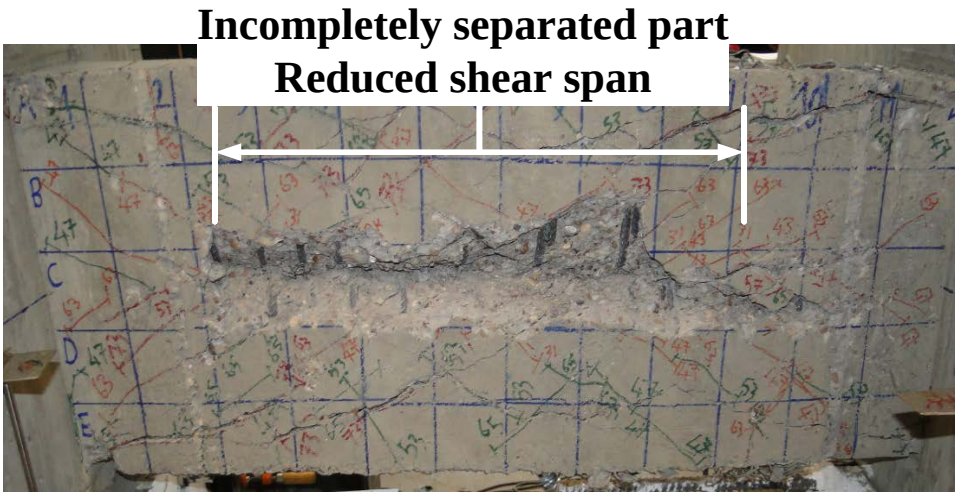

(a)

(b)

Figure 8.4 (a) Reduced shear span of DBCB and (b) Shear failure of DBCB due to reduced shear span

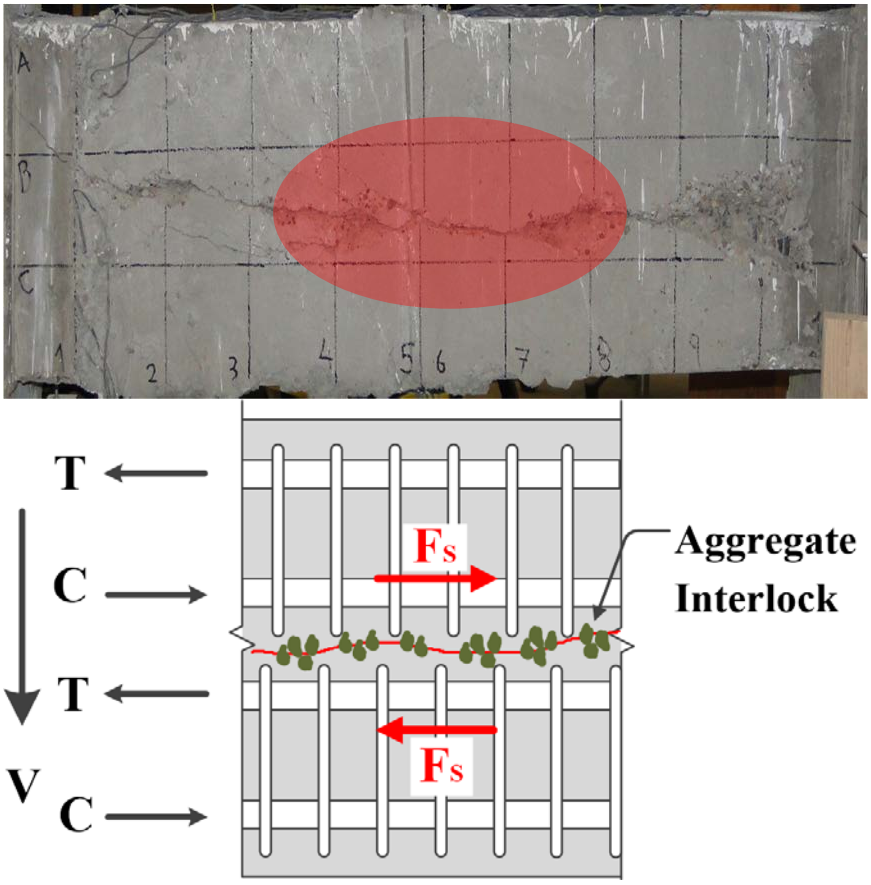

8.5 Additional force from aggregate interlock

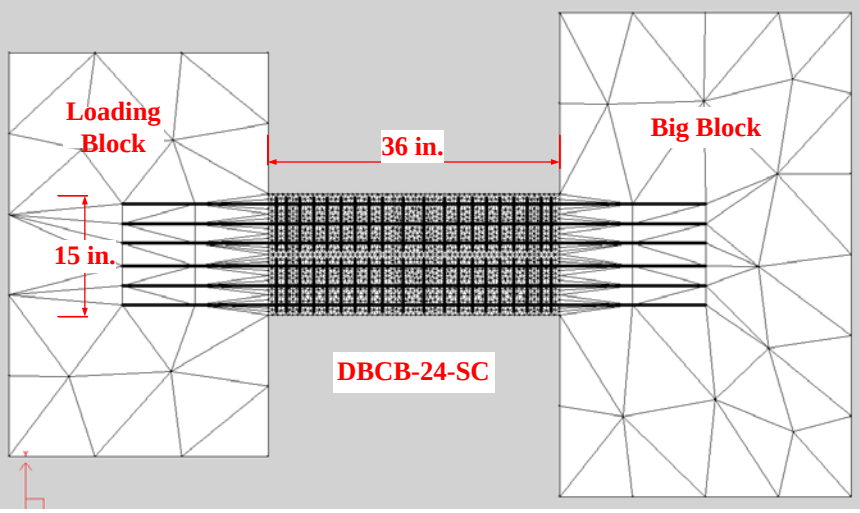

Figure 8.6 VecTor2 Model

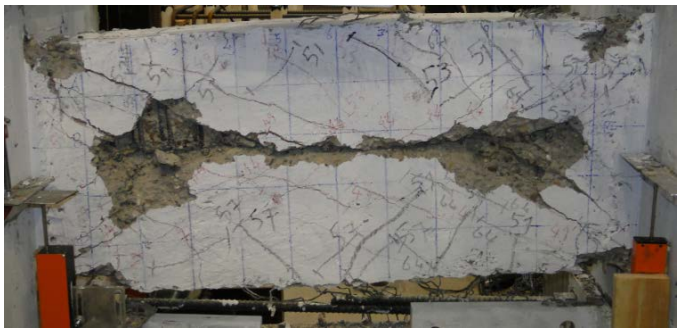

(a)

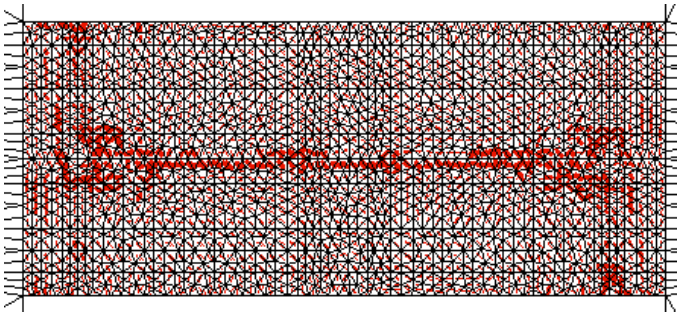

(b)

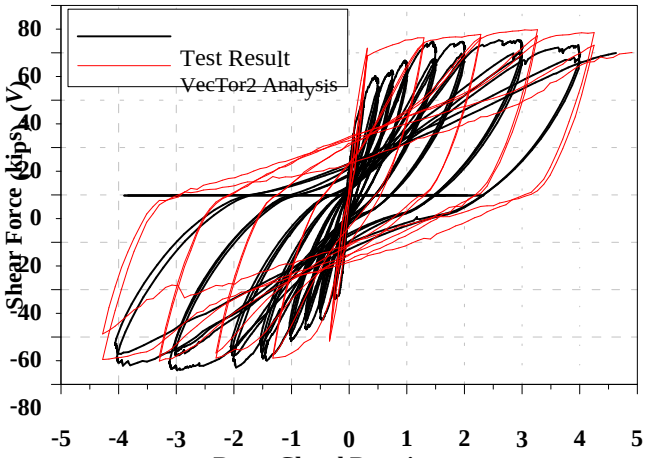

Figure 8.7 (a) Damage pattern of R2.4-SC-1 at 4% beam rotation , (b) Damage pattern of R2.4-SC-1at 4.3% beam rotation (VecTor2), and (c) Comparison of experimental and VecTor2 analysis

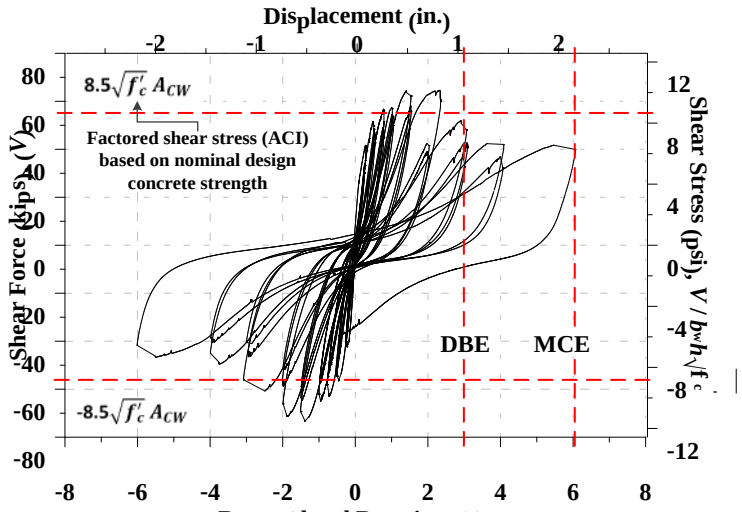

(a)

(b)

Figure 8.8 (a) Hysteresis response of specimen with 0.25 in.-wide gap and (b) damage pattern at 6% beam chord rotation

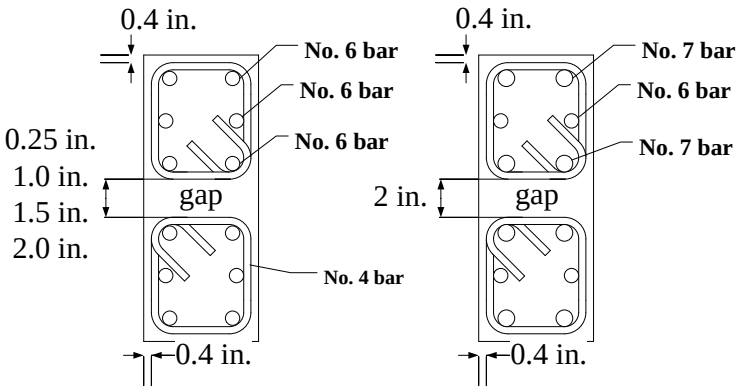

Figure 8.9 Cross sections of the models

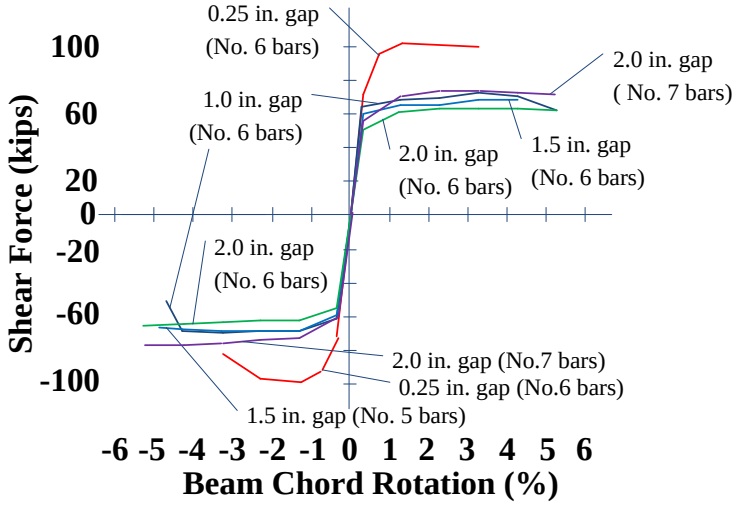

Figure 8.10 Effect of size of the unreinforced concrete strip

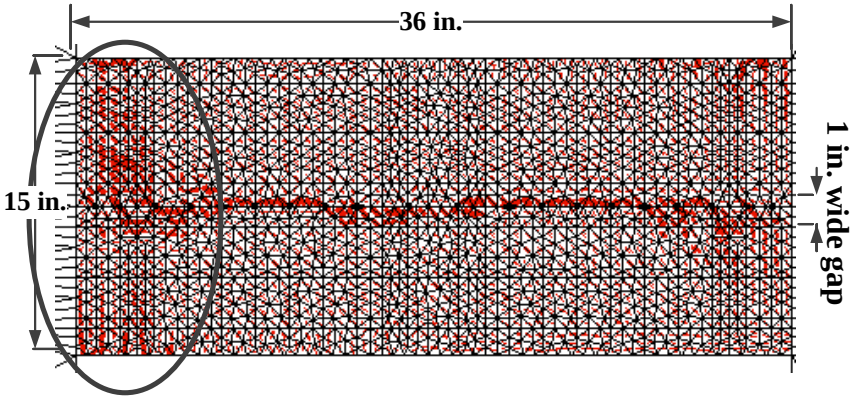

Figure 8.11 Damage pattern of the model with 0.25 in.-wide gap (VecTor 2)

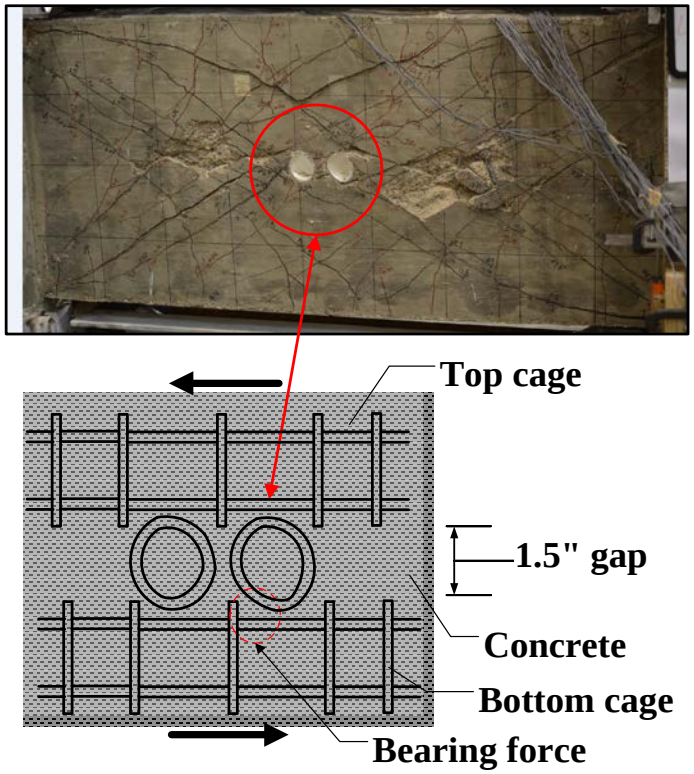

Figure 8.12 Force-resisting mechanism with utility pipes at mid-span

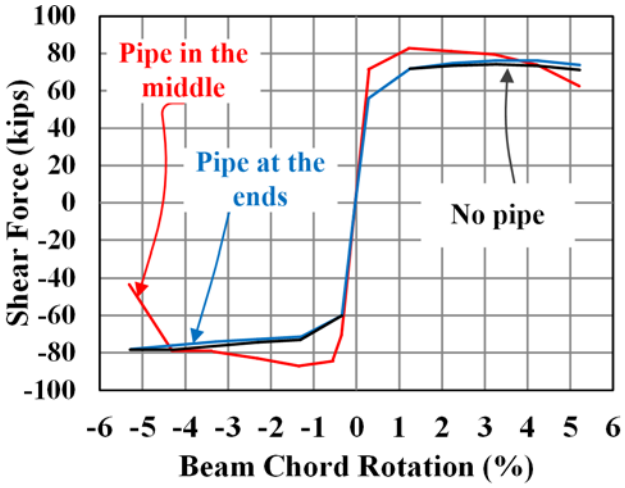

Figure 8.13 Shear force / rotation response

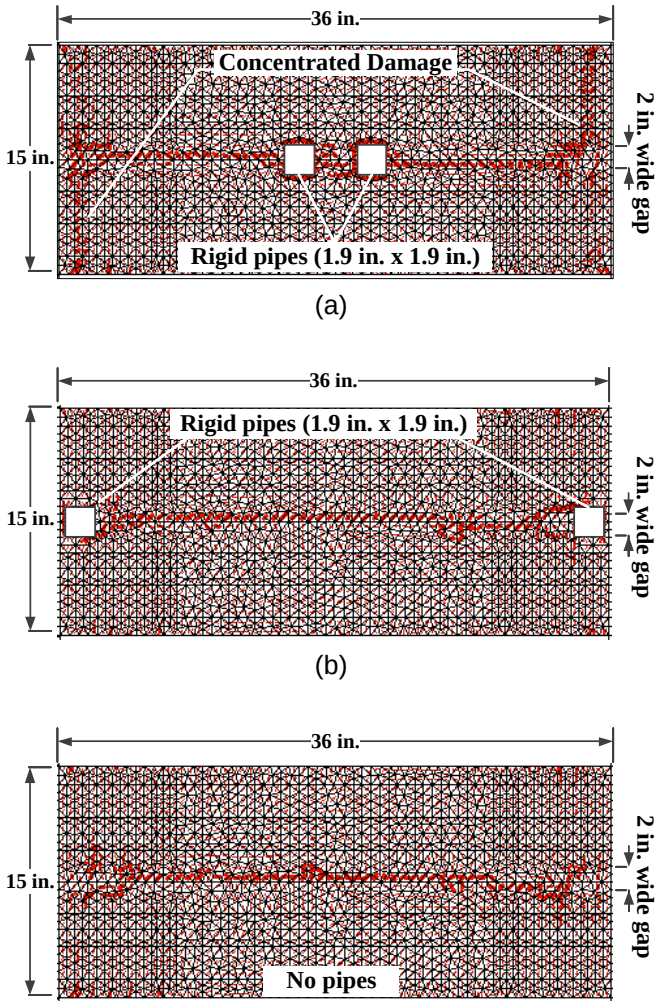

Figure 8.14 Damage patterns of the models at 3% beam chord rotation; (a) DBCB-PM, (b) DBCB-PS, and (c) DBCB

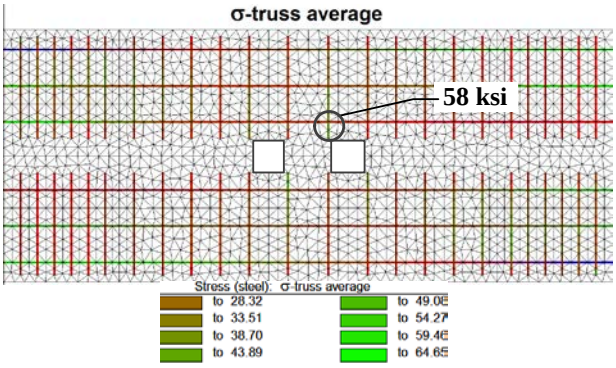

(a)

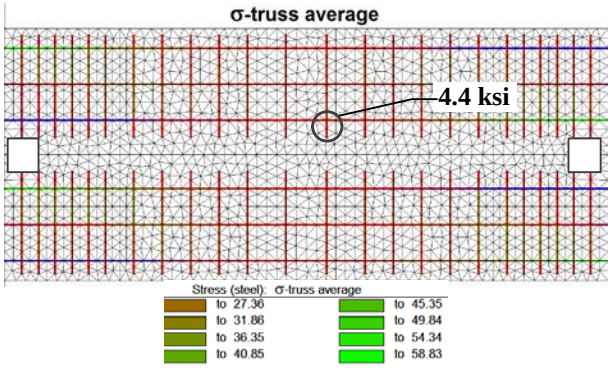

(b)

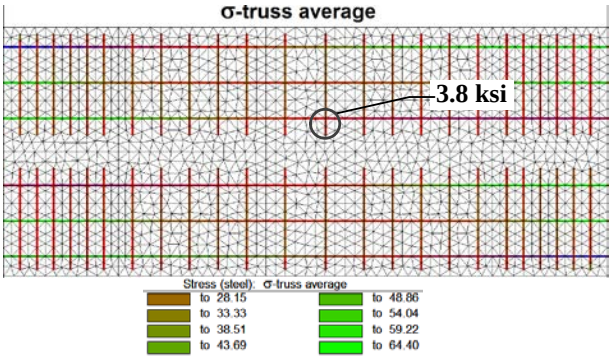

(c)

Figure 8.15 Strain in reinforcement in the models (1% beam chord rotation); (a) DBCB-PM, (b) DBCB-PS, (c) DBCB

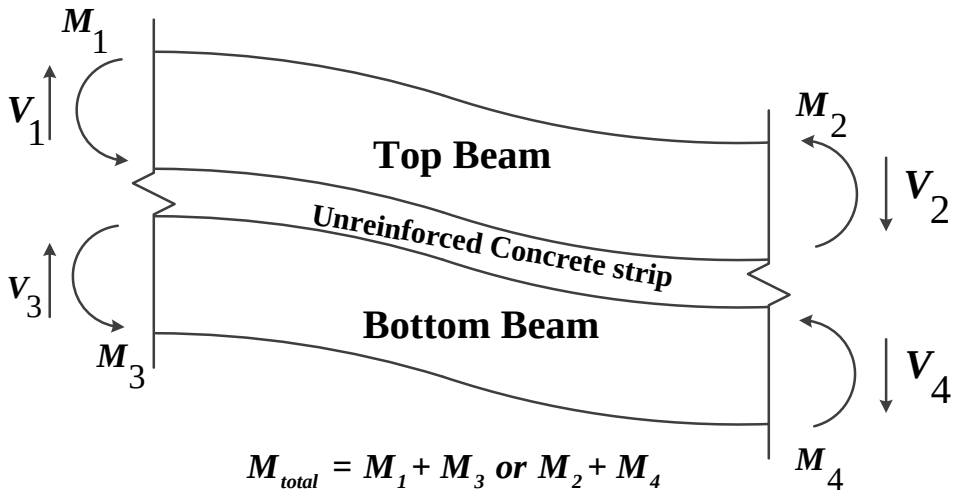

Figure 8.16 Calculation of flexural strength

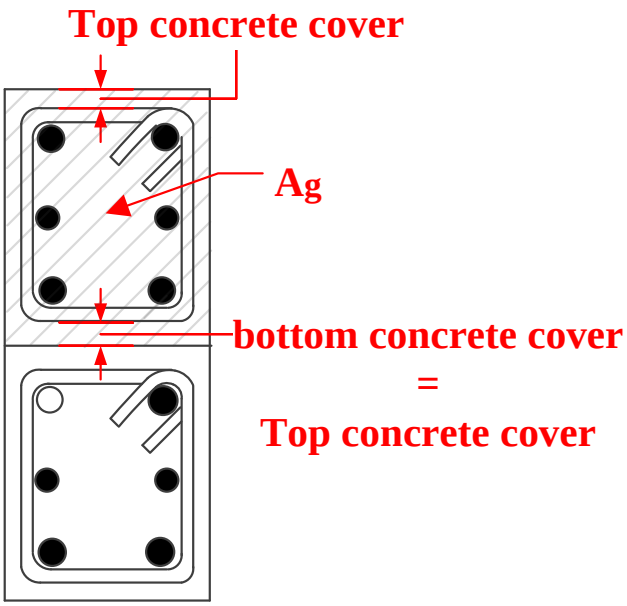

Figure 8.17 Determination of cover thickness

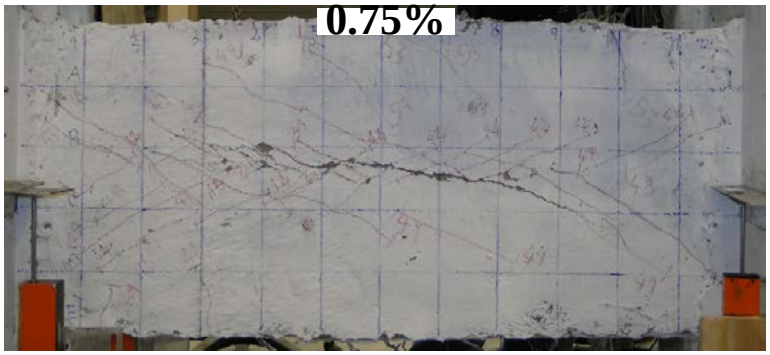

(a)

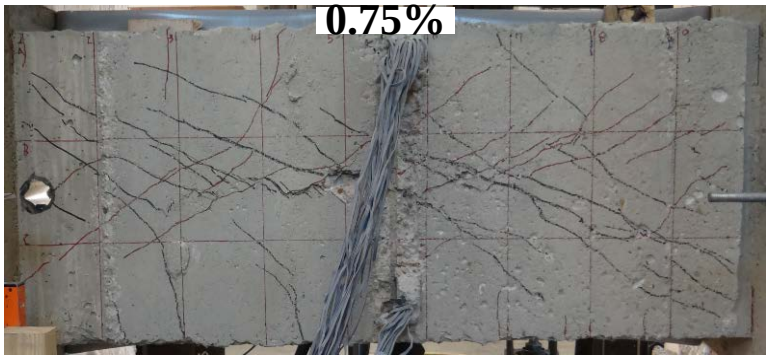

(b)

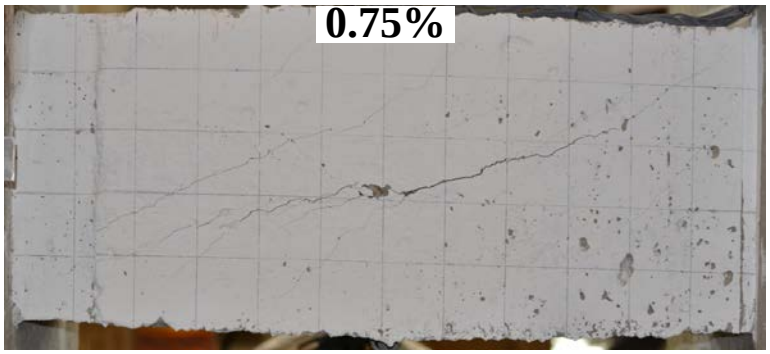

(c)

Figure 8.18 Damage status before separation with various transverse reinforcement ratios ; (a) R2.4-SC-1 (4.9%), (b) R2.4-SC-2-PE (3.7%), and (c) R2.4-SC-2-W

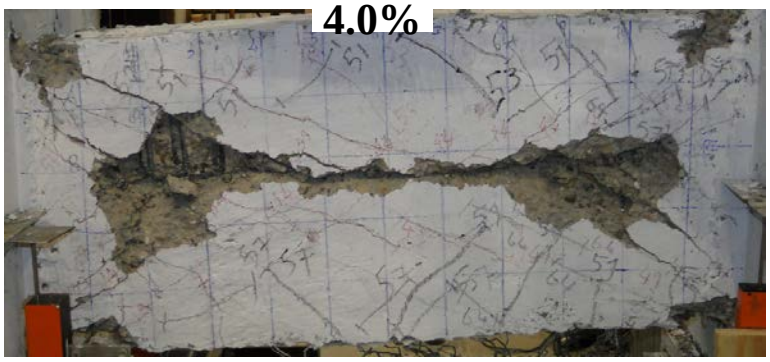

(a)

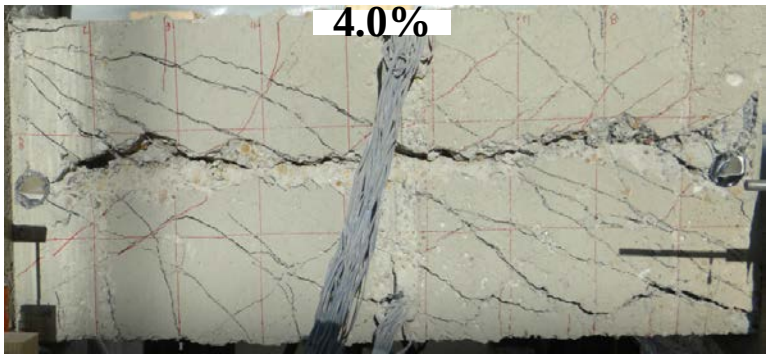

(b)

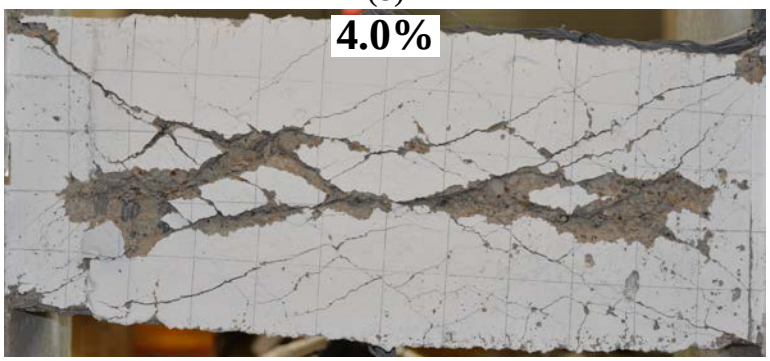

(c)

Figure 8.19 Damage status after separation with various transverse reinforcement ratios ; (a) R2.4-SC-1 (4.9%), (b) R2.4-SC-2-PE (3.7%), and (c) R2.4-SC-2-W

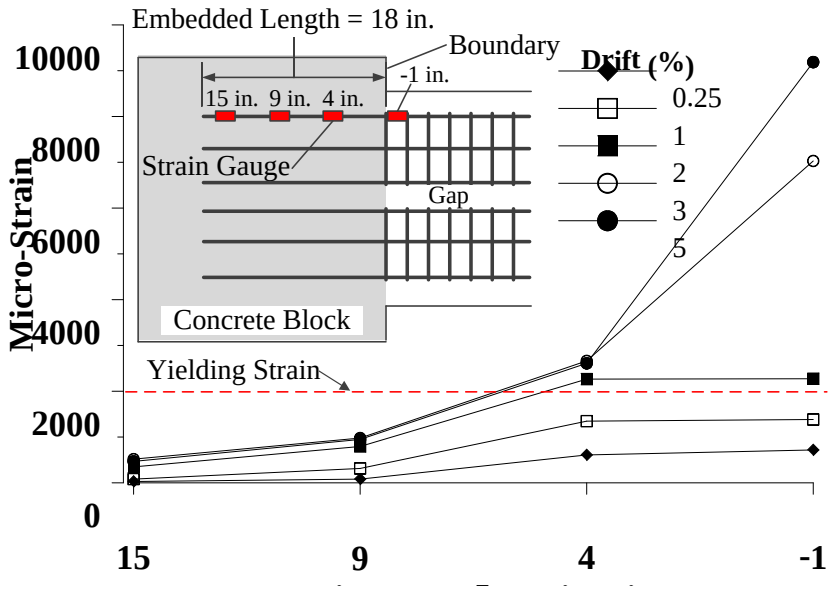

Figure 8.20 Strain of longitudinal bar inside loading block (R2.4-SC-2-P)

Chapter 9

SUMMARY AND CONCLUSION FROM THE SECOND PHASE

This study investigated an innovative and simplistic reinforcing layout for RC coupling beams that can significantly reduce design and construction difficulties when using diagonally reinforced coupling beams. The new double-beam coupling beam (DBCB) consists of two separate cages similar to those used for typical beams in reinforced concrete special moment frames. The two cages are separated by a small spacing from one to two inches. Only vertical and horizontal rebars are needed. Upon large displacements, cracks begin developing at a DBCB's mid-span and mid-height, then gradually propagate towards the beam's ends. The cracks eventually separate the coupling beam into two relatively slender beams where each has nearly twice the aspect ratio of the original coupling beam. This split essentially transforms the shear-dominated single deep beam behavior into a flexure-dominated slender beam behavior. Because damage initiates from the center of the beam, and then spreads towards the ends, the beam ends are able to maintain their integrity even under very large displacements, thereby eliminating the sliding shear failure at the beam-to-wall interface. Although DCBs have excellent seismic performance, they are very difficult to construct with a beam span-to-depth ratio higher than 3. On the other hand, the proposed DBCBs possess simultaneously high shear strength and ductility with a much simpler design and construction process. The width of adjacent walls does not have to be increased due to the required width of coupling beams because the width of DBCBs can be largely reduced compared to DCBs. In addition, the placement of longitudinal rebars in DBCBs can be easily adjusted to accommodate the locations of vertical longitudinal rebars in the

wall pier's boundary elements. Furthermore, diagonal bars in DCBs need to be bent at top floor in order not to protrude into the outer environment it is set in. This could make the construction even harder and affect the force transferring mechanism. On the other hand, DBCBs can easily resolve these issues.

The following conclusions are drawn from the study:

1. The test results on half-scale coupling beam specimens with a span-to-depth ratio of 2.4 and 3.3 showed that coupling beams with the proposed reinforcement scheme were able to simultaneously sustain high shear stresses (10–12$\sqrt{f_{cm}}$, psi)) and large rotations (6–11%) before strength degradation occurred.

2. Experimental results showed that both DBCB and ACI compliant diagonally reinforced coupling beams (DCBs) with a 2.4 span-to depth ratio were able to sustain a high shear stress of 10$\sqrt{f_{cm}}$ (psi) up to 6% beam rotation (approximate rotational demand for MCE ground motion) and Collapse Prevention Performance Level). However, for the specimens with 3.3 span-to-depth ratio, DBCB not only showed better ductility (up to 8% beam rotation) than the DCB (up to 6% beam rotation), but also reached greater shear strength (10$\sqrt{f_{cm}}$ versus 6.6$\sqrt{f_{cm}}$, psi). These improvements offered higher safety by maintaining the structure's stable global response without loss of coupling between walls.

3. The beam-to-wall interface in DBCBs experienced much less damage when compared to that of DCBs; therefore, a smaller development length is required for the longitudinal rebars (approximately 60% of that required by ACI 318-14 Sect. 18.8.5.3(b)).

4. Experimental and nonlinear FEA shows that the height of the unreinforced concrete strip does not have a significant effect on the elastic stiffness of the DBCBs. However, a smaller height (0.25 in. [6.35 mm]) could not separate the two beams before the major diagonal cracks developed, thereby reducing the ductility of the DBCBs. On the other hand, a large height will decrease the moment arm of each beam, leading to a smaller capacity. Nevertheless, this can be easily compensated for by using slightly larger rebars or wider DBCBs with slightly more rebars.

5. Because the cracks at DBCBs always initiate at the mid-span and mid-height, the damage location can be easily accessed, which makes repair work easier after moderate earthquakes. Test results showed that at 1% beam rotation (rotational demand for Immediate Occupancy Performance Level, ACI 374, 2013) DBCBs only had cosmetic concrete cracking and the peak strengths had not yet been reached. The beam-to-wall interfaces were essentially undamaged. This makes repair work easier after moderate earthquakes. This is opposite to DCBs where the major damage is at the beam-wall boundary as a result of the slip and extension of the diagonal bars (Naish et al., 2013), which is in general difficult to repair.

6. Based on the experimental and analytical results, for each individual beam in a DBCB, the span-to-depth ratio should be at least 5.0 to ensure that the unreinforced concrete strip is large enough to allow the DBCB to separate. The depth of each beam was calculated as 0.5 × (depth of entire DBCB minus height of the unreinforced concrete strip).

7. Another potential advantage of DBCBs is that the utility pipes can be passed through the beam at the gap location without compromising the performance. Experimental and nonlinear FEA indicated that the location of these pipes, if placed, can be critical. It is shown that the utility pipes should not be placed at mid-span of DBCBs. A suitable location is at both ends of the beam.

References

ACI Committee 318 (2014). “Building Code Requirements for Structural Concrete (ACI 318-14) and Commentary,” American Concrete Institute, Farmington Hills, MI.

ACI Committee 374 (2013). “Guide for Testing Reinforced Concrete Structural Elements under Slowly Applied Simulated Seismic Loads,” American Concrete Institute, Farmington Hills, MI.

ACI Committee 352 (2002). “Recommendations for Design of Beam-Column Connections in Monolithic Reinforced Concrete Structures,” American Concrete Institute, Farmington Hills, MI.

Blunt, J. D., and Ostertag C. P. (2009). “Deflection Hardening and Workability of Hybrid Fiber Composites,” ACI Materials Journal, V. 106, No. 3, May-Jun 2009, pp. 265-272.

Bonacci, J. and Pantazopoulou, S. (1993). “Parametric Investigation of Joint Mechanics,” ACI Structural Journal, V. 90, No. 1, Jan.-Feb. 1993, pp. 61-71.

Chao, S.-H., Naaman, A. E., Parra-Montesinos, G. J. (2009). “Bond Behavior of Reinforcing Bars in Tensile Strain Hardening Fiber-Reinforced Cement Composites,” ACI Structural Journal, V. 106, No. 6, Nov.-Dec. 2009, pp. 897-906.

Cheung, P. C., Paulay, T., and Park, R. (1991). “New Zealand Tests on Full-Scale Reinforced Concrete Beam-Column-Slab Subassemblages Designed for Earthquake Resistance,” SP-123, American Concrete Institute, Farmington Hills, MI, pp. 1–37.

Choi, J.-H., Stojadinovic, B., and Goel, S. C. (2003). “Design of Free Flange Moment Connection,” Engineering Journal, American Institute of Steel Construction, V. 40, pp. 25-41.

Eligehausen, R., Popov, E. P. and Bertero, V. V. (1983). “Local Bond Stress-Slip Relationships of Deformed Bars under Generalized Excitations,” Report No. 1983/23, Pacific Earthquake Engineering Research Center, Berkeley, CA.

French, C. W. and Moehle, J. P. (1991). “Effect of Floor Slab on Behavior of Slab-Beam-Column Connections,” SP-123, American Concrete Institute, Farmington Hills, MI, pp. 225-258.

Kurose, Y., Guimaraes, G. N., Liu, Z., Kreger, M.E., and Jirsa, J. O. (1988). “Study of Reinforced Concrete Beam-Column Joints under Uniaxial and Biaxial Loading,” PMFSEL Report No. 88-2, The University of Texas at Austin, 146 pp.

Lequesne, R., Setkit, M., Parra-Montesinos, G. J., and Wight, J. K. (2010). “Seismic Detailing and Behavior of Coupling Beams with High-Performance Fiber- Reinforced Concrete,” ACI Special Publication 272, pp. 189-204.

Li, B and Leong, C.-L. (2015). “Experimental and Numerical Investigations of the Seismic Behavior of High-Strength Concrete Beam-Column Joints with Column Axial Load,” Journal of Structural Engineering V. 141, No. 9, pp. 04014220-1 to 04014220-14.

Parra-Montesinos, G. J., Peterfreund, S. W., and Chao, S-H. (2005). “Highly Damage Tolerant Beam-Column Joints Through the Use of High-Performance Fiber Reinforced Cement Composites,” ACI Structural Journal, V. 102, No. 3, May-Jun 2005, pp. 487-495.

Sakai, J., and Kawashima, K. (2003). “Modification of the Giuffre, Menegotto and Pinto Model for Unloading and Reloading Paths with Small Strain Variations,” Journal of Structural Mechanics and Earthquake Engineering, JSCE, No. 738/I-64, 2003, pp. 159-169 (in Japanese).

Visnjic, T., Antonellis, G., Panagiotou, M., and Moehle J. P. (2016). “Large Reinforced Concrete Special Moment Frame Beams under Simulated Seismic Loading,” ACI Structural Journal, V. 113, No. 3, May-Jun 2011, pp. 469-480.

Aktan, A. E., and Bertero, V. V., (1981), *The Seismic Resistant Design of R/C Coupled Structural Walls, Report No. UCB/EERC-81/07*, Earthquake Engineering Research Center, University of California, Berkeley.

Aristizabal-Ochoa, J. D. (1987), “Seismic Behavior of Slender Coupled Wall Systems,” Journal of the Structural Division, V. 113, No. 10, Oct., pp. 2221-2234.

ASCE (2014), ASCE/SEI Standard 41-13 Seismic Evaluation and Retrofit of Existing Buildings American Society of Civil Engineers, Reston, Virginia, USA. 518 pp.

Barney, G. B., Shiu, K. N., Rabbat, B. G., Fiorato, A. E., Russell, H. G., and Corley, W. G. (1980), “Behavior of Coupling Beams Under Load Reversals (RD068.01B),” Portland Cement Association, Skokie, IL.

Canbolat, B. A., Parra-Montesinos, G. J., and Wight, J. K. (2005), “Experimental Study on Seismic Behavior of High-Performance Fiber-Reinforced Cement Composite Coupling Beams,” ACI Structural Journal, V. 102, No. 1, Jan.-Feb., pp. 159-166.

Engindeniz, M., Kahn, L. F., and Zureick, A. –H. (2005), “Repair and Strengthening of Reinforced Concrete Beam-Column Joints: State of the Art,” ACI Structural Journal, V. 102, No. 2, March-April 2005, pp. 1-14

Galano, L., and Vignoli, A., (2000), “Seismic Behavior of Short Coupling Beams with Different Reinforcement Layouts,” ACI Structural Journal, V. 97, No. 6, Nov.-Dec., pp. 876-885.

Harries, K. A., Fortney, P. J., Shahrooz, B.M., and Brienen, P. J. (2005), “Practical Design of Diagonally Reinforced Concrete Coupling Beams” – Critical Review of ACI 318 Requirements, ACI Structural Journal, V. 102, No. 6, Nov.-Dec., pp. 876-882.

Harries, K. A., McNeice, D. S. (2006), “Performance-Based Design of high-Rise Coupling Wall Systems” The Structural Design of Tall and Special Buildings. 15, 289-306.

Hooper, J. D. (2014), “Couplings – Current Practice, Issues, and Opportunities,” ID ORAL20D, Tenth U.S. National Conference in Earthquake Engineering, Earthquake Engineering Research Institute, Anchorage, AK, July 21-25, 2014.

Lequesne, R. D. (2011), “Behavior and Design of High-Performance Fiber-Reinforced Concrete Coupling Beams and Coupled-Wall Systems.” PhD dissertation, Department of Civil and Environmental Engineering, the University of Michigan, Ann Arbor, 277 pp.

Lim, E., Hwang, S. J., Cheng, C. H., and Lin, P. Y. (2016), “Cyclic Tests of Reinforced Concrete Coupling Beam with Intermediate Span-Depth Ratio,” ACI Structural Journal, V. 113, No. 3, May-June., pp. 515-524.

Moehle, J. P., Ghodsi, T., Hooper, J. D., Fields, D. C., and Gedhada, R. (2011), *Seismic Design of Cast-In-Place Concrete Special Structural Walls and Coupling Beams: A Guide*

for Practicing Engineers, NEHRP Seismic Design Technical Brief No. 6, produced by the NEHRP Consultants Joint Venture, a partnership of the Applied Technology Council and the Consortium of Universities for Research in Earthquake Engineering, for the National Institute of Standards and Technology, Gaithersburg, MD, NIST GCR 11-917-11REV-1.

Moehle, J., Seismic Design of Reinforced Concrete Buildings, McGraw-Hill Education, 2015, 760 pp.

Naish, D., Wallace, J., Fry, J. A., and Klemencic, R. (2009), Reinforced Concrete Link Beams: Alternative Details for Improved Constructability, Report to Charles Pankow Foundation. UCLA-SGEL, 103 pp.

Naish, D., Fry, J. A., Klemencic, R., and Wallace, J. (2013), "Reinforced Concrete Coupling Beams—Part I: Testing," ACI Structural Journal, V. 110, No. 6, Nov.-Dec., pp. 1057-1066.

Park, R. and Paulay, T. (1975), Reinforced Concrete Structures, John Wiley & Sons, 769 pages.

Paulay, T., and Binney, J. R. (1974), "Diagonally Reinforced Coupling Beams of Shear Walls," Shear in Reinforced Concrete, SP-42, V. 2, American Concrete Institute, Farmington Hills, Mich., pp. 579-598. Paulay, T. (1969), "The Coupling of Shear Walls." PhD dissertation, Department of Civil Engineering, University of Canterbury, Christchurch, New Zwaland, 432 pp.

Paulay, T. (1977), "Ductility of Reinforced Concrete Shearwalls for Seismic Areas," ACI-Special Publication, SP-53, Jan., pp. 127-148.

Tassios, T. P., Moretti, M., and Bezas A. (1996), “On the Behavior and Ductility of Reinforced Concrete Coupling Beams of Shear Walls,” ACI Structural Journal, V. 93, No. 6, Nov.-Dec., pp. 711-720.

Teshigawara, M., Kato, M., Sugaya, K., and Matsushima, Y. (1998), “Energy Absorption Mechanism and the Fluctuation of shear Force in the Coupled shear Walls,” Structural Engineering World Wide 1998 – Proceedings, Paper Number T-186-5, Elsevier Science Ltd., 8 pp.

Wong, P. K. C, Priestley, M. J. N., and Park, R. (1990), “Seismic Resistance of Frames with Vertically Distributed Longitudinal Reinforcement in Beams,” ACI Structural Journal, V. 87, No. 4, Jul.-Aug., pp. 488-498.

Wong, P. S. and Vecchio, F. J. (2002), “VecTor2 & Formworks User’s Manual,” August.

Xoao, Y., Esmaeily-Ghasemabadi, A., and Wu, H. (1999), High-Strength Concrete Short Beams Subjected to Cyclic Shear,” ACI Structural Journal, V. 96, No. 3, May.-June., pp. 392-400.

Biographical Information

Youngjae Choi received his Ph.D. degree from The University of Texas at Arlington. His research focuses on design and behavior of reinforced concrete structures subjected to extreme loads.